New methods and applications of ptychography

Wei, X.

DOI
10.4233/uuid:d9491dbc-5649-4eb9-be1f-163ecf727d04

Publication date
2022

Document Version
Final published version

Citation (APA)
Wei, X. (2022). *New methods and applications of ptychography*. [Dissertation (TU Delft), Delft University of Technology]. https://doi.org/10.4233/uuid:d9491dbc-5649-4eb9-be1f-163ecf727d04

NEW METHODS AND APPLICATIONS OF PTYCHOGRAPHY

NEW METHODS AND APPLICATIONS OF PTYCHOGRAPHY

Proefschrift

ter verkrijging van de graad van doctor
aan de Technische Universiteit Delft,
op gezag van de Rector Magnificus Prof.dr.ir. T.H.J.J. van der Hagen,
voorzitter van het College voor Promoties,
in het openbaar te verdedigen op
maandag 14 maart 2022 om 10:00 uur

door

Xukang WEI

Bachelor of Science in Applied Physics,
Nankai University, Tianjin, China,
geboren te Tianjin, China.

Dit proefschrift is goedgekeurd door de

promotor: prof. dr. H.P. Urbach
copromotor: dr. O. El Gawhary

Samenstelling promotiecommissie:

Rector Magnificus,	voorzitter
Prof. dr. H.P. Urbach,	Technische Universiteit Delft, promotor
Dr. O. El Gawhary,	Technische Universiteit Delft, copromotor

Onafhankelijke leden:

Dr. A. Menzel,	Paul Scherrer Institute, Switzerland
Dr. S. Witte,	Vrije Universiteit Amsterdam
Prof. dr. A.P. Mosk,	Universiteit Utrecht
Prof. dr. S. Stallinga,	Technische Universiteit Delft
Prof. dr. G. Vdovine,	Technische Universiteit Delft, reservelid

Overige leden:
Prof. dr. W.M.J.M. Coene,
Technische Universiteit Delft

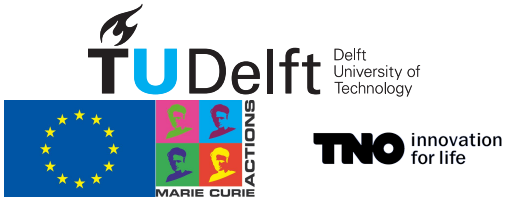

This PhD project is funded under H2020 Marie Skłodowska-Curie Actions (Grant ID: 675745).

Keywords: computational imaging, ptychography, Cramér Rao Lower Bound, parameter retrieval
Printed by: Ridderprint
Front & Back: X. Wei

ISBN 978-94-6384-308-9

An electronic version of this dissertation is available at
http://repository.tudelft.nl/.

CONTENTS

SUMMARY

This thesis addresses new methods and applications of ptychography which is a scanning Coherent Diffraction Imaging(CDI) method for reconstructing a complex valued object function from intensity measurements recorded in the Fraunhofer or Fresnel diffraction region. The technique provides a solution to the so-called 'phase problem' and is found to be very suitable for Extreme Ultraviolet (EUV) and X-ray imaging applications due to its high fidelity and its minimum requirement on optical imaging elements. Moreover, abundant studies show that ptychography is able to provide a wide field-of-view and retrieve the illumination probe also. During the last two decades, ptychography has been successfully demonstrated with X-ray radiation sources, electron beams and visible light sources.

Chapter 1 is an introductory chapter which gives an overview of CDI techniques. The goal is to provide the necessary knowledge so that readers with different background can easily understand the following chapters. This chapter contains three parts. For the first part we introduce the problem statement of CDI, the approximations that are commonly used in CDI, i.e. the projection approximation, the Fraunhofer approximation, and the required conditions of these approximations. This part also includes the introduction about the discrete Fourier transform, the chirp-Z transform, the issue of sampling and the coherence requirements. The second part of this chapter gives a brief introduction about iterative and non-iterative phase retrieval methods in CDI. For the final part of this chapter, we discuss the fundamental of ptychography which is the main topic of this thesis. We first derive an iterative ptychographic algorithm based on the steepest descent method, then explain the extended field-of-view and the ambiguities in ptychography. Some of the recent developments of ptychography are included in this part as well.

For performing phase retrieval in the EUV regime more efficiently, developing polychromatic ptychography is desirable. As an alternative to the existing ptychographic information multiplexing (PIM) method, we present in **Chapter 2** an another scheme where all monochromatic exit waves are expressed in terms of the amplitude of the transmission function and the thickness function of the object. Our proposed algorithm is a gradient based method and its validity is studied numerically. In addition, the sampling issue which appears in the polychromatic ptychography scheme and its influence to the reconstruction quality are discussed.

In **Chapter 3** we investigate the performance of ptychography with noisy data by analyzing the Cramér Rao Lower Bound (CRLB). The lower bound of ptychography is derived and numerically computed for both top-hat plane wave and structured illumination. The influence of Poisson noise on the ptychography reconstruction is discussed. The computation result shows that, if the estimator is unbiased, the minimum variance for Poisson noise is mostly determined by the illumination power and the transmission function of the object. Monte Carlo analysis is conducted to validate our calculation results for different photon flux numbers. Furthermore, the performance of the maximum

likelihood method and the approach of amplitude-based cost function minimization is studied in the Monte Carlo analysis.

In **Chapter 4** we present a parameter retrieval method which combines ptychography and additional prior knowledge about the object. The proposed method is applied to two applications: (1) parameter retrieval of small particles from Fourier ptychographic dark field measurements; (2) parameter retrieval of a rectangular structure with real-space ptychography. The influence of Poisson noise is discussed in the second part of the chapter. The CRLB in both applications is computed and Monte Carlo analysis is used to verify the calculated lower bound. With the computation results we report the lower bound for various noise levels and the correlation of particles in application 1. For application 2 the correlation of parameters of the rectangular structure is discussed.

The thesis is concluded with **Chapter 5** where the main contribution of this thesis is listed. Furthermore, the unfinished work during my PhD and the possible extensions of the topics discussed in this thesis are addressed in this last chapter.

1

INTRODUCTION

1

1.1. INTRODUCTION OF CDI

Coherent Diffraction Imaging (CDI) is a class of computational imaging approaches, where an object is illuminated by a fully coherent light beam and the scattered light is collected by an electronic image sensor array. The technique is useful in wavelength ranges where imaging components are not available or difficult to use. In CDI, the object of interest can be 2D or 3D, reflective or transmissive. The detected light is an electromagnetic wavefield which typically oscillates at $10^{14} \sim 10^{19}$Hz. This oscillation is too rapid to be captured by the image sensor, hence only the time-averaged intensity of the wavefield can be measured. For this reason, half of the information, namely the phase, of the wavefield is lost if we do not consider any polarization effect. Therefore, the reconstruction of the object is mostly unsatisfactory. This is called 'the phase problem' because one needs to find a way to recover the phase, i.e. the wavefront, of the wavefield, so that sufficient knowledge about the wavefield is obtained and backward propagation of the wavefield can be done [1–4]. Solving the phase problem is crucial in x-ray microscopy [5–11], electron microscopy [12–14], astronomy [15, 16], optical microscopy [17, 18] and other signal processing applications. The computational methods that are designed to solve the phase problem are called 'phase retrieval' algorithms [2, 4, 19–23]. These algorithms are particularly useful when other phase-imaging techniques, e.g. holographic methods [24–26], Shack-Hartmann sensing [27–29], etc., are not available or unpractical. One of the recently developed phase retrieval algorhtms, namely ptychography [30–36], is the main topic that is addressed in thesis. Note that the polarization effects are neglected throughout this thesis since they are used in Chapter 2 - Chapter 5.

1.1.1. FUNDAMENTALS OF CDI

Let us first consider the configuration as shown in Fig. 1.1, which is a simplified transmission setup for a CDI experiment and has been often used in the CDI literature. However, it is worth noting that there are other configurations where the same CDI algorithms can be applied, as will be discussed later in this chapter.

In Fig. 1.1, a fully coherent light beam with temporal frequency ω, denoted by P, is used to illuminate an object of interest, with complex transmission function O. The light wave propagates through the object and is scattered by it. The exit wave immediately transmitted or reflected by the object propagates through free space and forms a diffraction pattern. The intensity I of the diffracted wavefield is recorded by a 2D image detector, e.g. a charge-coupled device (CCD). The goal of CDI is to reconstruct the complex valued object function O from the measured diffraction pattern.

Fig. 1.1 is a lensless imaging setup. Compared to conventional lens-based imaging systems, it has the following advantages:

(1) It is possible to retrieve the complex valued transmission function, i.e. the amplitude and the phase of the object, without using a reference beamline. This is because the wavefront deviation introduced by the object is encoded in the recorded pattern due to diffraction. However, we note that we have to retrieve the phase of the field in detector plane.

(2) Suppose one can reconstruct the complex transmission function of the object from the recorded coherent diffraction pattern, the resolution of the reconstruction is not

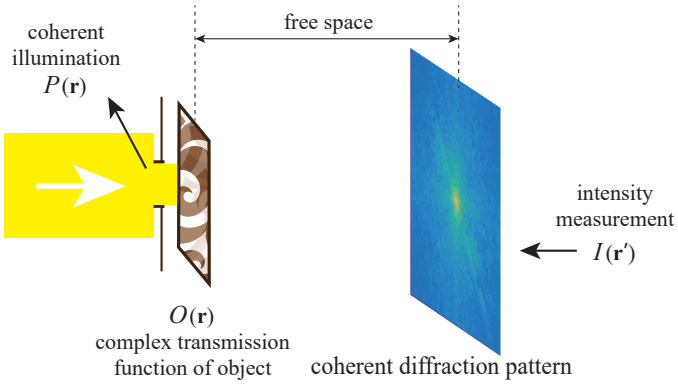

Figure 1.1: A simplified setup illustrating a CDI experiment.

limited by any imaging optics. The resolution is then only limited by noise and by the numerical aperture defined by the size of the detector.

MODELING OF THE WAVEFIELD

Throughout this thesis, we consider the object and the free space as consisting of a linear, isotropic and nonmagnetic media, and furthermore that free space is lossless. The object may partially absorb the wavefield. In this thesis we use a Cartesian coordinate system $[x, y, z]^T$ where the z-axis coincides with the optical axis of the system. Let $\mathbf{r}$ be the position vector of a point in real space:

$$\mathbf{r} = [x, y, z]^T = [\mathbf{r}_\perp, z]^T, \tag{1.1}$$

where $\mathbf{r}_\perp$ denotes the transverse coordinates $\mathbf{r}_\perp = [x, y]^T$

The governing equations which describe the propagation of the wavefield both inside and outside the object are Maxwell's equations [25, 37–41]:

$$\nabla \cdot \mathbf{D}(\mathbf{r}, t) = 0, \tag{1.2}$$
$$\nabla \cdot \mathbf{B}(\mathbf{r}, t) = 0, \tag{1.3}$$
$$\nabla \times \mathbf{E}(\mathbf{r}, t) = \frac{\partial \mathbf{B}(\mathbf{r}, t)}{\partial t}, \tag{1.4}$$
$$\nabla \times \mathbf{H}(\mathbf{r}, t) = \frac{\partial \mathbf{D}(\mathbf{r}, t)}{\partial t}. \tag{1.5}$$

Here $\mathbf{E}(\mathbf{r}, t)$ is the electrical field and $\mathbf{B}(\mathbf{r}, t)$ the magnetic strength, $\mathbf{D}(\mathbf{r}, t)$ and $\mathbf{H}(\mathbf{r}, t)$ are auxiliary fields which are the magnetic field, respectively. Assuming the bandwidth of the light is sufficiently narrow, $\mathbf{E}$, $\mathbf{D}$, $\mathbf{B}$ and $\mathbf{H}$ in linear and isotropic media are related by:

$$\mathbf{D}(\mathbf{r}, t) = \epsilon_0 \mathbf{E}(\mathbf{r}, t), \tag{1.6}$$
$$\mathbf{B}(\mathbf{r}, t) = \mu_0 \mathbf{H}(\mathbf{r}, t), \tag{1.7}$$

where ϵ_0 is the relative permittivity and μ_0 the relative permeability of the medium. Combining Eq. (1.2) - Eq. (1.7), we can derive:

$$\nabla^2\mathbf{E}(\mathbf{r},t) - \frac{\epsilon_0\mu_0}{c}\frac{\partial^2}{\partial t^2}\mathbf{E}(\mathbf{r},t) = 0, \tag{1.8}$$

$$\nabla^2\mathbf{H}(\mathbf{r},t) - \frac{\epsilon_0\mu_0}{c}\frac{\partial^2}{\partial t^2}\mathbf{H}(\mathbf{r},t) = 0, \tag{1.9}$$

where c is the speed of light in vacuum. Suppose we neglect the polarization effects, it is seen that every Cartesian components of $\mathbf{E}$ and $\mathbf{H}$ obeys the same scalar differential equation:

$$\nabla^2 U(\mathbf{r},t) - \frac{\epsilon\mu}{c}\frac{\partial^2}{\partial t^2}U(\mathbf{r},t) = 0. \tag{1.10}$$

A generic method for solving Eq. (1.10) is the technique of separation of variables, in which the wavefield is written in the form of a time-harmonic field:

$$U(\mathbf{r},t) = U(\mathbf{r})e^{-\mathrm{i}\omega t}, \tag{1.11}$$

where $\omega > 0$. Substituting Eq. (1.11) into Eq. (1.10) leads us to the Helmholtz equation:

$$\nabla^2 U(\mathbf{r}) + k^2 n_{\mathrm{r}}^2(\mathbf{r})U(\mathbf{r}) = 0, \tag{1.12}$$

where $k = 2\pi/\lambda$ denotes the wave number and $n_{\mathrm{r}} = \sqrt{\epsilon\mu}$ is the refractive index of the medium, and λ is the wavelength in vacuum.

FREE SPACE PROPAGATION AND PLANE WAVE EXPANSION

In free space the refractive index is 1, therefore a wavefield U_{f}, which propagates propagating in free space, obeys:

$$\nabla^2 U_{\mathrm{f}}(\mathbf{r}) + k^2 U_{\mathrm{f}}(\mathbf{r}) = 0. \tag{1.13}$$

Note that we will not consider polarization effect in this thesis. Suppose we want to study the propagation of the wavefield from plane $z = 0$ to plane $z = z'$, as shown in Fig. 1.2. Let $\mathbf{k}$ be 3D Cartesian coordinates in reciprocal space:

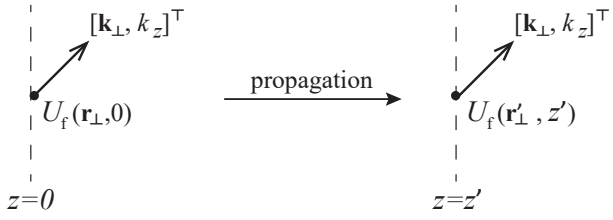

Figure 1.2: The propagation of the wavefield in free space.

$$\mathbf{k} = \left[k_x, k_y, k_z\right]^T = [\mathbf{k}_\perp, k_z]^T. \tag{1.14}$$

The definition of k_z and its sign can be found in Eq. (1.18).

We start by Fourier transforming U_f with respect to (w.r.t.) $\mathbf{r}_\perp$:

$$\mathscr{F}_\perp\left(U_\mathrm{f}\right)(\mathbf{k}_\perp, z) = \int U_\mathrm{f}(\mathbf{r}_\perp, z) e^{-\mathrm{i}\mathbf{k}_\perp\cdot\mathbf{r}_\perp} d\mathbf{r}_\perp, \tag{1.15}$$

where $\mathscr{F}_\perp$ denotes 2D Fourier transform. The inverse Fourier transform is given by:

$$U_\mathrm{f}(\mathbf{r}_\perp, z) = \mathscr{F}_\perp^{-1}\left(\mathscr{F}_\perp\left(U_\mathrm{f}\right)\right)(\mathbf{r}_\perp, z) = \frac{1}{4\pi^2}\int \mathscr{F}_\perp\left(U_\mathrm{f}\right) e^{\mathrm{i}\mathbf{k}_\perp\cdot\mathbf{r}_\perp} d\mathbf{k}_\perp. \tag{1.16}$$

By substituting Eq. (1.16) into Eq. (1.13), it follows that:

$$\frac{\partial^2}{\partial z^2}\mathscr{F}_\perp\left(U_\mathrm{f}\right) = -\left(k^2 - |\mathbf{k}_\perp|^2\right)\mathscr{F}_\perp\left(U_\mathrm{f}\right). \tag{1.17}$$

Eq. (1.17) has two fundamental solutions and one of which is given by:

$$\mathscr{F}_\perp\left(U_\mathrm{f}\right)(\mathbf{k}_\perp, z) = \mathscr{F}_\perp\left(U_\mathrm{f}\right)(\mathbf{k}_\perp, 0) e^{\mathrm{i}\sqrt{k^2-|\mathbf{k}_\perp|^2}z} = \mathscr{F}_\perp\left(U_\mathrm{f}\right)(\mathbf{k}_\perp, 0) e^{\mathrm{i}k_z z}. \tag{1.18}$$

The another solution is given by replacing $e^{\mathrm{i}\sqrt{k^2-|\mathbf{k}_\perp|^2}z}$ and $e^{\mathrm{i}k_z z}$ in Eq. (1.18) by $e^{-\mathrm{i}\sqrt{k^2-|\mathbf{k}_\perp|^2}z}$ and $e^{-\mathrm{i}k_z z}$, respectively. Here the square root $k_z = \sqrt{k^2 - |\mathbf{k}_\perp|^2}$ is positive imaginary when $|\mathbf{k}_\perp| > k$ and is positive real otherwise. The first case occurs for evanescent waves, the latter for propagating waves. In this thesis we choose to use the solution given in Eq. (1.18) so that the wave propagates or is exponentially decreasing along the $+z$ direction. Combining Eq. (1.16) and Eq. (1.18) we conclude:

$$U_\mathrm{f}(\mathbf{r}_\perp, z) = \int e^{\mathrm{i}(\mathbf{k}_\perp\cdot\mathbf{r}_\perp + k_z z)} \cdot \mathscr{F}_\perp\left(U_\mathrm{f}\right)(\mathbf{k}_\perp, 0) d\mathbf{k}_\perp, \tag{1.19}$$

where $e^{\mathrm{i}(\mathbf{k}_\perp\cdot\mathbf{r}_\perp + k_z z)}$ can be regarded as a plane wave and $\mathscr{F}_\perp\left(U_\mathrm{f}\right)(\mathbf{k}_\perp, 0)$ can be regarded the spatial field of a plane wave with wave vector $\mathbf{k} = [\mathbf{k}_\perp, k_z]^T$. Therefore, Eq. (1.19) shows that the wavefield U_f is a superposition of infinitely many propagating plane waves and evanescent waves in the free space. In this thesis, evanescent waves are not of interest. Although the integral Eq. (1.19) includes evanescent waves, i.e. waves with $|\mathbf{k}_\perp| > k$, we shall omit these waves in the rest of this thesis.

THE WAVEFIELD FROM A SCATTERING OBJECT

When a scattering object with a volume V is excited by a time-harmonic incident field U_in, it is common to write the total wavefield U as:

$$U(\mathbf{r}) = U_\mathrm{in}(\mathbf{r}) + U_\mathrm{scat}(\mathbf{r}), \tag{1.20}$$

where U_scat is the scattered field. U_in and U_scat satisfy:

$$\nabla^2 U_\mathrm{in}(\mathbf{r}) + k^2 U_\mathrm{in}(\mathbf{r}) = 0, \tag{1.21}$$

$$\nabla^2 U_\mathrm{scat}(\mathbf{r}) + k^2 U_\mathrm{scat}(\mathbf{r}) = -k^2\left(n_\mathrm{r}^2(\mathbf{r}) - 1\right)U(\mathbf{r}). \tag{1.22}$$

To solve Eq. 1.22, a scalar Green's function $G(\mathbf{r}',\mathbf{r})$ is used [40], which satisfies:

$$\nabla'^2 G(\mathbf{r}',\mathbf{r}) + k^2 G(\mathbf{r}',\mathbf{r}) = -\delta_{\mathrm{D}}(\mathbf{r}'-\mathbf{r}), \tag{1.23}$$

and $\delta_{\mathrm{D}}(\mathbf{r}) = \delta_{\mathrm{D}}(x)\delta_{\mathrm{D}}(y)\delta_{\mathrm{D}}(z)$ is the Dirac delta function which is defined such that for every continuous function $f(t)$:

$$\int_{-\infty}^{\infty} f(t)\delta_{\mathrm{D}}(t-t')dt = f(t'). \tag{1.24}$$

In free space, $G(\mathbf{r}',\mathbf{r})$ is an outgoing spherical wave given by:

$$G\left(\mathbf{r}',\mathbf{r}\right) = \frac{1}{4\pi}\frac{e^{\mathrm{i}k|\mathbf{r}'-\mathbf{r}|}}{|\mathbf{r}'-\mathbf{r}|}, \tag{1.25}$$

which is a spherical wave with amplitude decreasing with distance to the point source. By substituting Eq. (1.23) into Eq. (1.22) we have [25, 41]:

$$U_{\mathrm{scat}}(\mathbf{r}') = \int k^2\left(n_{\mathrm{r}}^2(\mathbf{r})-1\right)U(\mathbf{r})G(\mathbf{r}',\mathbf{r})d\mathbf{r}, \tag{1.26}$$

and hence the total wavefield is:

$$U(\mathbf{r}') = U_{\mathrm{in}}(\mathbf{r}') + \int k^2\left(n_{\mathrm{r}}^2(\mathbf{r})-1\right)U(\mathbf{r})G(\mathbf{r}',\mathbf{r})d\mathbf{r}, \tag{1.27}$$

which is a very useful equation, called the Lippmann-Schwinger integral equation, for solving the forward scattering problem, i.e. computing $U(\mathbf{r}')$ when $U_{\mathrm{in}}(\mathbf{r})$ and $n_{\mathrm{r}}^2(\mathbf{r})-1$ are known. Eq. (1.27) is also useful for solving the inverse scattering problem, i.e. computing $n_{\mathrm{r}}^2(\mathbf{r})-1$ provided that $U(\mathbf{r}')$ has been measured for a set of incident fields $U_{\mathrm{in}}(\mathbf{r})$. However, the inverse problem is considered difficult to be solved both analytically and numerically [42]. To gain some insight, it is convenient to make the assumption that the scattering object is weakly scattering and sufficiently thin, because then the Lippmann-Schwinger integral equation can be simplified.

THE WEAK SCATTERING APPROXIMATION

Now we focus on the wavefield scattered by the object U_{scat}. When the volume of the object is sufficiently small and the refractive index of the object is close to that of free space, i.e. $n_{\mathrm{r}}^2(\mathbf{r})-1$ is sufficiently small, one can approximate U_{scat} by [25]:

$$U_{\mathrm{scat}}(\mathbf{r}') \approx U_{\mathrm{scat}}^{(1)}(\mathbf{r}') = \int k^2\left(n_{\mathrm{r}}^2(\mathbf{r})-1\right)U_{\mathrm{in}}(\mathbf{r})G(\mathbf{r}',\mathbf{r})d\mathbf{r}, \tag{1.28}$$

which is the weak scattering approximation or the first Born approximation. In this approximation we assume the object is only excited by the incident beam and multiple scattering can be neglected. Note that when $n_{\mathrm{r}}^2(\mathbf{r})-1$ is large, the higher order of the Born series have to be considered and the multiple scattering effect must be included in the model [25]. This requires that the Lippmann-Schwinger equation is solved numerically. Alternatively, higher order Born approximations could be computed, however

the Born series typically does not converge when the optical contrast is larger. To nevertheless the Born series, one can apply a Pade approximant [42]. However, the strong scattering regime is out of the scope of this thesis and hence we assume that the weak scattering approximation is valid throughout this thesis.

In most applications of CDI, it is common that the size of the scattering object is much smaller than the distance between the object and the detector, i.e. $|\mathbf{r}'| \gg |\mathbf{r}|$. For this case the Green's function can be approximated by:

$$G(\mathbf{r}',\mathbf{r}) \approx \frac{1}{4\pi}\frac{e^{ik|\mathbf{r}'|}}{|\mathbf{r}'|} e^{-ik\frac{|\mathbf{r}|^2}{2|\mathbf{r}'|}} e^{-ik\frac{\mathbf{r}'\cdot\mathbf{r}}{|\mathbf{r}'|}}, \qquad \text{the Fresnel approximation,} \tag{1.29}$$

$$\approx \frac{1}{4\pi}\frac{e^{ik|\mathbf{r}'|}}{|\mathbf{r}'|} e^{-ik\frac{\mathbf{r}'\cdot\mathbf{r}}{|\mathbf{r}'|}}, \qquad \text{the Fraunhofer approximation.} \tag{1.30}$$

By substituting Eq. (1.30) into Eq. (1.28) we get:

$$\begin{aligned} U^{(1)}_{\text{scat}}(\mathbf{r}') &\approx \frac{k^2}{4\pi}\frac{e^{ik|\mathbf{r}'|}}{|\mathbf{r}'|}\int \left(n_{\text{r}}^2(\mathbf{r})-1\right) U_{\text{in}}(\mathbf{r}) e^{-ik\frac{\mathbf{r}'\cdot\mathbf{r}}{|\mathbf{r}'|}} d\mathbf{r} \\ &= \frac{k^2}{4\pi}\frac{e^{ik|\mathbf{r}'|}}{|\mathbf{r}'|}\mathscr{F}\left[\left(n_{\text{r}}^2(\mathbf{r})-1\right) U_{\text{in}}(\mathbf{r})\right]\left(k\frac{\mathbf{r}'}{|\mathbf{r}'|}\right), \end{aligned} \tag{1.31}$$

where $\mathscr{F}$ is 3D Fourier transform. It is seen that, within the weak scattering and the Fraunhofer approximation, the amplitude of the scattered wavefield $U^{(1)}_{\text{scat}}$ is the 3D Fourier transform of $\left(n_{\text{r}}^2-1\right)U_{\text{in}}$. If U_{in} is a plane wave and hence can be written as $e^{i\mathbf{k}_{\text{in}}\cdot\mathbf{r}}$, the scattered wavefield can be written as:

$$U^{(1)}_{\text{scat}}(\mathbf{r}') \approx \frac{k^2}{4\pi}\frac{e^{ik|\mathbf{r}'|}}{|\mathbf{r}'|}\mathscr{F}\left[\left(n_{\text{r}}^2(\mathbf{r})-1\right)\right]\left(k\frac{\mathbf{r}'}{|\mathbf{r}'|}-\mathbf{k}_{\text{in}}\right). \tag{1.32}$$

If the scattering is elastic, i.e. wavenumber of the scattered wavefield equals $|\mathbf{k}_{\text{in}}|$, then Eq. (1.32) is the 3D Fourier transform of $\left(n_{\text{r}}^2(\mathbf{r})-1\right)$ evaluated on a part of a sphere in reciprocal space, namely the Ewald sphere. In this thesis we stay within the elastic scattering regime and the Fraunhofer approximation (adaptation to the case of detectors at Fresnel distances are straightforward).

THE PARAXIAL DIFFRACTION FORMULAS AND THE PROJECTION APPROXIMATION

Since U_{in} is a solution of Eq. (1.21), i.e. the Helmholtz equation in free space, it is allowed to expand U_{in} into plane waves as in Eq. (1.19). By substituting Eq. (1.19) into Eq. (1.31) we have:

$$U_{\text{scat}}(\mathbf{r}') \approx \frac{k^2}{4\pi}\frac{e^{ik|\mathbf{r}'|}}{|\mathbf{r}'|}\int U_{\text{in}}(\mathbf{r}_\perp,0) e^{-ik\frac{\mathbf{r}'_\perp\cdot\mathbf{r}_\perp}{|\mathbf{r}'|}} d\mathbf{r}_\perp \int_{-z_o}^{0} \left(n_{\text{r}}^2(\mathbf{r})-1\right) e^{i\left(k_z z - k\frac{z'z}{|\mathbf{r}'|}\right)} dz, \tag{1.33}$$

where z_o is the thickness of the scattering object which is contained in the slab $-z_o \le z \le 0$ and z' is the detector plane, as shown in Fig. 1.3.

To further simplify the model, it is common to use the paraxial approximation. That is, only the part of the scattered wavefield which predominately propagates in the positive z-direction is measured by the detector. Therefore, we can write:

$$|\mathbf{r}'| \approx z', \qquad \text{and} \qquad k \approx k_z. \tag{1.34}$$

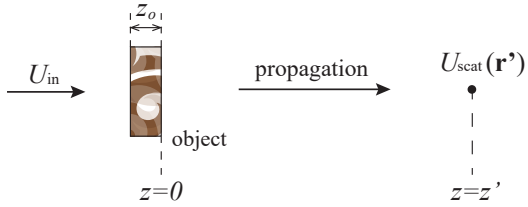

Figure 1.3: The propagation of the wavefield when the scattering object is present.

By applying Eq. (1.34) in the exponential terms in Eq. (1.33), we get:

$$\begin{aligned} U_{\text{scat}}(\mathbf{r}') &\approx \frac{k^2}{4\pi}\frac{e^{\mathrm{i}kz'}}{|\mathbf{r}'|}\int U_{\text{in}}(\mathbf{r}_\perp,0)e^{-\mathrm{i}\frac{k}{z'}\mathbf{r}'_\perp\cdot\mathbf{r}_\perp}d\mathbf{r}_\perp\int_{-z_o}^{0}\left(n_{\text{r}}^2(\mathbf{r})-1\right)dz \\ &\approx \frac{k^2}{4\pi}\frac{e^{\mathrm{i}kz'}}{|\mathbf{r}'|}\mathscr{F}_\perp\left[U_{\text{in}}(\mathbf{r}_\perp,0)\int_{-z_o}^{0}\left(n_{\text{r}}^2(\mathbf{r})-1\right)dz\right]\left(\frac{k}{z'}\mathbf{r}'_\perp\right), \end{aligned} \tag{1.35}$$

which is the 2D Fourier transform of $U_{\text{in}}(\mathbf{r}_\perp,0)\int_{-z_o}^{0}\left(n_{\text{r}}^2(\mathbf{r})-1\right)dz$. The approximation which has led us to Eq. (1.35) is also called the projection approximation or flat Ewald sphere approximation [43]. The validity of the projection approximation has been studied in [12, 35]. Suppose the transverse resolution of the reconstructed object is Δr along the x and y axis, then it was found that the projection approximation is valid when the thickness satisfies:

$$z_o \lesssim \frac{2|\Delta r|^2}{\lambda} = \frac{2\lambda}{|\lambda/\Delta r|^2}. \tag{1.36}$$

The derivation of Eq. (1.36) is given in [12, 35]. Note that $\lambda\left(|\lambda/\Delta r|^2\right)^{-1}$ is sometimes called the depth-of-focus (DoF) [44, 45].

THE PROBLEM STATEMENT IN CDI

We have shown that, in the projection approximation and the Fraunhofer region, the scattered wavefield $U_{\text{scat}}(\mathbf{r}'_\perp,z')$ is the 2D Fourier transform of $U_{\text{in}}(\mathbf{r}_\perp,0)\int_{-z_o}^{0}\left(n_{\text{r}}^2(\mathbf{r})-1\right)dz$ with an energy scaling factor $k^2\left(4\pi\left|\mathbf{r}'\right|\right)^{-1}$. In most of the literature about CDI, it is common to assume that the scattering object is a thin slab, which means the exit wave immediately behind the object can be written by:

$$\Psi(\mathbf{r}_\perp) = P(\mathbf{r}_\perp)\cdot O(\mathbf{r}_\perp), \tag{1.37}$$

and hence the complex valued diffracted wavefield can be written by:

$$\mathscr{F}_\perp[\Psi]\left(\frac{k}{z'}\mathbf{r}'_\perp\right) = \int \Psi(\mathbf{r}_\perp)e^{-\mathrm{i}\frac{k}{z'}\mathbf{r}'_\perp\cdot\mathbf{r}_\perp}d\mathbf{r}_\perp, \tag{1.38}$$

All fields $\Psi(\mathbf{r}_\perp)$, $P(\mathbf{r}_\perp)$ and $O(\mathbf{r}_\perp)$ are complex valued 2D functions in the plane $z=0$. P and O are the complex probe function and transmission function of the object, respectively. It is seen in Eq. (1.35) that, in the first Born approximation, the 2D functions P

and O correspond to:

$$P^{(1)}(\mathbf{r}_\perp) = U_{\text{in}}(\mathbf{r}_\perp, 0), \qquad O^{(1)}(\mathbf{r}_\perp) = 1 + \int_{-z_o}^{0} \left(n_{\text{r}}^2(\mathbf{r}) - 1\right) dz, \tag{1.39}$$

with the energy scaling factor omitted. The subscription (1) in Eq. (1.39) means the function is in the first Born approximation. However, this interpretation is not complete. This is because we are assuming that $\mathscr{F}_\perp[\Psi]$ is the scattered field far away at $\mathbf{r}'$ and that the projection approximation is valid. Developing a more precise model of the scattered wavefield, which also applies to an object that is not thin, is being researched by many groups currently. Some of the recent progress will be briefly reviewed later in this chapter.

Throughout this thesis, we will use the notation used in Eq. (1.37) and Eq. (1.38). The main problem in CDI is the 'phase problem', i.e. how to retrieve $O(\mathbf{r}_\perp)$ or $\Psi(\mathbf{r}_\perp)$ from the intensity measurements of the far field diffraction, given by:

$$I(\mathbf{r}'_\perp, z') = \left| \int \Psi(\mathbf{r}_\perp) e^{-\text{i}\frac{k}{z'}\mathbf{r}'_\perp \cdot \mathbf{r}_\perp} d\mathbf{r}_\perp \right|^2. \tag{1.40}$$

where Ψ is given by Eq. (1.37).

1.1.2. THE DISCRETE FOURIER TRANSFORM AND THE Z-TRANSFORM

In practice, $I(\mathbf{r}'_\perp, z')$ is measured by a 2D detector with discrete pixels. Therefore, I is sampled on a meshgrid of $\mathbf{r}'$ at plane $z = z'$. Since I is the absolute square of the 2D Fourier transform of the exit wave $\Psi(\mathbf{r}_\perp)$, it is reasonable to also approximate $\Psi(\mathbf{r}_\perp)$ by a 2D array. Let $\mathbf{n}_{\mathbf{r},\perp}$ and $\mathbf{n}_{\mathbf{k},\perp}$ be the indices of 2D rectangular and uniform meshgrids in real space and reciprocal space, respectively:

$$\mathbf{n}_{\mathbf{r},\perp} = \left[n_{\mathbf{r},x}, n_{\mathbf{r},y}\right]^T, \qquad \mathbf{n}_{\mathbf{k},\perp} = \left[n_{\mathbf{k},x}, n_{\mathbf{k},y}\right]^T, \tag{1.41}$$

and let $\Delta\mathbf{r}_\perp$ and $\Delta\mathbf{k}_\perp$ be translation factors of adjacent cells of the periodic 2D real and reciprocal meshgrids:

$$\Delta\mathbf{r}_\perp = \left[\Delta x, \Delta y\right]^T, \qquad \Delta\mathbf{k}_\perp = \left[\Delta k_x, \Delta k_y\right]^T. \tag{1.42}$$

The mesh points of the grids can be written as:

$$\mathbf{r}_\perp = \mathbf{n}_{\mathbf{r},\perp}\Delta\mathbf{r}_\perp, \qquad \mathbf{k}_\perp = \mathbf{n}_{\mathbf{k},\perp}\Delta\mathbf{k}_\perp. \tag{1.43}$$

The 2D Fourier transform is approximated by the 2D discrete Fourier transform (DFT) on these meshes, i.e.:

$$\mathscr{F}_\perp(\Psi)(\mathbf{k}_\perp) = \sum_{\mathbf{n}_{\mathbf{r},\perp}}^{N_x,N_y} \Psi(\mathbf{r}_\perp) e^{-\text{i}2\pi n_{\mathbf{r},x} n_{\mathbf{k},x}/N_x} e^{-\text{i}2\pi n_{\mathbf{r},y} n_{\mathbf{k},y}/N_y}, \tag{1.44}$$

where N_x and N_y are the number of pixels of the 2D array along the x-axis and y-axis, respectively. Note that the pixel spacing $\Delta\mathbf{r}_\perp$ and $\Delta\mathbf{k}_\perp$ are assumed to fulfill the Nyquist sampling, i.e.:

$$\left[\Delta x, \Delta y\right]^T = 2\pi \left[(N_x\Delta k_x)^{-1}, (N_y\Delta k_y)^{-1}\right]^T. \tag{1.45}$$

In practice, the Fast Fourier Transform algorithm (FFT) is the most commonly used choice for computing the DFT.

There exists a generalization of the DFT, namely the chirp Z-transform (CZT) [46–48]. In the CZT the pixel spacing $\Delta\mathbf{r}_\perp$ and $\Delta\mathbf{k}_\perp$ can be sampled arbitrarily, therefore the CZT can be used to calculate spectrum in the reciprocal space on a finer mesh. To show an example, we start by re-writing the 1D Fourier series along the x-axis in a more generic form, using the symbol W. For 1D DFT along the x-axis, we have:

$$\mathscr{F}_x(\Psi)(k_x) = \sum_{n_{\mathbf{r},x}}^{N_x} \Psi(n_{\mathbf{r},x}\Delta x)\cdot e^{-\mathrm{i}2\pi n_{\mathbf{r},x} n_{\mathbf{k},x}/N_x} = \sum_{n_{\mathbf{r},x}}^{N_x} \Psi(n_{\mathbf{r},x}\Delta x)\cdot W^{n_{\mathbf{r},x} n_{\mathbf{k},x}}, \tag{1.46}$$

where $W^{n_{\mathbf{r},x}} = e^{-\mathrm{i}2\pi n_{\mathbf{r},x}/N_x}$ is a complex valued sinusoidal waveform. To adjust the pixel spacing in the reciprocal space is equivalent to evaluate this waveform on a finer mesh along the x-axis. This can be done by replacing W by a power W^s, yields:

$$\mathrm{CZT}_x(\Psi)(sk_x) = \sum_{n_{\mathbf{r},x}}^{N_x} \Psi\cdot\left(W^s\right)^{n_{\mathbf{r},x} n_{\mathbf{k},x}}, \tag{1.47}$$

It has been shown [46, 49] that one can compute the CZT by applying twice the FFT and once the inverse FFT. Hence the computation time required for the CZT is around 3 times more than the FFT. The CZT is a very popular choice when it is needed to compute the Fourier transform on a finer mesh than the one implied by Nyquist's criterion.

1.1.3. SAMPLING REQUIREMENT

Since now the exit wave Ψ and the intensity measurement I have been approximated by discretized 2D arrays, the 'phase problem' we need to address becomes to reconstruct the array $\Psi(\mathbf{r}_\perp)$ from the data given by:

$$I(\mathbf{r}'_\perp, z') = \left| \sum_{\mathbf{n}_{\mathbf{r},\perp}}^{N_x,N_y} \Psi(\mathbf{r}_\perp) e^{-\mathrm{i}\frac{2\pi}{\lambda z'} n_{\mathbf{r},x} n'_{\mathbf{r},x}/N_x} e^{-\mathrm{i}\frac{2\pi}{\lambda z'} n_{\mathbf{r},y} n'_{\mathbf{r},y}/N_y} \right|^2. \tag{1.48}$$

It is seen that, $\Psi(\mathbf{r}_\perp)$ consists of $2\times N_x\times N_y$ real independent variables because Ψ is a complex valued wavefield. However, I is a 2D array consisting of $N_x\times N_y$ real valued numbers. Hence Eq. (1.48) contains $N_x\times N_y$ equations and $2\times N_x\times N_y$ unknowns, hence is a under-determined system. In conventional CDI [5, 19], this under-sampling problem is addressed by imposing a finite size boundary support to $\Psi(\mathbf{r}_\perp)$, as shown in Fig. 1.4. We can write the boundary support as:

$$\Psi(\mathbf{r}_\perp) = \begin{cases} \Psi(\mathbf{r}_\perp), & \mathbf{r}_\perp \in S, \\ 0, & \mathbf{r}_\perp \notin S. \end{cases} \tag{1.49}$$

where S denotes the pixels in the object plane in which Ψ is nonzero. Furthermore, an over-sampling factor is defined by:

$$\sigma_S = \frac{N_x\times N_y}{\text{the number of pixels in } S}. \tag{1.50}$$

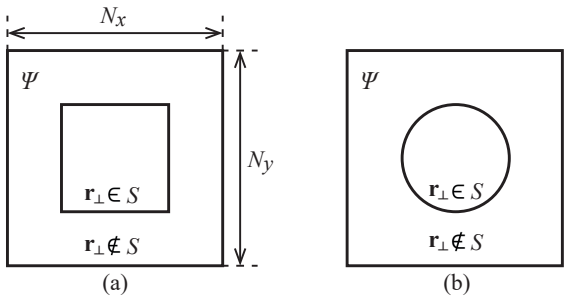

Figure 1.4: (a) Illustration of a rectangular boundary support. (b) Illustration of a circular boundary support.

To be able to solve the equation system in Eq. (1.48), it is reasonable to let $\sigma_S = 2$, because in this way the number of unknown and the number of measurements are the same. This is the oversampling criteria proposed in [5]. It was shown [50] that one needs a larger σ_S, e.g. $\sigma_S \approx 5$, so that Ψ can be successfully reconstructed with noisy data.

Another relevant remark about the sampling criteria is that, since we are measuring the absolute square of the Fourier transform of Ψ, we need to sample the intensity at the Nyquist sampling interval of $|\mathscr{F}(\Psi)|^2(\mathbf{k}_\perp)$ in reciprocal space [51]. This sampling interval is two times finer than the Nyquist sampling interval of $\mathscr{F}(\Psi)(\mathbf{k}_\perp)$. The reason is that the inverse Fourier transform of $|\mathscr{F}(\Psi)|^2(\mathbf{k}_\perp)$ is the auto-correlation of $\Psi(\mathbf{r}_\perp)$, and the support of the auto-correlation of $\Psi(\mathbf{r}_\perp)$ is two time larger than the support of $\Psi(\mathbf{r}_\perp)$, as shown in Fig. 1.5. To make the sampling interval in reciprocal space two times finer,

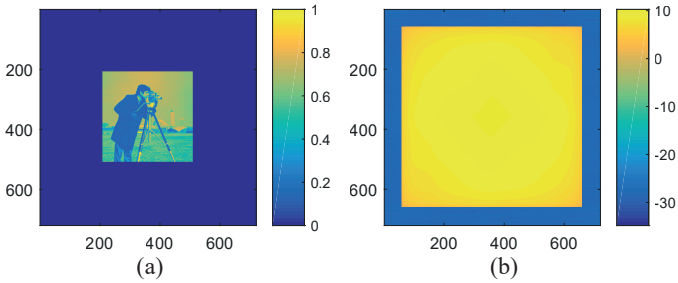

Figure 1.5: (a) An example of the discretized exit wave $\Psi(\mathbf{r}_\perp)$ with a rectangular support. (b) The nature logarithm of the auto-correlation of $\Psi(\mathbf{r}_\perp)$, i.e. $\ln\left[\mathscr{F}^{-1}\left(|\mathscr{F}(\Psi)|^2\right)\right]$.

it is reasonable to choose the size of the 2D grid in ordinary space twice as big (i.e. the surface area is four times as big) as the support S. In this case we have $\sigma_S = 4$, which is a more demanding oversampling criterion than the one given in [5].

In practice, the proper support can be realized by e.g. placing an aperture in front of the object. The size and the shape of this support is assumed to be known and is used during the reconstruction. It should be remarked that these over-sampling requirement can be released by increasing the information of the data. For instance, it was claimed [52] that one does not have to fulfill the above sampling requirement in ptychography, however it is still an open question to what extend the sampling requirement can be re-

1

laxed. Ptychography will be introduced and discussed in more detail later in this chapter.

1.1.4. COHERENCE REQUIREMENT

We have been assuming so far that the wavefield is fully coherent and hence perfectly monochromatic. However, such a light source does not exist. Therefore, it is necessary to find out the tolerances are on the degree of coherence for the light source so that our model can be used.

SPATIAL COHERENCE REQUIREMENT

First we consider the case that the illumination to be quasi-monochromatic, which means that its temporal spectrum only consists of one narrow peak and the effect of its bandwidth is negligible. If we focus on the wavefield radiated from two separate points in the object plane $z = 0$, denoted by $\Psi_1(\mathbf{r}_{\perp,1})$ and $\Psi_2(\mathbf{r}_{\perp,2})$, as shown in Fig. 1.6. The intensity

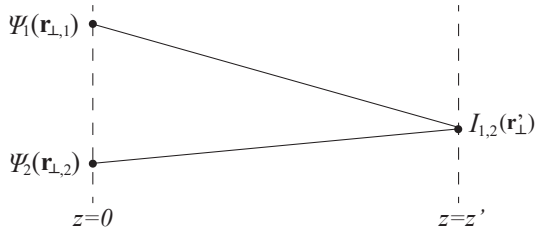

Figure 1.6: The propagation of the wavefield in free space.

of the diffracted wavefield in the detector plane is given by:

$$I_{1,2}(\mathbf{r}'_{\perp}) = |\mathscr{F}_{\perp}(\Psi_1)|^2 + |\mathscr{F}_{\perp}(\Psi_2)|^2 + |\mathscr{F}_{\perp}(\Psi_1)||\mathscr{F}_{\perp}(\Psi_2)|\gamma_{1,2}(\mathbf{r}_{\perp,1}, \mathbf{r}_{\perp,2}), \tag{1.51}$$

where $\gamma_{1,2}$ is the complex degree of coherence and $|\gamma_{1,2}|$ represents the degree of coherence between the two points $\mathbf{r}_{\perp,1}$ and $\mathbf{r}_{\perp,2}$. In Young's interference experiment, the value of $|\gamma_{1,2}|$ equals the visibility of fringes that are produced when two pinholes at $\mathbf{r}_{\perp,1}$ and $\mathbf{r}_{\perp,2}$ are illuminated with equal intensity [25]. It is seen that $\gamma_{1,2}$ is a 4D function and has $(N_x \times N_y)^2$ variables. To simplify the model, it is common and convenient to assume that the degree of coherence is translational invariant, i.e. $|\gamma_{1,2}|(\mathbf{r}_{\perp,1}, \mathbf{r}_{\perp,2}) = |\gamma_{1,2}|(|\mathbf{r}_{\perp,1} - \mathbf{r}_{\perp,2}|)$. When $|\gamma_{1,2}| = 1$ the wavefield at the two points are fully coherent, when $|\gamma_{1,2}| = 0$ the wavefield at the two points are incoherent. It was shown [53] that, if the extent in the x and y direction of the object are L_x and L_y, the exit wavefield can be considered as fully coherent when:

$$|\gamma_{1,2}|(|\mathbf{r}_{\perp,1} - \mathbf{r}_{\perp,2}|) = 1, \qquad \text{for} \quad |\mathbf{r}_{\perp,1} - \mathbf{r}_{\perp,2}| \leq 2 \times |\mathbf{L}_{\perp}|, \tag{1.52}$$

where $|\mathbf{L}_{\perp}| = \sqrt{|L_x|^2 + |L_y|^2}$. In other words, the transverse coherence width at the sample should be two time larger than the finite extent of the object support. This coherence requirement agrees with the sampling requirement given in the previous section, because the nonzero area of the domain of the auto-correlation of $\Psi(\mathbf{r}_{\perp})$, which needs to be sampled at Nyquist frequency, is two time larger than the object support.

TEMPORAL COHERENCE REQUIREMENT

Now we assume that an illumination consists of two distinct wavelengths λ and $\lambda + \Delta\lambda$, and we assume that for each wavelength the wavefield is fully spatially coherent. The measured intensity in the far field I is the incoherent sum over all monochromatic diffraction patterns, because the measured averages over time of the interference between different wavelengths is canceled. It is seen in Eq. (1.40) that, the radiated wavefield for different wavelength have different scattering angles, which means that the diffraction pattern scales differently for different wavelengths. For our mono-chromatic model, it is necessary that this different scaling of the diffraction pattern is negligible compared to the spacing of the pixels of the detector. We consider the scaling difference of the diffraction patterns along the x-axis as an example. Suppose we have a fixed meshgrid in object plane x. Then for different wavelengths λ and $\lambda + \Delta\lambda$ we get different grids x'_λ and $x'_{\lambda+\Delta\lambda}$ according to the Nyquist's criterion. Suppose the size of the cells of the grid x'_λ is $\Delta x'_\lambda$, we require $\Delta\lambda$ to be so small that:

$$\begin{aligned} \max\left(x'_{\lambda+\Delta\lambda}\right) - \max\left(x'_\lambda\right) &\leq \Delta x'_\lambda, \\ \frac{(\lambda+\Delta\lambda)z'}{\Delta x} - \frac{\lambda z'}{\Delta x} &\leq \frac{\lambda z'}{N_x \Delta x}, \\ \Delta\lambda &\leq \frac{\lambda}{N_x}. \end{aligned} \tag{1.53}$$

1.2. PHASE RETRIEVAL METHODS

To solve the phase problem, many methods have been proposed since the 1970s. Modern phase retrieval methods in CDI heavily depend on the use of modern computer and either are iterative computation algorithms or direct inversion algorithms. In this section we discuss a few of many phase retrieval methods which appear frequently in the recent research literature.

1.2.1. PHASE RETRIEVAL METHODS USING A SINGLE DIFFRACTION MEASUREMENT

GERCHBERG-SAXTON ALGORITHM

In conventional CDI, only one diffraction pattern is measured. The first successful phase retrieval method in conventional CDI is the iterative algorithm proposed by Gerchberg and Saxton in 1972 [2]. For this algorithm, it is required that both the intensity of the diffraction pattern and the exit wave, denoted by $I(\mathbf{k}_\perp)$ and $|\Psi_o(\mathbf{r}_\perp)|^2$, respectively, are known. These two intensities are used to perform a projection operation in the Fourier plane and the object plane, respectively. Suppose that $\Psi_n(\mathbf{r}_\perp)$ is the obtained exit wave after the nth iteration. The projection operation in the Fourier plane, denoted by π_F, is defined by replacing the amplitude of the diffracted wavefield $|\mathscr{F}(\Psi_n)(\mathbf{k}_\perp)|$ by $\sqrt{I(\mathbf{k}_\perp)}$. While the projection operation in the object plane, denoted by π_O, is defined by replacing $|\Psi_n(\mathbf{r}_\perp)|$ by the known amplitude $|\Psi_o(\mathbf{r}_\perp)|$. In summary, the Gerchberg-Saxton algo-

rithm is given by:

$$\Psi_{n+1}(\mathbf{r}_\perp) = \pi_O \pi_F [\Psi_n(\mathbf{r}_\perp)] = |\Psi_o(\mathbf{r}_\perp)| \frac{\mathscr{F}_\perp^{-1}\left[\sqrt{\frac{I(\mathbf{k}_\perp)}{|\mathscr{F}_\perp(\Psi_n)(\mathbf{k}_\perp)|^2}}\mathscr{F}_\perp(\Psi_n)(\mathbf{k}_\perp)\right]}{\left|\mathscr{F}_\perp^{-1}\left[\sqrt{\frac{I(\mathbf{k}_\perp)}{|\mathscr{F}_\perp(\Psi_n)(\mathbf{k}_\perp)|^2}}\mathscr{F}_\perp(\Psi_n)(\mathbf{k}_\perp)\right]\right|}, \tag{1.54a}$$

$$\pi_F [\Psi_n(\mathbf{r}_\perp)] = \mathscr{F}_\perp^{-1}\left[\sqrt{\frac{I(\mathbf{k}_\perp)}{|\mathscr{F}_\perp(\Psi_n)(\mathbf{k}_\perp)|^2}}\mathscr{F}_\perp(\Psi_n)(\mathbf{k}_\perp)\right], \tag{1.54b}$$

$$\pi_O [\Psi_n(\mathbf{r}_\perp)] = |\Psi_o(\mathbf{r}_\perp)| \frac{\Psi_n(\mathbf{r}_\perp)}{|\Psi_n(\mathbf{r}_\perp)|}, \tag{1.54c}$$

where the subscript n is the iteration index. In fact, the known amplitude $|\Psi_o(\mathbf{r}_\perp)|$ is a very powerful *a priori* knowledge. Therefore the Gerchberg-Saxton algorithm is famous for it fast convergent speed, i.e. the algorithm can provide the solution after only a few iterations.

It should be remarked that there is an alternative way to understand the Gerchberg-Saxton algorithm. Suppose the field $\Psi(\mathbf{r}_\perp)$ fulfills the requirement that the intensity of its diffraction pattern and its exit wave are $I(\mathbf{k}_\perp)$ and $|\Psi_o(\mathbf{r}_\perp)|^2$, respectively. Then we have the nonlinear equation of $\Psi(\mathbf{r}_\perp)$:

$$\Psi(\mathbf{r}_\perp) = |\Psi_o(\mathbf{r}_\perp)| \frac{\mathscr{F}_\perp^{-1}\left[\sqrt{\frac{I(\mathbf{k}_\perp)}{|\mathscr{F}_\perp(\Psi)(\mathbf{k}_\perp)|^2}}\mathscr{F}_\perp(\Psi)(\mathbf{k}_\perp)\right]}{\left|\mathscr{F}_\perp^{-1}\left[\sqrt{\frac{I(\mathbf{k}_\perp)}{|\mathscr{F}_\perp(\Psi)(\mathbf{k}_\perp)|^2}}\mathscr{F}_\perp(\Psi)(\mathbf{k}_\perp)\right]\right|}, \tag{1.55}$$

which can be solved by using iterative algorithms. If we apply the method of fixed-point iteration to Eq. (1.55), we will arrive at the same formula as Eq. (1.54a).

THE ERROR-REDUCTION ALGORITHM

Although the Gerchberg-Saxton algorithm is a robust method, it requires one must know the intensity of the wavefield in the sample plane. In 1978, Fienup developed the Error-Reduction (ER) algorithm [3] in which use is made of knowledge of the support of the object while the intensity of the object field is not needed. The ER algorithm can be written as follows:

$$\Psi_{n+1}(\mathbf{r}_\perp) = \pi_O \pi_F [\Psi_n(\mathbf{r}_\perp)] = \begin{cases} \mathscr{F}_\perp^{-1}\left[\sqrt{\frac{I(\mathbf{k}_\perp)}{|\mathscr{F}_\perp(\Psi_n)(\mathbf{k}_\perp)|^2}}\mathscr{F}_\perp(\Psi_n)(\mathbf{k}_\perp)\right], & \mathbf{r}_\perp \in S, \\ 0, & \mathbf{r}_\perp \notin S, \end{cases} \tag{1.56a}$$

$$\pi_F [\Psi_n(\mathbf{r}_\perp)] = \mathscr{F}_\perp^{-1}\left[\sqrt{\frac{I(\mathbf{k}_\perp)}{|\mathscr{F}_\perp(\Psi_n)(\mathbf{k}_\perp)|^2}}\mathscr{F}_\perp(\Psi_n)(\mathbf{k}_\perp)\right], \tag{1.56b}$$

$$\pi_O [\Psi_n(\mathbf{r}_\perp)] = \begin{cases} \Psi_n(\mathbf{r}_\perp), & \mathbf{r}_\perp \in S, \\ 0, & \mathbf{r}_\perp \notin S, \end{cases} \tag{1.56c}$$

where S is the finite size boundary support constraint in real space, as shown in Eq. (1.49). Again we note that Eq. (1.56a) can be interpreted as a fix-point iteration algo-

rithm which solves the nonlinear equation:

$$\Psi(\mathbf{r}_\perp) = \mathbf{1}_S(\mathbf{r}_\perp)\mathscr{F}_\perp^{-1}\left[\sqrt{\frac{I(\mathbf{k}_\perp)}{|\mathscr{F}_\perp(\Psi)(\mathbf{k}_\perp)|^2}}\mathscr{F}_\perp(\Psi)(\mathbf{k}_\perp)\right](\mathbf{r}_\perp), \tag{1.57}$$

where $\mathbf{1}_S(\mathbf{r}_\perp)$ is a binary window function representing the object support:

$$\mathbf{1}_S(\mathbf{r}_\perp) = \begin{cases} 1, & \mathbf{r}_\perp \in S, \\ 0, & \mathbf{r}_\perp \notin S. \end{cases} \tag{1.58}$$

It is seen that the ER algorithm does not require the intensity of the wavefield in the sample plane, but only requires one to know the support of the object, i.e. the region where the exit wave is nonzero. Compared to the Gerchberg-Saxton algorithm, this relaxed requirement is very convenient, because one can easily estimate the support S by observing the auto-correlation of $\Psi(\mathbf{r}_\perp)$. The auto-correlation can be computed provided that the diffraction measurement is over-sampled, as shown in Fig. 1.5. Furthermore, it was shown [19, 54] that the ER algorithm can be formulated as the minimization of an error functional, which can solved using a gradient descent scheme. This property guarantees that the error functional decreases after every iterations. However, if the landscape of the error function has many local minima and if the starting point is far from the actual solution, it can happen that the algorithm stagnates at one of the local minimums.

THE HYBRID-INPUT-OUTPUT ALGORITHM AND THE DIFFERENCE-MAP ALGORITHM

In an attempt to solve the stagnation problem of the ER algorithm, the Hybrid-Input-Output (HIO) algorithm was proposed in 1982 [19]. In this work, the HIO algorithm is given by:

$$\Psi_{n+1}(\mathbf{r}_\perp) = \begin{cases} \pi_F[\Psi_n(\mathbf{r}_\perp)], & \mathbf{r}_\perp \in S, \\ \left(1-\beta\pi_F\right)[\Psi_n(\mathbf{r}_\perp)], & \mathbf{r}_\perp \notin S, \end{cases} \tag{1.59a}$$

$$\pi_F[\Psi_n(\mathbf{r}_\perp)] = \mathscr{F}_\perp^{-1}\left[\sqrt{\frac{I(\mathbf{k}_\perp)}{|\mathscr{F}_\perp(\Psi_n)(\mathbf{k}_\perp)|^2}}\mathscr{F}_\perp(\Psi_n)(\mathbf{k}_\perp)\right], \tag{1.59b}$$

where β is a coefficient which is normally chosen be 0.8. Many studies have shown that [7, 9, 17, 55–57] the HIO algorithm is superior to the ER algorithm in the sense that the HIO algorithm can escape from converging to local minima and can find the global minima, provided that the diffraction intensity measurement is noise-free. However, for noisy measurements, the HIO algorithm is sometimes unstable as well, therefore its convergence is not guaranteed in practice. Based on these studies, it is now common to use the HIO algorithm for the first few iterations, and then use the ER algorithm in the final stages of the algorithm.

Although the HIO method was proposed in the 1980s, the reason why the method often works has not been fully understood until 2003. It was shown by Elser [20, 58, 59] that when the feedback coefficient β is 1, the HIO algorithm is the same as the difference-map (DM) method. The later algorithm is formulated in terms of finding the intersection of two constraint sets [20]. The original formula of the DM method has three auxiliary

parameters which need to be properly chosen. A common way of implementing the DM algorithm is:

$$\Psi_{n+1} = \Psi_n + \pi_O\left[2\pi_F\left(\Psi_n\right) - \Psi_n\right] - \pi_F\left(\Psi_n\right), \tag{1.60a}$$

$$\pi_F\left[\Psi_n(\mathbf{r}_\perp)\right] = \mathscr{F}_\perp^{-1}\left[\sqrt{\frac{I(\mathbf{k}_\perp)}{\left|\mathscr{F}_\perp\left(\Psi_n\right)(\mathbf{k}_\perp)\right|^2}}\mathscr{F}_\perp\left(\Psi_n\right)(\mathbf{k}_\perp)\right], \tag{1.60b}$$

$$\pi_O\left[\Psi_n(\mathbf{r}_\perp)\right] = \begin{cases} \Psi_n(\mathbf{r}_\perp), & \mathbf{r}_\perp \in S, \\ 0, & \mathbf{r}_\perp \notin S, \end{cases} \tag{1.60c}$$

Following the idea of finding the intersection solution of two constraint sets, many other phase retrieval approaches have been proposed [57], e.g. the hybrid projection–reflection method [60], the relaxed averaged alternating reflections approach [21] and others.

THE SHRINK-WRAP APPROACH

It is seen that all phase retrieval algorithms require *a priori* knowledge about the domain of the object (except for the Gerchberg-Saxton algorithm where one must know the wavefield intensity in the sample plane). In fact, the quality of the reconstruction always relies on how accurately the support is known. To release this requirement, the so-called 'shrink-wrap' method was proposed [7]. The idea is to update the support iteratively by convolving the reconstructed image with an Gaussian filter and then finding a new binary support constraint by applying a threshold. For example, in [7] the authors convolve the estimated image of the object by a Gaussian kernel after every 20 iterations when applying a phase retrieval algorithm. The full width at half maximum of the Gaussian kernel is set to 3 pixels, and reduced by 1% every 20 iterations down to a minimum of 1.5 pixels. The updated binary support is obtained by applying a threshold at 20% of the maximum of the absolute of the convolved image. The shrink-wrap method is commonly used recently in conventional CDI setup [61] due to its ability of estimating the support.

1.2.2. PTYCHOGRAPHY

The word 'ptychography' is derived from the Greek word 'ptycho', meaning 'fold', and from the word 'graphy', meaning 'record'. Ptychography was first introduced by Hoppe [30] as a method to retrieve the phase of the Bragg reflection pattern in crystallography [62, 63]. Although the technique was not very popular before the 2000s, it was at the time already been implemented before 2000 in scanning X-ray microscopy [64] and in scanning electron microscopy [12]. During this period, methods to reconstruct the object were mostly direct inversion algorithms, e.g. the Wigner Distribution De-convolution method (WDD). Since 2007, the technique become much more popular and a lot of research has been done. Some reasons for this are: (1) the recent development of coherent high intensity X-ray sources, e.g. the third generation synchrotrons [9, 11, 35, 65] and table-top high-harmonic generation lasers [66–71]; (2) the development of robust iterative algorithms which are designed for processing ptychographic data, e.g. the Ptychographic Iterative Engine (PIE) [31–33] and the introduction of the DM method [36, 72], etc. [22, 23, 73, 74]. Nowadays, ptychography usually means performing CDI with the ptychographic data by using an iterative algorithm.

The idea of ptychography is to create data redundancy in the CDI measurement by recording many diffraction measurements by laterally shifting the object, as shown in Fig. 1.7. The object is partially illuminated multiple times for a number of different

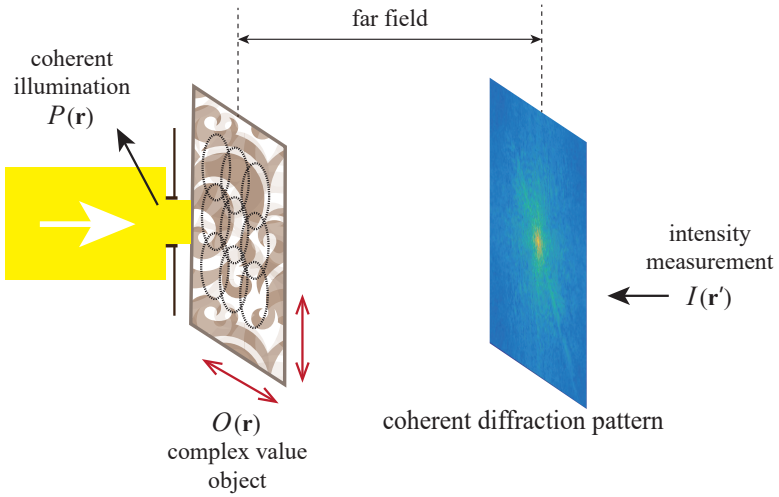

Figure 1.7: A simplified illustration of ptychography.

positions of the illuminating beam such that the entire object is covered and adjacent illuminations partially overlap. This data redundancy due to the partial overlap of the illuminations and the *a priori* information about the relative position of the illumination light beam and the object are the cause for the robustness of ptychography [75]. Compared with other phase retrieval methods, the advantages of ptychography are:

(1) Both the probe $P(\mathbf{r}_\perp)$ and the object $O(\mathbf{r}_\perp)$ can be retrieved simultaneously.

(2) DPtychography is more robust than phase retrieval methods that use only a single measurement due to the data redundancy. In particular, the 'twin image' problem, which often occurs in conventional phase retrieval methods [55, 76], is eliminated in ptychography.

(3) In ptychography the Field-of-View (FoV) of the reconstructed image of the object is extended compared to the support of the object or the lateral extent of the illumination because ptychography is a scanning imaging technique.

(4) For single measurement phase retrieval, it is shown in Section 1.1.3 that the sampling interval of $I(\mathbf{r}'_\perp)$ in detector plane must be two times finer than the Nyquist sampling interval of $\mathscr{F}(\Psi)(\mathbf{k}_\perp)$. Suppose now we have a measurement $I'(\mathbf{r}'_\perp)$ of which the sampling interval is less than the required Nyquist sampling interval. Then by Fourier transforming I' we will get the auto-correlation of $\Psi(\mathbf{r}_\perp)$ but part of the auto-correlation at its boundary is wrapped around and added to its opposite side. However, it was shown that in ptychography the sampling interval of each measurement

can be less than the above Nyquist sampling interval. The related discussion is given in [52].

(5) It has been shown that in ptychography one can perform CDI with spatially [77–79] or temporally [80–82] partially coherent illumination. It should be remarked that recent research has shown that it is also possible to perform CDI with partially coherent illumination using only a single diffraction measurement by applying more advanced algorithms [83–85].

There are of course other ways to create data redundancy in the CDI measurement, e.g. by placing a wavefront modulator between the object and the detector [86], by scanning the wavelength [87], by using patterned illumination which is created by two beam interference [88], etc. However, these methods are out of the scope of this thesis, therefore they are not4 discussed further. In the rest of this section we shortly outline the most simple and popular iterative algorithms for ptychography, namely the PIE and the DM method, and a non-iterative method, the WDD approach. More properties of ptychograpghy are discussed in Section 1.3.

PTYCHOGRAPHIC ITERATIVE ENGINE

The PIE algorithm [31, 32, 34, 89] is an iterative method which is designed to create an image of both the probe function $P(\mathbf{r}_\perp)$ and the object function $O(\mathbf{r}_\perp)$ by processing the ptychographic data-set. A probe is laterally translated to illuminate the object multiple times. For the jth illumination, the exit wave immediately behind the object is:

$$\Psi_j(\mathbf{r}_\perp) = P(\mathbf{r}_\perp - \mathbf{R}_{\perp,j}) \cdot O(\mathbf{r}_\perp) = P_j(\mathbf{r}_\perp) \cdot O(\mathbf{r}_\perp), \tag{1.61}$$

where $\mathbf{R}_{\perp,j}$ specifies the jth relative position between the probe and the object. The probe function has a finite size boundary support denoted by S:

$$P(\mathbf{r}_\perp) = \begin{cases} P(\mathbf{r}_\perp), & \mathbf{r}_\perp \in S, \\ 0, & \mathbf{r}_\perp \notin S. \end{cases} \tag{1.62}$$

For instance, if the probe is constrained by a circular boundary, we have:

$$P(\mathbf{r}_\perp) = \begin{cases} P(\mathbf{r}_\perp), & |\mathbf{r}_\perp| \le r_0, \\ 0, & |\mathbf{r}_\perp| > r_0. \end{cases} \tag{1.63}$$

For a detector located at distance z' in the far field, the diffraction intensity pattern $I_j(\mathbf{r}'_\perp)$ for the jth illumination is:

$$I_j(\mathbf{r}'_\perp) = \left| \iint \Psi_j(\mathbf{r}_\perp) e^{-\mathrm{i}\frac{2\pi}{\lambda z'}\mathbf{r}_\perp \cdot \mathbf{r}'_\perp} d\mathbf{r}_\perp \right|^2 = \left| \mathscr{F}_\perp \left(\Psi_j \right) \left(\mathbf{k}'_\perp \right) \right|^2. \tag{1.64}$$

where $\mathscr{F}_\perp$ is the Fourier transform operator, $\mathbf{r}'_\perp$ is the transverse position vector of a point in the detector plane and $\mathbf{k}'_\perp$ is the transverse vector of spatial frequency in reciprocal space. The relation between $\mathbf{r}'_\perp$ and $\mathbf{k}'_\perp$ is:

$$\mathbf{k}'_\perp = 2\pi \mathbf{r}'_\perp (\lambda z')^{-1}. \tag{1.65}$$

The PIE algorithm updates the probe $P(\mathbf{r}_\perp)$ and the object $O(\mathbf{r}_\perp)$ sequentially (or in a random order) for every $\mathbf{R}_{\perp,j}$ for all j. The update formula for jth illumination is:

$$\pi_F\left[\Psi_{j,n}(\mathbf{r}_\perp)\right] = \mathscr{F}_\perp^{-1}\left[\sqrt{\frac{I_j(\mathbf{k}'_\perp)}{\left|\mathscr{F}_\perp\left(\Psi_{j,n}\right)(\mathbf{k}'_\perp)\right|^2}}\mathscr{F}_\perp\left(\Psi_{j,n}\right)(\mathbf{k}'_\perp)\right], \tag{1.66a}$$

$$O_{n+1}(\mathbf{r}_\perp) = O_n(\mathbf{r}_\perp) + \beta_O \frac{P^*(\mathbf{r}_\perp - \mathbf{R}_{\perp,j})}{\max\left|P(\mathbf{r}_\perp - \mathbf{R}_{\perp,j})\right|^2}\left(\pi_F\left[\Psi_{j,n}(\mathbf{r}_\perp)\right] - \Psi_{j,n}(\mathbf{r}_\perp)\right), \tag{1.66b}$$

$$P_{n+1}(\mathbf{r}_\perp) = P_n(\mathbf{r}_\perp) + \beta_P \frac{O^*(\mathbf{r}_\perp + \mathbf{R}_{\perp,j})}{\max\left|O(\mathbf{r}_\perp + \mathbf{R}_{\perp,j})\right|^2}\left(\pi_F\left[\Psi_{j,n}(\mathbf{r}_\perp)\right] - \Psi_{j,n}(\mathbf{r}_\perp)\right), \tag{1.66c}$$

where the subscript n is again the iteration index. β_O and β_P are step-sizes of the update formula and both step-sizes are normally chosen fixed and from 0.6 to 1.2 in many PIE literature. Eq. (1.66c) is applied for every j sequentially to corporate the overlap.

Among all ptychographic algorithms, the PIE algorithm is one of the most popular methods which is often used in recent research. It was shown [33] that the PIE algorithm can be regarded as a cost function minimization method where the cost function $\mathscr{E}_j$ for jth illumination is given by:

$$\mathscr{E}_j = \sum_{\mathbf{k}'_\perp}^{N_x^{\text{det}},N_y^{\text{det}}}\left[\sqrt{I_j(\mathbf{k}'_\perp)} - \left|\mathscr{F}_\perp\left(\Psi_j\right)(\mathbf{k}'_\perp)\right|\right]^2, \tag{1.67}$$

where N_x^{det} and N_y^{det} are the number of pixels of the detector in the x and y directions, respectively. Furthermore, it was found that the PIE algorithm can be derived from the Maximum Likelihood estimation when the measurements have Gaussian noise [72, 90]. These facts most likely explain why the PIE approach is robust and stable. We present a detailed derivation of a global cost function minimization algorithm of ptychography in Section 1.3.

DIFFERENCE-MAP ALGORITHM

Another commonly used iterative algorithm in ptychography is the DM algorithm [35, 36, 77]. The original formula of the DM approach has been proposed in 2003 [20, 58, 59]. The the algorithm constructs the intersection of two constraint sets. The DM approach was applied to ptychography in 2009 [36], where the constraint set in object plane is defined by:

$$\pi_O\left[\Psi_{j,n}(\mathbf{r}_\perp)\right] = P_n(\mathbf{r}_\perp - \mathbf{R}_{\perp,j}) \cdot O_n(\mathbf{r}_\perp), \tag{1.68a}$$

for every j. Note that Eq. (1.68a) incorporates the *a priori* knowledge, i.e. the probe position $\mathbf{R}_{\perp,j}$ and the finite support of the probe. The constraint set in reciprocal plane is defined by:

$$\pi_F\left[\Psi_{j,n}(\mathbf{r}_\perp)\right] = \mathscr{F}_\perp^{-1}\left[\sqrt{\frac{I_j(\mathbf{k}'_\perp)}{\left|\mathscr{F}_\perp\left(\Psi_{j,n}\right)(\mathbf{k}'_\perp)\right|^2}}\mathscr{F}_\perp\left(\Psi_{j,n}\right)(\mathbf{k}'_\perp)\right], \tag{1.68b}$$

for every j. The update formula is given by:

$$\Psi_{j,n+1} = \Psi_{j,n} + \pi_F\left[2\pi_O\left(\Psi_{j,n}\right) - \Psi_{j,n}\right] - \pi_O\left(\Psi_{j,n}\right), \tag{1.68c}$$

$$O_{n+1}(\mathbf{r}_\perp) = \frac{\sum_j P_n^*(\mathbf{r}_\perp - \mathbf{R}_{\perp,j}) \cdot \Psi_{j,n+1}(\mathbf{r}_\perp)}{\sum_j \left|P_n(\mathbf{r}_\perp - \mathbf{R}_{\perp,j})\right|^2}, \tag{1.68d}$$

$$P_{n+1}(\mathbf{r}_\perp) = \frac{\sum_j O_n^*(\mathbf{r}_\perp + \mathbf{R}_{\perp,j}) \cdot \Psi_{j,n+1}(\mathbf{r}_\perp + \mathbf{R}_{\perp,j})}{\sum_j \left|O_n(\mathbf{r}_\perp + \mathbf{R}_{\perp,j})\right|^2}, \tag{1.68e}$$

where Eq. (1.68c) is derived from the original DM algorithm [35, 36]. Eq. (1.68d) and Eq. (1.68e) can be derived by applying the fix-point iteration algorithm to following nonlinear equations:

$$O(\mathbf{r}_\perp) = \frac{\sum_j P^*(\mathbf{r}_\perp - \mathbf{R}_{\perp,j}) \cdot \Psi_j(\mathbf{r}_\perp)}{\sum_j \left|P(\mathbf{r}_\perp - \mathbf{R}_{\perp,j})\right|^2}, \tag{1.69a}$$

$$P(\mathbf{r}_\perp) = \frac{\sum_j O^*(\mathbf{r}_\perp + \mathbf{R}_{\perp,j}) \cdot \Psi_j(\mathbf{r}_\perp + \mathbf{R}_{\perp,j})}{\sum_j \left|O(\mathbf{r}_\perp + \mathbf{R}_{\perp,j})\right|^2}. \tag{1.69b}$$

Eq. (1.69a) and Eq. (1.69b) are the closed form solutions obtained by minimizing the cost function given by [36]:

$$\mathscr{E} = \sum_j \sum_{\mathbf{r}_\perp} \left|P(\mathbf{r}_\perp - \mathbf{R}_{\perp,j})O(\mathbf{r}_\perp) - \Psi_j(\mathbf{r}_\perp)\right|^2, \tag{1.70}$$

w.r.t $O(\mathbf{r}_\perp)$ and $P(\mathbf{r}_\perp)$, respectively. It was shown [57] that the DM algorithm can avoid stagnation in a local minima. A schematic description about this geometric interpretation, which explains why the DM algorithm can avoid stagnation, can be found in Fig. 3 of the review [57] written by Marchesini in 2007. However, for the same reason, the DM approach does not guarantee convergence especially when the measurement is noisy or there are other systematic errors in the setup. Since in this thesis we only use the steepest descent method, we will not discuss in more detail about the DM method.

WIGNER DISTRIBUTION DE-CONVOLUTION METHOD

Although the iterative algorithms of ptychography are quite successful, there is still plenty of room for improvement. For instance, a common problem of the iterative computation methods is that the numerical calculation time cost can be very long (e.g. hours). This time depends on many aspects, e.g. the initial guess, the criterion to stop the algorithm, the computation power of the computer, etc. There exists a direct inversion algorithm which is designed to process ptychographic data, namely the Wigner distribution deconvolution (WDD) method [12, 64, 91]. In this section we give a brief overview of this method.

We start by taking the inverse Fourier transform of I_j which is given in Eq. (1.64):

$$\begin{aligned}\mathscr{F}_\perp^{-1}\left(I_j\right)(\mathbf{r}_\perp) &= \int \Psi_j^*(\tilde{\mathbf{r}}_\perp)\Psi_j(\mathbf{r}_\perp + \tilde{\mathbf{r}}_\perp)d\tilde{\mathbf{r}}_\perp \\ &= \int P^*(\tilde{\mathbf{r}}_\perp - \mathbf{R}_{\perp,j})O^*(\tilde{\mathbf{r}}_\perp)P(\mathbf{r}_\perp + \tilde{\mathbf{r}}_\perp - \mathbf{R}_{\perp,j})O(\mathbf{r}_\perp + \tilde{\mathbf{r}}_\perp)d\tilde{\mathbf{r}}_\perp,\end{aligned} \tag{1.71}$$

where $\tilde{\mathbf{r}}_\perp$ are integration variables. Now we take the Fourier transform of Eq. (1.71) w.r.t. $\mathbf{R}_{\perp,j}$:

$$\begin{aligned} H(\mathbf{r}_\perp,\mathbf{K}_\perp) &= \sum_j \mathscr{F}_\perp^{-1}\left(I_j\right)(\mathbf{r}_\perp) e^{-i\mathbf{K}_\perp\cdot\mathbf{R}_{\perp,j}} \\ &= \int O^*(\tilde{\mathbf{r}}_\perp) O(\mathbf{r}_\perp+\tilde{\mathbf{r}}_\perp) e^{-i\mathbf{K}_\perp\cdot\tilde{\mathbf{r}}_\perp} d\tilde{\mathbf{r}}_\perp \left[\sum_j P^*(\tilde{\mathbf{R}}_{\perp,j}) P(\mathbf{r}_\perp+\tilde{\mathbf{R}}_{\perp,j}) e^{i\mathbf{K}_\perp\cdot\tilde{\mathbf{R}}_{\perp,j}}\right] \\ &\approx W_O(\mathbf{r}_\perp,\mathbf{K}_\perp) W_P(\mathbf{r}_\perp,-\mathbf{K}_\perp), \end{aligned} \tag{1.72}$$

where we use the substitutions:

$$\tilde{\mathbf{R}}_{\perp,j} = \tilde{\mathbf{r}}_\perp - \mathbf{R}_{\perp,j}, \tag{1.73a}$$

$$\begin{aligned} W_P(\mathbf{r}_\perp,-\mathbf{K}_\perp) &= \int P^*(\tilde{\mathbf{R}}_\perp) P(\mathbf{r}_\perp+\tilde{\mathbf{R}}_\perp) e^{i\mathbf{K}_\perp\cdot\tilde{\mathbf{R}}_\perp} d\tilde{\mathbf{R}}_\perp \\ &\approx \sum_j P^*(\tilde{\mathbf{R}}_{\perp,j}) P(\mathbf{r}_\perp+\tilde{\mathbf{R}}_{\perp,j}) e^{i\mathbf{K}_\perp\cdot\tilde{\mathbf{R}}_{\perp,j}}, \end{aligned} \tag{1.73b}$$

$$W_O(\mathbf{r}_\perp,\mathbf{K}_\perp) = \int O^*(\tilde{\mathbf{r}}_\perp) O(\mathbf{r}_\perp+\tilde{\mathbf{r}}_\perp) e^{-i\mathbf{K}_\perp\cdot\tilde{\mathbf{r}}_\perp} d\tilde{\mathbf{r}}_\perp, \tag{1.73c}$$

and $\mathbf{K}_\perp$ and $\mathbf{R}_\perp$ are transverse position vector and transverse wave vector. W_P and W_O have the form of a Wigner distribution function. We can see that, when the measurement is noise free and when $P(\mathbf{r}_\perp-\mathbf{R}_{\perp,j})$ is known, it is not difficult to obtain $W_O(\mathbf{r}_\perp,\mathbf{K}_\perp)$ through applying a division algorithm. To extract the object function, one can start by Fourier transforming $W_O(\mathbf{r}_\perp,\mathbf{K}_\perp)$ w.r.t. $\mathbf{r}_\perp$:

$$\mathscr{F}_\perp(W_O)(\mathbf{k}_\perp,\mathbf{K}_\perp) = \mathscr{F}_\perp(O)(\mathbf{k}_\perp)\cdot\mathscr{F}_\perp(O)^*(\mathbf{k}_\perp+\mathbf{K}_\perp), \tag{1.74}$$

It is seen that the Fourier transform of the object can be obtained by [64]:

$$\mathscr{F}_\perp(O)(\mathbf{K}_\perp) = \left[\frac{\mathscr{F}_\perp(W_O)(0,\mathbf{K}_\perp)}{\sqrt{\mathscr{F}_\perp(W_O)(0,0)}}\right]^*, \tag{1.75}$$

where we ignored the multiplicative phasor of $\mathscr{F}_\perp(O)(0)$. In Eq. (1.75), one may be encountered with the divided-by-zero problem. To avoid this problem we can apply Wiener filter as shown in [91]. Note that the reconstructed object is discretized on the grid $\mathbf{K}_\perp$, which is the reciprocal grid of $\mathbf{R}_{\perp,j}$. Therefore, one must scan the probe over a grid of positions separated by the desired resolution, such that the function $\mathscr{F}_\perp(O)(\mathbf{K}_\perp)$ is sampled with a sufficiently broad and fine mesh. Hence, the required measurements constitute a very large and strongly redundant 4D data-set. On the other hand, we can see in Eq. (1.74) that $W_O(\mathbf{r}_\perp,\mathbf{K}_\perp)$ consists of information about $\mathscr{F}_\perp(O)$ that is not restricted by the grids $\mathbf{K}_\perp$. To extract more information of $\mathscr{F}_\perp(O)$, one can use the so-called 'step-out' method [12] in addition to Eq. (1.75). The 'step-out' method is given by:

$$\mathscr{F}_\perp(O)(\mathbf{k}_\perp+\mathbf{K}_\perp) = \left[\frac{\mathscr{F}_\perp(W_O)(\mathbf{k}_\perp,\mathbf{K}_\perp)}{\mathscr{F}_\perp(O)(\mathbf{K}_\perp)}\right]^*. \tag{1.76}$$

However, even with this large data-set, it is still an open question whether the WDD method is as robust as the iterative algorithms for noisy environment and whether the WDD method performs well when the probe is unknown.

1

1.2.3. TRANSPORT OF INTENSITY EQUATION METHOD

The transport-of-intensity equation(TIE) method [4, 92] is a propagation based method where one aims to retrieve the phase of the wavefield from the change of the squared modulus of the wavefield in different planes. Let us start with the free space propagation formula as given by Eq. (1.13). Suppose that the paraxial approximation is valid, we then write:

$$U_{\mathrm{f}}(\mathbf{r}) \approx V_{\mathrm{f}}(\mathbf{r}) e^{\mathrm{i}kz} = A_{\mathrm{f}}(\mathbf{r}) e^{\mathrm{i}\phi_{\mathrm{f}}(\mathbf{r})} e^{\mathrm{i}kz}, \tag{1.77}$$

where A_{f} and ϕ_{f} are real valued and $V_{\mathrm{f}}(\mathbf{r})$ is a slowly varying function of z such that:

$$\left| \frac{\partial^2 V_{\mathrm{f}}(\mathbf{r})}{\partial z^2} \right| \ll \left| \mathrm{i}k \frac{\partial V_{\mathrm{f}}(\mathbf{r})}{\partial z} \right|. \tag{1.78}$$

By substituting Eq. (1.77) into Eq. (1.13) and using Eq. (1.78), we obtain V_{f} the paraxial wave equation:

$$\nabla_{\perp}^2 V_{\mathrm{f}}(\mathbf{r}) + 2\mathrm{i}k \frac{\partial V_{\mathrm{f}}(\mathbf{r})}{\partial z} = 0, \tag{1.79}$$

where $\nabla_{\perp}$ and $\nabla_{\perp}^2$ are the operators defined by:

$$\nabla_{\perp} = \left[\frac{\partial}{\partial x}, \frac{\partial}{\partial y} \right]^T, \qquad \nabla_{\perp}^2 = \frac{\partial^2}{\partial x^2} + \frac{\partial^2}{\partial y^2}. \tag{1.80}$$

By separating the real part and the imaginary part of Eq. (1.79), we arrive at two equations:

$$\frac{\nabla_{\perp}^2 A_{\mathrm{f}}}{A_{\mathrm{f}}} - \left(\nabla_{\perp}\phi_{\mathrm{f}}\right)^2 - 2k \frac{\partial \phi_{\mathrm{f}}}{\partial z} = 0, \quad \text{(the real part)}, \tag{1.81a}$$

$$\nabla_{\perp} A_{\mathrm{f}} \cdot \nabla_{\perp} \phi_{\mathrm{f}} + A_{\mathrm{f}} \frac{\partial \phi_{\mathrm{f}}}{\partial z} + 2k \frac{\partial A_{\mathrm{f}}}{\partial z} = 0, \quad \text{(the imaginary part)}. \tag{1.81b}$$

Let Eq. (1.81b) be multiplied by A_{f}^*, we have:

$$\nabla_{\perp} \cdot \left(|A_{\mathrm{f}}|^2 \nabla_{\perp} \phi_{\mathrm{f}} \right) + k \frac{\partial |A_{\mathrm{f}}|^2}{\partial z} = 0. \tag{1.82}$$

Eq. (1.82) is called the 'transport-of-intensity equation' (TIE) because it involves the derivative of the intensity of the wavefield $|A_{\mathrm{f}}|^2$ along the z direction. The TIE relates the phase of the wavefield to the variation of the intensity along the propagation direction. To retrieve $\phi_{\mathrm{f}}(\mathbf{r})$ in the plane $z = z_o$, it was suggested [93] that one can solve Eq. (1.82) by using numerical solvers for Poisson's equation. In practice, the gradient of the intensity $|A_{\mathrm{f}}|^2$ along the z direction is obtained by taking multiple measurements and each measurement is taken at a different z plane which is sufficiently close to z_o plane. Therefore the accuracy of knowing the z-positions of the planes of the detector is an important factor on which the quality of the reconstruction depends..

As it is a non-iterative method which enables solving the phase problem directly, the TIE method is a promising alternative to the iterative phase retrieval methods and therefore gets a lot of attention. [9, 93–98]. However, we will not discuss the method further in detail since the main topic of this thesis is ptychography.

1.2.4. FOURIER TRANSFORM HOLOGRAPHY

Another important CDI method is Fourier Transform Holography (FTH) [99] which is found suitable for X-ray imaging applications [100–105]. In conventional FTH one uses a laser beam to illuminates the object and a pinhole which is in the same z-plane as the object but separated from it in the transverse direction. Hence in the far field we measure the interference pattern of the diffracted object field and the field of the pinhole. Suppose that the pinhole is at position $\mathbf{r}_{\perp,\mathrm{p}}$ and the size of the pinhole is sufficiently small, then the intensity of the interference pattern in the far field is given by:

$$\begin{aligned} I(\mathbf{k}'_\perp) &= \left|\mathscr{F}_\perp\left[O(\mathbf{r}_\perp)+\delta_D(\mathbf{r}_{\perp,\mathrm{p}})\right]\right|^2(\mathbf{k}'_\perp) \\ &= 1+\left|\mathscr{F}_\perp(O)\right|^2(\mathbf{k}'_\perp)+2\Re\left[\mathscr{F}(O)^*(\mathbf{k}'_\perp)e^{-\mathrm{i}\mathbf{k}'_\perp\cdot\mathbf{r}_{\perp,\mathrm{p}}}\right]. \end{aligned} \tag{1.83}$$

By computing the inverse Fourier transform of Eq. (1.83) we get:

$$\mathscr{F}_\perp(I)^{-1}(\mathbf{r}_\perp) = \delta_D(0)+O(\mathbf{r}_\perp)\star O(\mathbf{r}_\perp)+O(\mathbf{r}_\perp-\mathbf{r}_{\perp,\mathrm{p}})+O^*(-\mathbf{r}_\perp+\mathbf{r}_{\perp,\mathrm{p}}), \tag{1.84}$$

where $\star$ denotes the auto-correlation, i.e. convolution with a complex conjugation, and $*$ denotes complex conjugation. We can see that the third term in Eq. (1.84) is a shifted version of the actual object function $O(\mathbf{r}_\perp)$ and the fourth term is the twin image. Therefore, when the pinhole is sufficiently far away from the object and when the object has a finite extent, the different terms in Eq. (1.84) are separated in space and hence we can obtain the complex valued transmission of the object by simply computing the Fourier transform of the measurement.

1.3. MORE PROPERTIES OF PTYCHOGRAPHY

A brief introduction of ptychography has already been given in Secion 1.2.2. In this section we discuss some more properties of ptychography. In Section 1.3.1 we derive a ptychographic algorithm by applying the steepest descent method to a global cost function. Then we explain the extended FoV of ptychography and ambiguities in ptychography in Section 1.3.2 and Section 1.3.3, respectively. Finally, in Section 1.3.4. we mention some recent developments of ptychography.

1.3.1. GRADIENT DESCENT OPTIMIZATION

In this section we show in detail the derivation of a ptychograpy algorithm which is based on the steepest descent method. The results of this derivation will be used in several of the subsequent chapters in this thesis. As shown in Section 1.2.2, we use a laterally shifted probe to illuminate the thin-slab object multiple times. For the jth illumination, the exit wave immediately behind the object is:

$$\Psi_j(\mathbf{r}_\perp) = P(\mathbf{r}_\perp-\mathbf{R}_{\perp,j})\cdot O(\mathbf{r}_\perp) = P_j(\mathbf{r}_\perp)\cdot O(\mathbf{r}_\perp), \tag{1.85}$$

where $\mathbf{R}_{\perp,j}$ is the jth relative position of the probe and the object. The probe function is assumed to has a finite support S:

$$P(\mathbf{r}_\perp) = \begin{cases} P(\mathbf{r}_\perp), & \mathbf{r}_\perp \in S, \\ 0, & \mathbf{r}_\perp \notin S, \end{cases} \tag{1.86}$$

and the probe function for $\mathbf{r}_\perp \in S$ is assumed unknown. For a detector located at distance z' in the far field, the diffraction intensity pattern $I(\mathbf{r}')$ for the jth illumination is:

$$I_j(\mathbf{r}'_\perp) = \left| \iint \Psi_j(\mathbf{r}_\perp) e^{-\mathrm{i}\frac{2\pi}{\lambda z'}\mathbf{r}_\perp \cdot \mathbf{r}'_\perp} d\mathbf{r}_\perp \right|^2 = \left| \mathscr{F}_\perp \left(\Psi_j\right)(\mathbf{k}'_\perp) \right|^2, \tag{1.87}$$

where $\mathbf{k}'_\perp = 2\pi \mathbf{r}'_\perp / \lambda z'$.

The aim in ptychography is to estimate the complex object function which fits the given *a priori* knowledge by minimizing a cost function $\mathscr{E}$ which is the difference between simulated and measured far field intensities. For real-space ptychography, the *a priori* knowledge consists of the finite support S and the set of relative positions $\mathbf{R}_j$. The cost function $\mathscr{E}$ is defined as the l_2-distance between the modulus of the far field diffraction pattern $\left|\mathscr{F}_\perp \left(\Psi_j\right)(\mathbf{k}'_\perp)\right|$ and the square root of the measured intensity $I_j^{\mathrm{m}}(\mathbf{k}'_\perp)$:

$$\mathscr{E} = \sum_j \mathscr{E}_j = \sum_j \sum_{\mathbf{k}'_\perp}^{N_x^{\mathrm{det}}, N_y^{\mathrm{det}}} \left| \sqrt{I_j^{\mathrm{m}}(\mathbf{k}'_\perp)} - \left|\mathscr{F}_\perp \left(\Psi_j\right)(\mathbf{k}'_\perp)\right| \right|^2, \tag{1.88}$$

where $\mathbf{k}'_\perp$ is meshed on a grid is discritized defined according to the distance z' and the pixel size of the detector and N_x^{det} and N_y^{det} are the number of pixels of the detector along the x-axis and the y-axis, respectively.

First, we compute the retrieval formula for the object function $O(\mathbf{r}_\perp)$ while assume that the probe function and probe positions are known. We calculate the functional derivative of $\mathscr{E}_j$ with respect to O at every point $\mathbf{r}$ in the direction of perturbation δO and denote this derivative as $\delta\mathscr{E}_j(P, O, \delta O)$. The perturbation δO is on a discretized grid $\mathbf{r}_\perp$ given by:

$$\delta O(\mathbf{r}_\perp) = \sum_{n_{\mathbf{r},y}} \sum_{n_{\mathbf{r},x}} \delta O(\mathbf{r}_\perp) \delta(\mathbf{r}_\perp - \mathbf{n}_{\mathbf{r},\perp} \Delta\mathbf{r}_\perp), \tag{1.89}$$

where $\Delta\mathbf{r}_\perp$ is the translation vector to translate one cell to its immediate neighbor, as given in Eq. (1.42). The derivative of $\mathscr{E}$ is:

$$\begin{aligned}
\delta\mathscr{E}(P, O, \delta O) &= 2 \sum_j \sum_{\mathbf{k}'_\perp} \left(\frac{\sqrt{I_j^{\mathrm{m}}(\mathbf{k}'_\perp)}}{\left|\mathscr{F}_\perp \left(\Psi_j\right)(\mathbf{k}'_\perp)\right|} - 1 \right) \Re \left[\mathscr{F}_\perp \left(P_j O\right)(\mathbf{k}'_\perp) \cdot \mathscr{F}_\perp \left(P_j \delta O\right)(\mathbf{k}'_\perp)^* \right] \\
&= 2\Re \left[\sum_j \sum_{\mathbf{k}'_\perp} \left(\frac{\sqrt{I_j^{\mathrm{m}}(\mathbf{k}'_\perp)}}{\left|\mathscr{F}_\perp \left(\Psi_j\right)(\mathbf{k}'_\perp)\right|} - 1 \right) \cdot \mathscr{F}_\perp \left(P_j O\right)(\mathbf{k}'_\perp) \cdot \mathscr{F}_\perp \left(P_j \delta O\right)(\mathbf{k}'_\perp)^* \right] \\
&= 2\Re \left\{ \sum_j \sum_{\mathbf{r}_\perp} \mathscr{F}_\perp^{-1} \left[\left(\frac{\sqrt{I_j^{\mathrm{m}}(\mathbf{k}'_\perp)}}{\left|\mathscr{F}_\perp \left(\Psi_j\right)(\mathbf{k}'_\perp)\right|} - 1 \right) \mathscr{F}_\perp \left(P_j O\right)(\mathbf{k}'_\perp) \right] P_j(\mathbf{r}_\perp)^* \cdot \delta O(\mathbf{r}_\perp)^* \right\} \\
&= 2\Re \left[\sum_j \sum_{\mathbf{r}_\perp} \Delta\Psi_j(\mathbf{r}_\perp) \cdot P_j(\mathbf{r}_\perp)^* \cdot \delta O(\mathbf{r}_\perp)^* \right],
\end{aligned} \tag{1.90}$$

where the Parseval's theorem for DFT was used and $\Delta\Psi_j(\mathbf{r})$ is an auxiliary function given by:

$$\Delta\Psi_j(\mathbf{r}) = \mathscr{F}_\perp^{-1}\left[\left(\frac{\sqrt{I_j^{\mathrm{m}}(\mathbf{k}'_\perp)}}{\left|\mathscr{F}_\perp\left(\Psi_j\right)(\mathbf{k}'_\perp)\right|} - 1\right)\cdot\mathscr{F}_\perp\left(\Psi_j\right)(\mathbf{k}'_\perp)\right](\mathbf{r}_\perp), \tag{1.91}$$

and $\Re$ is the real part of a complex number. To determine the steepest descent direction, we consider the following problem:

$$\begin{aligned} &\underset{\delta O}{\text{minimize}} \quad \delta\mathscr{E}(\delta O) \\ &\text{subject to} \quad \|\delta O\|^2 = \text{constant}, \end{aligned} \tag{1.92}$$

where $\|\delta O\|^2$ is given by:

$$\|\delta O\|^2 = \sum_{\mathbf{r}_\perp}\delta O(\mathbf{r}_\perp)\cdot\delta O^*(\mathbf{r}_\perp). \tag{1.93}$$

To solve this problem, we construct a Lagrange function:

$$L(\delta O) = \delta\mathscr{E}(\delta O) - \lambda_L\|\delta O\|^2, \tag{1.94}$$

where λ_L is a real Lagrange multiplier. Now, we differentiate L by perturbing the function δO with an arbitrary auxiliary function $\delta\tilde{O}$. According to the Lagrange multiplier rule, for the optimal solution of the problem in (1.92), we have:

$$\Re\left[\sum_j\sum_{\mathbf{r}_\perp}\Delta\Psi_j(\mathbf{r}_\perp)\cdot P_j^*(\mathbf{r}_\perp)\cdot\delta\tilde{O}^*(\mathbf{r}_\perp)\right] = -\Re\left[\lambda_L\sum_{\mathbf{r}_\perp}\delta O(\mathbf{r}_\perp)\cdot\delta\tilde{O}^*(\mathbf{r}_\perp)\right]. \tag{1.95}$$

Note that (1.95) is for all $\delta\tilde{O}(\mathbf{r}_\perp)$. If we assign $\delta\tilde{O}(\mathbf{r}_\perp)$ to be pure real-valued, then we have:

$$\sum_{\mathbf{r}_\perp}\Re\left[\sum_j\Delta\Psi_j(\mathbf{r}_\perp)\cdot P_j^*(\mathbf{r}_\perp)\right]\cdot\delta\tilde{O}(\mathbf{r}_\perp) = -\lambda_L\sum_{\mathbf{r}_\perp}\Re\left[\delta O(\mathbf{r}_\perp)\right]\cdot\delta\tilde{O}(\mathbf{r}_\perp). \tag{1.96}$$

One solution for this equation is:

$$\Re\left[\sum_j\Delta\Psi_j(\mathbf{r}_\perp)\cdot P_j^*(\mathbf{r}_\perp)\right] = -\lambda_L\Re\left[\delta O(\mathbf{r}_\perp)\right]. \tag{1.97}$$

On the other hand, if we assign $\delta\tilde{O}(\mathbf{r}_\perp)$ to be pure imaginary-valued, then we have:

$$\sum_{\mathbf{r}_\perp}\Im\left[\sum_j\Delta\Psi_j(\mathbf{r}_\perp)\cdot P_j^*(\mathbf{r}_\perp)\right]\cdot\left[\mathrm{i}\cdot\delta\tilde{O}(\mathbf{r}_\perp)\right] = -\lambda_L\sum_{\mathbf{r}_\perp}\Im\left[\delta O(\mathbf{r}_\perp)\right]\cdot\left[\mathrm{i}\cdot\delta\tilde{O}(\mathbf{r}_\perp)\right], \tag{1.98}$$

which leads to:

$$\Im\left[\sum_j\Delta\Psi_j(\mathbf{r}_\perp)\cdot P_j^*(\mathbf{r}_\perp)\right] = -\lambda_L\Im\left[\delta O(\mathbf{r}_\perp)\right], \tag{1.99}$$

where $\Im$ takes the imaginary part of a complex number. Combining (1.97) and (1.99) gives us:

$$\sum_j \Delta\Psi_j(\mathbf{r}_\perp)\cdot P_j^*(\mathbf{r}_\perp) = -\lambda_L \delta O(\mathbf{r}_\perp). \tag{1.100}$$

Hence, the steepest descent direction of $\mathscr{E}$ at $O(\mathbf{r}_\perp)$ is proportional to the function $\Delta\Psi_j(\mathbf{r}_\perp)\cdot P_j^*(\mathbf{r}_\perp)$ at every point $\mathbf{r}_\perp$ for all j. The iteration formula for the object function is then given by:

$$O_{n+1}(\mathbf{r}_\perp) = O_n(\mathbf{r}_\perp) - \beta_O \sum_j P_n^*(\mathbf{r}_\perp - \mathbf{R}_{\perp,j})\cdot \Delta\Psi_{j,n}(\mathbf{r}_\perp), \tag{1.101}$$

where β_O is the step-size which is normally chosen be $0.8 \sim 1$.

In a similar fashion, we can derive the iteration formula for updating the probe function using the steepest decent direction. We find:

$$P_{n+1}(\mathbf{r}_\perp) = P_n(\mathbf{r}_\perp) - \beta_P \sum_j O_n^*(\mathbf{r}_\perp + \mathbf{R}_{\perp,j})\cdot \Delta\Psi_{j,n}(\mathbf{r}_\perp + \mathbf{R}_{\perp,j}), \tag{1.102}$$

where β_P is a constant step-size which takes the same value as β_O.

1.3.2. THE EXTENDED FIELD-OF-VIEW OF PTYCHOGRAPHY

The ptychographic measurement $I_j(\mathbf{k}'_\perp)$ is commonly recorded by a 2D detector, e.g. a charge-coupled device (CCD). Therefore $\mathbf{k}'_\perp$ is a discretized grid and is meshed according to the distance z' and the size of pixel of the detector. The retrieved object function is also on a discretized grid $\mathbf{r}_\perp$. $\mathbf{r}_\perp$ and $\mathbf{k}'_\perp$ are related by:

$$\left[\Delta x, \Delta y\right]^T = 2\pi \left[(N_x^{\text{det}}\Delta k'_x)^{-1}, (N_y^{\text{det}}\Delta k'_y)^{-1}\right]^T, \tag{1.103}$$

where Δx and Δy are the sizes of a single grid cell along the x-axis and y-axis, respectively, and $\Delta k'_x$ and $\Delta k'_y$ are the spacing of a grid cell in k_x and k_y, respectively. The field-of-view (FoV) given by single measurement of the ptychographic data-set is therefore:

$$\text{FoV} = \left[N_x^{\text{det}}\Delta x, N_y^{\text{det}}\Delta y\right]^T, \tag{1.104}$$

Because ptychography is a scanning imaging technique, the total number of illuminated grid cells of the object, denoted by N_x and N_y, is larger than the number of pixels of the detector. Hence we have $N_x > N_x^{\text{det}}$ and $N_y > N_y^{\text{det}}$. The total field-of-view (FoV) in the object plane is:

$$\text{extented FoV} = \left[N_x\Delta x, N_y\Delta y\right]^T, \tag{1.105}$$

In line with this extended FoV, we have the effective spacing of the grid cell in reciprocal space:

$$\left[\Delta k_x, \Delta k_y\right]^T = \left[(N_x)^{-1}N_x^{\text{det}}\Delta k'_x, (N_y)^{-1}N_y^{\text{det}}\Delta k'_y\right]^T. \tag{1.106}$$

Therefore, this effective sampling of the reciprocal of the object is finer than the discretized grid $\mathbf{k}'_\perp$ which is meshed according to the distance z' and the size of pixel of the detector.

1.3.3. AMBIGUITIES

Compared to traditional single-measurement phase retrieval methods, ptychography solves some problems that occur with other phase retrieval methods that can disrupt the reconstruction. In ptytography it is still possible that the computed solution is not correct.

GLOBAL PHASE SHIFT

Due to the fact that in ptychography only diffracted intensities are detected, we have for all j:

$$\begin{aligned} I_j(\mathbf{k}'_\perp) &= \left|\mathscr{F}_\perp\left(\Psi_j\right)(\mathbf{k}'_\perp)\right|^2 \\ &= \left|\exp(\mathrm{i}f)\,\mathscr{F}_\perp\left(\Psi_j\right)(\mathbf{k}'_\perp)\right|^2 = \left|\mathscr{F}_\perp\left[\Psi_j \exp(\mathrm{i}f)\right](\mathbf{k}'_\perp)\right|^2 \\ &= \left|\mathscr{F}_\perp\left(\Psi'_j\right)(\mathbf{k}'_\perp)\right|^2, \end{aligned} \tag{1.107}$$

where f is an arbitrary constant, and $\Psi'_j(\mathbf{r}_\perp) = \Psi_j(\mathbf{r}_\perp)\exp(\mathrm{i}f)$ is an alternative ptychographic measurement.

RASTER GRID PATHOLOGY

The raster grid pathology is a periodical defect which can occur in ptychography reconstruction, when the relative positions $\mathbf{R}_{\perp,j}$ between the probe and the object are on a regular grid. To be explicit, we start with the expression of the exit wave in Eq. (1.85):

$$\begin{aligned} \Psi_j(\mathbf{r}_\perp) &= P(\mathbf{r}_\perp - \mathbf{R}_{\perp,j}) \cdot O(\mathbf{r}) \\ &= P(\mathbf{r}_\perp - \mathbf{R}_{\perp,j}) \cdot C(\mathbf{r}_\perp) \cdot O(\mathbf{r}_\perp) \cdot \frac{1}{C(\mathbf{r}_\perp)} \\ &= P'(\mathbf{r}_\perp - \mathbf{R}_{\perp,j}) \cdot O'(\mathbf{r}_\perp), \end{aligned} \tag{1.108}$$

with

$$\begin{cases} P'(\mathbf{r}_\perp - \mathbf{R}_{\perp,j}) = P(\mathbf{r}_\perp - \mathbf{R}_{\perp,j}) \cdot C(\mathbf{r}_\perp), \\ O'(\mathbf{r}_\perp) = O(\mathbf{r}_\perp) \cdot \dfrac{1}{C(\mathbf{r}_\perp)}. \end{cases} \tag{1.109}$$

Suppose now that $\mathbf{R}_{\perp,j}$ are on a equidistant grid and that $C(\mathbf{r}_\perp)$ is periodic on this grid, which means that $C(\mathbf{r}_\perp)$ satisfies for all j:

$$C(x,y) = C\left(x - \frac{X_j}{m_x}, y - \frac{Y_j}{m_y}\right), \tag{1.110}$$

where m_x and m_y are arbitrary integers and $\mathbf{R}_{\perp,j} = \left[X_j, Y_j\right]^T$, then Eq. (1.108) is true for all position j. Therefore $P'(\mathbf{r}_\perp)$ and $O'(\mathbf{r}_\perp)$ can be an alternative probe and object reconstruction for the same ptychographic measurement.

1.3.4. RECENT DEVELOPMENTS OF PTYCHOGRAPHY

In this section we briefly consider some recent developments of ptychography. Since the topics covered in this section are mostly outside the scope of the following chapters of this thesis, we only outline the topics according to the recent published literature and will not include detailed mathematical formulas. We only select a few topics which have attracted a lot of attention and we do not claim to be complete.

PARTIAL COHERENT PTYCHOGRAPHY

As in other CDI techniques, it is usually assumed in ptychography that the illumination is fully coherent and monochromatic. More precisely, the coherence of the wavefield should fulfill the requirements given in Section 1.1.4. However, these requirements are often not fulfilled in many important applications of ptychography. For example, in the X-ray regime, where ptychography has been widely used, light sources are either spatially partially coherent (e.g. synchrotron radiation [78, 83, 106–110]) or temporally partially coherent (e.g. tabletop high-harmonic generation laser [66, 68, 80, 85, 111, 112]). To mitigate the unwanted effect due to partial coherence, and also to improve the throughput of the imaging system, novel algorithms have been introduced in ptychography during the last decade. It was proposed in 2013 [77] that one can perform partial coherent ptychography by using the mode decomposition method [113–115]. For a quasi-monochromatic and spatially partial coherent illumination, the mode-decomposition method decomposes the wavefield in the illumination into modes which can be treated as fully coherent wavefields but mutually incoherent. The mode decomposition method was first applied to spatially coherent illumination [77, 116] and later to light sources with multiple wavelengths [112, 117].

For quasi-monochromatic and spatially partial coherent illumination, one can represent the field in illumination by mutual coherent function denoted by $J(\mathbf{r}_{\perp,1}, \mathbf{r}_{\perp,2})$. The mutual coherent function describes the coherence between two points $\mathbf{r}_{\perp,1}$ and $\mathbf{r}_{\perp,2}$ in the object plane and is a 4D array in principle. For the sake of simplicity, J is usually approximated by a 2D array because it is assumed to be a function of the difference of two position vectors [78, 108, 110]: $J = J(\mathbf{r}_{\perp,1} - \mathbf{r}_{\perp,2})$. Under this approximation, one can describe the measured partial coherent diffraction pattern by a fully coherent diffraction pattern convoluted with the Fourier transform of the mutual coherent function in the object plane [25, 113]. It was shown [74, 81, 110, 118, 119] that one can retrieve both the object field and $J(\mathbf{r}_{\perp,1} - \mathbf{r}_{\perp,2})$ from ptychographic data by applying blind de-convolution algorithms or cost function minimization algorithms. However, this convolution model can only describe the partial transverse coherence of the wavefield, i.e. the case of quasi-monochromatic spatially partial coherent light. This is because for temporally partial coherent light the propagation equation is wavelength dependent, and hence the blurring of the speckles in the far field depends on wavelength and is not transversely invariant. Therefore, many alternative phase retrieval methods for boardband illumination have been proposed [68, 85, 120] during the last decade to overcome this problem..

3D PTYCHOGRAPHY

To obtain a 3D image of an object from the measured diffraction pattern is one of the most important current topics of CDI and is still in the frontier of current research. In

many applications of CDI, e.g. X-ray microscopy [61] and transmission electron microscopy [63], the samples which need to be reconstructed do not fulfill the 'weak scattering thin object' approximation of Eq. (1.35) and Eq. (1.36). Once this approximation is lifted, we can see in Eq. (1.27) and Eq. (1.28) that it is possible to extract at least some 3D information about the sample from the diffraction pattern either with or without the first Born approximation. Suppose now that the first Born approximation is valid [25, 121], then we can see in Eq. (1.32) that the 3D distribution of the scattered wavefield is approximately mapped to a part of the refractive index contrast distribution in reciprocal space. However, apart from the issue of sampling, one should obtain the complex valued scattering amplitude for sufficiently many $\mathbf{k}$ in 3D reciprocal space so that it is possible to reconstruct the 3D refractive index contrast distribution by a back Fourier transform. From the Fourier slice theorem [25, 122, 123] we know that, if we have obtained the exit wavefield immediately behind the object which is an integral over the thickness of the object, then the 2D transverse Fourier transform of this exit wavefield is approximately equal to a slice through the origin of the 3D Fourier transform of the object. This theorem is the fundamental for tomography. Hence, the primary issues in 3D CDI are: (1) One needs to measure the scattered wavefield for many different incident angles around a common rotational axis, as shown in Fig. 1 of [123], and to stack these measurements into the spatial spectrum of the object in reciprocal space by using tomographic algorithms [123–125]. (2) For each rotational angle, one have to measure the complex valued amplitude of the scattered wavefield, which could be obtained through applying phase retrieval methods. It has been shown numerically and experimentally [126–128] that it is possible to achieve 3D reconstruction by combining conventional phase retrieval methods with tomography with limited resolution. After ptychography was developed, many attempts have been done to retrieve 3D information of the sample with high resolution by combining tomography and ptychography [10, 129–138].

However, it should be remarked that the tomographic methods mentioned above are mostly based on the first Born approximation or other weak scattering approximations, e.g. the multiplicative approximation as given in Eq. (1.37). Such approximations are often not valid in practice. An attempt to bypass the weak scattering approximation is the introduction of the multi-slice approach [63, 139, 140]. In the multi-slice method, an object which cannot be described by the multiplicative approximation is numerically modeled by a sequence of slices, and the slices are sufficiently thin so that each individually satisfies the multiplicative approximation. Between every two adjacent slices the propagation of the wavefield is approximated by free-space propagation, which usually is computed through the angular spectrum propagator [141]. The multi-slice approach was introduced to ptychography in 2012 [140] and it was shown [44, 142, 143] that, due to the information redundancy of the ptychographic data-set, one can retrieve the slices in ptychography for a properly chosen number of slices, and therefore one can obtain 3D information about the object without rotating the object during the measurement. It was conceptually shown [144, 145] that, by introducing the multi-slice approach to tomography, one can reduce the required number of rotation angles in tomography but still achieve adequate angular sampling in reciprocal space. It has been proposed [135, 146, 147] recently that it is beneficial to combine ptychography, tomography and the multi-slice approach in 3D CDI.

DE-NOISING PTYCHOGRAPHY

In practice, one has to consider in ptychography that various levels of noise in the measurements will cause inaccuracies in the reconstructions [72, 90, 148]. The common sources of noise in ptychography are [149]: the saturation effect of the detector, the thermal fluctuation of the light source, the photon counting noise, the dark current and dead pixels of the detector, etc. To prevent the effect caused by saturation of the detector, dark-field and near-field ptychography have been introduced [150, 151]. Moreover, it has been shown that adaptive step size strategies are able to improve the performance of ptychography in the presence of noise [89, 152]. It has also been demonstrated that one can increase the signal-to-noise ratio (SNR) by engineering the wavefront of the illumination [153, 154], which can be analytically explained by studying the spatial-frequency spectrum of the probe [91]. In general, the most powerful and robust de-noising methods are based on the maximum likelihood principle [72, 90, 149, 155–158]. The likelihood function used in the maximum likelihood method depends on the noise model. Common choices for the noise model in ptychography are Poisson noise, Gaussian noise and the mixed Poisson-Gaussian model. It has been demonstrated [72, 90, 159, 160] that, by using the variance stabilization transform given by Bartlett [161] and Anscombe [162], one can approximate the maximum likelihood method of Poisson noise by the minimization of the cost function given in Eq. (1.88). Therefore both the approach of maximum likelihood and the cost function minimization algorithm are suitable for ptychography with noisy data [72, 90].

POSITION CORRECTED PTYCHOGRAPHY

Apart from the influence of noise, the accuracy of the *a priori* knowledge about the probe's scanning grid is another important factor which influences the quality of the reconstruction in ptychography. To improve the reconstruction, it was first proposed in 2012 [163] that one can apply the annealing approach to find the probe's positions which fit better to the measurements. In 2013, it was proposed [164] that, for each assumed position of the probe, we can correct that position by observing the cross-correlation between the estimated object in the current iteration and the one in the previous iteration. More recently, various of probe position correction algorithms have been proposed [165–167]. It was shown that, when the *a priori* knowledge about the position of the probe is inaccurate, one can indeed eliminate defects in the reconstructed image by correcting these positions.

FOURIER PTYCHOGRAPHY

Fourier ptychographic microscopy was proposed in 2013 [18, 168]. It can be regarded as an extension of ptychography [169]. The technique overcomes the resolution limit of conventional microscopy by enlarging the effective spatial frequency cut-off in the pupil plane. This is done by applying several broad illuminations similar to plane waves of the sample. The detector is in the plane conjugate to the sample plane, and each measurement corresponds to an individual incident angle of the illumination. With each tilted illumination $e^{i\mathbf{k}_{\perp,j}\cdot\mathbf{r}_\perp}$, the diffraction pattern of the sample in the plane of the exit pupil of the lens, denoted by $O(\mathbf{k}_\perp)$, is shifted to $O(\mathbf{k}_\perp - \mathbf{k}_{\perp,j})$ over the aperture used for imaging. Consecutive illumination tilts generate partially overlapping diffraction patterns within the aperture. With all the Fourier ptychographic measurements, the spatial spectrum

of the sample can be synthesized by using ptychographic algorithms while interchanging the real space and reciprocal space coordinates compared to normal ptychography [73, 157, 170].

REFERENCES

[1] D. Sayre, *Some implications of a theorem due to shannon,* Acta Crystallographica **5**, 843 (1952).

[2] R. W. Gerchberg and W. O. Saxton, *A practical algorithm for the determination of phase from image and diffraction plane pictures,* Optik **35**, 237 (1972).

[3] J. R. Fienup, *Reconstruction of an object from the modulus of its fourier transform,* Optics Letters **3**, 27 (1978).

[4] M. R. Teague, *Deterministic phase retrieval: a green's function solution,* Journal of the Optical Society of America **73**, 1434 (1983).

[5] J. Miao, D. Sayre, and H. N. Chapman, *Phase retrieval from the magnitude of the fourier transforms of nonperiodic objects,* Journal of the Optical Society of America A **15**, 1662 (1998).

[6] H. N. Chapman, *Phase-retrieval x-ray microscopy by wigner-distribution deconvolution,* Ultramicroscopy **66**, 153 (1996).

[7] S. Marchesini, H. He, H. N. Chapman, S. P. Hau-Riege, A. Noy, M. R. Howells, U. Weierstall, and J. C. H. Spence, *X-ray image reconstruction from a diffraction pattern alone,* Physical Review B **68** (2003), 10.1103/physrevb.68.140101.

[8] B. Abbey, K. A. Nugent, G. J. Williams, J. N. Clark, A. G. Peele, M. A. Pfeifer, M. de Jonge, and I. McNulty, *Keyhole coherent diffractive imaging,* Nature Physics **4**, 394 (2008).

[9] K. A. Nugent, *Coherent methods in the x-ray sciences,* Advances in Physics **59**, 1 (2010).

[10] M. Dierolf, A. Menzel, P. Thibault, P. Schneider, C. M. Kewish, R. Wepf, O. Bunk, and F. Pfeiffer, *Ptychographic x-ray computed tomography at the nanoscale,* Nature **467**, 436 (2010).

[11] F. Pfeiffer, *X-ray ptychography,* Nature Photonics **12**, 9 (2017).

[12] J. M. Rodenburg and R. H. T. Bates, *The theory of super-resolution electron microscopy via wigner-distribution deconvolution,* Philosophical Transactions of the Royal Society of London. Series A: Physical and Engineering Sciences **339**, 521 (1992).

[13] S. Gao, P. Wang, F. Zhang, G. T. Martinez, P. D. Nellist, X. Pan, and A. I. Kirkland, *Electron ptychographic microscopy for three-dimensional imaging,* Nature Communications **8** (2017), 10.1038/s41467-017-00150-1.

[14] Y. Jiang, Z. Chen, Y. Han, P. Deb, H. Gao, S. Xie, P. Purohit, M. W. Tate, J. Park, S. M. Gruner, V. Elser, and D. A. Muller, *Electron ptychography of 2d materials to deep sub-ångström resolution,* Nature **559**, 343 (2018).

[15] H. Stark, *Image Recovery: Theory and Application* (Academic Press, Orlando, 1987).

[16] J. R. Fienup, J. C. Marron, T. J. Schulz, and J. H. Seldin, *Hubble space telescope characterized by using phase-retrieval algorithms,* Applied Optics **32**, 1747 (1993).

[17] Y. Shechtman, Y. C. Eldar, O. Cohen, H. N. Chapman, J. Miao, and M. Segev, *Phase retrieval with application to optical imaging: A contemporary overview,* IEEE Signal Processing Magazine **32**, 87 (2015).

[18] G. Zheng, R. Horstmeyer, and C. Yang, *Wide-field, high-resolution fourier ptychographic microscopy,* Nature Photonics **7**, 739 (2013).

[19] J. R. Fienup, *Phase retrieval algorithms: a comparison,* Applied Optics **21**, 2758 (1982).

[20] V. Elser, *Phase retrieval by iterated projections,* Journal of the Optical Society of America A **20**, 40 (2003).

[21] D. R. Luke, *Relaxed averaged alternating reflections for diffraction imaging,* Inverse Problems **21**, 37 (2004).

[22] E. J. Candès, Y. C. Eldar, T. Strohmer, and V. Voroninski, *Phase retrieval via matrix completion,* SIAM Journal on Imaging Sciences **6**, 199 (2013).

[23] E. J. Candes, X. Li, and M. Soltanolkotabi, *Phase retrieval via wirtinger flow: Theory and algorithms,* IEEE Transactions on Information Theory **61**, 1985 (2015).

[24] D. GABOR, *A new microscopic principle,* Nature **161**, 777 (1948).

[25] M. Born, *Principles of Optics* (Elsevier Science, City, 1980).

[26] T. J. Davis, D. Gao, T. E. Gureyev, A. W. Stevenson, and S. W. Wilkins, *Phase-contrast imaging of weakly absorbing materials using hard x-rays,* Nature **373**, 595 (1995).

[27] B. C. Platt and R. Shack, *History and principles of shack-hartmann wavefront sensing,* Journal of Refractive Surgery **17**, S573 (2001).

[28] J. Liang, B. Grimm, S. Goelz, and J. F. Bille, *Objective measurement of wave aberrations of the human eye with the use of a hartmann–shack wave-front sensor,* Journal of the Optical Society of America A **11**, 1949 (1994).

[29] H. Gong, O. Soloviev, D. Wilding, P. Pozzi, M. Verhaegen, and G. Vdovin, *Holographic imaging with a shack-hartmann wavefront sensor,* Optics Express **24**, 13729 (2016).

[30] W. Hoppe, *Beugung im inhomogenen primärstrahlwellenfeld. i. prinzip einer phasenmessung von elektronenbeungungsinterferenzen,* Acta Crystallographica Section A **25**, 495 (1969).

[31] H. M. L. Faulkner and J. M. Rodenburg, *Movable aperture lensless transmission microscopy: A novel phase retrieval algorithm,* Physical Review Letters **93**, 023903 (2004).

[32] J. M. Rodenburg and H. M. L. Faulkner, *A phase retrieval algorithm for shifting illumination,* Applied Physics Letters **85**, 4795 (2004).

[33] M. Guizar-Sicairos and J. R. Fienup, *Phase retrieval with transverse translation diversity: a nonlinear optimization approach,* Optics Express **16**, 7264 (2008).

[34] A. M. Maiden and J. M. Rodenburg, *An improved ptychographical phase retrieval algorithm for diffractive imaging,* Ultramicroscopy **109**, 1256 (2009).

[35] P. Thibault, M. Dierolf, A. Menzel, O. Bunk, C. David, and F. Pfeiffer, *High-resolution scanning x-ray diffraction microscopy,* Science **321**, 379 (2008).

[36] P. Thibault, M. Dierolf, O. Bunk, A. Menzel, and F. Pfeiffer, *Probe retrieval in ptychographic coherent diffractive imaging,* Ultramicroscopy **109**, 338 (2009).

[37] D. J. Griffiths, *Introduction to Electrodynamics (3rd Edition)* (Prentice Hall, 1999).

[38] G. R. Fowles, *Introduction to Modern Optics* (Dover Publications Inc., 1990).

[39] L. Novotny and B. Hecht, *Principles of Nano-Optics* (Cambridge University Press, 2012).

[40] H. J. W. George B. Arfken, *Mathematical Methods for Physicists* (Elsevier LTD, Oxford, 2012).

[41] A. Zangwill, *Modern Electrodynamics* (Cambridge University Pr., 2013).

[42] T. A. van der Sijs, O. E. Gawhary, and H. P. Urbach, *Electromagnetic scattering beyond the weak regime: Solving the problem of divergent born perturbation series by padé approximants,* Physical Review Research **2** (2020), 10.1103/physrevresearch.2.013308.

[43] P. W. Hawkes and J. C. H. Spence, eds., *Springer Handbook of Microscopy* (Springer International Publishing, 2019).

[44] E. H. R. Tsai, I. Usov, A. Diaz, A. Menzel, and M. Guizar-Sicairos, *X-ray ptychography with extended depth of field,* Optics Express **24**, 29089 (2016).

[45] M. A. Gilles, Y. S. G. Nashed, M. Du, C. Jacobsen, and S. M. Wild, *3d x-ray imaging of continuous objects beyond the depth of focus limit,* Optica **5**, 1078 (2018).

[46] L. Rabiner, R. Schafer, and C. Rader, *The chirp z-transform algorithm,* IEEE Transactions on Audio and Electroacoustics **17**, 86 (1969).

[47] A. S. Jurling and J. R. Fienup, *Phase retrieval with unknown sampling factors via the two-dimensional chirp z-transform,* Journal of the Optical Society of America A **31**, 1904 (2014).

[48] A. S. Jurling, M. D. Bergkoetter, and J. R. Fienup, *Techniques for arbitrary sampling in two-dimensional fourier transforms,* Journal of the Optical Society of America A **35**, 1784 (2018).

[49] G. D. Martin, *Chirp Z-transform spectral zoom optimization with MATLAB.*, Tech. Rep. (2005).

[50] J. Miao, T. Ishikawa, E. H. Anderson, and K. O. Hodgson, *Phase retrieval of diffraction patterns from noncrystalline samples using the oversampling method,* Physical Review B **67** (2003), 10.1103/physrevb.67.174104.

[51] U. Weierstall, Q. Chen, J. Spence, M. Howells, M. Isaacson, and R. Panepucci, *Image reconstruction from electron and x-ray diffraction patterns using iterative algorithms: experiment and simulation,* Ultramicroscopy **90**, 171 (2002).

[52] T. B. Edo, D. J. Batey, A. M. Maiden, C. Rau, U. Wagner, Z. D. Pešić, T. A. Waigh, and J. M. Rodenburg, *Sampling in x-ray ptychography,* Physical Review A **87** (2013), 10.1103/physreva.87.053850.

[53] J. Spence, U. Weierstall, and M. Howells, *Coherence and sampling requirements for diffractive imaging,* Ultramicroscopy **101**, 149 (2004).

[54] J. R. Fienup, *Invariant error metrics for image reconstruction,* Applied Optics **36**, 8352 (1997).

[55] J. R. Fienup and C. C. Wackerman, *Phase-retrieval stagnation problems and solutions,* Journal of the Optical Society of America A **3**, 1897 (1986).

[56] J. R. Fienup, *Reconstruction of a complex-valued object from the modulus of its fourier transform using a support constraint,* Journal of the Optical Society of America A **4**, 118 (1987).

[57] S. Marchesini, *Invited article: A unified evaluation of iterative projection algorithms for phase retrieval,* Review of Scientific Instruments **78**, 011301 (2007).

[58] V. Elser, *Solution of the crystallographic phase problem by iterated projections,* Acta Crystallographica Section A Foundations of Crystallography **59**, 201 (2003).

[59] V. Elser, I. Rankenburg, and P. Thibault, *Searching with iterated maps,* Proceedings of the National Academy of Sciences **104**, 418 (2007).

[60] H. H. Bauschke, P. L. Combettes, and D. R. Luke, *Hybrid projection–reflection method for phase retrieval,* Journal of the Optical Society of America A **20**, 1025 (2003).

[61] H. N. Chapman and K. A. Nugent, *Coherent lensless x-ray imaging,* Nature Photonics **4**, 833 (2010).

[62] J. Rodenburg, *Ptychography and related diffractive imaging methods,* in *Advances in Imaging and Electron Physics* (Elsevier, 2008) pp. 87–184.

[63] P. W. Hawkes, *Springer handbook of microscopy* (Springer, Cham, Switzerland, 2019).

[64] H. N. Chapman, *Phase-retrieval x-ray microscopy by wigner-distribution deconvolution,* Ultramicroscopy **66**, 153 (1996).

[65] J. M. Rodenburg, A. C. Hurst, A. G. Cullis, B. R. Dobson, F. Pfeiffer, O. Bunk, C. David, K. Jefimovs, and I. Johnson, *Hard-x-ray lensless imaging of extended objects,* Physical Review Letters **98**, 034801 (2007).

[66] T. Popmintchev, M.-C. Chen, D. Popmintchev, P. Arpin, S. Brown, S. Alisauskas, G. Andriukaitis, T. Balciunas, O. D. Mucke, A. Pugzlys, A. Baltuska, B. Shim, S. E. Schrauth, A. Gaeta, C. Hernandez-Garcia, L. Plaja, A. Becker, A. Jaron-Becker, M. M. Murnane, and H. C. Kapteyn, *Bright coherent ultrahigh harmonics in the keV x-ray regime from mid-infrared femtosecond lasers,* Science **336**, 1287 (2012).

[67] M. D. Seaberg, B. Zhang, D. F. Gardner, E. R. Shanblatt, M. M. Murnane, H. C. Kapteyn, and D. E. Adams, *Tabletop nanometer extreme ultraviolet imaging in an extended reflection mode using coherent fresnel ptychography,* Optica **1**, 39 (2014).

[68] S. Witte, V. T. Tenner, D. W. Noom, and K. S. Eikema, *Lensless diffractive imaging with ultra-broadband table-top sources: from infrared to extreme-ultraviolet wavelengths,* Light: Science & Applications **3**, e163 (2014).

[69] M. Odstrcil, J. Bussmann, D. Rudolf, R. Bresenitz, J. Miao, W. S. Brocklesby, and L. Juschkin, *Ptychographic imaging with a compact gas–discharge plasma extreme ultraviolet light source,* Optics Letters **40**, 5574 (2015).

[70] C. L. Porter, M. Tanksalvala, M. Gerrity, G. Miley, X. Zhang, C. Bevis, E. Shanblatt, R. Karl, M. M. Murnane, D. E. Adams, and H. C. Kapteyn, *General-purpose, wide field-of-view reflection imaging with a tabletop 13 nm light source,* Optica **4**, 1552 (2017).

[71] D. F. Gardner, M. Tanksalvala, E. R. Shanblatt, X. Zhang, B. R. Galloway, C. L. Porter, R. K. Jr, C. Bevis, D. E. Adams, H. C. Kapteyn, M. M. Murnane, and G. F. Mancini, *Subwavelength coherent imaging of periodic samples using a 13.5 nm tabletop high-harmonic light source,* Nature Photonics **11**, 259 (2017).

[72] P. Thibault and M. Guizar-Sicairos, *Maximum-likelihood refinement for coherent diffractive imaging,* New Journal of Physics **14**, 063004 (2012).

[73] R. Horstmeyer, R. Y. Chen, X. Ou, B. Ames, J. A. Tropp, and C. Yang, *Solving ptychography with a convex relaxation,* New Journal of Physics **17**, 053044 (2015).

[74] J. Zhong, L. Tian, P. Varma, and L. Waller, *Nonlinear optimization algorithm for partially coherent phase retrieval and source recovery,* IEEE Transactions on Computational Imaging **2**, 310 (2016).

[75] J. C. da Silva and A. Menzel, *Elementary signals in ptychography,* Optics Express **23**, 33812 (2015).

[76] M. Guizar-Sicairos and J. R. Fienup, *Understanding the twin-image problem in phase retrieval,* Journal of the Optical Society of America A **29**, 2367 (2012).

[77] P. Thibault and A. Menzel, *Reconstructing state mixtures from diffraction measurements,* Nature **494**, 68 (2013).

[78] J. Clark, X. Huang, R. Harder, and I. Robinson, *High-resolution three-dimensional partially coherent diffraction imaging,* Nature Communications **3** (2012), 10.1038/ncomms1994.

[79] N. Burdet, X. Shi, D. Parks, J. N. Clark, X. Huang, S. D. Kevan, and I. K. Robinson, *Evaluation of partial coherence correction in x-ray ptychography,* Optics Express **23**, 5452 (2015).

[80] B. Chen, R. A. Dilanian, S. Teichmann, B. Abbey, A. G. Peele, G. J. Williams, P. Hannaford, L. Van Dao, H. M. Quiney, and K. A. Nugent, *Multiple wavelength diffractive imaging,* Phys. Rev. A **79**, 023809 (2009).

[81] B. Enders, M. Dierolf, P. Cloetens, M. Stockmar, F. Pfeiffer, and P. Thibault, *Ptychography with broad-bandwidth radiation,* Applied Physics Letters **104**, 171104 (2014).

[82] P. D. Baksh, M. Odstrčil, H.-S. Kim, S. A. Boden, J. G. Frey, and W. S. Brocklesby, *Wide-field broadband extreme ultraviolet transmission ptychography using a high-harmonic source,* Optics Letters **41**, 1317 (2016).

[83] L. W. Whitehead, G. J. Williams, H. M. Quiney, D. J. Vine, R. A. Dilanian, S. Flewett, K. A. Nugent, A. G. Peele, E. Balaur, and I. McNulty, *Diffractive imaging using partially coherent x rays,* Phys. Rev. Lett. **103**, 243902 (2009).

[84] E. Malm, H. Wikmark, B. Pfau, P. Villanueva-Perez, P. Rudawski, J. Peschel, S. Maclot, M. Schneider, S. Eisebitt, A. Mikkelsen, A. L'Huillier, and P. Johnsson, *Singleshot polychromatic coherent diffractive imaging with a high-order harmonic source,* Optics Express **28**, 394 (2020).

[85] J. Huijts, S. Fernandez, D. Gauthier, M. Kholodtsova, A. Maghraoui, K. Medjoubi, A. Somogyi, W. Boutu, and H. Merdji, *Broadband coherent diffractive imaging,* Nature Photonics (2020), 10.1038/s41566-020-0660-7.

[86] F. Zhang, B. Chen, G. R. Morrison, J. Vila-Comamala, M. Guizar-Sicairos, and I. K. Robinson, *Phase retrieval by coherent modulation imaging,* Nature Communications **7** (2016), 10.1038/ncomms13367.

[87] Y. Bai, S. Vettil, X. Pan, C. Liu, and J. Zhu, *Ptychographic microscopy via wavelength scanning,* APL Photonics **2**, 056101 (2017).

[88] D. E. B. Flaes and S. Witte, *Interference probe ptychography for computational amplitude and phase microscopy,* Optics Express **26**, 31372 (2018).

[89] A. Maiden, D. Johnson, and P. Li, *Further improvements to the ptychographical iterative engine,* Optica **4**, 736 (2017).

[90] P. Godard, M. Allain, V. Chamard, and J. Rodenburg, *Noise models for low counting rate coherent diffraction imaging,* Optics Express **20**, 25914 (2012).

[91] P. Li, T. B. Edo, and J. M. Rodenburg, *Ptychographic inversion via wigner distribution deconvolution: Noise suppression and probe design,* Ultramicroscopy **147**, 106 (2014).

[92] N. Streibl, *Phase imaging by the transport equation of intensity,* Optics Communications **49**, 6 (1984).

[93] L. Waller, L. Tian, and G. Barbastathis, *Transport of intensity imaging with higher order derivatives,* Optics Express **18**, 12552 (2010).

[94] L. Allen and M. Oxley, *Phase retrieval from series of images obtained by defocus variation,* Optics Communications **199**, 65 (2001).

[95] T. E. Gureyev, A. Roberts, and K. A. Nugent, *Phase retrieval with the transport-of-intensity equation: matrix solution with use of zernike polynomials,* Journal of the Optical Society of America A **12**, 1932 (1995).

[96] T. E. Gureyev and K. A. Nugent, *Phase retrieval with the transport-of-intensity equation II orthogonal series solution for nonuniform illumination,* Journal of the Optical Society of America A **13**, 1670 (1996).

[97] L. Waller, M. Tsang, S. Ponda, S. Y. Yang, and G. Barbastathis, *Phase and amplitude imaging from noisy images by kalman filtering,* Optics Express **19**, 2805 (2011).

[98] S. Zheng, B. Xue, W. Xue, X. Bai, and F. Zhou, *Transport of intensity phase imaging from multiple noisy intensities measured in unequally-spaced planes,* Optics Express **20**, 972 (2012).

[99] G. W. Stroke, *LENSLESS FOURIER-TRANSFORM METHOD FOR OPTICAL HOLOGRAPHY,* Applied Physics Letters **6**, 201 (1965).

[100] I. McNulty, J. Kirz, C. Jacobsen, E. H. Anderson, M. R. Howells, and D. P. Kern, *High-resolution imaging by fourier transform x-ray holography,* Science **256**, 1009 (1992).

[101] S. Eisebitt, J. Lüning, W. F. Schlotter, M. Lörgen, O. Hellwig, W. Eberhardt, and J. Stöhr, *Lensless imaging of magnetic nanostructures by x-ray spectro-holography,* Nature **432**, 885 (2004).

[102] W. F. Schlotter, R. Rick, K. Chen, A. Scherz, J. Stöhr, J. Lüning, S. Eisebitt, C. Günther, W. Eberhardt, O. Hellwig, and I. McNulty, *Multiple reference fourier transform holography with soft x rays,* Applied Physics Letters **89**, 163112 (2006).

[103] R. L. Sandberg, D. A. Raymondson, C. L. o vorakiat, A. Paul, K. S. Raines, J. Miao, M. M. Murnane, H. C. Kapteyn, and W. F. Schlotter, *Tabletop soft-x-ray fourier transform holography with 50 nm resolution,* Optics Letters **34**, 1618 (2009).

[104] Y. Meng, C. Zhang, C. Marceau, A. Y. Naumov, P. B. Corkum, and D. M. Villeneuve, *Octave-spanning hyperspectral coherent diffractive imaging in the extreme ultraviolet range,* Optics Express **23**, 28960 (2015).

[105] K. H. Lee, H. Yun, J. H. Sung, S. K. Lee, H. W. Lee, H. T. Kim, and C. H. Nam, *Autocorrelation-subtracted fourier transform holography method for large specimen imaging,* Applied Physics Letters **106**, 061103 (2015).

[106] C. Q. Tran, A. G. Peele, A. Roberts, K. A. Nugent, D. Paterson, and I. McNulty, *Synchrotron beam coherence: a spatially resolved measurement,* Optics Letters **30**, 204 (2005).

[107] C. Q. Tran, G. J. Williams, A. Roberts, S. Flewett, A. G. Peele, D. Paterson, M. D. de Jonge, and K. A. Nugent, *Experimental measurement of the four-dimensional coherence function for an undulator x-ray source,* Physical Review Letters **98** (2007), 10.1103/physrevlett.98.224801.

[108] J. N. Clark and A. G. Peele, *Simultaneous sample and spatial coherence characterisation using diffractive imaging,* Applied Physics Letters **99**, 154103 (2011).

[109] B. Abbey, L. W. Whitehead, H. M. Quiney, D. J. Vine, G. A. Cadenazzi, C. A. Henderson, K. A. Nugent, E. Balaur, C. T. Putkunz, A. G. Peele, G. J. Williams, and I. McNulty, *Lensless imaging using broadband x-ray sources,* Nature Photonics **5**, 420 (2011).

[110] D. H. Parks, X. Shi, and S. D. Kevan, *Partially coherent x-ray diffractive imaging of complex objects,* Physical Review A **89** (2014), 10.1103/physreva.89.063824.

[111] P. D. Baksh, M. Odstrčil, H.-S. Kim, S. A. Boden, J. G. Frey, and W. S. Brocklesby, *Wide-field broadband extreme ultraviolet transmission ptychography using a high-harmonic source,* Optics Letters **41**, 1317 (2016).

[112] B. Zhang, D. F. Gardner, M. H. Seaberg, E. R. Shanblatt, C. L. Porter, R. Karl, C. A. Mancuso, H. C. Kapteyn, M. M. Murnane, and D. E. Adams, *Ptychographic hyperspectral spectromicroscopy with an extreme ultraviolet high harmonic comb,* Optics Express **24**, 18745 (2016).

[113] E. Wolf, *New theory of partial coherence in the space–frequency domain part i: spectra and cross spectra of steady-state sources,* Journal of the Optical Society of America **72**, 343 (1982).

[114] A. Starikov and E. Wolf, *Coherent-mode representation of gaussian schell-model sources and of their radiation fields,* Journal of the Optical Society of America **72**, 923 (1982).

[115] S. Flewett, H. M. Quiney, C. Q. Tran, and K. A. Nugent, *Extracting coherent modes from partially coherent wavefields,* Optics Letters **34**, 2198 (2009).

[116] P. Li, T. Edo, D. Batey, J. Rodenburg, and A. Maiden, *Breaking ambiguities in mixed state ptychography,* Optics Express **24**, 9038 (2016).

[117] D. J. Batey, D. Claus, and J. M. Rodenburg, *Information multiplexing in ptychography,* Ultramicroscopy **138**, 13 (2014).

[118] N. Burdet, X. Shi, D. Parks, J. N. Clark, X. Huang, S. D. Kevan, and I. K. Robinson, *Evaluation of partial coherence correction in x-ray ptychography,* Optics Express **23**, 5452 (2015).

[119] W. Yu, S. Wang, S. Veetil, S. Gao, C. Liu, and J. Zhu, *High-quality image reconstruction method for ptychography with partially coherent illumination,* Physical Review B **93** (2016), 10.1103/physrevb.93.241105.

[120] X. Dong, X. Pan, C. Liu, and J. Zhu, *Single shot multi-wavelength phase retrieval with coherent modulation imaging,* Optics Letters **43**, 1762 (2018).

[121] E. Wolf, *Three-dimensional structure determination of semi-transparent objects from holographic data,* Optics Communications **1**, 153 (1969).

[122] R. Bracewell, *Strip integration in radio astronomy,* Australian Journal of Physics **9**, 198 (1956).

[123] A. Devaney, *A filtered backpropagation algorithm for diffraction tomography,* Ultrasonic Imaging **4**, 336 (1982).

[124] R. Gordon, R. Bender, and G. T. Herman, *Algebraic reconstruction techniques (ART) for three-dimensional electron microscopy and x-ray photography,* Journal of Theoretical Biology **29**, 471 (1970).

[125] P. Gilbert, *Iterative methods for the three-dimensional reconstruction of an object from projections,* Journal of Theoretical Biology **36**, 105 (1972).

[126] M. H. Maleki and A. J. Devaney, *Phase-retrieval and intensity-only reconstruction algorithms for optical diffraction tomography,* Journal of the Optical Society of America A **10**, 1086 (1993).

[127] H. N. Chapman, A. Barty, S. Marchesini, A. Noy, S. P. Hau-Riege, C. Cui, M. R. Howells, R. Rosen, H. He, J. C. H. Spence, U. Weierstall, T. Beetz, C. Jacobsen, and D. Shapiro, *High-resolution ab initio three-dimensional x-ray diffraction microscopy,* Journal of the Optical Society of America A **23**, 1179 (2006).

[128] C. T. Putkunz, M. A. Pfeifer, A. G. Peele, G. J. Williams, H. M. Quiney, B. Abbey, K. A. Nugent, and I. McNulty, *Fresnel coherent diffraction tomography,* Optics Express **18**, 11746 (2010).

[129] M. Guizar-Sicairos, A. Diaz, M. Holler, M. S. Lucas, A. Menzel, R. A. Wepf, and O. Bunk, *Phase tomography from x-ray coherent diffractive imaging projections,* Optics Express **19**, 21345 (2011).

[130] I. Peterson, B. Abbey, C. Putkunz, D. Vine, G. van Riessen, G. Cadenazzi, E. Balaur, R. Ryan, H. Quiney, I. McNulty, A. Peele, and K. Nugent, *Nanoscale fresnel coherent diffraction imaging tomography using ptychography,* Optics Express **20**, 24678 (2012).

[131] M. Stockmar, M. Hubert, M. Dierolf, B. Enders, R. Clare, S. Allner, A. Fehringer, I. Zanette, J. Villanova, J. Laurencin, P. Cloetens, F. Pfeiffer, and P. Thibault, *X-ray nanotomography using near-field ptychography,* Optics Express **23**, 12720 (2015).

[132] S. V. Venkatakrishnan, M. Farmand, Y.-S. Yu, H. Majidi, K. van Benthem, S. Marchesini, D. A. Shapiro, and A. Hexemer, *Robust x-ray phase ptycho-tomography,* IEEE Signal Processing Letters **23**, 944 (2016).

[133] M. Holler, M. Guizar-Sicairos, E. H. R. Tsai, R. Dinapoli, E. Müller, O. Bunk, J. Raabe, and G. Aeppli, *High-resolution non-destructive three-dimensional imaging of integrated circuits,* Nature **543**, 402 (2017).

[134] D. Gürsoy, *Direct coupling of tomography and ptychography,* Optics Letters **42**, 3169 (2017).

[135] K. Shimomura, M. Hirose, T. Higashino, and Y. Takahashi, *Three-dimensional iterative multislice reconstruction for ptychographic x-ray computed tomography,* Optics Express **26**, 31199 (2018).

[136] S. Sala, D. J. Batey, A. Prakash, S. Ahmed, C. Rau, and P. Thibault, *Ptychographic x-ray computed tomography at a high-brilliance x-ray source,* Optics Express **27**, 533 (2019).

[137] M. Kahnt, J. Becher, D. Brückner, Y. Fam, T. Sheppard, T. Weissenberger, F. Wittwer, J.-D. Grunwaldt, W. Schwieger, and C. G. Schroer, *Coupled ptychography and tomography algorithm improves reconstruction of experimental data,* Optica **6**, 1282 (2019).

[138] S. Aslan, V. Nikitin, D. J. Ching, T. Bicer, S. Leyffer, and D. Gürsoy, *Joint ptycho-tomography reconstruction through alternating direction method of multipliers,* Optics Express **27**, 9128 (2019).

[139] J. M. Cowley and A. F. Moodie, *The scattering of electrons by atoms and crystals. i. a new theoretical approach,* Acta Crystallographica **10**, 609 (1957).

[140] A. M. Maiden, M. J. Humphry, and J. M. Rodenburg, *Ptychographic transmission microscopy in three dimensions using a multi-slice approach,* Journal of the Optical Society of America A **29**, 1606 (2012).

[141] P. R. T. Munro, *Rigorous multi-slice wave optical simulation of x-ray propagation in inhomogeneous space,* Journal of the Optical Society of America A **36**, 1197 (2019).

[142] T. M. Godden, R. Suman, M. J. Humphry, J. M. Rodenburg, and A. M. Maiden, *Ptychographic microscope for three-dimensional imaging,* Optics Express **22**, 12513 (2014).

[143] A. Suzuki, S. Furutaku, K. Shimomura, K. Yamauchi, Y. Kohmura, T. Ishikawa, and Y. Takahashi, *High-resolution multislice x-ray ptychography of extended thick objects,* Physical Review Letters **112** (2014), 10.1103/physrevlett.112.053903.

[144] C. Jacobsen, *Relaxation of the crowther criterion in multislice tomography,* Optics Letters **43**, 4811 (2018).

[145] E. H. R. Tsai, F. Marone, and M. Guizar-Sicairos, *Gridrec-MS: an algorithm for multi-slice tomography,* Optics Letters **44**, 2181 (2019).

[146] P. Li and A. Maiden, *Multi-slice ptychographic tomography,* Scientific Reports **8** (2018), 10.1038/s41598-018-20530-x.

[147] M. A. Gilles, Y. S. G. Nashed, M. Du, C. Jacobsen, and S. M. Wild, *3d x-ray imaging of continuous objects beyond the depth of focus limit,* Optica **5**, 1078 (2018).

[148] N. Burdet, G. R. Morrison, X. Huang, X. Shi, J. N. Clark, F. Zhang, M. Civita, R. Harder, and I. K. Robinson, *Observations of artefacts in the x-ray ptychography method,* Optics Express **22**, 10294 (2014).

[149] H. Chang, P. Enfedaque, J. Zhang, J. Reinhardt, B. Enders, Y.-S. Yu, D. Shapiro, C. G. Schroer, T. Zeng, and S. Marchesini, *Advanced denoising for x-ray ptychography,* Optics Express **27**, 10395 (2019).

[150] A. Suzuki and Y. Takahashi, *Dark-field x-ray ptychography,* Optics Express **23**, 16429 (2015).

[151] M. Stockmar, P. Cloetens, I. Zanette, B. Enders, M. Dierolf, F. Pfeiffer, and P. Thibault, *Near-field ptychography: phase retrieval for inline holography using a structured illumination,* Scientific Reports **3**, 1927 (2013).

[152] C. Zuo, J. Sun, and Q. Chen, *Adaptive step-size strategy for noise-robust fourier ptychographic microscopy,* Optics Express **24**, 20724 (2016).

[153] M. Odstrčil, M. Lebugle, M. Guizar-Sicairos, C. David, and M. Holler, *Towards optimized illumination for high-resolution ptychography,* Optics Express **27**, 14981 (2019).

[154] M. Guizar-Sicairos, M. Holler, A. Diaz, J. Vila-Comamala, O. Bunk, and A. Menzel, *Role of the illumination spatial-frequency spectrum for ptychography,* Physical Review B **86** (2012), 10.1103/physrevb.86.100103.

[155] B. R. Frieden, *Restoring with maximum likelihood and maximum entropy,* Journal of the Optical Society of America **62**, 511 (1972).

[156] S. M. Kay, *Fundamentals Of Statistical Signal Processing, Volume 1: Estimation Theory* (Pearson, 2009).

[157] L.-H. Yeh, J. Dong, J. Zhong, L. Tian, M. Chen, G. Tang, M. Soltanolkotabi, and L. Waller, *Experimental robustness of fourier ptychography phase retrieval algorithms,* Optics Express **23**, 33214 (2015).

[158] M. Odstrčil, A. Menzel, and M. Guizar-Sicairos, *Iterative least-squares solver for generalized maximum-likelihood ptychography,* Optics Express **26**, 3108 (2018).

[159] Y. Zhang, P. Song, and Q. Dai, *Fourier ptychographic microscopy using a generalized anscombe transform approximation of the mixed poisson-gaussian likelihood,* Optics Express **25**, 168 (2017).

[160] A. P. Konijnenberg, W. M. J. Coene, and H. P. Urbach, *Model-independent noise-robust extension of ptychography,* Optics Express **26**, 5857 (2018).

[161] M. S. Bartlett, *The square root transformation in analysis of variance,* Supplement to the Journal of the Royal Statistical Society **3**, 68 (1936).

[162] F. J. Anscombe, *The transformation of poisson, binomial and negative-binomial data,* Biometrika **35**, 246 (1948).

[163] A. Maiden, M. Humphry, M. Sarahan, B. Kraus, and J. Rodenburg, *An annealing algorithm to correct positioning errors in ptychography,* Ultramicroscopy **120**, 64 (2012).

[164] F. Zhang, I. Peterson, J. Vila-Comamala, A. Diaz, F. Berenguer, R. Bean, B. Chen, A. Menzel, I. K. Robinson, and J. M. Rodenburg, *Translation position determination in ptychographic coherent diffraction imaging,* Optics Express **21**, 13592 (2013).

[165] D. B. Moore and J. R. Fienup, *Ptychography for optical metrology with limited translation knowledge,* Applied Optics **55**, 4596 (2016).

[166] P. Dwivedi, A. Konijnenberg, S. Pereira, and H. Urbach, *Lateral position correction in ptychography using the gradient of intensity patterns,* Ultramicroscopy **192**, 29 (2018).

[167] L. Rong, C. Tang, D. Wang, B. Li, F. Tan, Y. Wang, and X. Shi, *Probe position correction based on overlapped object wavefront cross-correlation for continuous-wave terahertz ptychography,* Optics Express **27**, 938 (2019).

[168] X. Ou, G. Zheng, and C. Yang, *Embedded pupil function recovery for fourier ptychographic microscopy,* Optics Express **22**, 4960 (2014).

[169] R. Horstmeyer and C. Yang, *A phase space model of fourier ptychographic microscopy,* Optics Express **22**, 338 (2014).

[170] Y. Zhang, W. Jiang, and Q. Dai, *Nonlinear optimization approach for fourier ptychographic microscopy,* Optics Express **23**, 33822 (2015).

2

PTYCHOGRAPHY WITH MULTIPLE WAVELENGTH ILLUMINATION

Parts of this chapter have been published in Optics Express **27**, 25 (2019) [1].

2.1. INTRODUCTION

In principle, a highly coherent illumination is always demanded while performing ptychography [2, 3]. However, in the X-ray regime, where ptychography has been widely used, light sources are either spatially partially coherent (e.g. synchrotron radiation [4, 5]) or temporally partially coherent (e.g. tabletop high-harmonic generation laser [6, 7]). To mitigate the unwanted effect due to the partial coherence, and also to improve the throughput of the imaging system, more novel algorithms have been introduced into ptychography during the last decade, among which the most popular approaches are the blind deconvolution method [8] and the modes decomposition method [9]. Both of these approaches were initially utilized for performing ptychography with spatially partially coherent illumination. The mode decomposition method was later used to perform ptychography with spatially coherent but temporally broadband illumination. The polychromatic ptychography was named ptychographic information multiplexing (PIM) met-hod [10], in which the object is illuminated by a spatially fully coherent light beam, which spectrum however consists of several wavelengths. The exit wave immediately behind the object is decomposed into mutually incoherent modes, each mode corresponding to one wavelength. Then these modes are reconstructed simultaneously by minimizing the distance between the estimated diffraction intensity and the measurement, which is the incoherent sum of the intensities of the separate wavelengths.

In this chapter, we propose an alternative polychromatic ptychography scheme where the modes in the PIM method are all expressed in the transmission and the thickness function of the sample. We consider both the case that the probe for the different wavelengths is assumed known, and the case of simultaneous reconstruction of unknown probe and the object. Our method is described and derived in Section 2.2. After introducing the error functions in Section 2.2.3, our simulation settings and results are presented in Subsection 2.3, followed by a quantitative study on the error functions and a comparison with the PIM method in the same subsection. The simulation includes probe reconstruction is demonstrated in Subsection 2.3.7. We conclude the chapter with a summary and outlook in Section 2.4.

2.2. METHOD

2.2.1. PLANE-WAVE ILLUMINATION

We start by considering a polychromatic ptychography configuration as depicted in Fig. 2.1. A part of the object is illuminated by a spatially coherent plane-wave, which has distinct peaks in its temporal spectrum $\Lambda(\lambda)$. The object is moved to a number of positions while a set of ptychographic data is collected in the far field. For one position of the object and for one wavelength λ, we denote the exit wave immediately behind the object by $\Psi(\mathbf{r}_\perp, \lambda)$ and the measured intensity of the diffracted field by $I^{\mathrm{m}}(\mathbf{r}'_\perp)$. Here $\mathbf{r}_\perp$ and $\mathbf{r}'_\perp$ are 2-D coordinates in the object-plane and the detector-plane, respectively.

In our proposed scheme, instead of decomposing the exit wave into mutually incoherent modes and calculating their diffraction intensities, we consider the relation between these modes. In the plane-wave illumination configuration, the exit wave $\Psi(\mathbf{r}_\perp, \lambda)$ is given by the object's complex transmission function multiplied by a planar wave with wavelength λ. For the case where the illumination contains several separate wavelengths

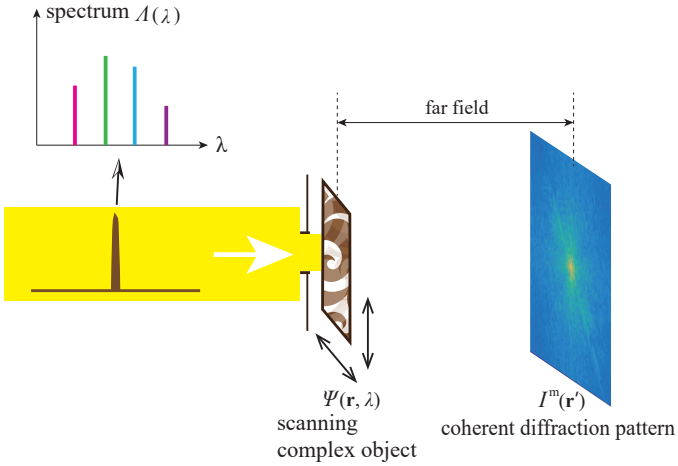

Figure 2.1: Polychromatic ptychography configuration with plane-wave illumination.

$\lambda_1 < \lambda_2 < \cdots < \lambda_k < \cdots < \lambda_N$ in its temporal spectrum $\Lambda(\lambda)$. The exit wave $\Psi(\mathbf{r}_\perp, \lambda)$ for wavelength λ_k and probe position $\mathbf{R}_{\perp,j}$ is (apart from a phase constant, see in Section 1.3.3):

$$\Psi_j(\mathbf{r}_\perp, \lambda_k) = P(\mathbf{r}_\perp - \mathbf{R}_{\perp,j}) \cdot A(\mathbf{r}_\perp) \cdot \exp\left[\mathrm{i}\frac{\lambda_1}{\lambda_k}\phi(\mathbf{r}_\perp)\right], \tag{2.1}$$

where $\mathbf{R}_{\perp,j}$ represents the jth relative position between the probe and the object. $A(\mathbf{r}_\perp)$ is the object's transmission function and $\phi(\mathbf{r}_\perp)$ stands for 2π times the ratio of the object thickness function and wavelength λ_1. Note that both $A(\mathbf{r}_\perp)$ and $\phi(\mathbf{r}_\perp)$ are real valued and that $A(\mathbf{r}_\perp)$ is positive. $P(\mathbf{r}_\perp)$ stands for the illumination (or probe) function, which in this subsection is treated as a planar wavefield multiplied by an circular aperture with radius r_0:

$$P(\mathbf{r}_\perp) = \begin{cases} P(\mathbf{r}_\perp), & |\mathbf{r}_\perp| \le r_0, \\ 0, & |\mathbf{r}_\perp| > r_0. \end{cases} \tag{2.2}$$

Note that in Eq. (2.1) we assume that the object has no dispersion. For dispersive materials, the exponential term in Eq. (2.1) should be modified by introducing the ratio of the refractive indices at wavelengths λ_1 and λ_k, and the absorption should be represented by the imaginary part of the refractive indices.

The goal in our polychromatic ptychography scheme, for the case that the probe P is known , is to retrieve $A(\mathbf{r}_\perp)$ and $\phi(\mathbf{r}_\perp)$ simultaneously. To do that, we minimize the following cost function:

$$\mathscr{E} = \sum_j \mathscr{E}_j = \sum_j \sum_{\mathbf{r}'_\perp} \left[\sqrt{I_j^{\mathrm{m}}(\mathbf{r}'_\perp)} - \sqrt{I_j(\mathbf{r}'_\perp)}\right]^2, \tag{2.3}$$

where $I_j^{\mathrm{m}}(\mathbf{r}'_\perp)$ is the measured intensity when the probe is at position $\mathbf{R}_{\perp,j}$ and $I_j(\mathbf{r}'_\perp)$ is the estimated polychromatic far field diffraction intensity which is an incoherent sum

over all calculated monochromatic diffraction patterns [11]:

$$I_j(\mathbf{r}'_\perp) = \mathbf{1}_D(\mathbf{r}'_\perp) \cdot \sum_k \left| \mathscr{F}_\perp \left[\Psi_j(\mathbf{r}_\perp, \lambda_k) \right] \left(\frac{\mathbf{r}'_\perp}{\lambda_k z'} \right) \right|^2, \tag{2.4}$$

where $\mathbf{1}_D(\mathbf{r}'_\perp)$ is a binary window function representing the region of the detector:

$$\mathbf{1}_D(\mathbf{r}'_\perp) = \begin{cases} 1, & |x'| \leq x'_D, |y'| \leq y'_D, \\ 0, & |x'| > x'_D, |y'| > y'_D, \end{cases} \tag{2.5}$$

and $\mathscr{F}_\perp$ denoting the Fourier transform, which is used to propagate the exit wave to the far field over the large distance z'.

The reconstruction of $A(\mathbf{r}_\perp)$ and $\phi(\mathbf{r}_\perp)$ is done by applying the steepest decent procedure to the cost function $\mathscr{E}(A, \phi)$. In Supplement section 2.5.1 detailed derivations are given of the following formulas for updating $A(\mathbf{r}_\perp)$ and $\phi(\mathbf{r}_\perp)$:

$$A_{n+1}(\mathbf{r}_\perp) = A_n(\mathbf{r}_\perp) + \beta_A \sum_j \sum_k \Re \left\{ \left[P_j(\mathbf{r}_\perp) \right]^* \cdot \exp \left[-\mathrm{i} \frac{\lambda_1}{\lambda_k} \phi_n(\mathbf{r}_\perp) \right] \cdot \Delta\Psi_{j,n}(\mathbf{r}_\perp, \lambda_k) \right\}, \tag{2.6a}$$

$$\begin{aligned} \phi_{n+1}(\mathbf{r}_\perp) = & \phi_n(\mathbf{r}_\perp) + \\ & \beta_\phi \sum_j \sum_k \Re \left\{ \left[P_j(\mathbf{r}_\perp) \right]^* \cdot -\mathrm{i} \frac{\lambda_1}{\lambda_k} \cdot A_n(\mathbf{r}_\perp) \cdot \exp \left[-\mathrm{i} \frac{\lambda_1}{\lambda_k} \phi_n(\mathbf{r}_\perp) \right] \cdot \Delta\Psi_{j,n}(\mathbf{r}_\perp, \lambda_k) \right\}, \end{aligned} \tag{2.6b}$$

where $\Re$ denotes the real part of a complex number, $*$ is complex conjugation, β_A and β_ϕ are constant step sizes taken along the direction of gradient descent of the cost function, the index n stands for the iteration number, and $\Delta\Psi(\mathbf{r}_\perp, \lambda_k)$ is defined by:

$$\Delta\Psi_{j,n}(\mathbf{r}_\perp, \lambda_k) = \mathscr{F}_\perp^{-1} \left\{ \mathbf{1}_D(\mathbf{r}'_\perp) \cdot \left(\frac{\sqrt{I_j^{\mathrm{m}}(\mathbf{r}'_\perp)}}{\sqrt{I_{j,n}(\mathbf{r}'_\perp)} + \gamma} - 1 \right) \cdot \mathscr{F}_\perp \left[\Psi_{j,n}(\mathbf{r}_\perp, \lambda_k) \right] \left(\frac{\mathbf{r}'_\perp}{\lambda_k z'} \right) \right\} (\mathbf{r}_\perp, \lambda_k), \tag{2.7}$$

where $\gamma > 0$ is a regularization parameter which prevents division by zero. Its value should be chosen comparable to the noise level so that an accurate reconstruction can be guaranteed. The Eq. (2.6) are implemented sequentially for all lateral positions as one complete iteration. Note that $A(\mathbf{r}_\perp)$ and $\phi(\mathbf{r}_\perp)$ are only updated where $P_j(\mathbf{r}_\perp)$ is nonzero. Here we stress that the expression for $\Delta\Psi(\mathbf{r}_\perp, \lambda_k)$ can also be identified as the gradient descent direction of the cost function with respect to each mode in the PIM method.

For successfully retrieving $A(\mathbf{r}_\perp)$ and $\phi(\mathbf{r}_\perp)$, the complete ptychographic dataset must be used. To do that, we sequentially implement Eq. (2.6) on every lateral position of the object as a complete reconstruction procedure within one iteration. In the meantime, we also introduce a positive-value correction to the amplitude reconstruction $A(\mathbf{r}_\perp)$ at the end of each iteration, so that a positive amplitude is obtained and hence the phase is well defined. A framework of our proposed model is summarized in **Algorithm 1**.

2.2.2. WITH PROBE RECONSTRUCTION

In the previous subsection we restricted ourselves to the case where the illumination (or probe) is a localized plane-wave. One can imagine that if in practice this condition is vio-

Algorithm 1 polychromatic ptychography algorithm with plane-wave illumination

```
iteration number n = 1
Δ_A = a small positive number (e.g. 10^−3)
repeat
  for each probe position R_⊥,j do
    for each λ_k do
      forward propagate the wavefield;
    end for
    use Eq. (2.4) to calculate I(r'_⊥);
    for each λ_k do
      use Eq .(2.7) to apply intensity constraint on the total diffraction field;
      backward propagate the wavefields for every λ_k;
    end for
    use Eq. (2.6) to update A(r_⊥) and φ(r_⊥);
    if A_n(r_⊥) < 0 then
      A_n(r_⊥) = Δ_A;
    end if
  end for
  n = n + 1;
until algorithm converges
```


lated, directly applying the algorithm will end up with stagnation or an inaccurate reconstruction. Therefore to achieve a better of the reconstruction's quality, simultaneously retrieving the probe function and the object's transmission and thickness functions is necessary in such cases. As shown in Fig. 2.1, in our model the object is illuminated by a wavefield which contains multiple wavelength components. If these components have different intensity and wavefront profiles, then we have to model this polychromatic probe function as an incoherent superposition of different modes and using the PIM formula to reconstruct these modes would be the most reasonable choice. Here we only consider a simple situation where every mode shares the same intensity and wavefront profile. In that case the exit wave field $\Psi(\mathbf{r}_\perp,\lambda)$ can be written as in Eq. (2.1). However, now $P(\mathbf{r}_\perp)$ is a complex-valued probe function which represents the illumination wave field of all wavelengths. To incorporate the reconstruction of this probe function, Eq. (2.6) is modified as :

$$A_{n+1}(\mathbf{r}_\perp) = A_n(\mathbf{r}_\perp) + \beta_A \sum_k \Re\left\{\left[P_{j,n}(\mathbf{r}_\perp)\right]^* \cdot \exp\left[-\mathrm{i}\frac{\lambda_1}{\lambda_k}\phi_n(\mathbf{r}_\perp)\right] \cdot \Delta\Psi_{j,n}(\mathbf{r}_\perp,\lambda_k)\right\}, \tag{2.8a}$$

$$\phi_{n+1}(\mathbf{r}_\perp) = \phi_n(\mathbf{r}_\perp) + \beta_\phi \sum_k \Re\left\{\left[P_{j,n}(\mathbf{r}_\perp)\right]^* \cdot -\mathrm{i}\frac{\lambda_1}{\lambda_k} \cdot A_n(\mathbf{r}_\perp) \cdot \exp\left[-\mathrm{i}\frac{\lambda_1}{\lambda_k}\phi_n(\mathbf{r}_\perp)\right] \cdot \Delta\Psi_{j,n}(\mathbf{r}_\perp,\lambda_k)\right\}, \tag{2.8b}$$

$$P_{n+1}(\mathbf{r}_\perp) = P_n(\mathbf{r}_\perp) + \beta_P \sum_k A_n(\mathbf{r}_\perp + \mathbf{R}_{\perp,j}) \cdot \exp\left[-\mathrm{i}\frac{\lambda_1}{\lambda_k}\phi_n(\mathbf{r}_\perp + \mathbf{R}_{\perp,j})\right] \cdot \Delta\Psi_{j,n}(\mathbf{r}_\perp + \mathbf{R}_{\perp,j},\lambda_k), \tag{2.8c}$$

where $\Delta\Psi(\mathbf{r}_\perp, \lambda_k)$ is again given by Eq. (2.7). Note that Eq. (2.8) are designed for the simple situation mentioned above, and should be implemented sequentially for all the lateral positions as one complete iteration. In Section 2.3, numerical experiments are performed to test our algorithm.

2.2.3. DEFINITION OF ERROR FUNCTIONS

To monitor our numerical experiment, we define an error function given by:

$$E_F(n) = \frac{\sum_j \sum_{\mathbf{r}'_\perp} \left| \sqrt{I_j^{\mathrm{m}}(\mathbf{r}'_\perp)} - \sqrt{I_{j,n}(\mathbf{r}'_\perp)} \right|^2}{\sum_j \sum_{\mathbf{r}'_\perp} \left| I_j^{\mathrm{m}}(\mathbf{r}'_\perp) \right|}, \tag{2.9}$$

as before, the subscript j is an index that labels the object's lateral position and the subscript n is the current iteration number. We refer to E_F as the normalized error in Fourier space (NEF), which is commonly used in practical experiments due to the availability of I^{m} and I. Due to the close relation between the NEF and the cost function as defined in Eq. (2.3), it is more suitable to assess the convergence of our algorithm by monitoring the evolution of the NEF than the NER. To estimate the quality of the results, we also define a normalized error E_R in real space (NER), defined by:

$$E_R(n) = \frac{\sum_{\mathbf{r}_\perp} \left| O(\mathbf{r}_\perp) - g O_n(\mathbf{r}_\perp) \right|^2}{\sum_{\mathbf{r}_\perp} |O(\mathbf{r}_\perp)|^2}, \tag{2.10}$$

where $O(\mathbf{r}_\perp) = A(\mathbf{r}_\perp) \cdot \exp\left[\mathrm{i}\phi(\mathbf{r}_\perp)\right]$ is the actual object function which is defined as the exit wave at wavelength λ_1. $O_n(\mathbf{r}_\perp)$ and g are given by:

$$\begin{cases} O_n(\mathbf{r}_\perp) = A_n(\mathbf{r}_\perp) \cdot \exp\left[\mathrm{i}\phi_n(\mathbf{r}_\perp)\right], \\ g = \dfrac{\sum_{\mathbf{r}_\perp} O(\mathbf{r}_\perp) O_n^*(\mathbf{r}_\perp)}{\sum_{\mathbf{r}_\perp} |O_n(\mathbf{r}_\perp)|^2}. \end{cases} \tag{2.11}$$

Hence $O_n(\mathbf{r}_\perp)$ is the reconstructed object, i.e. the reconstructed exit wave for wavelength λ_1, after n iterations. The parameter γ is a multiplication constant that makes the NER invariant with respect to phase offset [12]. The NER can be regarded as a direct measure of the quality of the reconstructions. This suggests that in numerical experiments, the NER is more suitable to monitor the error, however in real experiments only NEF can be used.

2.3. SIMULATION AND DISCUSSION

2.3.1. PLANE-WAVE ILLUMINATION

To examine our **Algorithm 1**, the results of numerical experiments are reported in this section. A detailed introduction and demonstration of our simulation is presented in the

Table 2.1: The maximum measurable spatial frequency for $30nm$, $40nm$ and $50nm$ wavelength, with a detector which contains a 320×320 array of $15\mu m$ pixels. The propagation distance is assumed to be $1cm$. The diameter of the circular aperture which lies inside the probe function is $10\mu m$. Hence the Fresnel number is $1/3$ for $30nm$ wavelength.

Wavelength (nm)	30	40	50
Detector size (mm)	4.8	4.8	4.8
Maximum spatial frequency ($cy/\mu m$)	8.0	6.0	4.8

first part of this section, then in the following subsection we analysis the performance of the algorithm by studying the error functions. In the final part of the section a comparison study between **Algorithm 1** and the PIM method is reported.

2.3.2. PARAMETER SETTINGS OF THE SIMULATION

We first construct a complex-valued object with as amplitude map the 'Mona Lisa' painting and as phase map the 'camera man' picture. The amplitude map contains non-zero values ranging in $[0.1,1]$ to avoid phase uncertainty, and the phase map varies between $[0,\pi]$ to prevent phase wrapping effect. A planar wavefield which contains a certain number of wavelength components, and which was transmitted by a circular aperture, is used as the probe function. For each wavelength component, the exit wavefield is modeled as in Eq. (2.1) and then is propagated to the far field where their intensities are added up. The measured total intensity is the polychromatic ptychographic data set in accordance with Eq. (2.4). Note that for every wavelength λ_k other than the shortest one λ_1, the propagated wavefield is zoomed in with a rate $=\lambda_k/\lambda_1$. The far field diffraction patterns scale with the reciprocal wavelength. Since the discrete mesh in the far field region should correspond to the pixels of the detector, we use the chip z-transform [13, 14] instead of the FFT to enable the desired flexibility of the mesh. The discretised regions of the diffraction patterns are limited to spatial frequencies that are below the maximum spatial limit defined by the Nyquist sampling for the shortest wavelength λ_1. To give an example, we assume in the configuration of Fig. 2.1 that there is a detector with a 320×320 array of $15\mu m$ pixels, at a propagation distance of $z'=1cm$ behind the object. Accordingly, the maximum spatial frequency that can be measured by this detector for the wavelengths $30nm$, $40nm$ and $50nm$ are listed in Table.2.1.

The probe function that we use is a matrix with 320×320 pixels, which is in line with the number of pixels of the detector. The probe has circular support with diameter of 160 pixels, which is equivalent to a diameter size of $10\mu m$. The Fresnel number is $1/3$ for $30nm$ wavelength, and is smaller than $1/3$ for larger wavelengths. Therefore the detector is in the Fraunhofer region. The circular support is used as a priori knowledge in the reconstruction. In addition, the *a priori* knowledge is used that the object is moved over an equidistant 4x4 grid with 80% overlap between adjacent illuminated areas. Suppose the diameter of the circular support is L, and the distance between adjacent illumination positions is denoted by $d\in[0,L]$. The overlap ratio is defined by:

$$\text{overlap ratio} = 1-\frac{d}{L}, \tag{2.12}$$

which is usually be assigned from 60% to 85% to achieve optimal performance of the

reconstruction algorithm [15]. A detailed demonstration regarding how the overlap ratio influences the reconstruction quality can be found in Supplement section 2.5.5. This scanning procedure of the probe gives us an object array with 480×480 pixels in total. For the pixels of the discretized object region which are not illuminated, the value of $A(\mathbf{r}_\perp)$ are set to be zero during the iteration. The width of this region of zeros is roughly 80 pixels. In practice, the object's moving grid could be obtained from a translation stage's reading, which can be refined using some proposed algorithms [16, 17]. On the other hand, the *a priori* knowledge about the probe's support size can be estimated by Fourier transforming the diffraction intensity, and then can be registered with real-world spatial scale according to the propagation distance and camera's parameters.

It is worth noting that, by taking more wavelengths into account, the computational cost of the algorithm is generally more expensive than the case of monochromatic illumination. This can be understood by inspecting the framework of **Algorithm 1** and Eq. (2.7). To complete a single iteration in **Algorithm 1**, one needs to perform forward and backward propagation of the wavefield for every wavelengths and for every probe positions, which involve multiple FFTs. If the propagation is calculated for each λ_k sequentially, the required computation time will increase almost linearly with respect to the number of wavelengths. To shorten the calculation duration, one can modify the code based on accelerated gradient-based algorithms (e.g. nonlinear optimization methods [18, 19] and momentum-based methods [20]) or take an advantage of modern computational devices (e.g. GPU-based parallel computing [21–23]). In our numerical experiments, 1000 iterations were applied for each single simulation to ensure the convergence. To make the algorithm converge faster, Nesterov momentum-based algorithm [20] was implemented between 50th and 500th iteration. The momentum is added to the reconstruction formula in the manner as suggested in [24]. Our simulation is running on a NVIDIA GeForce GTX 1060 GPU. For easy integration with the device, our code is written in Python using the *scikit-cuda* package for calculating 2D-FFT and *pycuda* package for performing other operations.

Because in this part of our simulation the probe includes polychromatic plane-waves, we first investigate how the number of wavelengths in the probe's temporal spectrum influence the quality of the reconstruction. The probe's spectrum was generated as follows: (i) when the illumination is a monochromatic plane-wave, the wavelength is 30nm. (ii) for the polychromatic situation, we start with generating two spectral components at 30nm and 50nm. To include more spectral component (when $N > 2$), we add the additional frequencies between 30nm and 50nm, while the distances in frequency between adjacent frequencies are identical. A schematic demonstration regarding how we generate the temporal spectrum can be found at the left of Fig. 2.2. When the measurements are noise free, we let all the wavelengths have the same intensity in the probe spectrum as shown in Fig. 2.2. Whereas for the noisy situation, we built the probe spectrum such that all the wavelengths share the same number of photons. A more detailed description about the noisy case can be found in the next subsection.

2.3.3. ADDING NOISE TO THE MEASUREMENTS

To investigate the influence of noise, we added Poisson noise to every diffraction intensity measurements. Considering that one of the tasks in the numerical experiment is to

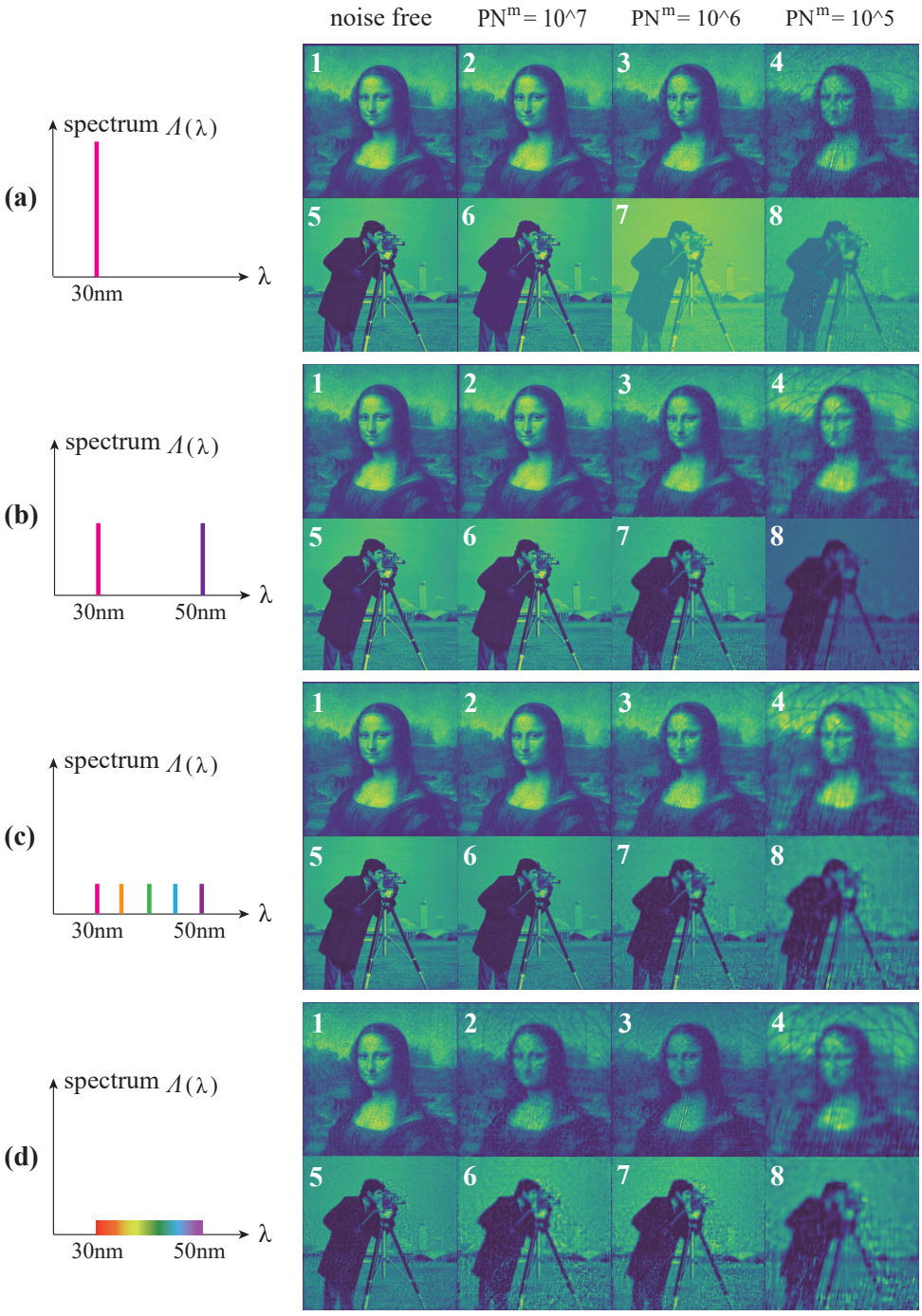

Figure 2.2: Simulation results for validating **Algorithm 1**. The illumination includes polychromatic plane-waves. (a1)-(a8) are the simulation results when the illumination is monochromatic, reconstructed by employing the PIE algorithm. (b1)-(b8), (c1)-(c8) and (d1)-(d8) show the reconstructions with implementing **Algorithm 1**, for the case where 2, 5 and 20 spectral components are included in the probe's spectrum, respectively. A schematic demonstration regarding how we generate the temporal spectrum can be found on the left hand column. Note that the distances in frequency between adjacent frequencies are identical, and all the wavelengths share the same number of photons.

investigate how the algorithm performs with different number of wavelengths when the noise is kept at a certain amount, it is important to build a criterion of the noise level which is insensitive to the number of wavelength in the probe's spectrum. In the simulation we pay attention to the total photon number counting over the measured diffraction intensity which is denoted by PN^{m}:

$$\mathrm{PN}^{\mathrm{m}} = \sum_{j,k} \frac{\lambda_k}{hc} \sum_{\mathbf{r}'_\perp} \mathbf{1}_D(\mathbf{r}'_\perp) \cdot \left| \mathscr{F}_\perp \left[\Psi_j(\mathbf{r}_\perp, \lambda_k) \right] \left(\frac{\mathbf{r}'_\perp}{\lambda_k z'} \right) \right|^2 \tag{2.13}$$

where h is the Planck constant. and we use it as a reference to define the Poisson noise level. In accordance with the Poisson noise model, the signal-to-noise ratio (SNR) equals to $\sqrt{\mathrm{PN}^{\mathrm{m}}}$. Hence when the PN^{m} remains at the same value, each measurement will also stays at the same noise level for different number of wavelengths. Here it is notable that a single photon includes hc/λ_k of energy for each wavelength λ_k, therefore each wavelength has different intensities with the same photon number. However, though a simple calculation we can find that the total energy of the diffraction intensity is the same for a fixed PN^{m}. The calculation is presented in Supplement section 2.5.2.

2.3.4. RECONSTRUCTION RESULTS

In Fig. 2.2, we present our simulation results for the cases where 1, 2, 5 and 20 spectral components are included in the probe's spectrum, respectively. The results in Fig. 2.2(a1)-2.2(a8) are obtained with the PIE algorithm, while Fig. 2.2(b1)-2.2(b8), 2.2(c1)-2.2(c8) and 2.2(d1)-2.2(d8) are the reconstructions by implementing our proposed **Algorithm 1**. We use a constant amplitude map $A_0(\mathbf{r}_\perp) = 0.5$ and a constant phase map $\phi_0(\mathbf{r}_\perp) = 1$ as an initial guess for the object function, which is proven to be sufficient for our proposed algorithm to successfully alleviate the ambiguities described in Section 1.3.3. Reconstruction results with different PN^{m} value are also depicted in Fig. 2.2. By roughly examining these pictures, one can conclude that the reconstructions are visually acceptable when the PN^{m} equals 10^7 and 10^6, whereas the reconstructions are corrupted by noise when the PN^{m} is decreased to 10^5. By carefully comparing the phase reconstructions (the 'camera man' pictures), it is also noticeable that stronger defects occur when the probe contains 20 spectral components. For a better understanding on this defect, in the following subsection a more quantitative analysis is given by inspecting the evolution of the error functions.

2.3.5. EVOLUTION OF THE ERROR FUNCTION

To better understand the simulation results, it is necessary to examine the evolution of the error functions that are described in Subsection 2.3. A series of NERs and NEFs, which were computed from the simulation results described in Subsection 2.3.2 and Fig. 2.2, are drawn in Fig. 2.3(a) and 2.3(b) respectively. All the NERs and the NEFs were computed for the case that the probe contains 1-20 components in its spectrum, and the PN^{m} varies from 10^5 to 10^7. If we only pay attention to a single PN^{m} value, it is seen that although the NEFs stay at almost the same value, the NER increases with the number of wavelengths almost linearly, which agrees with what we already observed in Fig .2.2(c1)-2.2(c8).

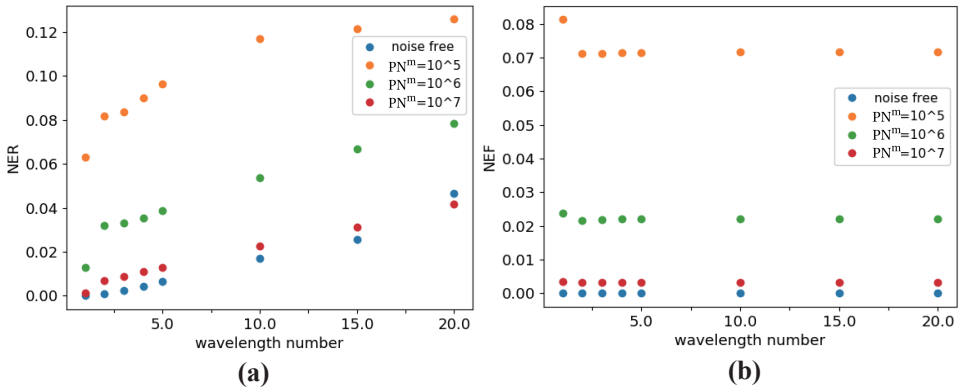

Figure 2.3: The final values of the NER and the NEF after our simulation converged. In (a) we show the calculated NERs with 1-20 spectral components in the probe's spectrum, and with the PN^m varies from 10^5 to 10^7. The NEFs for the same settings are depicted in (b). Note that the signal-to-noise ratio is so large that the noise has negligible influence when the PN^m equals 10^7, therefore in this plot the blue dots and red ones are almost overlap.

For seeking the reason behind this phenomenon, additional simulation have been performed. The difference between the new and previously discussed simulations is that we ignore the wavelength dependence in propagating the wavefields (see Eq. (2.4)). Fig .2.4 gives a schematic description of the two different ways of computing the polychromatic diffraction intensity pattern. In line with what has been discussed in Subsection 2.3.2, it is assumed that the shortest wavelength's (λ_1) contribution to the diffraction intensity always fulfills the Nyquist sampling criterion. Hence in Fig. 2.4 we use a red frame to represent the Nyquist frequency with respect to λ_1, which is equivalent to the boundary of an imaginary detector $\mathbf{1}_D(\mathbf{r}'_\perp)$. Fig. 2.4(a) illustrates the calculation process in Eq. (2.4), which includes the wavelength-dependency of the wavefield propagation. In the new numerical experiment the wavefield propagation is without the wavelength-dependency, as shown in Fig. 2.4(b).

In correspondence with the wavefield propagation model shown in Fig. 2.4(b), the simulated NERs and NEFs, gathered after our algorithm converged, are illustrated in Fig. 2.5(a) and 2.5(b) respectively. By comparing Fig. 2.3 and Fig. 2.5, it is obvious that the wavelength-dependent error in the reconstruction disappears once the wavelength-dependency in the propagation model is removed. Hence, one can conclude that the way we measure and compute the polychomatic diffraction wavefield is the cause for the increase in NER in Fig. 2.5(a). This is because when the binary function $\mathbf{1}_D(\mathbf{r}'_\perp)$ in Eq. (2.4) corresponds to a window size which fits the Nyquist sampling criterion for the short wavelength λ_1, the same maximum spatial frequency from larger wavelengths are not completely measurable (see in Table.2.1). As illustrated in Fig. 2.5(a), for wavelengths larger than λ_1, part of the diffraction wavefield (outside the red frame) is cut off by the boundary of the detector. Hence the recorded data is incomplete which leads to the increase of the NER. It follows that the theoretical resolution of the reconstruction cannot

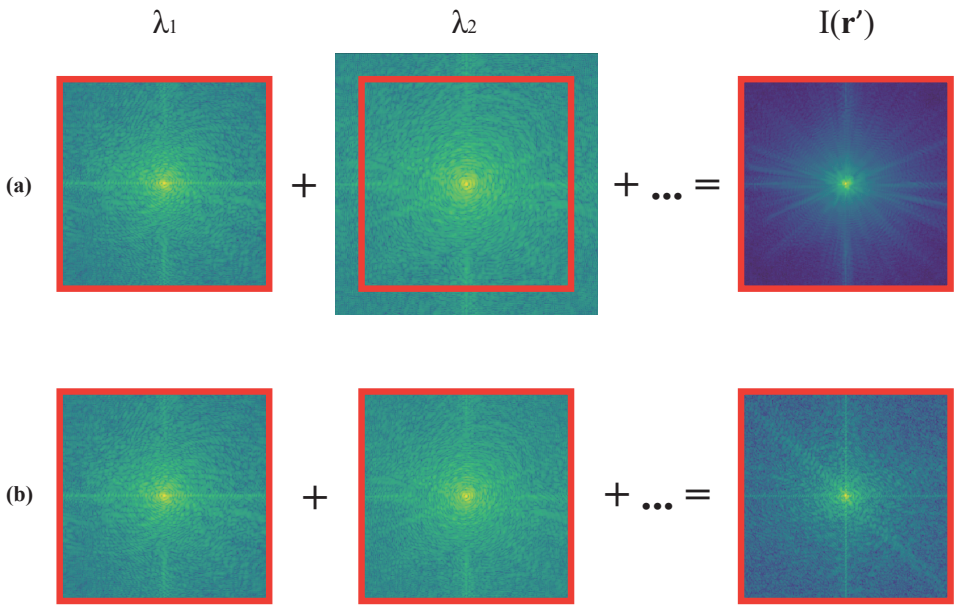

Figure 2.4: Graphical description of the two different ways of computing the polychromatic diffraction intensity pattern in our simulation. (a) illustrates the calculation process in Eq. (2.4), which includes the wavelength-dependency of the wavefield propagation. (b) describes the wavefield propagation model which is without the wavelength-dependency. The red frame represents the boundary of an imaginary detector $\mathbf{1}_D(\mathbf{r}'_\perp)$.

be estimated only by the size of the detector and the sampling rule of the shortest wavelength. This is important if one performs polychromatic ptychography without using wavelength-scanning or spectroscopic detection to separately detect the diffracted intensities of the individual wavelengths. In other words, although in principle performing ptychography with a polychromatic light source can gives higher SNR and shorter acquisition time, the reconstruction quality is not necessarily better than the monochromatic ptychography result. A similar effect was also reported in [10].

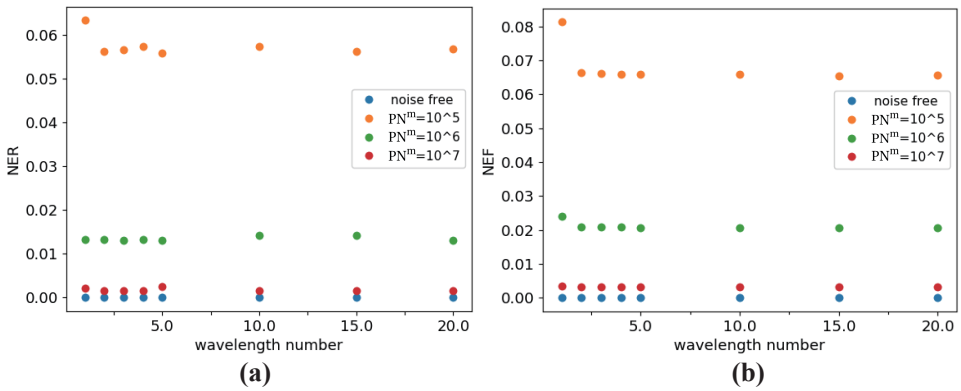

Figure 2.5: The numerical experiment results corresponding to the situation where the wavefield propagation is wavelength-independent, as in Fig. 2.4(b). In these plots same choices have been made for the number of wavelengths and noise as in Fig. 2.3.

2.3.6. COMPARISON WITH PIM METHOD

In order to study the different performance between our proposed algorithm and the PIM method, we present some numerical simulations in this subsection. All parameter values are chosen the same as in Subsection 2.3.2, i.e. the simulation for the case of plane wave illumination. In Fig. 2.6 we illustrate the final reconstructed NERs and NEFs for simulated noise-free measurements. The NERs of our proposed algorithm were calculated as described in Section 2.2.3. While the NERs of the PIM method were calculated also from Eq. (2.10), in which the reconstructed object $O(\mathbf{r}_\perp)_n$ is given by the exit wave in PIM corresponding to λ_1.

From Fig. 2.6 it can be concluded that although both **Algorithm 1** and the PIM method converged to a very low value of NEF, the reconstructed object functions have different qualities. When the probe function contains polychromatic plane waves with more than roughly 10 wavelengths, the PIM method suffers more from the limited detector size issue described in Fig. 2.4. As shown in Fig. 2.7, when the probe has 20 spectral components, all the reconstructed modes in the PIM method are disrupted. Hence in this case it is more suitable to employ **Algorithm 1**.

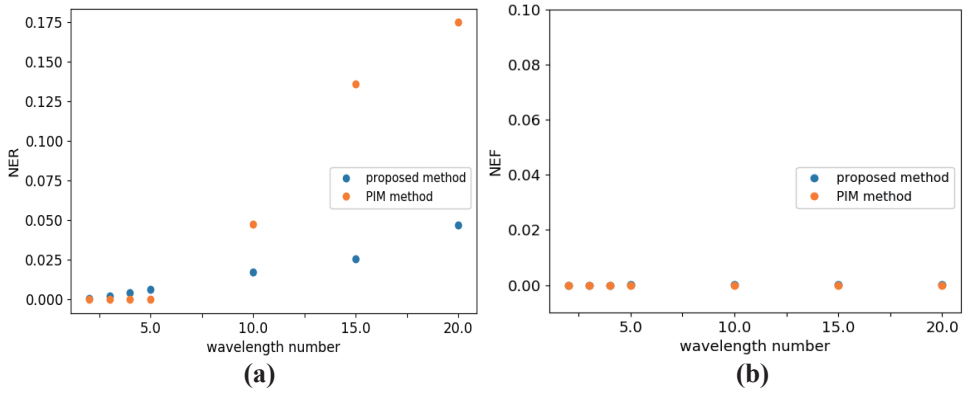

Figure 2.6: A comparison simulation result between **Algorithm 1** and the PIM method, with noise-free measurements. The NEF values in the right figure are identical for the two methods.

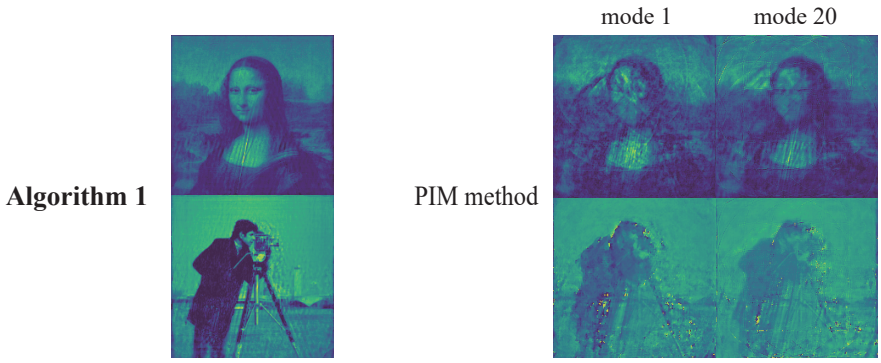

Figure 2.7: The reconstructed object functions for the situation where the probe has 20 spectral components. Noise-free measurements are used in this simulation and the propagation model follows the scheme in Eq. (2.4).

2.3.7. WITH PROBE RECONSTRUCTION

We also compare the simulation outcomes for different situations when the probe function is unknown. As has been mentioned in Subsection 2.2.2, we consider a relatively simple case where for every wavelength the complex probe function is the same. To inspect the performance of our proposed iterative scheme of Eq. (2.8), we use a complex initial probe function and show the noise-free reconstruction result in Fig. 2.8(a1)-2.8(a6). The probe's temporal spectrum is assumed to contain 3 components with identically long wavelength intervals between them, as illustrated at the left of Fig. 2.8. It can be confirmed that the update formula given in Eq. (2.8) is able to retrieve the object and the probe function, even when the probe has a very complicated profile. However, due to the fact that in this simulation we set the relative position between the probe and the object $\mathbf{R}_{\perp,j}$ to be a regular position grid in two orthogonal directions, raster grid pathology appears in both the reconstruction of the object and the probe. This kind of defect is more visually obvious when the initial probe function is a polychromatic plane-wave (the reconstruction result for this case is in Fig. 2.8(b1)-2.8(b4)). To eliminate the raster grid defect, ideas for optimizing the scanning trajectory were proposed in [25–27], which however are beyond the scope of this chapter.

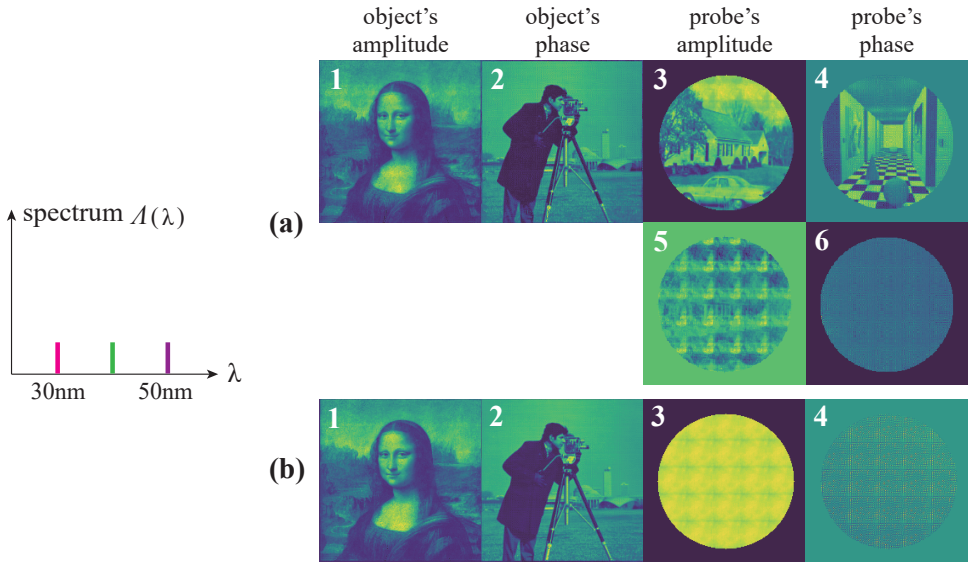

Figure 2.8: Simulation results with probe reconstruction following the scheme in Eq. (2.8). On the left the probe's temporal spectrum is shown. In (a1)-(a4) are the reconstructed probe function when the initial probe has a complex profile. The difference between the original complex profile probe and the reconstructed probe are illustrated in (a5)-(a6). (b1)-(b4) are the results with a polychromatic plane-wave initial probe function.

2.4. CONCLUSION AND OUTLOOK

In this chapter we have introduced a polychromatic ptychographic algorithm, which can be regarded as an alternative to the PIM approach. It is based on the idea that the mutually incoherent modes in the multiple wavelength scheme can be related by representing the object by real transmission and thickness functions. The algorithm is derived from the steepest descent method and is numerically validated. We first discussed polychromatic plane wave illumination which is assumed to be known and afterwards included the case of the reconstruction of an unknown probe. The results show that **Algorithm 1** performs nicely for a known probe, and that a reasonable level of noise can be handled by the algorithm. For a sufficiently thin object, the ptychography reconstruction given by the polychromatic approach has a higher NER than the case of monochromatic illumination. This is due to the fact that for longer wavelengths higher spatial frequencies are not capture by the detector because stronger diffraction effects. Hence, although in principle performing ptychography with a polychromatic light source can give higher SNR and shorter acquisition time, the reconstruction quality is not necessarily better than the monochromatic ptychography results. Compared to the PIM method, **Algorithm 1** is less sensitive to the missing data issue. However, defects are observed when a very complex unknown probe function is introduced and must be reconstructed as well. With varying parameter settings (i.e. noise and the number of spectral components in the probe), different behaviors are observed and discussed in this chapter. As next steps for improvement, pathologies cause by the raster scanning grid of the probe function should be eliminated and the performance of the algorithm should be validated using experimental data.

2.5. SUPPLEMENT

2.5.1. POLYCHROMATIC PTYCHOGRAPHY ALGORITHM

In this section we propose a ptychography algorithm for multiple-wavelength illumination with mutually incoherent wavelengths and using measured total diffracted intensities (i.e. the intensities are not spectrally separated). As mentioned in the main text, for an non-dispersive thin object we can express the exit wave for wavelength λ_k as:

$$\Psi_j(\mathbf{r}_\perp, \lambda_k) = P(\mathbf{r}_\perp - \mathbf{R}_{\perp,j}) \cdot A(\mathbf{r}_\perp) \cdot \exp\left[\mathrm{i}\frac{\lambda_1}{\lambda_k}\phi(\mathbf{r}_\perp)\right] \tag{2.14}$$

where $\mathbf{R}_{\perp,j}$ represents the jth relative position between the probe and the object. $A(\mathbf{r}_\perp)$ is the object's local transmission function and $\phi(\mathbf{r}_\perp)$ stands for 2π times the ratio of the object thickness function and wavelength λ_1. Note that both $A(\mathbf{r}_\perp)$ and $\phi(\mathbf{r}_\perp)$ are real valued and that $A(\mathbf{r}_\perp)$ is positive. As in Supplement section 2.5.1, the steepest descent method can provide to us with updating formulas for $A(\mathbf{r}_\perp)$, $\phi(\mathbf{r}_\perp)$ and $P(\mathbf{r}_\perp)$. Due to the fact that the exit wave in not monochromatic, we need to re-define the estimated

diffraction intensity $I(\mathbf{r}'_\perp)$ as an incoherent sum of every monochromatic component:

$$\begin{aligned} I_j(\mathbf{r}'_\perp) &= \mathbf{1}_D(\mathbf{r}'_\perp)\cdot\sum_{\lambda_k}\left|\iint \Psi_j(\mathbf{r}_\perp,\lambda_k)\exp\left(-\mathrm{i}\frac{2\pi}{\lambda_k z}\mathbf{r}_\perp\cdot\mathbf{r}'_\perp\right)d\mathbf{r}_\perp\right|^2 \\ &= \mathbf{1}_D(\mathbf{r}'_\perp)\cdot\sum_{\lambda_k}\left|\mathscr{F}_\perp\left[\Psi_j(\mathbf{r}_\perp,\lambda_k)\right]\left(\frac{\mathbf{r}'_\perp}{\lambda_k z}\right)\right|^2, \end{aligned} \tag{2.15}$$

where $\mathbf{1}_D(\mathbf{r}'_\perp)$ is a binary window function which represents the area of the detector.

To start with, we compute the functional derivative of $\mathscr{E}_j$, which was defined in Eq. (2.3), with respect to $A(\mathbf{r}_\perp)$, $\phi(\mathbf{r}_\perp)$ and $P(\mathbf{r}_\perp)$ at every point $\mathbf{r}_\perp$. To do that, we calculate the functional derivative of $\mathscr{E}_j$ with respect to A, ϕ and P at every point $\mathbf{r}_\perp$. The local perturbation of the value of O on a discretized grid $\mathbf{r}_\perp$ is defined by:

$$\delta A(\mathbf{r}_\perp) = \sum_{n_{\mathbf{r},y}}\sum_{n_{\mathbf{r},x}}\exp\left[\mathrm{i}\frac{\lambda_1}{\lambda_k}\phi(\mathbf{r}_\perp)\right]\delta(\mathbf{r}_\perp-\mathbf{n}_{\mathbf{r},\perp}\Delta\mathbf{r}_\perp), \tag{2.16a}$$

$$\delta\phi(\mathbf{r}_\perp) = \sum_{n_{\mathbf{r},y}}\sum_{n_{\mathbf{r},x}}\mathrm{i}\frac{\lambda_1}{\lambda_k}A(\mathbf{r}_\perp)\exp\left[\mathrm{i}\frac{\lambda_1}{\lambda_k}\phi(\mathbf{r}_\perp)\right]\delta(\mathbf{r}_\perp-\mathbf{n}_{\mathbf{r},\perp}\Delta\mathbf{r}_\perp), \tag{2.16b}$$

$$\delta P(\mathbf{r}_\perp) = \sum_{n_{\mathbf{r},y}}\sum_{n_{\mathbf{r},x}}P(\mathbf{r}_\perp)\delta(\mathbf{r}_\perp-\mathbf{n}_{\mathbf{r},\perp}\Delta\mathbf{r}_\perp), \tag{2.16c}$$

where $\mathbf{n}_{\mathbf{r},\perp}$ is the index of the 2D discretized cells on the meshgrid as defined in Eq. (1.41). $\Delta\mathbf{r}_\perp$ the size of every cells of the 2D meshgrid along the x and y direction, as given in Eq. (1.42).

$$\delta\mathscr{E}_j(P,A,\phi)(\delta A) = 2\sum_{\lambda_k}\iint\Re\left\{\Delta\Psi_j(\mathbf{r}_\perp,\lambda_k)\cdot P_j^*(\mathbf{r}_\perp)\cdot\exp\left[-\mathrm{i}\frac{\lambda_1}{\lambda_k}\phi(\mathbf{r}_\perp)\right]\right\}\cdot\delta A(\mathbf{r}_\perp)d\mathbf{r}_\perp, \tag{2.17a}$$

$$\begin{aligned} &\delta\mathscr{E}_j(P,A,\phi)(\delta\phi) \\ &= 2\sum_{\lambda_k}\iint\Re\left\{-\mathrm{i}\frac{\lambda_1}{\lambda_k}\cdot\Delta\Psi_j(\mathbf{r}_\perp,\lambda_k)\cdot P_j^*(\mathbf{r}_\perp)\cdot A(\mathbf{r}_\perp)\cdot\exp\left[-\mathrm{i}\frac{\lambda_1}{\lambda_k}\phi(\mathbf{r}_\perp)\right]\right\}\cdot\delta\phi(\mathbf{r}_\perp)d\mathbf{r}_\perp, \end{aligned} \tag{2.17b}$$

$$\begin{aligned} &\delta\mathscr{E}_j(P,A,\phi)(\delta P) \\ &= \sum_{\lambda_k}\Re\left\{\iint\Delta\Psi_j(\mathbf{r}_\perp,\lambda_k)\cdot P_j^*(\mathbf{r}_\perp)\cdot A(\mathbf{r}_\perp)\cdot\exp\left[-\mathrm{i}\frac{\lambda_1}{\lambda_k}\phi(\mathbf{r}_\perp)\right]\cdot\delta P^*(\mathbf{r}_\perp)d\mathbf{r}_\perp\right\}, \end{aligned} \tag{2.17c}$$

where we use the fact that both $A(\mathbf{r}_\perp)$, $\phi(\mathbf{r}_\perp)$ are real-valued by definition. Once again the auxiliary function is given by:

$$\Delta\Psi_{j,n}(\mathbf{r}_\perp,\lambda_k) = \mathscr{F}_\perp^{-1}\left\{\mathbf{1}_D(\mathbf{r}'_\perp)\cdot\left(\frac{\sqrt{I_j^{\mathrm{m}}(\mathbf{r}'_\perp)}}{\sqrt{I_{j,n}(\mathbf{r}'_\perp)}}-1\right)\cdot\mathscr{F}_\perp\left[\Psi_{j,n}(\mathbf{r}_\perp,\lambda_k)\right]\left(\frac{\mathbf{r}'_\perp}{\lambda_k z}\right)\right\}(\mathbf{r}_\perp,\lambda_k). \tag{2.18}$$

Similar to the derivation in Eq. (1.88) - (1.101), we arrive at the following formulas to update the estimates for $A(\mathbf{r}_\perp)$, $\phi(\mathbf{r}_\perp)$ and $P(\mathbf{r}_\perp)$ for each position j:

$$A_{n+1}(\mathbf{r}_\perp) = A_n(\mathbf{r}_\perp) + \beta_A \sum_k \Re\left\{\left[P_{j,n}(\mathbf{r}_\perp)\right]^* \cdot \exp\left[-\mathrm{i}\frac{\lambda_1}{\lambda_k}\phi_n(\mathbf{r}_\perp)\right] \cdot \Delta\Psi_n(\mathbf{r}_\perp, \lambda_k)\right\}, \tag{2.19a}$$

$$\phi_{n+1}(\mathbf{r}_\perp) = \phi_n(\mathbf{r}_\perp) + \beta_\phi \sum_k \Re\left\{-\mathrm{i}\frac{\lambda_1}{\lambda_k} \cdot \left[P_{j,n}(\mathbf{r}_\perp)\right]^* \cdot A_n(\mathbf{r}_\perp) \cdot \exp\left[-\mathrm{i}\frac{\lambda_1}{\lambda_k}\phi_n(\mathbf{r}_\perp)\right] \cdot \Delta\Psi_{j,n}(\mathbf{r}_\perp, \lambda_k)\right\}, \tag{2.19b}$$

$$P_{n+1}(\mathbf{r}_\perp) = P_n(\mathbf{r}_\perp) + \beta_P \sum_k A_n(\mathbf{r}_\perp + \mathbf{R}_{\perp,j}) \cdot \exp\left[-\mathrm{i}\frac{\lambda_1}{\lambda_k}\phi_n(\mathbf{r}_\perp + \mathbf{R}_{\perp,j})\right] \cdot \Delta\Psi_{j,n}(\mathbf{r}_\perp + \mathbf{R}_{\perp,j}, \lambda_k), \tag{2.19c}$$

where β_A, β_ϕ and β_P are constant step-sizes and n is the iteration number.

2.5.2. THE RELATIONSHIP BETWEEN THE PHOTON NUMBER AND THE TOTAL ENERGY

In this section we aim to prove that the total energy of the measurements is a constant for a fixed total photon number. In line with Section 2.3.1, we denote N as the number of wavelength and PN^m as the total photon number in the diffracted wavefield. Because every wavelengths are presumed to have the same number of photons, the total energy e_N of the measurement is given by:

$$e_N = \frac{\mathrm{PN}^\mathrm{m}}{N} \sum_{k=1}^{N} h\nu_k, \tag{2.20}$$

where h is the Planck constant and ν_k is the kth frequency. Considering that all the frequencies lie in the range $[\nu_1, \nu_N]$, and have equal distance in frequency between adjacent ones, Eq. (2.20) can be rewritten as:

$$e_N = \frac{\mathrm{PN}^\mathrm{m}}{N} h \left[\nu_1 + \nu_N + \sum_{m=1}^{N-2} \frac{m\nu_1 + (N-m-1)\nu_N}{N-1}\right], \tag{2.21}$$

where m is an auxiliary integer. The third term on the right side of Eq. (2.21) stands for the total energy from ν_2 to ν_{N-1}. By computing the sum in Eq. (2.21), the total energy e_N can be expressed as:

$$e_N = \frac{\mathrm{PN}^\mathrm{m}}{2} h(\nu_1 + \nu_N). \tag{2.22}$$

Hence for a fixed PN^m, ν_1 and ν_N, the total energy e_N of the polychromatic diffracted wavefield is a constant.

2.5.3. ADDITIONAL SIMULATIONS ABOUT THE EFFECT OF INCOMPLETE MEASUREMENTS

In Subsection 2.3.3, we demonstrated that the quality of the reconstruction could degrades in the polychromatic ptychography scheme because a detector of limited size

cannot capture strongly diffracted far field intensities at longer wavelengths. To demonstrate this, we described two simulations Subsection 2.3.3, namely: (1) with an incomplete ptychographic data-set; (2) with a complete measured data-set, which was obtained by ignoring the wavelength-dependency in the wavefield propagation model, as illustrated in Fig. 2.4. The simulation results are shown in Fig .2.5.

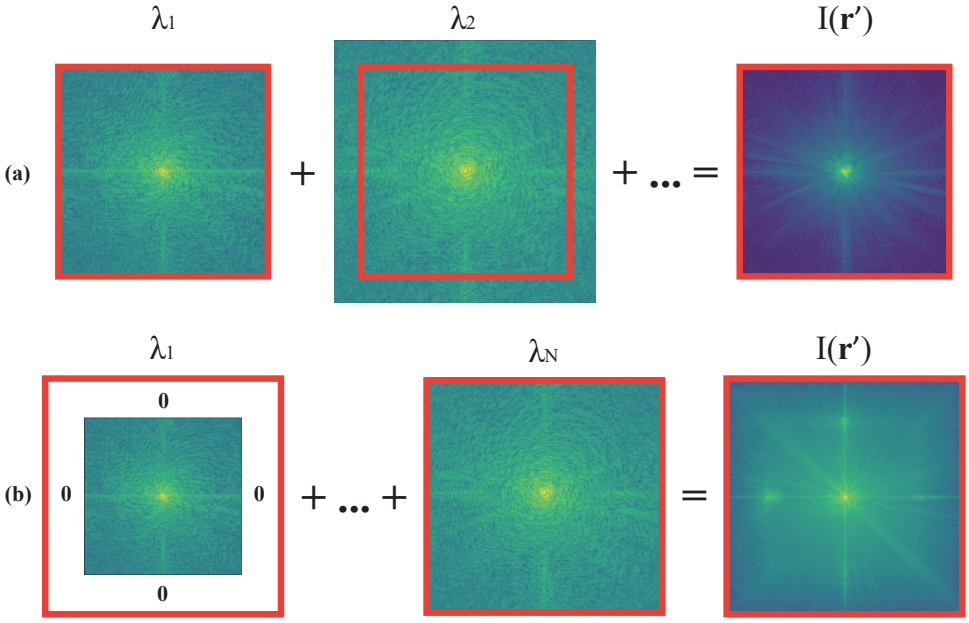

Figure 2.9: Graphical description of the two different ways of computing the polychromatic diffraction intensity pattern. The red frame represents the boundary of an imaginary detector $\mathbf{1}_D(\mathbf{r}'_\perp)$. (a) illustrates the situation where the detector can records incomplete data. (b) describes the situation where the detector is able to measure the maximum spatial frequency component for the largest wavelength λ_N, hence also for the wavelengths shorter than λ_N each monochromatic diffraction intensities are zero-padded in accordance with Eq. (2.4).

In this section, an alternative simulation is provided to further argue the cause of the inaccuracies of the reconstructions. As illustrated in Fig. 2.9(b), instead of ignoring the wavelength-dependency in the wavefield propagation model, we expand the boundary of the detector such that the maximum spatial frequency for the largest wavelength λ_N can be collected. We emphasize that in this simulation all monochromatic diffracted wavefields have the same maximum spatial frequency, which equals to the largest wavelength λ_N. This is because the discretized object has the same pixel size and illuminated area for every wavelength. For the wavelengths shorter than λ_N, the relevant parts of the diffraction patterns of all wavelengths fall inside the area of the detector, and the pixel size is assumed to be sufficiently small that for the smallest wavelength (and hence for all wavelengths), the intensity patterns are sufficiently well sampled. As a comparison, we again inspect the reconstruction with the incomplete measurement. The reconstructed error functions for these two numerical experiments are plotted in Fig. 2.10.

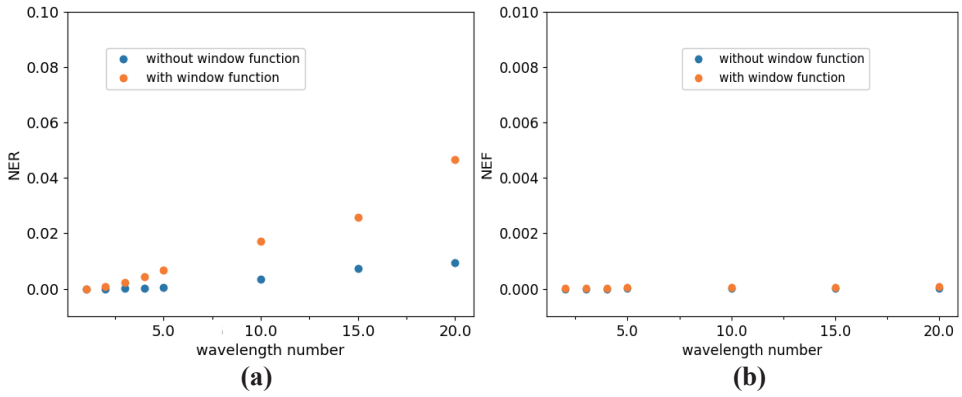

Figure 2.10: A comparison between simulation results of the two sampling situations shown in Fig. 2.9(a) and 2.9(b), with noise-free measurements. The orange dots are related to the propagation model which is illustrated in Fig. 2.9(a), while the blue dots corresponds to the sampling scheme which is shown in Fig. 2.9(b).

Because limited size of the detector only influences the quality of reconstruction for the propagation model as shown in Fig. 2.9(a), we call the model of Fig. 2.9(a) model as the case 'with window function' and similarly we call the model in Fig. 2.9(b) as the case 'without window function', which explains the legend in Fig. 2.10. From Fig. 2.10(b) we see that all the NEFs have reached zero-value, which indicates that the algorithm has converged to the solutions with the same NEF for all the situations. However in Fig. 2.10(a) the NERs of the solutions obtained with window function are higher than without the window function. Therefore one can conclude that the limited size of the detector is the cause of the degradation of the results.

2.5.4. EVOLUTION OF ERROR FUNCTIONS

In this section we give an example of the evolution of the error functions, which aims to show the convergence of the algorithm. Each curve in Fig. 2.11(a) and 2.11(b) is related to one situation in Fig. 2.2. Although we have not decided a terminate criterion in our numerical experiment, it is clear that employing the algorithm for 1000 iterations is sufficient for reaching the minima in our simulation.

2.5.5. INFLUENCE OF THE OVERLAP RATIO

Considering ptychography is a scanning diffraction imaging technique, it is reasonable that the overlap ratio defined in Eq. (4.2.5) plays an important role in the quality of the reconstructed image. In [15] the authors studied how the overlap ratio influences the performance of PIE through simulation and experiment for the first time. The result indicates that, with monochromatic and fully spatial coherent illumination, one can get hold of satisfactory reconstructions by employing 60%-85% of overlap ratio. It was also mentioned in the literature that 30% of overlap could be sufficient if fast overview scans are demanded. On the other hand, a theoretical explanation regarding how overlapped ptychographic scans facilitate the convergence of the algorithm was proposed in [28]. However, to the best of our knowledge, no optimal overlap ratio from theoretical point

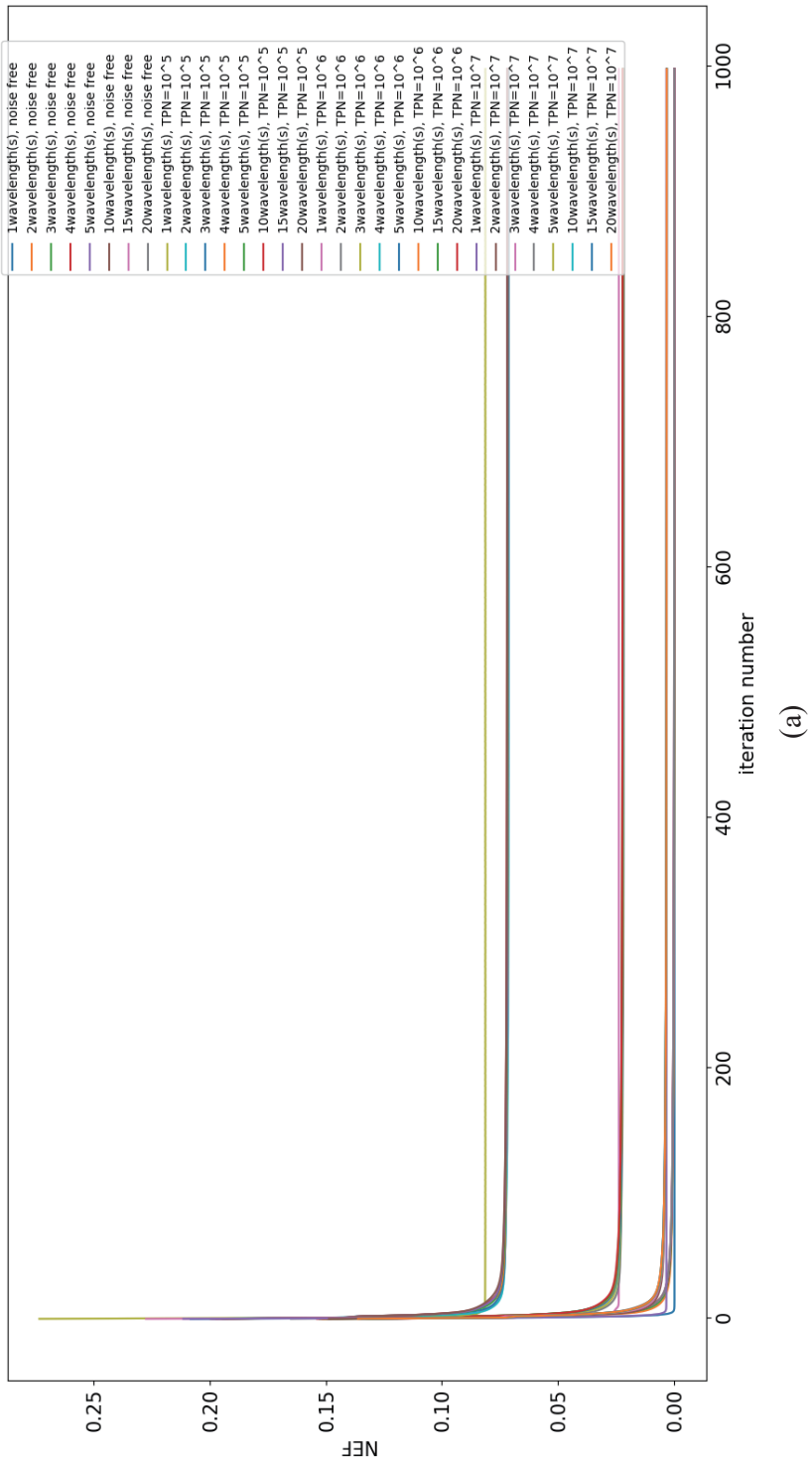
1wavelength(s), noise free
2wavelength(s), noise free
3wavelength(s), noise free
4wavelength(s), noise free
5wavelength(s), noise free
10wavelength(s), noise free
15wavelength(s), noise free
20wavelength(s), noise free
1wavelength(s), TPN=10^5
2wavelength(s), TPN=10^5
3wavelength(s), TPN=10^5
4wavelength(s), TPN=10^5
5wavelength(s), TPN=10^5
10wavelength(s), TPN=10^5
15wavelength(s), TPN=10^5
20wavelength(s), TPN=10^5
1wavelength(s), TPN=10^6
2wavelength(s), TPN=10^6
3wavelength(s), TPN=10^6
4wavelength(s), TPN=10^6
5wavelength(s), TPN=10^6
10wavelength(s), TPN=10^6
15wavelength(s), TPN=10^6
20wavelength(s), TPN=10^6
1wavelength(s), TPN=10^7
2wavelength(s), TPN=10^7
3wavelength(s), TPN=10^7
4wavelength(s), TPN=10^7
5wavelength(s), TPN=10^7
10wavelength(s), TPN=10^7
15wavelength(s), TPN=10^7
20wavelength(s), TPN=10^7
NEF
0.25
0.20
0.15
0.10
0.05
0.00
0
200
400
600
800
1000
iteration number

(a)

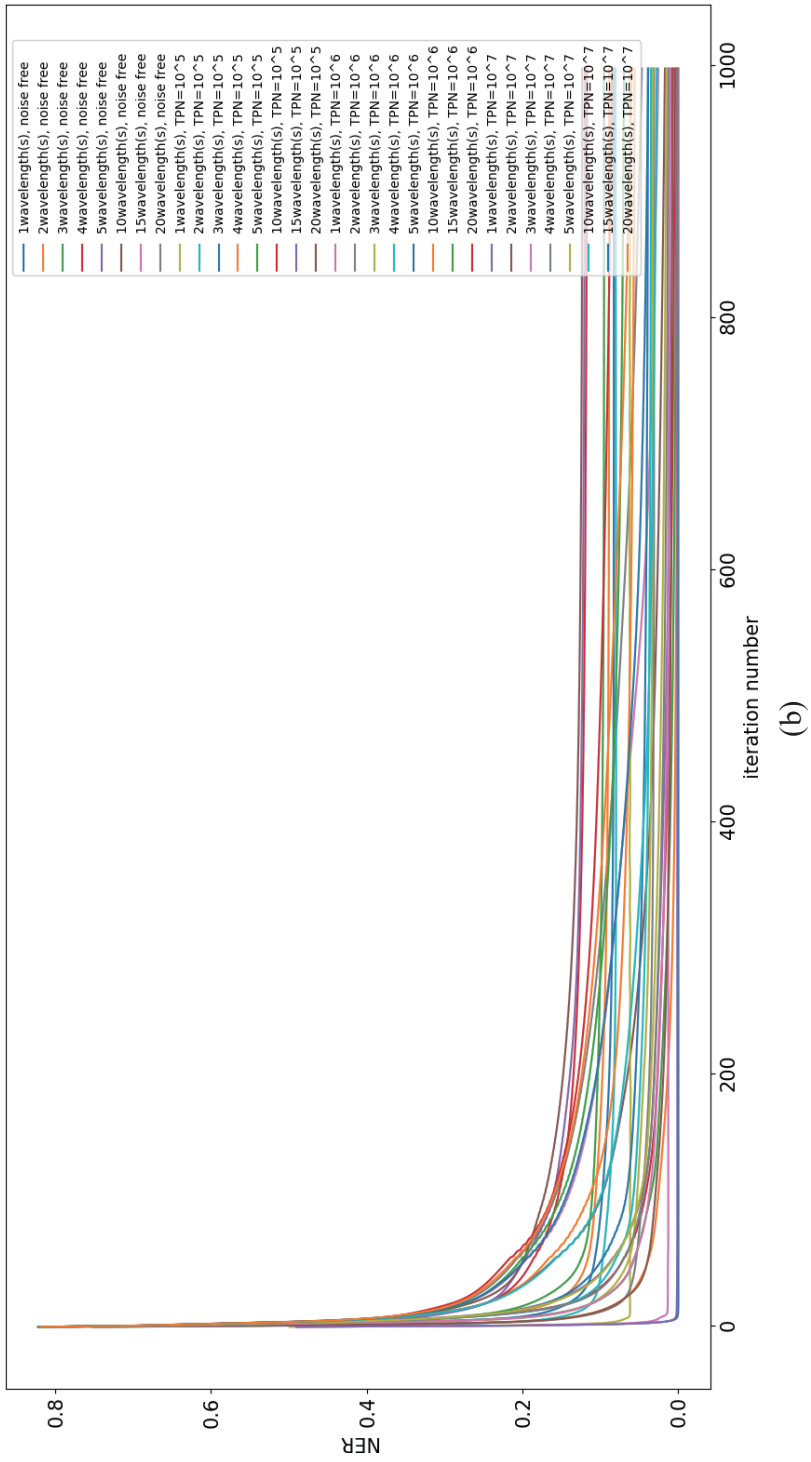

Figure 2.11: The evolution of NEF and NER in our simulation described in Subsection 3.1.1. Each curve in (a) and (b) is related to one situation in Fig. 2.3.

of view has been proposed yet.

In this section we conduct a simulation to demonstrate how the overlap ratio influences the performance of our proposed polychromatic ptychography method. In this numerical experiment, we presume the diffraction intensity measurements are noise free. The rest of the parameter settings for the simulation are duplicated from the Subsection 2.3.2. To observe how the overlap ratio affects the quality of the reconstruction, we adjust the overlap ratio from 0% to 100% with an interval of 10%. Once again in each simulation 1000 iterations were applied to ensure convergence. As an example of the reconstruction results, in Fig. 2.12(a) we show the reconstructed object when the probe only contains 5 wavelengths, and when the overlap ratio equals 0%, 80% and 99%, respectively. The NERs for a series of wavelengths overlap ratios can be found in Fig. 2.12(b). From Fig. 2.12(b), it can be concluded that the overlap ratio should be selected from 60% to 90% for achieving optimal performance of the algorithm, which is in good agreement with the monochromatic situation given in [15]. In line with this conclusion, we choose to employ 80% overlap ratio for the numerical studies in the main context.

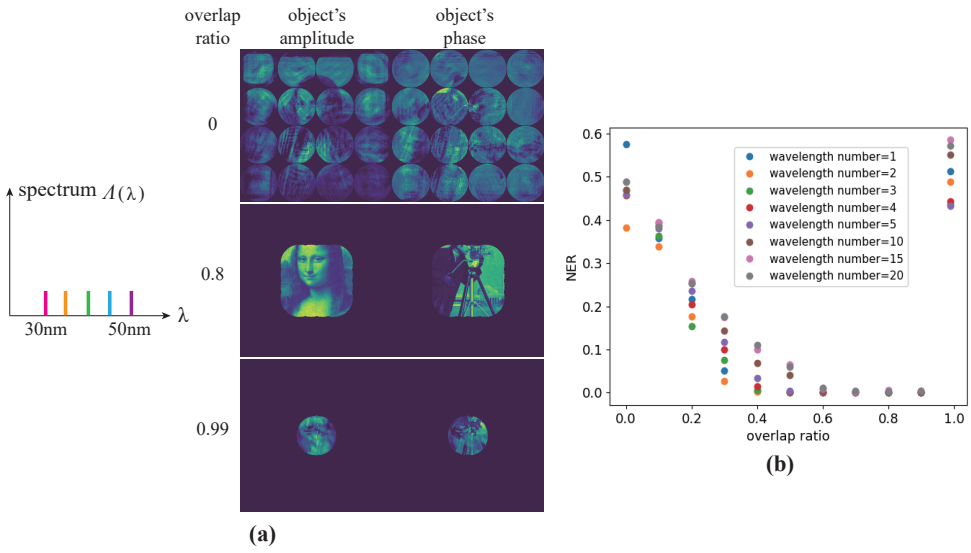

Figure 2.12: Simulation results about how the overlap ratio affects the performance of polychromatic ptychography. In this plot the diffraction intensity measurements are noise free. (a) shows the reconstructed object when the probe only contains 5 wavelengths, and when the overlap ratio equals 0%, 80% and 99%, respectively. In (b) we demonstrate the NERs for a series of wavelengths and for overlap ratios ranging from 0% to 99%.

REFERENCES

[1] X. Wei and P. Urbach, *Ptychography with multiple wavelength illumination,* Optics Express **27**, 36767 (2019).

[2] J. Spence, U. Weierstall, and M. Howells, *Coherence and sampling requirements for diffractive imaging,* Ultramicroscopy **101**, 149 (2004).

[3] K. A. Nugent, *Coherent methods in the x-ray sciences,* Advances in Physics **59**, 1 (2010).

[4] L. W. Whitehead, G. J. Williams, H. M. Quiney, D. J. Vine, R. A. Dilanian, S. Flewett, K. A. Nugent, A. G. Peele, E. Balaur, and I. McNulty, *Diffractive imaging using partially coherent x rays,* Phys. Rev. Lett. **103**, 243902 (2009).

[5] J. Clark, X. Huang, R. Harder, and I. Robinson, *High-resolution three-dimensional partially coherent diffraction imaging,* Nature Communications **3** (2012), 10.1038/ncomms1994.

[6] B. Chen, R. A. Dilanian, S. Teichmann, B. Abbey, A. G. Peele, G. J. Williams, P. Hannaford, L. Van Dao, H. M. Quiney, and K. A. Nugent, *Multiple wavelength diffractive imaging,* Phys. Rev. A **79**, 023809 (2009).

[7] S. Witte, V. T. Tenner, D. W. Noom, and K. S. Eikema, *Lensless diffractive imaging with ultra-broadband table-top sources: from infrared to extreme-ultraviolet wavelengths,* Light: Science & Applications **3**, e163 (2014).

[8] N. Burdet, X. Shi, D. Parks, J. N. Clark, X. Huang, S. D. Kevan, and I. K. Robinson, *Evaluation of partial coherence correction in x-ray ptychography,* Optics Express **23**, 5452 (2015).

[9] P. Thibault and A. Menzel, *Reconstructing state mixtures from diffraction measurements,* Nature **494**, 68 (2013).

[10] D. J. Batey, D. Claus, and J. M. Rodenburg, *Information multiplexing in ptychography,* Ultramicroscopy **138**, 13 (2014).

[11] J. Goodman, *Introduction to Fourier Optics*, McGraw-Hill physical and quantum electronics series (W. H. Freeman, 2005).

[12] J. R. Fienup, *Invariant error metrics for image reconstruction,* Applied Optics **36**, 8352 (1997).

[13] L. Rabiner, R. Schafer, and C. Rader, *The chirp z-transform algorithm,* IEEE Transactions on Audio and Electroacoustics **17**, 86 (1969).

[14] G. D. Martin, *Chirp Z-transform spectral zoom optimization with MATLAB.*, Tech. Rep. (2005).

[15] O. Bunk, M. Dierolf, S. Kynde, I. Johnson, O. Marti, and F. Pfeiffer, *Influence of the overlap parameter on the convergence of the ptychographical iterative engine,* Ultramicroscopy **108**, 481 (2008).

[16] M. Guizar-Sicairos and J. R. Fienup, *Phase retrieval with transverse translation diversity: a nonlinear optimization approach,* Optics Express **16**, 7264 (2008).

[17] F. Zhang, I. Peterson, J. Vila-Comamala, A. Diaz, F. Berenguer, R. Bean, B. Chen, A. Menzel, I. K. Robinson, and J. M. Rodenburg, *Translation position determination in ptychographic coherent diffraction imaging,* Optics Express **21**, 13592 (2013).

[18] W. Murray, M. H. Wright, and P. E. Gill, *Practical Optimization* (Emerald Publishing Limited, 1982).

[19] J. Zhong, L. Tian, P. Varma, and L. Waller, *Nonlinear optimization algorithm for partially coherent phase retrieval and source recovery,* IEEE Transactions on Computational Imaging **2**, 310 (2016).

[20] S. Ruder, *An overview of gradient descent optimization algorithms,* arXiv:1609.04747 (2016).

[21] S. Marchesini, H. Krishnan, B. J. Daurer, D. A. Shapiro, T. Perciano, J. A. Sethian, and F. R. N. C. Maia, *SHARP: a distributed GPU-based ptychographic solver,* Journal of Applied Crystallography **49**, 1245 (2016).

[22] Z. Dong, Y.-L. L. Fang, X. Huang, H. Yan, S. Ha, W. Xu, Y. S. Chu, S. I. Campbell, and M. Lin, *High-performance multi-mode ptychography reconstruction on distributed GPUs,* in *2018 New York Scientific Data Summit (NYSDS)* (IEEE, 2018).

[23] Y. S. G. Nashed, D. J. Vine, T. Peterka, J. Deng, R. Ross, and C. Jacobsen, *Parallel ptychographic reconstruction,* Optics Express **22**, 32082 (2014).

[24] A. Maiden, D. Johnson, and P. Li, *Further improvements to the ptychographical iterative engine,* Optica **4**, 736 (2017).

[25] X. Huang, H. Yan, R. Harder, Y. Hwu, I. K. Robinson, and Y. S. Chu, *Optimization of overlap uniformness for ptychography,* Optics Express **22**, 12634 (2014).

[26] X. Huang, K. Lauer, J. N. Clark, W. Xu, E. Nazaretski, R. Harder, I. K. Robinson, and Y. S. Chu, *Fly-scan ptychography,* Scientific Reports **5**, 9074 (2015).

[27] A. Fannjiang, *Raster grid pathology and the cure,* arXiv:1810.00852v3 (2018), http://arxiv.org/abs/1810.00852v3 .

[28] J. C. da Silva and A. Menzel, *Elementary signals in ptychography,* Optics Express **23**, 33812 (2015).

3

Cramér Rao Lower Bound and Maximum Likelihood Estimation in Ptychography with Poisson noise

Parts of this chapter have been published in Physical Review A **102**, 043516 (2020) [1].

3.1. INTRODUCTION

In this chapter our work contains two parts. In the first part we investigate the Cramér Rao Lower Bound (CRLB) for the variance of any unbiased estimator in ptychography [2–4]. To the best of our knowledge, this is the first investigation of the CRLB in ptychography. We study the lower bound for Poisson distributed photon counting noise, which is the most dominant source of noise which occurs even under the best experimental conditions [5, 6]. In Section 3.2, we briefly discuss ptychography, Poisson photon counting noise and the maximum likelihood method. We compute the Fisher information matrix of ptychography with Poisson noise and introduce the CRLB. In Section 3.3, the CRLB is numerically computed and the influence of illumination and of the object is discussed in detail. To validate the obtained CRLB, Monte Carlo analysis is implemented in Section 3.4.

For the second part of this chapter, the performance of the maximum likelihood method and the approach of amplitude-based cost function minimization are also compared using Monte Carlo simulations. Details of the implementation of the algorithms can be found in the Supplement section 3.7. We investigate the statistical property of the algorithms for various photon counts in Section 3.4. The chapter is concluded with a summary and outlook in section 3.6.

3.2. THEORY

3.2.1. PTYCHOGRAPHY, POISSON NOISE, AND MAXIMUM LIKELIHOOD METHOD

In this chapter we come back to the case where the effect of partial coherence is negligible, and we aim to study the influence of Poisson noise. Therefore, according to the thin object model as given in Eq. (1.37), the exit wave $\Psi(\mathbf{r}_\perp)$ for an illumination with a probe function $P(\mathbf{r}_\perp)$ which is centered on position $\mathbf{R}_{\perp,j}$ is given by

$$\begin{aligned}\Psi_j(\mathbf{r}_\perp) &= P(\mathbf{r}_\perp - \mathbf{R}_{\perp,j}) \cdot O(\mathbf{r}_\perp) \\ &= P_j(\mathbf{r}_\perp) \cdot O(\mathbf{r}_\perp),\end{aligned} \tag{3.1}$$

Apart from the influence of the illumination, we also wish to investigate the influence of the transmission function and the thickness function of the object. Hence the object $O(\mathbf{r}_\perp)$ is decomposed into two real valued functions $A(\mathbf{r}_\perp)$ and $\phi(\mathbf{r}_\perp)$:

$$O(\mathbf{r}_\perp) = A(\mathbf{r}_\perp) \cdot e^{\mathrm{i}\phi(\mathbf{r}_\perp)}, \tag{3.2}$$

where A is the object's local transmission function and ϕ stands for the phase of the exit wave immediately behind the object. Once again, the probe function is assumed to have a finite support with, for instance, circular boundary:

$$P(\mathbf{r}_\perp) = \begin{cases} P(\mathbf{r}_\perp), & |\mathbf{r}_\perp| \le r_0, \\ 0, & |\mathbf{r}_\perp| > r_0. \end{cases} \tag{3.3}$$

For a detector located at distance z' in the far field, the diffraction intensity pattern

$I(\mathbf{r}'_\perp)$ for the jth illumination is [7]:

$$\begin{aligned} I_j(\mathbf{r}'_\perp) &= \left|\mathscr{F}_\perp\left(\Psi_j\right)\left(\frac{\mathbf{r}'_\perp}{\lambda z}\right)\right|^2 \\ &= \left|\sum_{\mathbf{r}_\perp}\Psi_j(\mathbf{r}_\perp)\cdot\exp\left(-\mathrm{i}\frac{2\pi}{\lambda z}\mathbf{r}_\perp\cdot\mathbf{r}'_\perp\right)\right|^2, \end{aligned} \tag{3.4}$$

where $\mathscr{F}_\perp$ is the discrete Fourier transform operator.

The task of ptychography is to find an object function which takes account of the *a priori* knowledge, while a cost function $\mathscr{E}$ is minimized. In our case the *a priori* knowledge is the exact information of the probe function and the set of relative positions $\mathbf{R}_{\perp,j}$. The cost function $\mathscr{E}$ is defined as the l_2-distance between the modulus of the far field diffraction pattern $\left|\mathscr{F}_\perp\left(\Psi_j\right)(\mathbf{k}_\perp)\right|$ and the squared root of the measured intensity $I_j^{\mathrm{m}}(\mathbf{k}_\perp)$:

$$\mathscr{E} = \sum_j\sum_{\mathbf{k}_\perp}\left[\sqrt{I_j^{\mathrm{m}}(\mathbf{k}_\perp)} - \left|\mathscr{F}_\perp\left(\Psi_j\right)(\mathbf{k}_\perp)\right|\right]^2, \tag{3.5}$$

where $\mathbf{k}_\perp = \mathbf{r}'_\perp(\lambda z)^{-1} \approx \mathbf{n}_{\mathbf{k}_\perp}\Delta\mathbf{k}_\perp$ is the spatial spectrum coordinate as given in Eq. (1.43).

From I_j^{m}, one can estimate the number of detected photons:

$$n_j(\mathbf{k}_\perp) = \frac{I_j^{\mathrm{m}}(\mathbf{k}_\perp)}{\hbar\omega}, \qquad \text{where } \omega = \frac{2\pi c}{\lambda}, \tag{3.6}$$

where $\hbar$ is the Planck constant. Among a variety of noise models, we consider Poisson noise. The probability distribution of detecting $n_j(\mathbf{k}_\perp)$ photons by the detector at every $\mathbf{k}_\perp$ for all measurements ($j = 1,2,\cdots$) are given by:

$$\mathscr{P}_P = \prod_j\prod_{\mathbf{k}_\perp}\frac{N_j(\mathbf{k}_\perp)^{n_j(\mathbf{k}_\perp)}}{N_j(\mathbf{k}_\perp)!}e^{-N_j(\mathbf{k}_\perp)}, \tag{3.7}$$

where the cumulative product is over both the 2-D coordinate $\mathbf{k}_\perp$ and the probe position $\mathbf{R}_{\perp,j}$. The negative log-likelihood functional is defined by:

$$\begin{aligned} \mathscr{L}_P &= -\ln\mathscr{P}_P \\ &= -\sum_j\sum_{\mathbf{k}_\perp}\left[n_j\ln N_j - N_j - \ln n_j!\right]. \end{aligned} \tag{3.8}$$

The average number of photons $N_j(\mathbf{k}_\perp)$ depends on the object function $O(\mathbf{r}_\perp)$ through Eq. (3.4) and Eq. (3.6). To find the object function for which the negative log-likelihood functional is maximum, the derivative of $\mathscr{L}_P$ with respect to O is set equal to zero. Hence, for any small perturbation δO of the object function it should hold:

$$\mathscr{L}_P(\delta O) = 0. \tag{3.9}$$

where the local perturbation of the value of O on a discretized grid $\mathbf{r}_\perp \approx \mathbf{n}_{\mathbf{r}_\perp,\perp}\Delta\mathbf{r}_\perp$ is written as:

$$\begin{aligned}\delta O(\mathbf{r}_\perp) &= \sum_{\mathbf{n}_{\mathbf{r}_\perp,\perp}} \delta O(\mathbf{n}_{\mathbf{r}_\perp,\perp})\delta(\mathbf{r}_\perp - \mathbf{n}_{\mathbf{r}_\perp,\perp}\Delta\mathbf{r}_\perp) \\ &= \sum_{\mathbf{n}_{\mathbf{r}_\perp,\perp}} \begin{bmatrix} \delta A(\mathbf{n}_{\mathbf{r}_\perp,\perp}) \\ \mathrm{i}A(\mathbf{n}_{\mathbf{r}_\perp,\perp})\delta\phi(\mathbf{n}_{\mathbf{r}_\perp,\perp}) \end{bmatrix} e^{\mathrm{i}\phi(\mathbf{n}_{\mathbf{r}_\perp,\perp})}\delta(\mathbf{r}_\perp - \mathbf{n}_{\mathbf{r}_\perp,\perp}\Delta\mathbf{r}_\perp), \end{aligned} \tag{3.10}$$

where $\Delta\mathbf{r}_\perp$ is the size of every cells of the 2D meshgrids as given in Eq. (1.43). By substituting Eq. (3.10) into Eq. (3.9) we have:

$$\begin{aligned}\delta\mathscr{L}_P(\delta O) &= -\sum_j\sum_{\mathbf{k}_\perp}\left(\frac{n_j(\mathbf{k}_\perp)}{N_j(\mathbf{k}_\perp)} - 1\right)\delta N_j\left(\delta O(\mathbf{r}_\perp)\right) \\ &= -\frac{1}{\hbar\omega}\sum_j\sum_{\mathbf{k}_\perp}\left(\frac{n_j(\mathbf{k}_\perp)}{N_j(\mathbf{k}_\perp)} - 1\right)\delta I_j\left(\delta O\mathbf{r}_\perp\right) \\ &= -\frac{2}{\hbar\omega}\sum_j\sum_{\mathbf{k}_\perp}\left(\frac{n_j(\mathbf{k}_\perp)}{N_j(\mathbf{k}_\perp)} - 1\right)\Re\left[\mathscr{F}_\perp\left(P_jO\right)(\mathbf{k}_\perp)\mathscr{F}_\perp\left(P_j\delta O(\mathbf{r}_\perp)\right)^*(\mathbf{k}_\perp)\right] \\ &= -\frac{2}{\hbar\omega}\sum_j\sum_{\mathbf{r}_\perp}\Re\left\{\mathscr{F}_\perp^{-1}\left[\left(\frac{n_j}{N_j} - 1\right)\mathscr{F}_\perp\left(P_jO\right)\right](\mathbf{r}_\perp)P_j^*(\mathbf{r}_\perp)\delta O^*(\mathbf{r}_\perp)\right\}. \end{aligned} \tag{3.11}$$

In Eq. (3.11), the generalized Parseval's theorem was used. $\Re$ denotes the real part and $\mathscr{F}_\perp^{-1}$ the inverse Fourier transform. The solution of Eq. (3.11) can be found by the method of steepest descent [8–10]:

$$A_{n+1}(\mathbf{r}_\perp) = A_n(\mathbf{r}_\perp) + \beta_A\sum_j\Re\left\{P_j^*e^{-\mathrm{i}\phi_n}\mathscr{F}_\perp^{-1}\left[\left(\frac{n_j}{N_j} - 1\right)\mathscr{F}_\perp\left(P_jO_n\right)\right]\right\}(\mathbf{r}_\perp), \tag{3.12a}$$

$$\phi_{n+1}(\mathbf{r}_\perp) = \phi_n(\mathbf{r}_\perp) + \beta_\phi\sum_j\Im\left\{P_j^*A_ne^{-\mathrm{i}\phi_n}\mathscr{F}_\perp^{-1}\left[\left(\frac{n_j}{N_j} - 1\right)\mathscr{F}_\perp\left(P_jO_n\right)\right]\right\}(\mathbf{r}_\perp), \tag{3.12b}$$

where n is the iteration number, and β_A and β_ϕ are the step-sizes, which are normally chosen to be a constant, i.e. they are independent on the iteration number. $\Im$ denotes the imaginary part. Alternatively, projection based method or conjugate gradient method can be applied to achieve maximum likelihood [6].

3.2.2. THE CRLB AND THE FISHER MATRIX

In estimation theory, the CRLB gives a lower bound on the variance of any unbiased estimator for the parameter which must be estimated. The estimators that can reach the lower bound are called the minimum variance unbiased estimators. Minimum variance unbiased estimators are often not available [2, 11].

We recall the definition of the CRLB, using the notation as in [2]. Suppose we wish to retrieve a real valued vector parameter $\Theta = [\theta_1, \theta_2, \cdots]^T$ from a set of measurements $\mathbf{X} = [X_1, X_2, \cdots]^T$. There are infinite number of possible outcomes $\mathbf{X}_1, \mathbf{X}_2, \cdots, \mathbf{X}_s, \cdots$ occurring with probabilities $\mathscr{P}_1, \mathscr{P}_2, \cdots, \mathscr{P}_s, \cdots$, respectively. To determine the lower bound on the

variance of estimator $\hat{\Theta}$, one computes the Fisher information matrix I_F, given by:

$$I_F(\Theta) = -E\left[\frac{\partial^2 \ln \mathscr{P}(\mathbf{X}_s;\Theta)}{\partial \Theta^2}\right], \tag{3.13}$$

where $\mathscr{P}(\mathbf{X}_s;\Theta) = \mathscr{P}_s$ is the conditional probability distribution function and E is the expectation operator. The element of $I_F(\Theta)$ is given by:

$$I_F(\Theta)_{lm} = -\sum_s \frac{\partial^2 \ln \mathscr{P}(\mathbf{X}_s;\Theta)}{\partial \theta_l \partial \theta_m} \mathscr{P}(\mathbf{X}_s;\Theta), \tag{3.14}$$

where $l = 1,2,\cdots$ and $m = 1,2,\cdots$ are indices of elements. The CRLB is then given by the diagonal elements of the inverse of matrix I_F, i.e.

$$\mathrm{Var}\left(\hat{\theta}_l\right) \geq \left[I_F^{-1}(\Theta)\right]_{ll}, \tag{3.15}$$

where $\mathrm{Var}\left(\hat{\theta}_l\right)$ stands for the variance of estimator $\hat{\theta}_l$ for the unknown parameter θ_l.

It is important to note that the estimator based on the maximum likelihood principle $\hat{\theta}_{MLE}$ asymptotically becomes unbiased and achieves the CRLB for large data sets [2], that is:

$$\hat{\Theta}_{MLE} \overset{a}{\sim} \mathscr{N}\left\{\Theta, \mathbf{diag}\left[I_F^{-1}(\Theta)\right]\right\}, \tag{3.16}$$

where $\mathscr{N}$ stands for the normal distribution and **diag** takes the diagonal elements of a matrix.

3.2.3. THE FISHER MATRIX WITH POISSON NOISE IN PTYCHOGRAPHY

To find the Fisher information matrix, we start by computing the second order derivative of the likelihood functional $\mathscr{L}_P$ with respect to $O(\mathbf{r}_\perp)$:

$$\delta^2 \mathscr{L}_P(\delta O, \delta \tilde{O}) = \frac{1}{(\hbar\omega)^2} \sum_j \sum_{\mathbf{k}_\perp} \frac{n_j}{N_j^2} \left[\delta I_j(\delta O)\right]\left[\delta I_j(\delta \tilde{O})\right] - \frac{1}{\hbar\omega} \sum_j \sum_{\mathbf{k}_\perp} \left(\frac{n_j}{N_j} - 1\right) \delta^2 I_j(\delta O, \delta \tilde{O}), \tag{3.17}$$

where $\delta\tilde{O}$ is the local perturbation of the value of O on a discretized grid as well:

$$\delta \tilde{O} = \sum_{\mathbf{n}_{\mathbf{r}_\perp,\perp}} \begin{bmatrix} \delta \tilde{A}(\mathbf{n}_{\mathbf{r}_\perp,\perp}) \\ \mathrm{i}\tilde{A}(\mathbf{n}_{\mathbf{r}_\perp,\perp}) \delta\tilde{\phi}(\mathbf{n}_{\mathbf{r}_\perp,\perp}) \end{bmatrix} e^{\mathrm{i}\tilde{\phi}(\mathbf{n}_{\mathbf{r}_\perp,\perp})} \delta(\mathbf{r}_\perp - \mathbf{n}_{\mathbf{r}_\perp,\perp} \Delta \mathbf{r}_\perp). \tag{3.18}$$

By taking the expectation of Eq. (3.17), we get:

$$\begin{aligned} E\left(\delta^2 \mathscr{L}_P\right)(\delta O, \delta \tilde{O}) = & \frac{1}{(\hbar\omega)^2} \sum_j \sum_{\mathbf{k}_\perp} E\left\{\frac{n_j}{N_j^2}\left[\delta I_j(\delta O)\right]\left[\delta I_j(\delta \tilde{O})\right]\right\} \\ & - \frac{1}{\hbar\omega} \sum_j \sum_{\mathbf{k}_\perp} E\left[\left(\frac{n_j}{N_j} - 1\right) \delta^2 I_j(\delta O, \delta \tilde{O})\right], \end{aligned} \tag{3.19}$$

in which we swap the expectation and summation because the measurements $n_j(\mathbf{k}_\perp)$ are independent photon measurements for all pixels $\mathbf{k}_\perp$. Using the properties of the Poisson distribution [4]:

$$\sum_{n_j} \frac{N_j^{n_j}}{n_j!} e^{-N_j} = 1, \tag{3.20a}$$

$$\sum_{n_j} n_j \frac{N_j^{n_j}}{n_j!} e^{-N_j} = N_j, \tag{3.20b}$$

and using Eq. (3.11), we find:

$$\begin{aligned} E\left(\delta^2 \mathscr{L}_P\right)(\delta O, \delta\tilde{O}) &= \frac{1}{(\hbar\omega)^2} \sum_j \sum_{\mathbf{k}_\perp} \frac{1}{n_j(\mathbf{k}_\perp)} \delta I_j(\delta O)\, \delta I_j(\delta\tilde{O}) \\ &= \frac{2}{\hbar\omega} \sum_j \sum_{\mathbf{k}_\perp} \Re\left[\frac{\left[\mathscr{F}_\perp\left(\Psi_j\right)(\mathbf{k}_\perp)\right]^2}{I_j(\mathbf{k}_\perp)} \mathscr{F}_\perp\left(P_j \delta O\right)^* \mathscr{F}_\perp\left(P_j \delta\tilde{O}\right)^* \right] \\ &\quad + \frac{2}{\hbar\omega} \sum_j \sum_{\mathbf{k}_\perp} \Re\left[\mathscr{F}_\perp\left(P_j \delta O\right) \mathscr{F}_\perp\left(P_j \delta\tilde{O}\right)^*\right]. \end{aligned} \tag{3.21}$$

in which we use the following relation:

$$\Re(z_1)\Re(z_2) = \frac{1}{2}\left[\Re(z_1 z_2) + \Re(z_1 z_2^*)\right], \tag{3.22}$$

where z_1, z_2 are arbitrary complex numbers.

From Eq. (3.10), Eq. (3.18) and Eq. (3.21) we can derive the discretized Fisher information matrix with respect to the transmission and the thickness function of the object:

$$\begin{aligned} I_{F,lm} &= \begin{bmatrix} (I_F)_{AA,lm} & (I_F)_{A\phi,lm} \\ (I_F)_{\phi A,lm} & (I_F)_{\phi\phi,lm} \end{bmatrix} \\ &= \frac{2}{\hbar\omega} \sum_j \begin{bmatrix} \Re\left[f_j(\mathbf{r}_{\perp,l}, \mathbf{r}_{\perp,m})\right] & \Im\left[A(\mathbf{r}_{\perp,m}) f_j(\mathbf{r}_{\perp,l}, \mathbf{r}_{\perp,m})\right] \\ \Im\left[A(\mathbf{r}_{\perp,l}) f_j(\mathbf{r}_{\perp,l}, \mathbf{r}_{\perp,m})\right] & -\Re\left[A(\mathbf{r}_{\perp,l}) A(\mathbf{r}_{\perp,m}) f_j(\mathbf{r}_{\perp,l}, \mathbf{r}_{\perp,m})\right] \end{bmatrix} \\ &\quad + \frac{2}{\hbar\omega} \sum_j \begin{bmatrix} \left|P_j(\mathbf{r}_{\perp,l})\right|^2 \delta_{lm} & 0 \\ 0 & A^2(\mathbf{r}_{\perp,l}) \left|P_j(\mathbf{r}_{\perp,l})\right|^2 \delta_{lm} \end{bmatrix}, \end{aligned} \tag{3.23}$$

where the auxiliary function f is given by:

$$f_j(\mathbf{r}_{\perp,l}, \mathbf{r}_{\perp,m}) = \mathscr{F}_\perp^{-1}\left[\frac{\mathscr{F}_\perp\left(\Psi_j\right)}{\mathscr{F}_\perp\left(\Psi_j\right)^*}\right](\mathbf{r}_{\perp,l} + \mathbf{r}_{\perp,m}) \cdot P_j^*(\mathbf{r}_{\perp,l}) P_j^*(\mathbf{r}_{\perp,m}) e^{-\mathrm{i}[\phi(\mathbf{r}_{\perp,l}) + \phi(\mathbf{r}_{\perp,m})]}. \tag{3.24}$$

where we used Eq. (3.4) and the Kronecker's symbol δ_{lm}. $l = 1, 2, \cdots$ and $m = 1, 2, \cdots$ are indices of elements.

In Eq. (3.23) we see that the first term is symmetric and the second one is diagonal. The analytical expression for the CRLB, which is obtained from the inverse of the Fisher matrix, cannot be easily derived, but this inverse can be computed numerically. Detailed examples are presented in the next section.

Table 3.1: Four cases that are considered in the computation of the CRLB

Case-1	Both the transmission and thickness function of the object are uniform. The probe has structured wavefront but uniform illumination power in the circular support.
Case-2	Both the transmission and thickness function of the object are uniform. The probe has structured wavefront and structured illumination power in the circular support.
Case-3	The object has non-uniform transmission but uniform thickness function. The probe is a plane-wave with circular support.
Case-4	The object has uniform transmission but non-uniform thickness function. The probe is a plane-wave with circular support.

3.3. DIRECT CALCULATION OF THE CRLB

As shown in Eq. (3.15), the CRLB is given by the diagonal elements of the inverse of matrix I_F, which can be obtained by numerical computations. In this section, we present the results of some computed CRLB. To investigate how the illumination (i.e. the probe function P) and the object O influence the CRLB, we study four cases separately, as described in Table 3.1. Note that only Poisson noise is applied throughout our simulations. Other noise models (e.g. Gaussian noise or Poisson-Gaussian noise [12]) should be included when these are dominant. All of the calculation results given in this section are compared to the Monte Carlo experiment result that are presented in the next section.

For all cases shown in Table 3.1, the probe moves over the object by a 2×2 regular grid. In line with the conventional ptychography configuration, the overlap ratio between adjacent illuminated areas is 70%. The overlap ratio in each dimension is defined as follows. Suppose the diameter of the circular support is L, and the distance between corresponding points in adjacent illumination positions is d, where $0 < d < L$. The overlap ratio is the same as defined in Eq. (4.2.5):

$$\text{overlap ratio} = 1 - \frac{d}{L} \tag{3.25}$$

which is usually chosen between 60% and 85% to achieve optimal performance of the reconstruction algorithm [13]. The overlap ratio and the actual probe function are regarded as *a prior* knowledge and employed in the reconstruction algorithm.

The characteristic parameters for the numerical computations are shown in Table 3.2. The object is discretised and zero padded by a 70×70 square grid with grid spacing $1\mu m$. The total illuminated area is roughly $40 \times 40\mu m^2$. The circular probe has radius of $30\mu m$ and is discretised by a square grid of 60×60 grid points with grid spacing of $1\mu m$. The wavelength is 30 nm. The far field intensities are measured with a detector at propagation distance of $5cm$ behind the object. The detector consists of an array of 60×60 pixels with a pixel size of $50\mu m$. Hence the maximum spatial frequency (without factor 2π) that is measured is $1\mu m^{-1}$ and the frequency are sampled with distance $(30)^{-1}\,\mu m^{-1}$.

To compute the CRLB, we first construct the Fisher information matrix I_F using Eq. (3.23). Although the number of degrees of freedom used to describe the object is small,

Table 3.2: The characteristic parameters for the simulations

probe	grid size	grid spacing	wavelength	scanning grid	overlap ratio	radius of circular support
	60×60	$1\mu m$	$30nm$	2×2	70%	$30\mu m$

object	grid size	grid spacing	detector	pixel number	pixel size	propagation distance
	70×70	$1\mu m$		60×60	$50\mu m$	$5cm$

namely $70 \times 70 \times 2$ elements, where the factor 2 is due to the fact that the object function is complex, the discretised Fisher matrix already includes 9800×9800 elements. The CRLB is obtained by numerically computing the inverse of I_F. Since $I_{F,ij}$ is an symmetric matrix with real entries, one can apply the eigenvalue decomposition to find the inverse of the Fisher matrix. We select the eigenvalues of I_F that are bigger than a default tolerance, then use these eigenvalues and the corresponding eigenvectors to compute the inverse of I_F. This calculation is done by utilizing the 'pinv' routine in MATLAB. The diagonal elements of the inverse matrix I_F^{-1} consists of an array of $70 \times 70 \times 2$ elements, of which the first 70×70 elements correspond to the CRLB of $A(\mathbf{r}_\perp)$ and the last 70×70 elements contain the CRLB of $\phi(\mathbf{r}_\perp)$.

We define the illumination power by means of the total photon number (PN) counting over the cross section of the probe, given by:

$$\mathrm{PN} = \frac{\sum_{\mathbf{r}_\perp} |P(\mathbf{r}_\perp)|^2}{\hbar\omega}. \tag{3.26}$$

An important property of the CRLB is that it is proportional to the reciprocal of the illumination power. This property follows from the fact that Eq. (3.23) and Eq. (3.24) are proportional to the input power or the square of the probe P_j. The observation that the CRLB scales with the reciprocal of the illuminating power is confirmed by the computations discussed below.

In the remainder of this section we show the computed CRLB for high illumination power, i.e. $\mathrm{PN} = 10^9$, and for low illumination power, i.e. $\mathrm{PN} = 10^3$, as examples. The influence of the object and the probe on the CRLB will be discussed separately.

3.3.1. THE INFLUENCE OF THE ILLUMINATION ON THE CRLB

In order to investigate the influence of the illumination on the CRLB, we start by studying Case-1 and Case-2 described in Table 3.1. For these cases, the actual object, the actual illumination and the computed CRLB are shown in Fig. 3.1 and Fig. 3.2. We let the object have uniform transmission and thickness function for the time being. For Case-1, the probe function P has uniform power throughout its circular support and zero value outside its support, but the phase of the probe has variation in the form of two characters 'P' as shown in Fig. 1a4. On the other hand, the illumination in Case-2 has the shape of the character 'P' and truncated by the circular support as shown in Fig. 3.2a3, and its phase has the same features consisting of two characters 'P' as in Case-1 (see Fig. 2a3 and Fig. 2a4). Considering that a perfectly collimated beam is difficult to obtain, we

have chosen the wavefront of the illumination to be non-uniform for both Case-1 and Case-2.

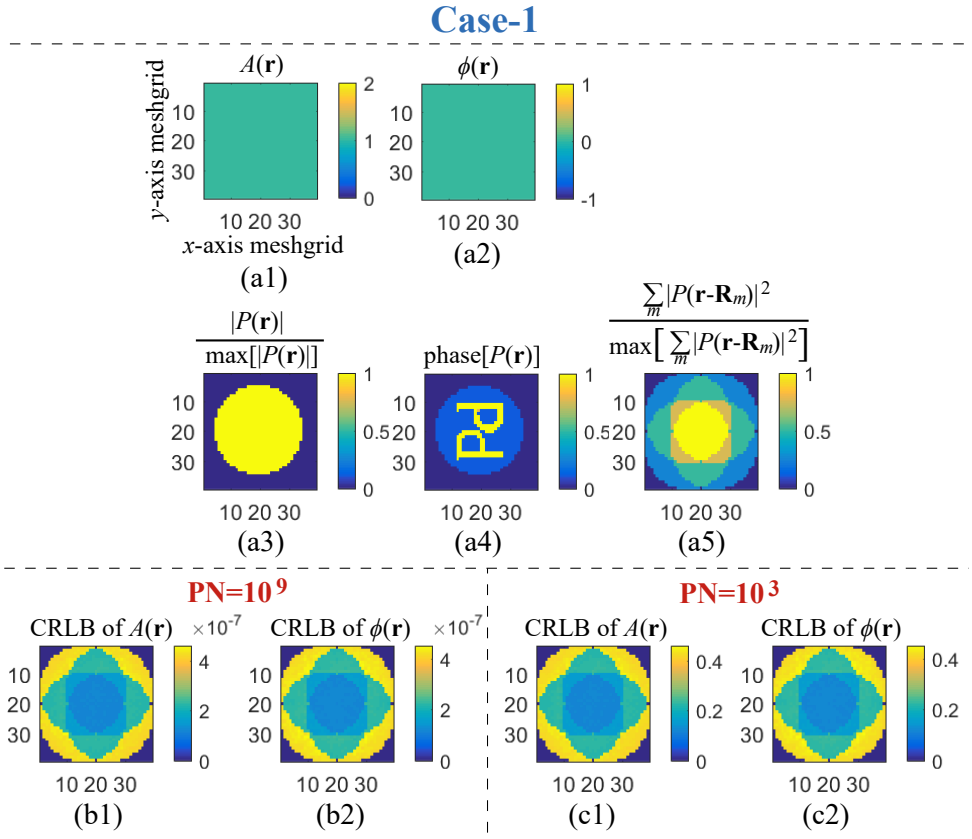

Figure 3.1: The CRLB computed from the Fisher matrix for Case-1. (a1) and (a2) are the object's actual transmission $A(\mathbf{r}_\perp)$ and actual phase function $\phi(\mathbf{r}_\perp)$, respectively. (a3) and (a4) show the actual amplitude and phase of the probe function, respectively. (a5) shows the normalized sum of the intensities of the illuminations. (b1) and (b2) show the CRLB of $A(\mathbf{r}_\perp)$ and $\phi(\mathbf{r}_\perp)$, respectively, for the case of PN = 10^9. (c1) and (c2) are the CRLB for the case of PN = 10^3.

It is seen in Fig. 3.1 that the CRLB of the object resembles the normalized sum of the intensities of the illuminations shown in Fig. 3.1a5. In particular, the part of the object which is illuminated 4 times reaches a variance approximately 4 times smaller than the part which is illuminated only once, and this conclusion holds for both the object's local transmission $A(\mathbf{r}_\perp)$ and phase function $\phi(\mathbf{r}_\perp)$. Interestingly, when the dose distribution of the illumination is more complicated as given in Fig. 3.2a3 and Fig. 3.2a4, the CRLB shown in Fig. 3.2b and Fig. 3.2c again resemble the overall illumination pattern shown in Fig. 3.2a5. In other words, the more illumination power we apply to the object, the lower the minimum variance of the obtained reconstruction. One can notice that the maximum of the CRLB in Fig. 3.2c and Fig. 3.2d is in the yellow corner and is larger than

the CRLB in Fig. 3.1. This is because for Case-2 the illuminating power is concentrated in the 'P' character, as shown in Fig. 3.2(a3). Around the yellow corner there are parts of the object where the computed CRLB is zero. These parts of the object are not illuminated. For the areas where I_F is zero, the computed CRLB is also put equal to zero because we ignore these singular values of I_F. In reality the CRLB there is infinite.

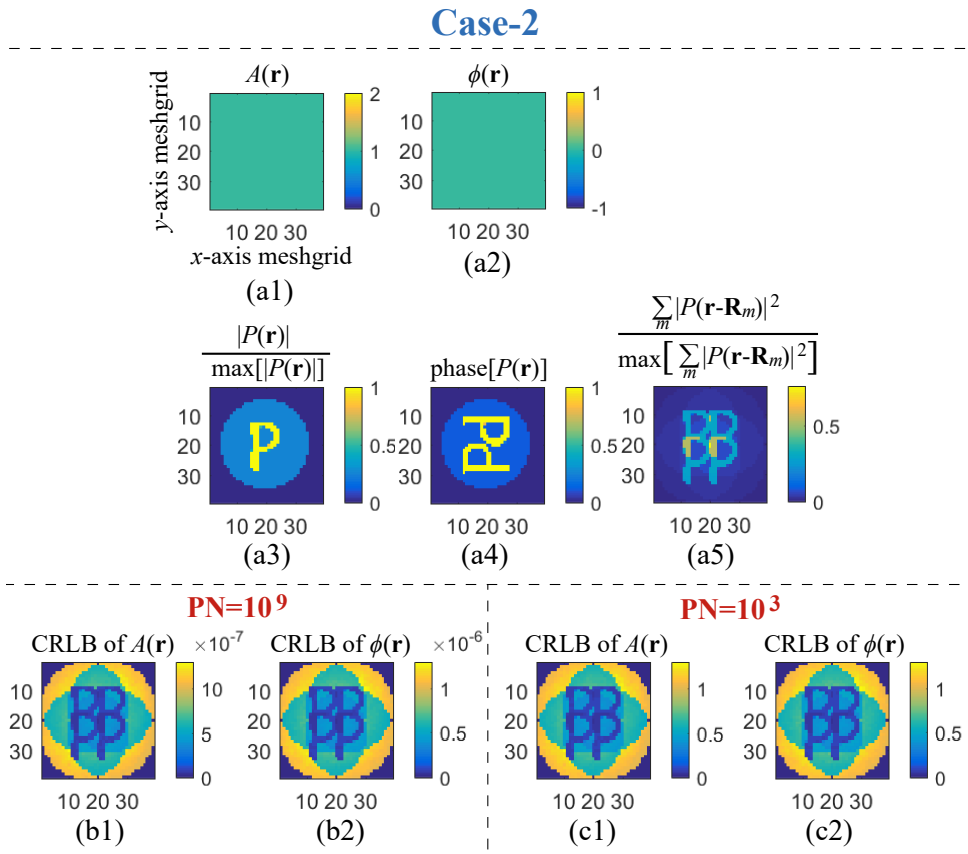

Figure 3.2: The calculated CRLB for Case-2. (a1) - (a5) are the actual object, probe and the normalized sum of the intensities of the illuminations, respectively. (b1) and (b2) are the CRLB of $A(\mathbf{r}_\perp)$ and $\phi(\mathbf{r}_\perp)$, respectively, for PN = 10^9. (c1) and (c2) are the CRLB for the case of PN = 10^3.

Moreover, we can see in Fig. 3.1 and Fig. 3.2 that the CRLB is linearly proportional to the inverse of PN (i.e. the illumination power). This calculation result is in agreement with Eq. (3.23) because the probe function $P(\mathbf{r}_\perp)$ can be written as the factor $\sqrt{\text{PN}}$ times the normalized $P(\mathbf{r}_\perp)$. On the other hand, the computed CRLB of both $A(\mathbf{r}_\perp)$ and $\phi(\mathbf{r}_\perp)$ do not show any influence due to the spatial variation of the phase of the probe. Therefore, we conclude that it is the illumination intensity pattern, i.e. the dose distribution, which strongly determines the CRLB in ptychography for Poisson noise.

3.3.2. THE INFLUENCE OF THE OBJECT ON THE CRLB

The Fisher matrix in Eq. (3.23) is in fact a function of the object, and hence so is the CRLB. To find the influence of $A(\mathbf{r}_\perp)$ and $\phi(\mathbf{r}_\perp)$ on the CRLB, we focus on Case-3 and Case-4 from now on. To reduce the influence of the illumination to a minimum, we let the probe function be a plane-wave with circular support. The influence of the object's transmission and phase function is investigated separately. In Case-3 we let the function $A(\mathbf{r}_\perp)$ have the shape of the character 'A' while $\phi(\mathbf{r}_\perp)$ is kept uniform, as shown in Fig. 3.3. The minimum value of $A(\mathbf{r}_\perp)$ is 0.1. For Case-4, the function $A(\mathbf{r}_\perp)$ is uniform whereas the phase function $\phi(\mathbf{r}_\perp)$ has the shape of the character 'T' as shown in Fig. 3.4.

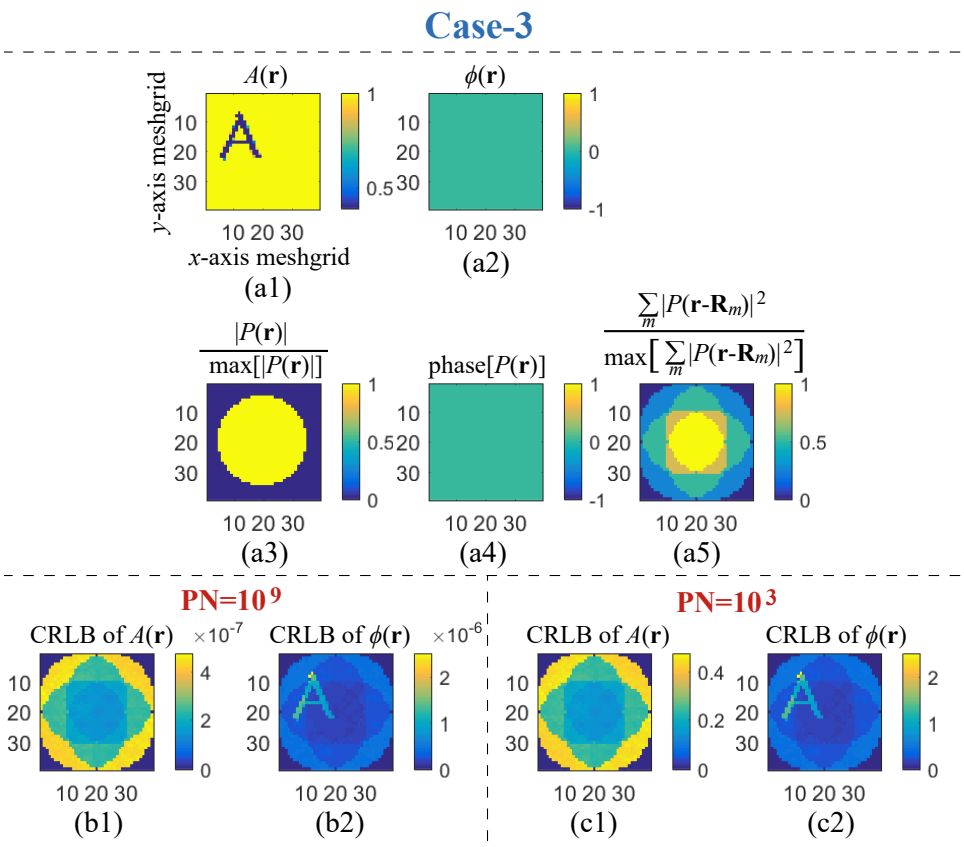

Figure 3.3: The CRLB for Case-3. (a1) - (a5) are the actual object, probe and the normalized sum of the intensities of the illuminations, respectively. (b1) and (b2) are the CRLB of $A(\mathbf{r}_\perp)$ and $\phi(\mathbf{r}_\perp)$, respectively, for PN = 10^9. (c1) and (c2) are the CRLB when PN = 10^3.

The computed CRLB of the object for Case-3 and Case-4 is illustrated in Fig. 3.3b, Fig. 3.3c, Fig. 3.4b and Fig. 3.4c, respectively. It is clear that our conclusion in Section 3.1 still holds, i.e. the CRLB is very similar to the pattern of the sum of the intensities of the illuminations. On the other hand, we can see also that the object's local transmission A is predominant in determining the CRLB of ϕ, as shown in Fig. 3.3(b2) and

Fig. 3.3(c2). This result agrees with Eq. (3.23), because the function A appears in the terms of I_F which relates to ϕ. However, the influence of ϕ on the CRLB is much less than A. Therefore, we conclude that the second term in Eq. (3.23) is dominant. In other words, when the estimator of ptychography is unbiased, the variance of the object's transmission $A(\mathbf{r}_\perp)$ is strongly determined by the illumination power and dose distribution, whereas the variance of the object's phase $\phi(\mathbf{r}_\perp)$ is influenced by both of the transmission $A(\mathbf{r}_\perp)$, the illumination power and the dose distribution.

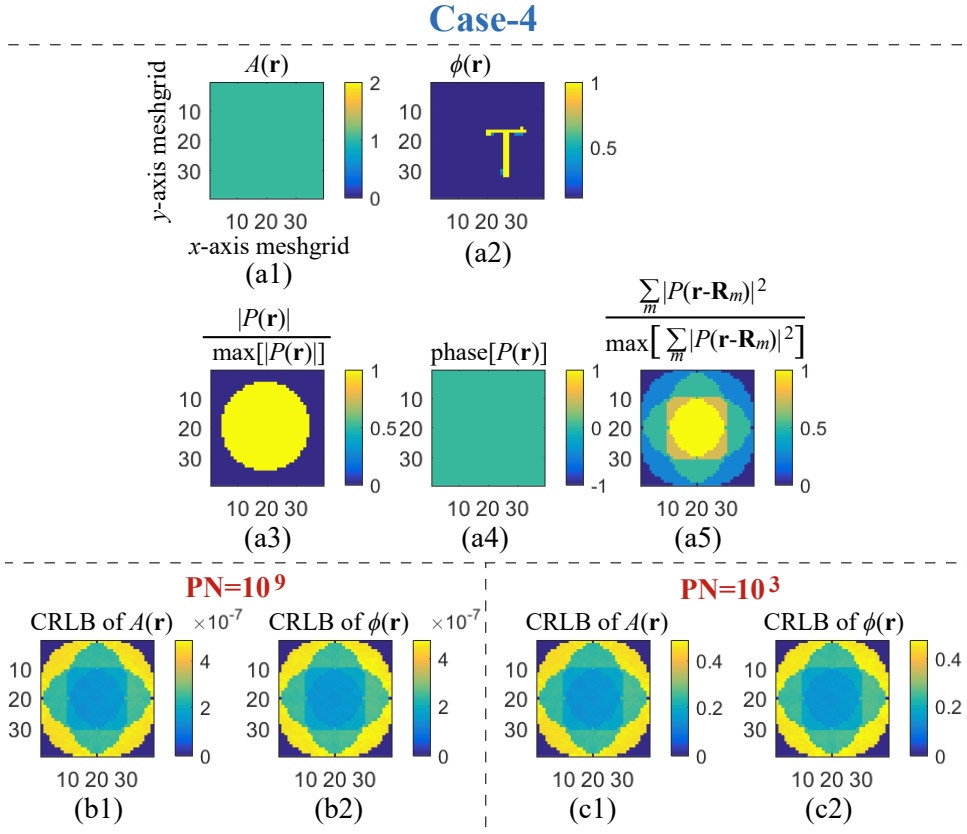

Figure 3.4: The CRLB for Case-4. (a1) - (a5) are the actual object, probe and the normalized sum of the intensities of the illuminations, respectively. (b1) and (b2) are the CRLB of $A(\mathbf{r}_\perp)$ and $\phi(\mathbf{r}_\perp)$, respectively, when PN = 10^9. (c1) and (c2) are the CRLB for PN = 10^3.

In the next section, the CRLB shown in Fig. 3.1 - Fig. 3.4 are used as references for Monte Carlo experiments.

3.4. MONTE CARLO ANALYSIS

To validate our calculation of the CRLB, Monte Carlo computations have been performed. For consistency, we discretise the probe and the object in the same way as described in Table 3.2. The wavelength, object, probe, far field measurements and grid sizes are as

described in Table 3.2 also. The Fresnel number of the system is 0.15. Hence for this configuration the detector is in the Fraunhofer region.

The ptychographic data with various level of noise is generated as follows. For every ptychography simulation and for every probe position, we first assign the probe function with corresponding photon numbers in accordance with the PN that is chosen. Then, the noise-free diffracted wavefield in the far field is calculated, and the Poisson random number generator in MATLAB is applied to generate the noisy data.

To verify the asymptotic property of the maximum likelihood method of Eq. (3.16), we developed and implemented **Algorithm 2** as described in the Supplement section 3.6. To mitigate ambiguity problems of ptychography [8], e.g. the global phase shift, the conjugate reconstruction and the raster grid pathology, it is assumed that the probe used in the Monte Carlo experiment is known. To shorten the computation time and to improve the convergence, the conjugate gradient method [6, 14] is implemented in **Algorithm 2**.

For comparison, the performance of another popular method, namely the amplitude-based cost function minimization approach [15], was investigated in the Monte Carlo experiment also. This is implemented in **Algorithm 3**. The idea of this algorithm is to retrieve the object by minimizing the cost function defined in Eq. (3.5). We remark that one can alternatively derive **Algorithm 3** from the maximum likelihood method by using the variance stabilization transform [5, 6, 12, 16, 17]. **Algorithm 3** is also described in the Supplement section 3.7.

To investigate the performance of the above mentioned algorithms, the variance and the squared bias of the estimator are evaluated in our Monte Carlo analysis. Explicitly, the variance of an estimator $\hat{O}(\mathbf{r}_\perp)$ is defined by [2]:

$$\mathrm{Var}\left[\hat{O}(\mathbf{r}_\perp)\right] = E\left\{\left[\hat{O}(\mathbf{r}_\perp) - \left\langle \hat{O}(\mathbf{r}_\perp)\right\rangle\right]^2\right\}, \tag{3.27}$$

where

$$\left\langle \hat{O}(\mathbf{r}_\perp)\right\rangle = E\left[\hat{O}(\mathbf{r}_\perp)\right], \tag{3.28}$$

and the squared bias of the estimator is given by:

$$\mathrm{Bias}^2\left[\hat{O}(\mathbf{r}_\perp)\right] = \left|\left\langle \hat{O}(\mathbf{r}_\perp)\right\rangle - O_\mathrm{o}(\mathbf{r}_\perp)\right|^2, \tag{3.29}$$

where O_o is the actual object function.

In order to compute the expectation accurately, 2000 individual ptychographic data sets have been generated for all for cases mentioned in Table 3.1 and for different value of PN. These data-sets have been post-processed by **Algorithm 2** and **Algorithm 3**, respectively, and the results are discussed next.

3.4.1. THE STATISTIC PROPERTIES OF THE MAXIMUM LIKELIHOOD METHOD AND THE AMPLITUDE-BASED COST MINIMIZATION METHOD, AND THE INFLUENCE OF THE ILLUMINATION

We begin with the case of uniform object function and structured illumination, i.e. Case-1 and Case-2. For these cases the actual object and probe function are as in Fig. 3.1a and Fig. 3.2a.

When the illumination have a uniform dose distribution but a structured wavefront, the variance and bias of both **Algorithm 2** and **Algorithm 3** are shown in Fig. 3.5. In line

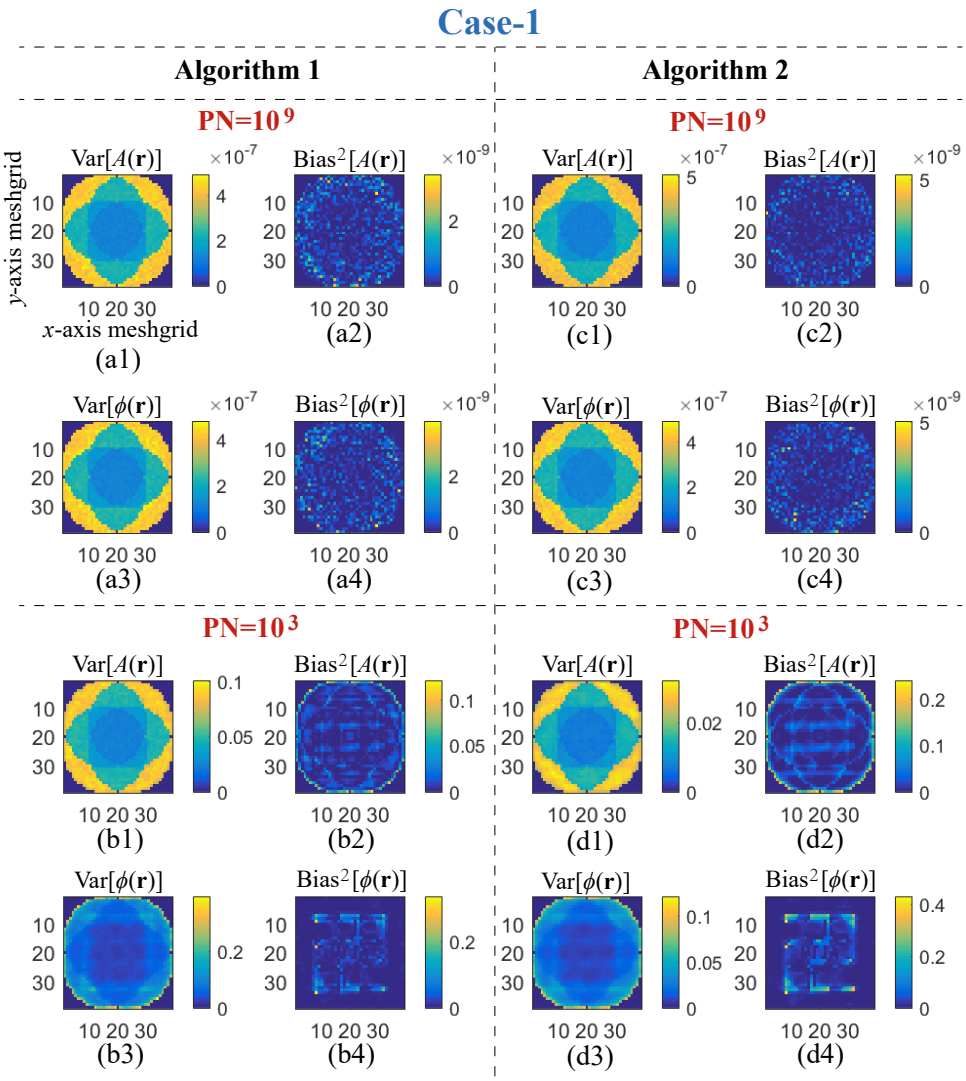

Figure 3.5: The result of Monte Carlo experiment for Case-1. (a1) and (a2) are the variance and bias squared of the object's transmission A when PN = 10^9, respectively, obtained with **Algorithm 2**. (a3) and (a4) are the variance and bias squared of the object's thickness ϕ, respectively. (b1)-(b4) show the variance and bias squared when PN = 10^3, respectively, obtained with **Algorithm 2**. (c1)-(c4) and (d1)-(d4) show the results obtained with Algorithm 2 when PN = 10^9 and PN = 10^3, respectively.

with the CRLB given in 3.1b, we see that both algorithms that asymptotically achieve the CRLB when PN = 10^9. The squared bias of the two algorithms are 100 times smaller than the variance, hence both **Algorithm 2** and **Algorithm 3** are asymptotically unbiased

when the photon number is high. Meanwhile, by inspecting Fig. 3.5a and Fig. 3.5c, one can infer that the variance of both algorithms are related to the local illuminating power as mentioned in Section 3.2, i.e. the parts of the object that are illuminated 4 times have a variance that is 4 times smaller than the parts that are illuminated only once. A very similar conclusion can be made for Case-2, i.e. when the illumination's local dose distribution is not uniform. As shown in Fig. 3.6a and Fig. 3.6c, the variance of both algorithms agree with the CRLB given in Fig. 3.2b and is inversely proportional to the local illumination power given in Fig. 3.2a5.

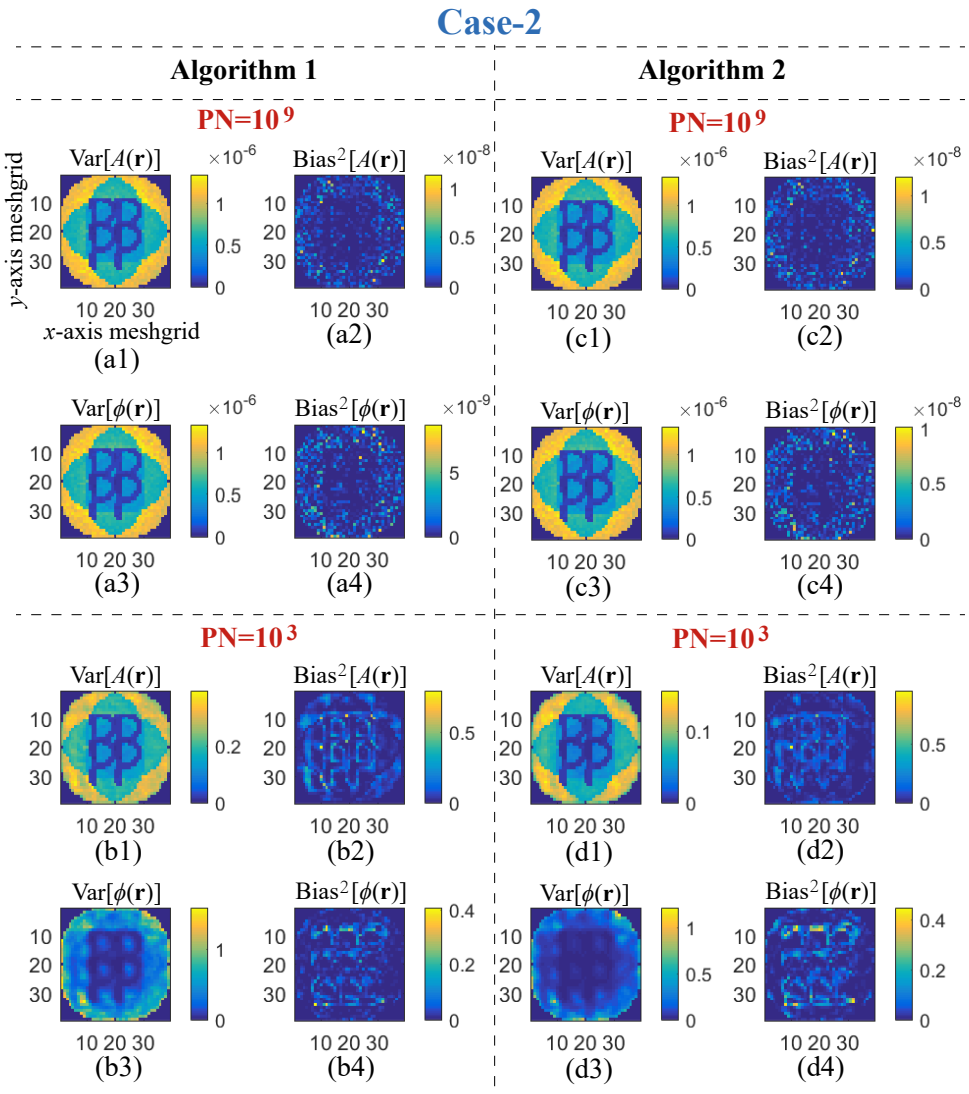

Figure 3.6: The Monte Carlo experiment result for Case-2.

When the photon number is low, i.e. PN = 10^3, **Algorithm 2** and **Algorithm 3** behave differently with the current data-set. In particular, we see in Fig. 3.5 and Fig. 3.6 that **Algorithm 2** in fact reaches smaller bias than **Algorithm 3** when the photon number is low. This suggests that the approach based on the maximum likelihood principle can provide less bias than the amplitude-based cost function minimization method. Meanwhile, the variance of the estimator **Algorithm 3** tends to be smaller than **Algorithm 2**. This can be explained from the fact that minimizing the amplitude-based cost function minimization can approximately be regarded as a variance stabilizing de-noising algorithm [5, 6, 12, 16]. On the other hand, the two algorithms share certain properties. For low photon count, both **Algorithm 2** and **Algorithm 3** have lower variance than the CRLB, which indicates they cannot converge to unbiased estimators and cannot reach the CRLB with the current Monte Carlo data-set. More discussion about the case of low photon count is given in Section 3.5.1.

In Fig. 3.5 and Fig. 3.6 we see that the wavefront profile of the probe only appears in the bias of the reconstruction when the photon count is low. The local illumination power determines the bias for Case-3 and Case-4 for PN = 10^3 as well. For higher photon number, e.g. PN = 10^9, there is no trace of the illumination in the bias for Case-3 and only negligible trace of illumination's local power for Case-4. Therefore, we conclude that the illumination's wavefront profile only influence the statistic property of the algorithms when the photon count is low, whereas the illumination's local power always influences the variance.

3.4.2. THE INFLUENCE OF THE OBJECT ON THE VARIANCE AND BIAS

Next we consider Case-3 where the object has a spatially varying amplitude but the phase is uniform and Case-4, where the amplitude is uniform but the phase has variation. In both cases the probe is a plane wave truncated by a circular aperture. We use the object and probe as in Fig. 3.3a and Fig. 3.4a. The Monte Carlo results obtained with **Algorithm 2** and **Algorithm 3** for Case-3 are shown in Fig. 3.7 and for Case 4 in Fig. 3.8.

When PN = 10^9, the variance shown in Fig. 3.7 and Fig. 3.8 agree with the computed CRLB in Fig. 3.3 and Fig. 3.4. To be explicit, the variance of the phase of the object $\phi(\mathbf{r}_\perp)$ is determined by both the object's transmission $A(\mathbf{r}_\perp)$ and the power of the illumination. The part of the object with lower local transmission will have high variance in reconstruction of the phase. On the other hand, the variance of $A(\mathbf{r}_\perp)$ is influenced by the sum of the intensities of the illuminations only. These conclusions are true for both algorithms. Meanwhile, we see that the object itself does not influence the bias of the reconstruction when the photon count is high, which means that both algorithms are unbiased for high photon count.

When the photon number is low, i.e. PN = 10^3, the profile of the variance deviates from the computed CRLB which is given in Section 3.2. This statement is true for both **Algorithm 2** and **Algorithm 3**, and is particularly obvious for $\phi(\mathbf{r}_\perp)$ as shown in Fig. 3.7 and Fig. 3.8. We can see that there is trace of the actual $A(\mathbf{r}_\perp)$ in Fig. 3.7b2 and in Fig. 3.7d2, and trace of the actual $\phi(\mathbf{r}_\perp)$ in 3.8b2 and in Fig. 3.8d2, respectively. This trace indicate that, with the current data-set, both algorithms cannot converge to the CRLB for low photon counts.

Interestingly, although the object's transmission $A(\mathbf{r}_\perp)$ predominately determines

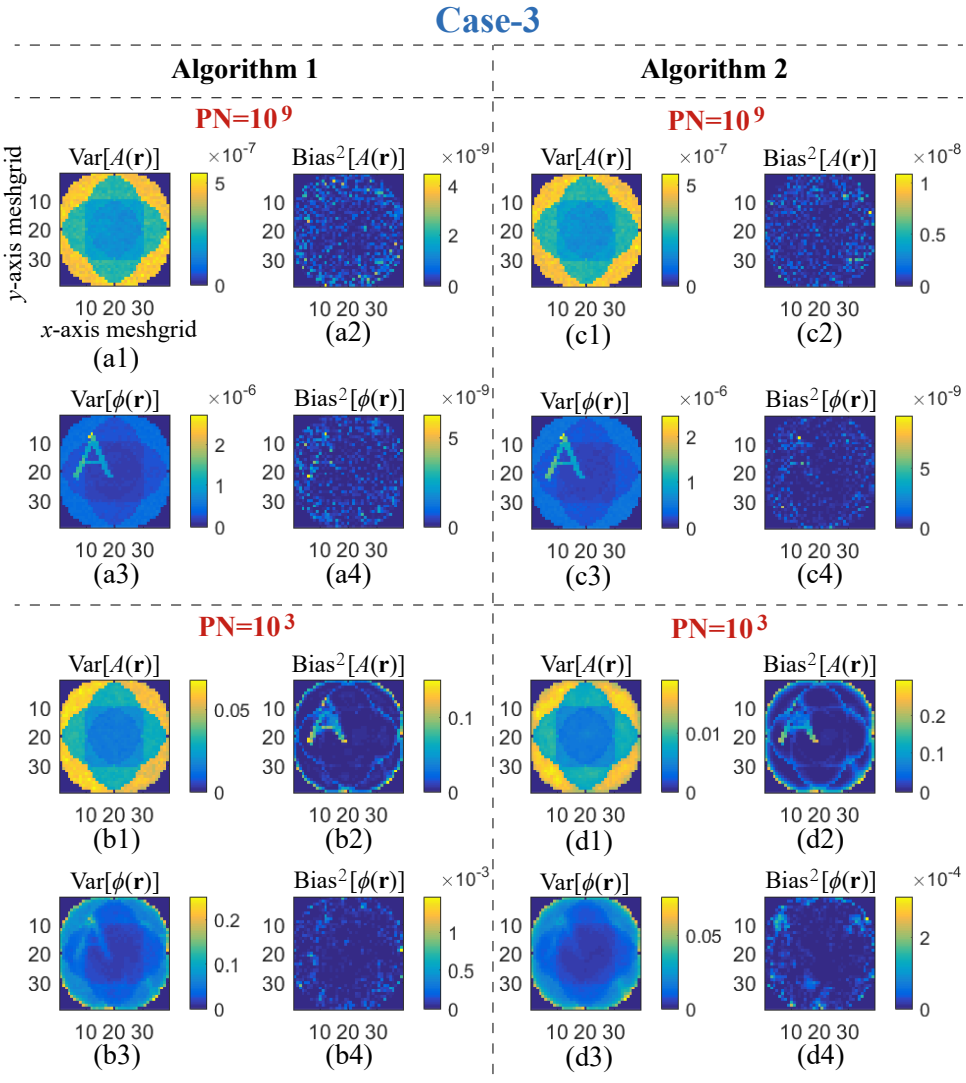

Figure 3.7: The Monte Carlo experiment result for Case-3.

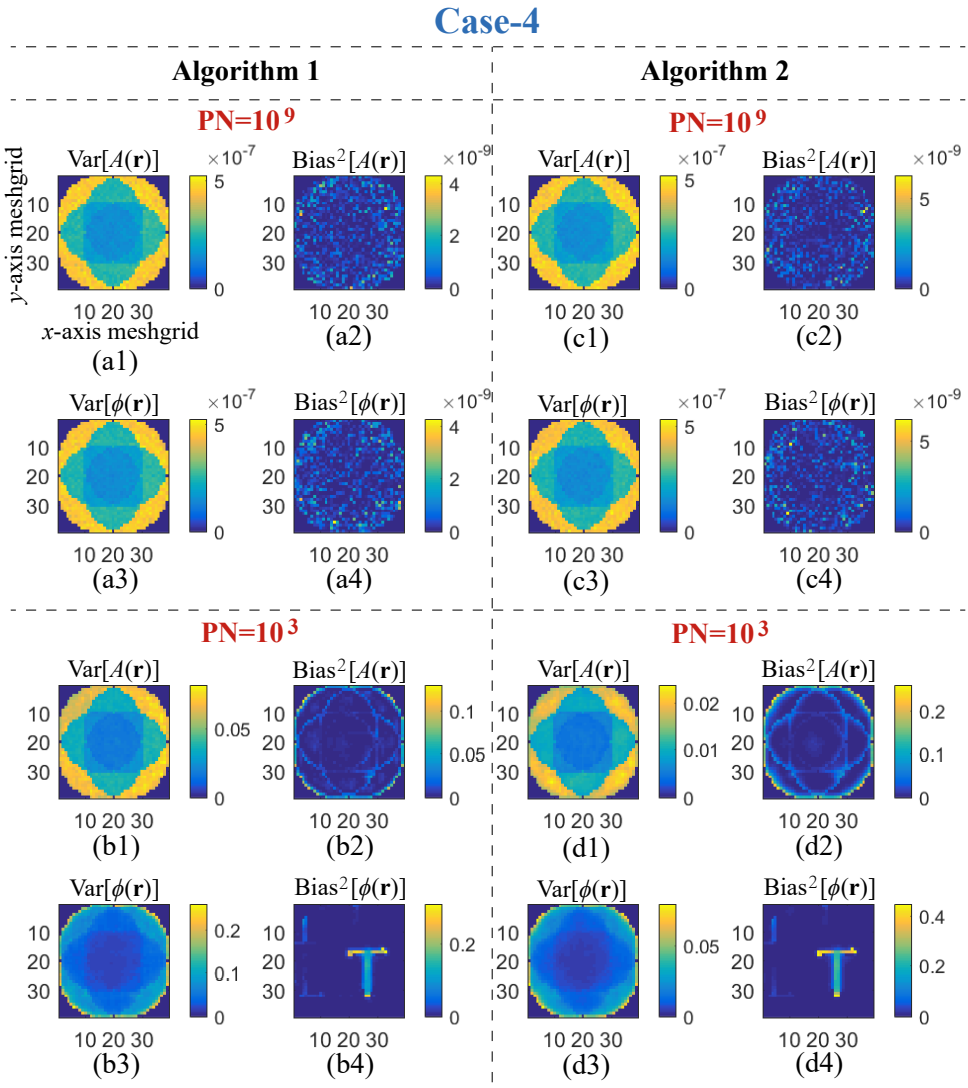

Figure 3.8: The Monte Carlo experiment result for Case-4.

the variance of the object's phase function $\phi(\mathbf{r}_\perp)$, there is no effect of A on the bias of ϕ for any value of PN. In the mean time, we see that ϕ do not influence the bias of A for any value of PN, as shown in Fig. 3.7 and Fig. 3.8. Together with Fig. 3.5 and Fig. 3.6 in the previous section, we conclude that the profile of the illumination and the object have more influence on the variance of the solutions obtained with **Algorithm 2** and **Algorithm 3**, more strongly than on the amount of bias.

3.4.3. THE CRLB, VARIANCE AND BIAS-VARIANCE-RATIO IN PTYCHOGRAPHY

It is seen in Fig. 3.5 - Fig. 3.8 that the ratio of the bias and the variance, as obtained with both algorithms, tend to increase when the photon count is lower. To further investigate this trend and the property of the two algorithms, we define the bias-variance-ratio (BVR) of the estimator $\hat{O}$ by:

$$\mathrm{BVR}\left(\hat{O}\right) = \frac{\sum_{\mathbf{r}_\perp} \mathrm{Bias}^2\left[\hat{O}(\mathbf{r}_\perp)\right]}{\sum_{\mathbf{r}_\perp} \mathrm{Var}\left[\hat{O}(\mathbf{r}_\perp)\right]}. \tag{3.30}$$

In Fig. 3.9 we show the BVR of **Algorithm 2** and **Algorithm 3** for various photon counts and for Case-1 to Case-4. The overall CRLB and variance of $A(\mathbf{r}_\perp)$ and $\phi(\mathbf{r}_\perp)$ obtained from both algorithms are also shown. We see that the overall variance of both algorithms are the same as the computed CRLB asymptotically when the photon number is high. For lower photon counts, the variance become lower than the CRLB, meanwhile the BVR of both algorithms increase. For our current configuration, this threshold is at PN = 10^6. When PN < 10^6, the variance of **Algorithm 2** is higher than **Algorithm 3** for all Case-1 to Case-4. On the other hand, the BVR of **Algorithm 2** is higher than **Algorithm 3**, which indicates that the **Algorithm 2** generally has lower bias than **Algorithm 3**.

3.5. DISCUSSION

3.5.1. DISCUSSION ABOUT IMPROVING THE SUFFICIENCY OF THE PTYCHOGRAPHIC DATA-SET.

It is seen in the Monte Carlo results that, for low photon counts, the variance with both **Algorithm 2** and **Algorithm 3** are lower than the computed CRLB. This observation indicates that, with the current data-set, the two estimators are unbiased for high photon count but cannot converge to the CRLB when the photon count is low.

One may argue that the variances shown in Fig. 3.9 are lower than the CRLB when PN< 10^6 because the current data-set is insufficient [2]. In particular, if sufficient amount of data is given, the maximum likelihood estimator should be asymptotically unbiased and achieves the CRLB if sufficient amount of data is given, as shown in Eq. (3.16). Indeed, we see in the simulation that Eq. (3.16) holds when PN> 10^6, which indicates that the current data-set is already sufficient when PN> 10^6. However, for low photon counts, the current data-set is insufficient for the maximum likelihood estimator to converge to the CRLB.

To explain this fact, we first investigate the signal-to-noise ratio (SNR) of each jth

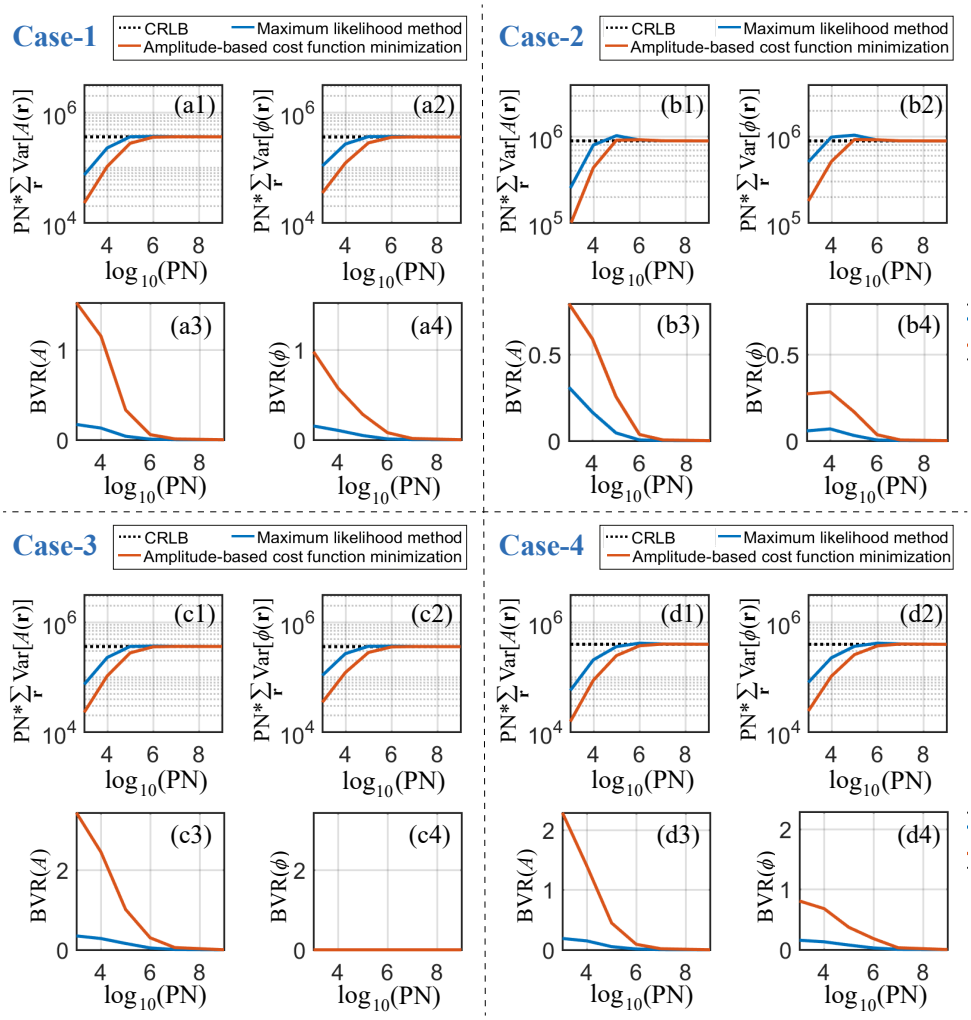

Figure 3.9: The CRLB, variance and bias-variance-ratio of two algorithms for various of values of PN. The value of BVR(ϕ) in (c4) is much smaller than BVR(A) in (c3), which agree with the Monte Carlo result shown in Fig. 3.7b and Fig. 3.7d.

ptychographyic measurement with Poisson noise:

$$\mathrm{SNR}_{P,j}(\mathbf{k}_\perp) = \sqrt{n_j(\mathbf{k}_\perp)}. \tag{3.31}$$

For typical far-field diffraction patterns the intensities are not uniform. Hence, the SNR should be a function of $\mathbf{k}_\perp$ and the value of SNR should vary per pixel on the detector. Nevertheless, we can still see that the SNR will in general decrease when the number of photons detected is decreased. Therefore, for Poisson noise, one can extract less and less information about the actual signal when the photon counts is decreasing.

Moreover, we note that the measurement $n_j(\mathbf{k}_\perp)$ is discrete and contains natural numbers only, which is associated with the particle nature of light leading to a quantization error at the detector. This discreteness has more disruptive effect on the measurement for the case of low photon counts than the case of high photon counts. Taking an extreme example, suppose only one photon is detected, this photon will most likely appear at $\mathbf{k}_\perp = 0$. Therefore, almost all of the spatial information about the object is lost in the measurement, and hence it is more difficult for estimators to converge to the CRLB.

If we want to increase the size of data-set while keeping the current characteristic simulation parameters, one way is to take multiple measurements for each jth probe's position. Suppose for each probe's position we take T measurements, denoted by: $n_{j,t}(\mathbf{k}_\perp)$, where $t = 1, 2, \cdots, T$. A straightforward way to process the data is simply to compute the mean of the measurements:

$$n_j^{(T)}(\mathbf{k}_\perp) = \frac{\sum_t n_{j,t}(\mathbf{k}_\perp)}{T}. \tag{3.32}$$

It has been shown that, when T is large enough, Eq. (3.32) is a sufficient statistic for Poisson distribution. That is, $n_j^{(T)}$ carries all the information as in the data-set: $n_{j,t}$, $t = 1, 2, \cdots, T$. In Fig. 3.10 the Monte Carlo result with data-set $n_{j,t}(\mathbf{k}_\perp)$ is shown. To give an example, we study Case-1 for low photon counts, i.e. PN=10^3. We note that, by summing over all T measurements, the total photon number $\mathrm{PN}^{(T)}$ counting in the probe is now given by:

$$\mathrm{PN}^{(T)} = \frac{\sum_{\mathbf{r}_\perp} |P(\mathbf{r}_\perp)|^2}{\hbar\omega} * T = \mathrm{PN} * T, \tag{3.33}$$

and the CRLB is proportional to the reciprocal of $\mathrm{PN}^{(T)}$ according to Eq. (3.23).

Fig. 3.10a shows the computed CRLB and the variance of reconstruction for various of number of measurements T. We see that, for both two algorithms, the variances approach the CRLB as the number of measurements is increasing. In particular, the variance of **Algorithm 2** have reached the CRLB when T is up to 200. Meanwhile, it is seen in Fig. 3.10b that the bias of **Algorithm 2** is considerably small compared to the variance when $T > 200$. Therefore, we confirm that, for low photon counts, **Algorithm 2** can be asymptotically unbiased and converge to the CRLB by increasing the number of measurements. We see in Fig. 3.10 that this conclusion is true for **Algorithm 3** also. However, the speed of this convergence for **Algorithm 3** is slower than for **Algorithm 2**.

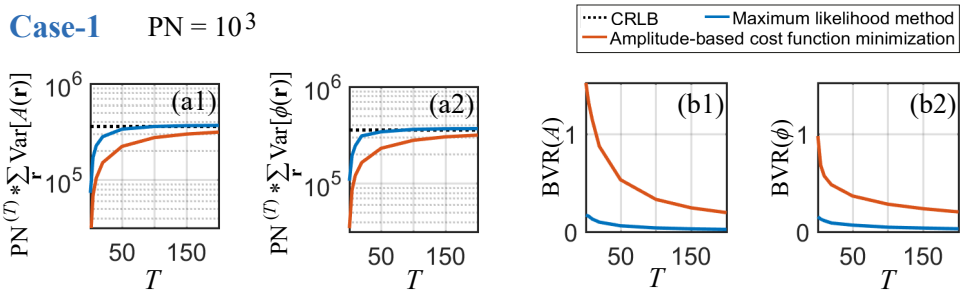

Figure 3.10: The CRLB, variance and bias-variance-ratio of two algorithms for various of number of measurements T. This plot is for Case-1 and for PN= 10^3.

On the other hand, the method proposed in this subsection can be regarded as a way to increase the total photon flux for each probe's positions. This method can be implemented by taking multiple acquisitions (with number T) for each probe's position. In this way, one can illuminate the sample with relatively high photon flux, while avoiding the influence of the limited dynamic range of the detector. Whether there are other approaches to improve the sufficiency of the ptychography data-set is above the scope of this chapter, but the subject will be studied in the future.

3.5.2. COMPARISON WITH THE WIGNER DISTRIBUTION DE-CONVOLUTION METHOD AND DISCUSSION ON THE MINIMIZATION OF THE CRLB

Till now we have investigated the statistic property of the iterative ptychographic algorithms. The Wigner distribution de-convolution (WDD) method [18–21] on the other hand, is an non-iterative ptychographic method and provides an approximate closed-form solution to ptychography. The framework of the WDD method have been introduced in Section 1.2.2, from Eq. (1.71) to Eq. (1.75), and is discussed further in the following. We can regard the ptychographic measurement be a 4D data-set with indices $\mathbf{k}_\perp$ and $\mathbf{R}_{\perp,j}$. By taking the Fourier transform of this 4D data-set w.r.t. $\mathbf{R}_{\perp,j}$ and the inverse Fourier transform w.r.t. $\mathbf{k}_\perp$, we arrive at a 4D array which is denoted by H [18]:

$$H(\mathbf{r}_\perp,\mathbf{K}_\perp) \approx W_O(\mathbf{r}_\perp,\mathbf{K}_\perp)\cdot W_P(\mathbf{r}_\perp,-\mathbf{K}_\perp), \tag{3.34}$$

where W_O and W_P are the Wigner distribution of the object $O(\mathbf{r}_\perp)$ and the probe $P(\mathbf{r}_\perp)$:

$$W_O(\mathbf{r}_\perp,\mathbf{K}_\perp) = \sum_{\tilde{\mathbf{r}}_\perp} O^*(\tilde{\mathbf{r}}_\perp)O(\mathbf{r}_\perp+\tilde{\mathbf{r}}_\perp)\exp(-\mathrm{i}\mathbf{K}_\perp\cdot\tilde{\mathbf{r}}_\perp), \tag{3.35}$$

where $\tilde{\mathbf{r}}_\perp$ is an auxiliary coordinate in object plane. $\mathbf{K}_\perp$ is a 2D coordinate in reciprocal space. Suppose $\mathbf{K}_\perp$ and $\mathbf{R}_{\perp,j}$ are meshed in rectangular grids and have the spacing:

$$\mathbf{K}_\perp = [m_x\Delta K_x, m_y\Delta K_y]^T, \tag{3.36a}$$

$$\mathbf{R}_{\perp,j} = [m_x\Delta R_x, m_y\Delta R_y]^T, \tag{3.36b}$$

where $m_x = 1, \cdots, M_x$ and $m_y = 1, \cdots, M_y$ are the indices of probe position along the x and y direction. The relation of $\mathbf{K}_\perp$ and $\mathbf{R}_{\perp,j}$ is:

$$[\Delta K_x, \Delta K_y]^T = 2\pi[(M_x \Delta R_x)^{-1}, (M_y \Delta R_y)^{-1}]^T. \tag{3.37}$$

Once $H(\mathbf{r}_\perp, \mathbf{K}_\perp)$ has been computed and if we have the knowledge about $P(\mathbf{r}_\perp)$, we can obtain $W_O(\mathbf{r}_\perp, \mathbf{K}_\perp)$ through an element-wise division. When the measurement is noisy or the array W_P contains zero value, this division is replaced by applying Wiener filter. To reconstruct the object O from $W_O(\mathbf{r}_\perp, \mathbf{K}_\perp)$, many strategies have been proposed [18–20]. Note that the resolution obtained through the WDD method equals to the spacing of the scanning step of the probe. Therefore, in order to achieve the same resolution and the same field-of-view as obtained from the iterative ptychographic methods, one needs to take finer scanning steps and to record more diffraction measurements in the WDD scheme. However, the line of thinking of the WDD method may provide an alternative insight of the mechanism of ptychography.

For the WDD scheme, it has been proposed [20] that a probe with a strong curved wavefront or a probe created by a diffuser is preferred in practice. This is because such probes are more evenly distributed over the function $W_P(\mathbf{r}_\perp, \mathbf{K}_\perp)$, hence it is less likely to divide $H(\mathbf{r}_\perp, \mathbf{K}_\perp)$ by zero in Eq. (3.34). For the iterative ptychographic methods, it has been shown experimentally that using such probes can give a more promising reconstruction than using plane wave illumination with a finite support [21, 22]. Indeed, comparing to plane wave illumination, such probes ease up the effect of the limited dynamic range of the detector and meanwhile change the distribution of SNR over the detector plane. However, to the best of our knowledge, it is still inconclusive in theory that whether such probes lead to a more noise-robust scheme in ptychography. This is because: (1) For iterative ptychographic methods, one does not compute the division as given in Eq. (3.34), but instead one updates the reconstruction of the object by applying optimization algorithms, e.g. gradient descent method or alternative projection method. Although regularization techniques are used in iterative ptychographic methods as shown in Supplement section 3.7, the regularization do not directly relates to the spatial-frequency spectrum of the probe. (2) For iterative ptychographic methods, the grid size of the probe's position is determined by the overlap ratio as given in Eq. (4.2.5). It has been reported that the preferred overlap ratio is 60% – 80% [13] so that one can obtain optimal reconstruction in ptychography. Hence, the grid size of the probe's position is smaller than the grid size of the discretized object function. For instance, we have shown in Table. 3.2 that we can reconstruct a 70×70 array object with a 2×2 grid of $\mathbf{R}_{\perp,j}$. Hence, $\mathbf{K}_\perp$ is merely meshed on a 2×2 grid according to Eq. (3.37). If we wish to apply the WDD analysis to this case, it is reasonable to design a probe which maximizes $W_P(\mathbf{r}_\perp, \mathbf{K}_\perp)$ rather than use a probe which has a evenly distributed spatial-frequency spectrum.

Although the computed CRLB and the Monte Carlo results presented in this chapter show that the CRLB is predominantly determined by the local illuminating power and the object's local transmission, we note that the wavefront of the probe may influence the reconstruction. Referring to the first term on the right hand side of Eq. (3.23), we see that the Fisher matrix is a function of the actual object and the complex valued probe. Therefore, for a certain object, it is possible to engineer the probe so that the CRLB is minimized. This minimization process can be done numerically because the CRLB is

obtained by computing the inverse of the Fisher matrix. It is likely that for different shape of object we will arrive at different design of the probe. This optimization of the CRLB is out of the scope of this chapter but is certainly an interesting subject which deserves further research.

3.6. CONCLUSION

In the first part of this chapter we have studied the influence of Poisson noise on ptychography by analyzing the CRLB. The CRLB was theoretically derived and numerically computed from the Fisher matrix for 4 different cases. It was found that if the estimator is unbiased, the minimum variance in the presence of Poisson noise is mostly determined by both the illumination's local dose distribution and the object's local transmission. The calculations of the CRLB indicate that the minimum variance is inversely proportional to the number of photons in the illumination beam. The computations of the CRLB using the Fisher matrix were validated with Monte Carlo analysis. It was confirmed that the local illumination power has a strong effect on the variance of the reconstruction of both object's transmission and phase function. Meanwhile the object's actual local transmission strongly influences the reconstruction of the object's phase.

In the second part of this work, the statistical properties of the maximum likelihood method and the amplitude-based cost function minimization algorithm are studied. Both algorithms were applied in the Monte Carlo simulations, using a conjugate gradient based implementation. It was shown that both approaches are asymptotically unbiased with variances that are slightly larger than the CRLB when the photon counts are high. For the case of lower photon number, the Monte Carlo analysis showed that both methods require more measurement to converge to the CRLB. While increasing the number of data, it was shown that the maximum likelihood method converges to the CRLB faster than the amplitude-based cost function minimization algorithm.

Our result can help to understand the defects that occur in the ptychograghy reconstruction from noisy data. Our conclusions suggest that more illumination power should be given to the part of object which is of most interest, although this may be difficult to realize in a practical ptychography experiment. As next steps of research, the performance of other ptychographic de-noising algorithm [23–27] deserve further investigation. Investigating the CRLB and the statistic properties of the two algorithms for Gaussian noise and the mixed Poisson-Gaussian noise is also an interesting topic for further research.

3.7. SUPPLEMENT

The detail of **Algorithm 2** is described in the pseudo-code. Unlike Eq. (3.12), the update step size β is not a constant anymore in **Algorithm 2**. Instead, an optimal β for every iteration n is obtained in the manner described in [28]: (1) Based on the computed kth local gradient, calculate the value of the likelihood function $\mathscr{L}_P$ for at least three different values of β, e.g. [0.01,0.5,1]. (2) Approximate $\mathscr{L}_P$ by a quadratic function of β. To do this we apply the 'polyfit' routine in MATLAB. (3) Choose the value for β for which the quadratic function is minimum. The parameter β_n is chosen such that the update direction of the object function is conjugate between two subsequent iterations, for which many propos-

Algorithm 2 Maximum likelihood method with Poisson noise

$\text{iter}_{\max} = 10^3$, $\delta_{\mathscr{L}} = 10^{-20}$, $\gamma = 10^{-5}$, $A_1 = A_{\text{o}}$, $\phi_1 = \phi_{\text{o}}$, $n = 1$.
repeat
  compute the steepest descent gradient of A and ϕ using Eq. (3.12):
  $g_{A,n} = \sum_j -\Re\left\{P_j^* e^{-\mathrm{i}\phi_n} \mathscr{F}_\perp^{-1}\left[\left(\frac{n_j}{N_j+\gamma} - 1\right)\mathscr{F}_\perp\left(P_j O_n\right)\right]\right\}$,
  $g_{\phi,n} = \sum_j -\Im\left\{P_j^* A_n e^{-\mathrm{i}\phi_n} \mathscr{F}_\perp^{-1}\left[\left(\frac{n_j}{N_j+\gamma} - 1\right)\mathscr{F}_\perp\left(P_j O_n\right)\right]\right\}$.
  if $n = 1$ **then**
    $\Delta_{A,n} = g_{A,n}, \quad \Delta_{\phi,n} = g_{\phi,n}$.
  else
    use the formula of Polak–Ribière:
    $\beta_{A,n}^{\text{PR}} = \frac{\langle (g_{A,n} - g_{A,n-1}) | g_{A,n}\rangle}{\|g_{A,n-1}\|_2^2}$,
    $\beta_{\phi,n}^{\text{PR}} = \frac{\langle (g_{\phi,n} - g_{\phi,n-1}) | g_{\phi,n}\rangle}{\|g_{\phi,n-1}\|_2^2}$,
    $\beta_{A,n} = \max\left(\beta_{A,n}^{\text{PR}}, 0\right), \quad \beta_{\phi,n} = \max\left(\beta_{\phi,n}^{\text{PR}}, 0\right)$,
    compute the conjugate direction:
    $\Delta_{A,n} = g_{A,n} + \beta_{A,n}\Delta_{A,n-1}$,
    $\Delta_{\phi,n} = g_{\phi,n} + \beta_{\phi,n}\Delta_{\phi,n-1}$.
  end if.
  optimize the update step size:
  $\beta_{A,n} = \arg\min_{\beta_A} \mathscr{L}_P\left(A_n + \beta_A \Delta_{A,n}\right)$,
  $\beta_{\phi,n} = \arg\min_{\beta_\phi} \mathscr{L}_P\left(\phi_n + \beta_\phi \Delta_{\phi,n}\right)$.
  update the object function:
  $A_{n+1} = A_n + \beta_{A,n}\Delta_{A,n}, \quad \phi_{n+1} = \phi_n + \beta_{\phi,n}\Delta_{\phi,n}$.
  if $n = 11$ **then**
    $\gamma = 10^{-20}$,
  end if.
  $n = n + 1$.
until $n = \text{iter}_{\max}$ or $\left|\mathscr{L}_{P,n} - \mathscr{L}_{P,n-1}\right| \le \delta_{\mathscr{L}}$.

als exist [29]. Based on the formula of Polak–Ribière [30], we choose $\beta_n = \max\left(\beta_n^{\mathrm{PR}}, 0\right)$, where β_n^{PR} is given by:

$$\beta_n^{\mathrm{PR}} = \frac{\langle \left(g_n - g_{k-1}\right) | g_n \rangle}{\left\| g_{k-1} \right\|_2^2}, \tag{3.38}$$

where g_n is the gradient of $\mathscr{L}_P$ with respect to $O(\mathbf{r}_\perp)$ in the kth iteration. When the calculated β_n^{PR} have negative value, β_n resets the search direction from the conjugate gradient back to the local decent gradient direction, i.e. $\Delta_n = g_n$.

Algorithm 3 Amplitude-based cost function minimization approach

1: $\mathrm{iter}_{\max} = 10^3$, $\delta_{\mathscr{E}} = 10^{-20}$, $\gamma = 10^{-3}$, $A_1 = A_{\mathrm{o}}$, $\phi_1 = \phi_{\mathrm{o}}$, $n = 1$,
2: **repeat**
3: compute the steepest descent gradient of A and ϕ:
$g_{A,n} = \sum_j -\Re\left\{ P_j^* e^{-\mathrm{i}\phi_n} \mathscr{F}_\perp^{-1}\left[\left(\frac{\sqrt{n_j}}{\sqrt{N_j+\gamma}} - 1 \right) \mathscr{F}_\perp\left(P_j O_n\right) \right] \right\}$,
$g_{\phi,n} = \sum_j -\Im\left\{ P_j^* A_n e^{-\mathrm{i}\phi_n} \mathscr{F}_\perp^{-1}\left[\left(\frac{\sqrt{n_j}}{\sqrt{N_j+\gamma}} - 1 \right) \mathscr{F}_\perp\left(P_j O_n\right) \right] \right\}$.
4: follow 4th-10th steps of **Algorithm 2**.
5: optimize the update step size:
$\beta_{A,n} = \arg\min_{\beta_A} \mathscr{E}\left(A_n + \beta_A \Delta_{A,n}\right)$,
$\beta_{\phi,n} = \arg\min_{\beta_\phi} \mathscr{E}\left(\phi_n + \beta_\phi \Delta_{\phi,n}\right)$.
6: follow 12th-16th steps of **Algorithm 2**.
7: **until** $n = \mathrm{iter}_{\max}$ or $|\mathscr{E}_n - \mathscr{E}_{n-1}| \le \delta_{\mathscr{E}}$.

In order to prevent that the algorithm terminates in a local minimum, the initial guess of the object is selected to be the actual object $A_{\mathrm{o}}(\mathbf{r}_\perp)$ and $\phi_{\mathrm{o}}(\mathbf{r})$. The denominator n_j in Eq. (3.12) is a function of $\mathbf{k}_\perp$, and may be close to zero for some $\mathbf{k}_\perp$. Hence the maximum likelihood method can be unstable. To avoid the instability, a regularization parameter γ is introduced in **Algorithm 2**, of which the value can be determined in practice depending on the noise level. Throughout this chapter, we let γ be 10^{-5} (note that n_j is non-negative integer) for the first 10 iterations, then reset γ to 10^{-20} after the 10th iteration. **Algorithm 2** terminates when the change of the likelihood function between two subsequent iterations is smaller than a threshold $\delta_{\mathscr{L}}$, or when the number of iteration reaches a maximum $\mathrm{iter}_{\max}$.

For comparison, the performance of another popular method, namely the amplitude-based cost function minimization approach [15], is investigated in the Monte Carlo experiment. The approach is described in **Algorithm 3**, in which the search of the optimal step size β_n and the method of conjugate gradient are added too. Similar to **Algorithm 2**, **Algorithm 3** stops when the change of the cost function between two subsequent iterations is smaller than a threshold $\delta_{\mathscr{E}}$, or when the number of iteration reaches a maximum $\mathrm{iter}_{\max}$.

Finally, we note that the characteristic parameters shown in the first step of **Algorithm 2** and **Algorithm 3**, i.e. $\mathrm{iter}_{\max}$, γ, $\delta_{\mathscr{L}}$ and $\delta_{\mathscr{E}}$ are chosen through a 'trial and error'

process. For each Monte Carlo simulation, we start with a relative large regularization factor, i.e. $\gamma = 10^{-5}$. After the algorithms have converged, we decrease the value of γ for final refinement. The error tolerance $\delta_{\mathscr{L}}$ and $\delta_{\mathscr{E}}$ are visually determined such that the algorithms are indeed converged. Throughout the simulation, we observed that the most influential factor which may devastate the simulation result is the choice of the initial guess of the object. How to obtain a initial guess which is closed to the actual object is an important issue in practice but is out of the scope of this chapter.

REFERENCES

[1] X. Wei, H. P. Urbach, and W. M. J. Coene, *Cramér-rao lower bound and maximum-likelihood estimation in ptychography with poisson noise,* Physical Review A **102** (2020), 10.1103/physreva.102.043516.

[2] S. M. Kay, *Fundamentals Of Statistical Signal Processing, Volume 1: Estimation Theory* (Pearson, 2009).

[3] J. N. Cederquist and C. C. Wackerman, *Phase-retrieval error: a lower bound,* Journal of the Optical Society of America A **4**, 1788 (1987).

[4] J. R. Fienup, J. C. Marron, T. J. Schulz, and J. H. Seldin, *Hubble space telescope characterized by using phase-retrieval algorithms,* Applied Optics **32**, 1747 (1993).

[5] P. Godard, M. Allain, V. Chamard, and J. Rodenburg, *Noise models for low counting rate coherent diffraction imaging,* Optics Express **20**, 25914 (2012).

[6] P. Thibault and M. Guizar-Sicairos, *Maximum-likelihood refinement for coherent diffractive imaging,* New Journal of Physics **14**, 063004 (2012).

[7] J. Goodman, *Introduction to Fourier Optics*, McGraw-Hill physical and quantum electronics series (W. H. Freeman, 2005).

[8] X. Wei and P. Urbach, *Ptychography with multiple wavelength illumination,* Optics Express **27**, 36767 (2019).

[9] M. Odstrčil, A. Menzel, and M. Guizar-Sicairos, *Iterative least-squares solver for generalized maximum-likelihood ptychography,* Optics Express **26**, 3108 (2018).

[10] W. Murray, M. H. Wright, and P. E. Gill, *Practical Optimization* (Emerald Publishing Limited, 1982).

[11] D. Bouchet, R. Carminati, and A. P. Mosk, *Influence of the local scattering environment on the localization precision of single particles,* Physical Review Letters **124** (2020), 10.1103/physrevlett.124.133903.

[12] Y. Zhang, P. Song, and Q. Dai, *Fourier ptychographic microscopy using a generalized anscombe transform approximation of the mixed poisson-gaussian likelihood,* Optics Express **25**, 168 (2017).

[13] O. Bunk, M. Dierolf, S. Kynde, I. Johnson, O. Marti, and F. Pfeiffer, *Influence of the overlap parameter on the convergence of the ptychographical iterative engine,* Ultramicroscopy **108**, 481 (2008).

[14] A. Tripathi, I. McNulty, and O. G. Shpyrko, *Ptychographic overlap constraint errors and the limits of their numerical recovery using conjugate gradient descent methods,* Optics Express **22**, 1452 (2014).

[15] M. Guizar-Sicairos and J. R. Fienup, *Phase retrieval with transverse translation diversity: a nonlinear optimization approach,* Optics Express **16**, 7264 (2008).

[16] M. S. Bartlett, *The square root transformation in analysis of variance,* Supplement to the Journal of the Royal Statistical Society **3**, 68 (1936).

[17] F. J. Anscombe, *The transformation of poisson, binomial and negative-binomial data,* Biometrika **35**, 246 (1948).

[18] J. M. Rodenburg and R. H. T. Bates, *The theory of super-resolution electron microscopy via wigner-distribution deconvolution,* Philosophical Transactions of the Royal Society of London. Series A: Physical and Engineering Sciences **339**, 521 (1992).

[19] H. N. Chapman, *Phase-retrieval x-ray microscopy by wigner-distribution deconvolution,* Ultramicroscopy **66**, 153 (1996).

[20] P. Li, T. B. Edo, and J. M. Rodenburg, *Ptychographic inversion via wigner distribution deconvolution: Noise suppression and probe design,* Ultramicroscopy **147**, 106 (2014).

[21] M. Guizar-Sicairos, M. Holler, A. Diaz, J. Vila-Comamala, O. Bunk, and A. Menzel, *Role of the illumination spatial-frequency spectrum for ptychography,* Physical Review B **86** (2012), 10.1103/physrevb.86.100103.

[22] M. Odstrčil, M. Lebugle, M. Guizar-Sicairos, C. David, and M. Holler, *Towards optimized illumination for high-resolution ptychography,* Optics Express **27**, 14981 (2019).

[23] Z. Wen, C. Yang, X. Liu, and S. Marchesini, *Alternating direction methods for classical and ptychographic phase retrieval,* Inverse Problems **28**, 115010 (2012).

[24] R. Horstmeyer, R. Y. Chen, X. Ou, B. Ames, J. A. Tropp, and C. Yang, *Solving ptychography with a convex relaxation,* New Journal of Physics **17**, 053044 (2015).

[25] A. Maiden, D. Johnson, and P. Li, *Further improvements to the ptychographical iterative engine,* Optica **4**, 736 (2017).

[26] A. P. Konijnenberg, W. M. J. Coene, and H. P. Urbach, *Model-independent noise-robust extension of ptychography,* Optics Express **26**, 5857 (2018).

[27] M. Pham, A. Rana, J. Miao, and S. Osher, *Semi-implicit relaxed douglas-rachford algorithm (sDR) for ptychography,* Optics Express **27**, 31246 (2019).

[28] W. Coene, A. Thust, M. O. de Beeck, and D. V. Dyck, *Maximum-likelihood method for focus-variation image reconstruction in high resolution transmission electron microscopy,* Ultramicroscopy **64**, 109 (1996).

[29] R. Fletcher, *Practical Methods of Optimization, 2nd Edition* (Wiley, 1988).

[30] J. R. Shewchuk, *An Introduction to the Conjugate Gradient Method Without the Agonizing Pain,* Tech. Rep. (Carnegie Mellon University, 1994).

4

PARAMETER RETRIEVAL OF SMALL PARTICLES IN DARK-FIELD FOURIER PTYCHOGRAPHY AND A RECTANGLE IN REAL-SPACE PTYCHOGRAPHY

Parts of this chapter have been published in Ultramicroscopy **229**, 113335 (2021) [1].

4.1. INTRODUCTION

According to Section 1.1.3, the ptychographic measurement $I_j(\mathbf{k}'_\perp)$ is commonly recorded by a 2D detector, e.g. a charge-coupled device (CCD). Therefore $\mathbf{k}'_\perp$ is a discretized grid and is meshed according to the distance z and the size of pixel of the detector. The retrieved object function, denoted by $\hat{O}$, is also on a discretized grid $\mathbf{r}_\perp$. $\mathbf{r}_\perp$ and $\mathbf{k}'_\perp$ have the relation:

$$\left[\Delta x, \Delta y\right]^T = 2\pi \left[(N_x^{\text{det}} \Delta k'_x)^{-1}, (N_y^{\text{det}} \Delta k'_y)^{-1}\right]^T, \tag{4.1}$$

where Δx and Δy are the spacing of a single grid cell in x-axis and y-axis, respectively, and $\Delta k'_x$ and $\Delta k'_y$ are the spacing of a grid cell in k_x and k_y, respectively. Note that the total field-of-view (FoV) in the object plane is:

$$\text{FoV} = \left[N_x \Delta x, N_x \Delta y\right]^T, \tag{4.2}$$

where $N_x > N_x^{\text{det}}$ and $N_y > N_y^{\text{det}}$ due to that ptychography is a scanning imaging technique which provides an extended FoV. In line with this extended FoV, we have the effective spacing of the grid cell in the reciprocal space:

$$\left[\Delta k_x, \Delta k_y\right]^T = \left[(N_x)^{-1} N_x^{\text{det}} \Delta k'_x, (N_y)^{-1} N_y^{\text{det}} \Delta k'_y\right]^T. \tag{4.3}$$

We can see that, when the influence of noise is negligible, the relation given in Eq. (4.1) imposes a resolution limit to the reconstruction in ptychography. To overcome this limit, several 'superresolution' methods have been proposed [2–4]. One of the ideas lying behind these methods is to impose additional *a priori* knowledge about the object, e.g. analytic continuation of the Fourier transform of bounded support [5–7] or sparsity [3, 4], to the algorithm. In this paper we show a parameter retrieval algorithm which incorporates additional *a priori* knowledge about the object into ptychography. We present this algorithm by numerically demonstrating two applications:

(1) Parameter retrieval of sub-wavelength particles using Fourier ptychography with dark field measurements only. For this example the configuration is in line with the 'Rapid-Nano' particle scanner developed by TNO [8, 9]. The particle scanner is supposed to detect nano-particles on an EUV reticle. Since only dark field images are recorded in the scanner, the part of the spatial spectrum of the object in the neighborhood of $|\mathbf{k}_\perp| = 0$ is lost. The missing data can in principle be filled in by analytic continuation using the fact that the object has bounded support, however, this method is unstable with noisy measurement and leads in practice to incorrect reconstructions [7, 10]. However. as shown in Section 4.2, the proposed parameter retrieval algorithm is able to extract information of sub-wavelength particles from the incomplete data.

(2) Parameter retrieval of rectangular objects using real-space ptychography. This example comes from practical applications in semiconductor industry where we often want to measure the transmission, the width and the position of the rectangules on flat substrates [11, 12]. We demonstrate the proposed parameter retrieval method for this application in Section 4.3.

To study the influence of Poisson noise on the proposed parameter retrieval scheme, we compute the Cramér Rao Lower Bound (CRLB) and perform Monte Carlo analysis for both two applications in the second part of this paper. We derive the general form of the Fisher information matrix in Section 4.4. For application 1, the calulated CRLB and Monte Carlo result are shown in Section 4.5. For application 2, the discussion about the correlation of the parameters of the rectangular structure can be found in Section 4.6.

4.2. APPLICATION 1: PARAMETER RETRIEVAL OF SUB-WAVELENGTH PARTICLES USING FOURIER PTYCHOGRAPHY WITH DARK FIELD MEASUREMENT

4.2.1. DESCRIPTION OF THE 'RAPIDNANO 3' PARTICLE SCANNER

The 'RapidNano 3' particle scanner [8, 9] is designed to detect small dielectric particles on a flat substrate. The particles are made of polystyrene latex (PSL) beads and the typical diameter of the particle is $\sim 50nm$. The scanner has detection limit of 42 nm PSL particles, i.e. the capture rate is 95% at this size. Note that the particles on the substrate can be any material and PSL is only the calibration standard. The particles are sparsely distributed on the sample mostly. The substrate is reflective, made of silicon, and its lateral size can be up to 6x6 inch, i.e. the size of an EUV mask. The illumination is a $532nm$, p-polarized, fully coherent plane wave laser beam. The incident angle of the illumination is 60 degree, with 9 regularly distributed azimuth incident directions around 360 degree. The numerical aperture(NA) of the objective lens is 0.4, therefore the measurement is a dark field image of the sample as is illustrated in Fig. 4.1.

4.2.2. SINGLE DIPOLE RADIATION

Considering that the diameter of the detected particles is around 10 times smaller than the illumination wavelength, we begin by using the dipole radiation formula to model the wavefield scattered by the particles. Suppose that there are N dipoles in the plane $z = 0$, and the ith oscillating dipole is located at position $\mathbf{r}_i = \left[\mathbf{r}_{\perp,i}, 0\right]^T, i = 1, 2, \cdots, N$, and is excited by an incident plane wave $\mathbf{E}_{\text{in},j}$:

$$\mathbf{E}_{\text{in},j} = A_{\text{in}} e^{i\mathbf{k}_j \cdot \mathbf{r}} \hat{\mathbf{e}}_p(\mathbf{k}_j) = A_{\text{in}} e^{i\mathbf{k}_{\perp,j} \cdot \mathbf{r}_\perp} \hat{\mathbf{e}}_p(\mathbf{k}_j), \tag{4.4}$$

where A_{in}^2 is proportional to the illumination power and $\hat{\mathbf{e}}_p(\mathbf{k}_j)$ denotes the polarization direction.

For the ith dipole with position $\mathbf{r}_{\perp,i}$, we denote the dipole moment by:

$$\mathbf{p}_{i,j} = \alpha_i \mathbf{E}_{\text{in},j} = \alpha_i A_{\text{in}} e^{i\mathbf{k}_{\perp,j} \cdot \mathbf{r}_{\perp,i}} \hat{\mathbf{e}}_p(\mathbf{k}_j), \tag{4.5}$$

where ϵ_0 is the permittivity of free space and α_i is the polarisability of the particle. For a dielectric sphere with diameter d, the dipole moment $\mathbf{p}_{i,j}^{\text{sphere}}$ in the quasi-static approximation is given by:

$$\mathbf{p}_{i,j}^{\text{sphere}} = \left(\frac{\epsilon_r - 2}{\epsilon_r + 1}\right) d_i^3 \mathbf{E}_{\text{in},j}, \tag{4.6}$$

where $\epsilon_r = n_{\mathrm{PSL}}^2$ is the relative permittivity of the dielectric. n_{PSL} is the refractive index of the small particles. Since the real part of n_{PSL} is $\sim 10^6$ times larger than the imaginary part, i.e. than the absorption index, we assume the α_i is real valued for the rest of this paper. We see that α_i is proportional to the volume of the dielectric particle.

The electric field radiating from the ith dipole due to the jth illumination is given by [13, 14]:

$$\mathbf{E}_{\mathrm{scat},i,j} = \overleftrightarrow{\mathbf{G}}(\mathbf{r},\mathbf{r}_i)\,\mathbf{p}_{i,j}, \tag{4.7}$$

where $\overleftrightarrow{\mathbf{G}}(\mathbf{r},\mathbf{r}_i)$ is the dyadic Green's function:

$$\overleftrightarrow{\mathbf{G}}(\mathbf{r},\mathbf{r}_i) = \frac{k^2}{4\pi\epsilon_0}\left(\overleftrightarrow{\mathbf{I}} + \frac{1}{k^2}\nabla\nabla\right)\frac{e^{\mathrm{i}k|\mathbf{r}-\mathbf{r}_i|}}{|\mathbf{r}-\mathbf{r}_i|}, \tag{4.8}$$

where $\overleftrightarrow{\mathbf{I}}$ is the 3×3 identity matrix. Considering that the detector of the particle scanner is insensitive to the polarization state and that the NA of the objective lens is 0.4, we ignore the effect of the polarization of the wavefield for simplicity. Hence we arrive at a scalar scattered amplitude given by:

$$E_{\mathrm{scat},i,j} = A_{\mathrm{in}}k^2\alpha_i e^{\mathrm{i}\mathbf{k}_{\perp,j}\cdot\mathbf{r}_{\perp,i}}G(\mathbf{r},\mathbf{r}_i), \tag{4.9}$$

where

$$G(\mathbf{r},\mathbf{r}_i) = \frac{k^2}{4\pi\epsilon_0}\frac{e^{\mathrm{i}k|\mathbf{r}-\mathbf{r}_i|}}{|\mathbf{r}-\mathbf{r}_i|}. \tag{4.10}$$

4.2.3. DARK FIELD MEASUREMENT FROM THE PARTICLE SCANNER

By Fourier transforming Eq. (4.9) with respect to $\mathbf{r}_\perp$, we have:

$$\mathscr{F}\left(E_{\mathrm{scat},i,j}\right)(\mathbf{k}_\perp,z) = A_{\mathrm{in}}k^2\frac{e^{\mathrm{i}k_z|z|}}{8\mathrm{i}\pi\epsilon_0 k_z}\alpha_i e^{-\mathrm{i}\mathbf{r}_{\perp,i}\cdot(\mathbf{k}_\perp-\mathbf{k}_{\perp,j})}. \tag{4.11}$$

$\mathscr{F}\left(E_{\mathrm{scat},i,j}\right)$ can be regarded as the 2D spatial spectrum of the scattered wavefield in the plane z. The wavefield passes through the imaging system and forms an image in the image plane. The imaging system acts as a low-pass filter as given in [15]. The detector measures the low-pass filtered image of the sample, i.e. the field in the plane $z\to 0$. We therefore let $e^{\mathrm{i}k_z|z|}\approx 1$ for this moment. The low-passed wavefield at the exit pupil is given by:

$$\mathscr{F}\left(E_{\mathrm{scat},i,j}\right)_{\mathrm{exit}}(\mathbf{k}_\perp) = \mathbf{1}_{k\mathrm{NA}}(\mathbf{k}_\perp)\frac{A_{\mathrm{in}}k^2}{8\mathrm{i}\pi\epsilon_0 k_z}\alpha_i e^{-\mathrm{i}\mathbf{r}_{\perp,i}\cdot(\mathbf{k}_\perp-\mathbf{k}_{\perp,j})}, \tag{4.12}$$

where $\mathbf{1}_{k\mathrm{NA}}(\mathbf{k}_\perp)$ represents the numerical aperture of the objective lens:

$$\mathbf{1}_{k\mathrm{NA}}(\mathbf{k}_\perp) = \begin{cases} 1, & |\mathbf{k}_\perp| \le k\mathrm{NA}, \\ 0, & |\mathbf{k}_\perp| > k\mathrm{NA}. \end{cases} \tag{4.13}$$

By summing over all the dipoles, we find the total field in the exit pupil, which is denoted by Ψ_j:

$$\begin{aligned}\Psi_j(\mathbf{k}_\perp) &= \sum_i \mathscr{F}\left(E_{\text{scat},i,j}\right)_{\text{exit}}(\mathbf{k}_\perp) \\ &= \mathbf{1}_{k\text{NA}}(\mathbf{k}_\perp)\frac{A_{\text{in}}k^2}{8\mathrm{i}\pi\epsilon_0 k_z}\sum_i \alpha_i e^{-\mathrm{i}\mathbf{r}_{\perp,i}\cdot(\mathbf{k}_\perp-\mathbf{k}_{\perp,j})} \\ &= Q(\mathbf{k}_\perp)\cdot O(\mathbf{k}_\perp-\mathbf{k}_{\perp,j}),\end{aligned} \tag{4.14}$$

where

$$Q(\mathbf{k}_\perp,z) = \mathbf{1}_{k\text{NA}}(\mathbf{k}_\perp)\frac{A_{\text{in}}k^2}{8\mathrm{i}\pi\epsilon_0 k_z}, \tag{4.15}$$

and $O(\mathbf{k}_\perp)$ is the Fourier transform of the object defined by

$$O(\mathbf{k}_\perp) = \sum_i \alpha_i e^{-\mathrm{i}\mathbf{k}_\perp\cdot\mathbf{r}_{\perp,i}}. \tag{4.16}$$

Note that the object function is assumed to be independent of the angle of incidence, i.e. the only effect of the tilted illumination is the shift of the Fourier transform of the object function over the pupil plane. Finally, by inverse Fourier transforming Ψ_j and taking the squared modulus, we arrive at the expression for the measured intensity in the detector plane:

$$\begin{aligned}I_j(\mathbf{r}'_\perp) &= \left|\mathscr{F}^{-1}\left(\Psi_j\right)\right|^2(\mathbf{r}'_\perp) \\ &= \left|\mathscr{F}^{-1}\left[Q(\mathbf{k}_\perp+\mathbf{k}_{\perp,j})\cdot O(\mathbf{k}_\perp)\right]\right|^2(\mathbf{r}'_\perp),\end{aligned} \tag{4.17}$$

where $\mathbf{r}'_\perp$ is the 2D regular grid.

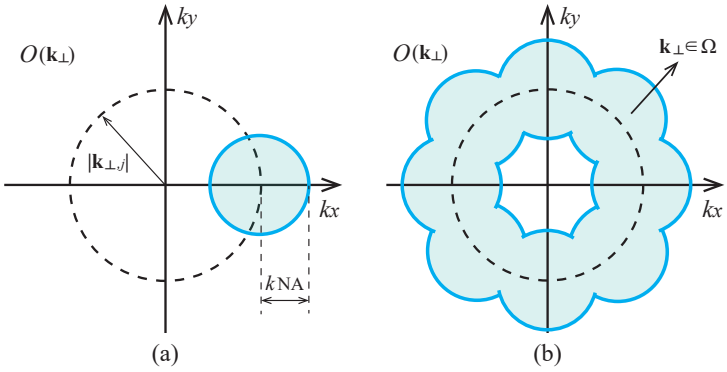

Figure 4.1: Graphical illustration of $O(\mathbf{k}_\perp)$. (a) The blue disk is defined by $\mathbf{1}_{k\text{NA}}(\mathbf{k}_\perp)$ and indicates information about O included in the single measurement $I_j(\mathbf{r}'_\perp)$. (b) The retrievable part of O from all given dark field measurements.

For the configuration of the particle scanner, $\left|\mathbf{k}_{\perp,j}\right|$ is fixed and equal to $k\sin(\frac{\pi}{3})$. This incident angle have been chosen in [8, 16], where the simulations show that ratio between the scattering amplitude of the particles and the background substrate is

maximized. In this paper we keep the value of $|\mathbf{k}_{\perp,j}|$ be $k\sin(\frac{\pi}{3})$, but the value can be varied which is regarded as a potential subject in the future. The NA of the objective lens is ~ 0.4. Therefore, the intensity measurements do not contain any information about $O(\mathbf{k}_\perp = 0)$ and its surrounding region, as shown in Fig. 4.1. The blue shaded area in Fig. 4.1(a) illustrates the information about $O(\mathbf{k}_\perp)$ included in the single measurement $I_j(\mathbf{r}'_\perp)$, while the blue shaded area in Fig. 4.1(b) represents the retrievable information from all measurements. We denote this retrievable part of O by $\mathbf{1}_\Omega O(\mathbf{k}_\perp)$:

$$\mathbf{1}_\Omega(\mathbf{k}_\perp) = \begin{cases} 1, & \mathbf{k}_\perp \in \Omega, \\ 0, & \mathbf{k}_\perp \notin \Omega, \end{cases} \tag{4.18}$$

where Ω is the blue shaded region in Fig. 4.1(b).

4

4.2.4. RETRIEVING THE PARAMETERS OF THE PARTICLES

To retrieve α_i and the position $\mathbf{r}_{\perp,i}$ of the dipoles, we first reconstruct the complex valued function $\mathbf{1}_\Omega O(\mathbf{k}_\perp)$ in the pupil plane from the set of intensity measurements $I_j(\mathbf{r}'_\perp)$. This can be done by applying a ptychographic algorithm. For noisy measurements, one may use the Maximum Likelihood estimator (MLE) if one can find a dominant noise model [17, 18]. For the case of Poisson noise, we can apply gradient descent methods [19, 20] to minimize the likelihood function $\mathscr{L}_P$ given by Eq. (3.8) in the Supplement. We use the MLE ptychographic algorithm which is given in [21] in the simulation and use $\mathbf{1}_\Omega \hat{O}(\mathbf{k}_\perp)$ to denote the reconstruction obtained by the ptychographic method.

Once $\mathbf{1}_\Omega \hat{O}(\mathbf{k}_\perp)$ is obtained, we apply the method of least square to estimate α_i and $\mathbf{r}_{\perp,i}$ of all dipoles. The number of freedom in this problem is $N\times 3$, where N is the number of dipoles within the field-of-view (FoV). Note that if α_i is complex valued, the degrees of freedom should be $N\times 4$. When N is in the order of $10^0 \sim 10^1$, we have much less degrees of freedom than in the traditional Fourier ptychography problem.

Our proposed parameter retrieval algorithm is shown in the following.

(1) Use the MLE ptychographic algorithm to retrieve the complex valued wavefield $\mathbf{1}_\Omega O(\mathbf{k}_\perp)$ in the pupil plane.

(2) From all the dark field intensity measurements, find the lower and upper bound of α_i and $\mathbf{r}_{\perp,i}$ for $i = 1,2,\cdots,N$. These bounds are denoted by: α_i^l, α_i^u, $\mathbf{r}_{\perp,i}^l$ and $\mathbf{r}_{\perp,i}^u$.

(3) Solve the following problem:

$$\begin{aligned} \arg\min_{\alpha_i,\mathbf{r}_{\perp,i}} & \left\| \mathbf{1}_\Omega \hat{O}(\mathbf{k}_\perp) - \sum_i \alpha_i e^{-i\mathbf{k}_\perp\cdot\mathbf{r}_{\perp,i}} \right\|^2_{\mathbf{k}_\perp\in\Omega}, \\ \text{subject to } & \alpha_i^l \le \alpha_i \le \alpha_i^u, \qquad i = 1,2,\cdots,N, \\ & \mathbf{r}_{\perp,i}^l \preceq \mathbf{r}_{\perp,i} \preceq \mathbf{r}_{\perp,i}^u, \quad i = 1,2,\cdots,N, \end{aligned} \tag{4.19}$$

where $\preceq$ denotes vector inequality: $\mathbf{r}_\perp^l \preceq \mathbf{r}_\perp^u$ means $x^l \le x^u$ and $y^l \le y^u$.

Table 4.1: Configuration settings in the simulation

illumination			imaging system	
wavelength	incident angle		NA	magnification
$500nm$	60 degree		0.4	20
detector			grid spacing in object plane	
pixel size	pixel number	FoV	Δx and Δy	
$5\mu m$	200×200	$50\mu m$	$133.3nm$	

4.2.5. SIMULATION

To validate the proposed parameter retrieval algorithm, a preliminary simulation is reported in this section. The configuration is drawn in Fig. 4.2 and the parameter settings of the setup is described in Table 4.1. Since the NA of the imaging system is smaller than $\left|\mathbf{k}_{\perp,j}\right|$, the measurements at the detector plane are always dark field images. We assume that the detector is insensitive to the polarization state of the wavefield.

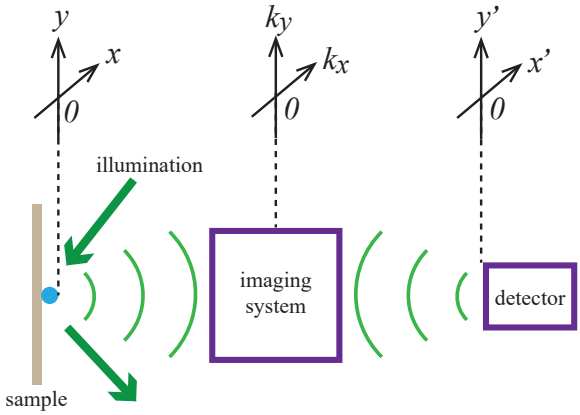

Figure 4.2: Illustration of the setup of application 1. The incident angle of the illumination is 60 degree, with multiple azimuth incident directions around 360 degree.

The simulated sample consists of two dipoles. The actual scattering strength α_i and the position $\mathbf{r}_{\perp,i}$ of the dipoles are listed in Table 4.2. Based on these given parameters, we first construct the actual complex valued function $\mathbf{1}_\Omega O(\mathbf{k}_\perp)$ according to Eq. (4.15). The dark field intensity measurements are noise-free and computed in accordance with Eq. (4.17). In line with the 1st step of the proposed method given in Section 4.2.4, the reconstructed object function, denoted by $\mathbf{1}_\Omega \hat{O}(\mathbf{k}_\perp)$, is obtained by applying the Fourier ptychography method. We assume that the function $Q(\mathbf{k}_\perp + \mathbf{k}_{\perp,j})$ is known and we ignore the polarization state. In the simulation we notice that only 9 incident plane waves cannot provide sufficient data redundancy. The percentage of sufficient data redundancy have been reported in ptychography literature when the illumination is bounded by circular support [22]. Suppose the diameter of the circular support is L, and the distance between adjacent illumination positions is denoted by $d \in [0, L]$. The overlap ratio is

defined by: $1-\frac{d}{L}$, which is usually be assigned from 60% to 85% to achieve optimal performance [22, 23]. In this simulation we use 36 plane waves, instead of 9, with regularly distributed azimuth incident directions around 360 degrees, which means the overlap ratio is 81.13%. The actual function O and the reconstructed one are shown in Fig. 4.3(a) and Fig. 4.3(b), respectively. Fig. 4.3(c) illustrates the illuminated area in the reciprocal space, i.e. $\sum_j \mathbf{1}_{k\mathrm{NA}}(\mathbf{k}_\perp+\mathbf{k}_{\perp,j})$, for 9 and 36 dark field measurements, respectively.

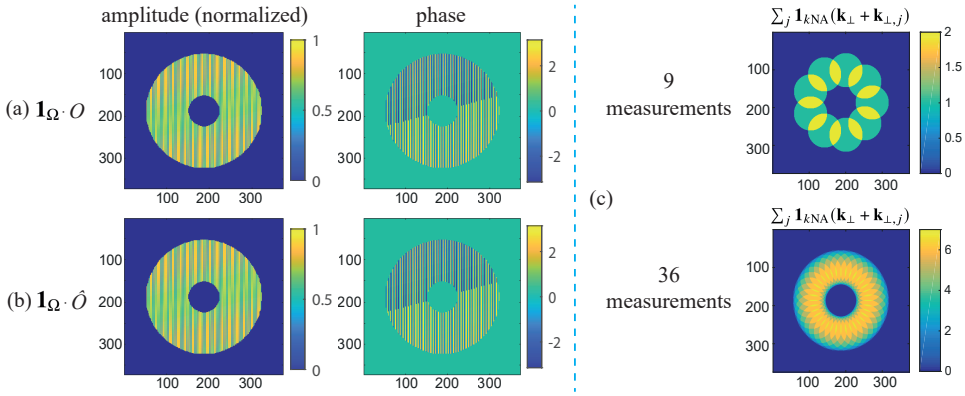

Figure 4.3: (a) The amplitude and phase of the actual complex function $\mathbf{1}_\Omega O(\mathbf{k}_\perp)$. (b) The amplitude and phase of $\mathbf{1}_\Omega O(\mathbf{k}_\perp)$ which is reconstructed from the Fourier ptychographic algorithm. (c) Illustration of the illuminated area in the reciprocal space, i.e. $\sum_j \mathbf{1}_{k\mathrm{NA}}(\mathbf{k}_\perp+\mathbf{k}_{\perp,j})$, for 9 and 36 dark field measurements, respectively

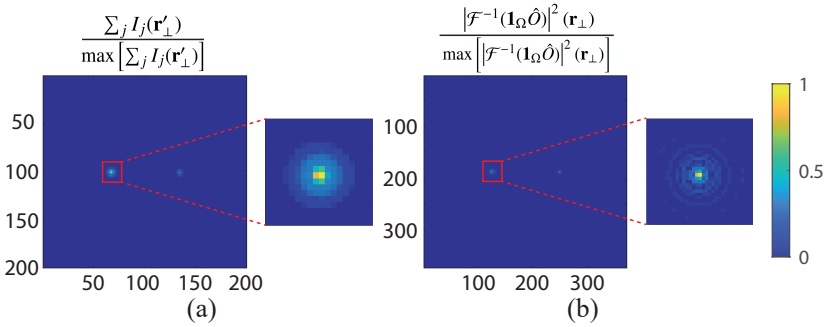

Figure 4.4: (a) The incoherent sum of all 36 dark field measurements, i.e. $\sum_j I_j(\mathbf{r}'_\perp)$. (b) The amplitude of scattering wavefield at plane $z \to 0$, i.e. $\left|\mathcal{F}^{-1}(\mathbf{1}_\Omega \hat{O})\right|^2(\mathbf{r}_\perp)$, which is reconstructed with the Fourier ptychography method. The inserted graphs correspond to the dipole $i=1$.

In Fig. 4.4(a) we show the incoherent sum of all 36 simulated noise-free intensity measurements, i.e. $\sum_j I_j(\mathbf{r}'_\perp)$, and in Fig. 4.4(b) we present the squared amplitude of the scattered field from the sample at plane $z \to 0$, i.e. $\left|\mathcal{F}^{-1}(\mathbf{1}_\Omega \hat{O})\right|^2(\mathbf{r}_\perp)$. For application 1 the spacing of grid $\mathbf{r}'_\perp$ and $\mathbf{r}'_\perp$ fulfills:

$$[\Delta x, \Delta y]^T = \left[(N_x)^{-1} N_x^{\mathrm{det}} \Delta x', (N_y)^{-1} N_y^{\mathrm{det}} \Delta y'\right]^T, \tag{4.20}$$

which can be derived from Eq. (4.3) by interchanging the real space and reciprocal space coordinates. The inserted graphs in Fig. 4.4 correspond to dipole $i = 1$. Note that every dark field measurement is a 200×200 array with a $250nm$ pixel size, which is due to the detector has 200×200 pixels with $5\mu m$ pixel size and the magnification of the imaging system is 20, as given in Table. 4.1. The reconstructed scattered field shown in Fig. 4.4(b) only contains information of $\mathbf{k}_\perp \in \Omega$. The side-lobe which appears in the neighborhood of the particles in Fig. 4.4(b) is due to the fact that the reconstruction is convolved by $\mathscr{F}^{-1}(\mathbf{1}_\Omega)(\mathbf{r}_\perp)$. Without knowing the wavefield at $\mathbf{k}_\perp = 0$ and its surrounding region or without considering any prior information about the sample, the reconstructed scattering field cannot provide a unique physical solution.

Once $\mathbf{1}_\Omega \hat{O}(\mathbf{k}_\perp)$ is obtained, we retrieve α_i and $\mathbf{r}_{\perp,i}$ by minimizing the least square function given in Eq. (4.19). This is done by using the 'fmincon' solver in MATLAB. To facilitate the solver to find the global minimum, a proper starting search point and a set of bounds for α_i and $\mathbf{r}_{\perp,i}$ are needed. From Fig. 4.4 we see that one can deduce a guess about the scattering strength and the position of the dipoles from the dark field measurements. Based on the guess we can obtain the starting point and the bounds. The accuracy of the guess of the position is limited by the pixel size of the detector. In the simulation we deduce the initial guess as follows. We first choose in Fig. 4.4(b) one pixel cell which approximately have minimal and equal distances from the centers of the images of two dipoles. In Fig. 4.4(b) the indices of this pixel cell in the x and y directions are $[195, 186]^T$. Then we set the top left corner of this pixel cell as origin. The initial guess of position of the dipoles are obtained by roughly measuring the distance between the origin and the center of the image of the dipoles in Fig. 4.4(b). To determine the bounds of the position, we first choose two 5×5 pixel arrays which center at the brightest pixel cells of the image of two dipoles, respectively. We choose to use the 5×5 arrays because the sum of the absolute square of the value of each corresponding 5×5 pixels is approximately equal to 90% of the total scattering intensity of each dipole. The bounds of the positions are determined by the outer boundary of the two 5×5 pixel arrays in the x and y, respectively. The starting search point of the position of each particle is randomly assigned inside the corresponding outer boundaries, respectively. The initial guess of the scattering strength of each dipole, on the other hand, is determined by summing the absolute square of the value over the corresponding 5×5 pixel arrays of each dipole, respectively. The lower bounds of the scattering strength of the dipoles are set to be 0 and the upper bound are left undetermined, i.e. positive infinity. The starting point of all parameters are shown in Table. 4.2. The retrieved parameters are listed in the most right column of the same table.

4.3. APPLICATION 2: PARAMETER RETRIEVAL OF A RECTANGULAR OBJECT USING REAL-SPACE PTYCHOGRAPHY

4.3.1. SINGLE OBJECT EMBEDDED IN CONSTANT SURROUNDING

Now we consider a real-space ptychography setup as shown in Fig. 4.5. The object can

Table 4.2: Retrieved parameters of two dipoles in the noise free simulation

	actual value	initial guess	retrieved value
$\alpha_1/(\lambda^3)$	1.000×10^{-3}	0.925×10^{-3}	1.000×10^{-3}
x_1	$-8.333\,\mu m$	$-8.349\,\mu m$	$-8.333\,\mu m$
y_1	$0.000\,\mu m$	$0.113\,\mu m$	$0.000\,\mu m$
$\alpha_2/(\lambda^3)$	0.512×10^{-3}	0.429×10^{-3}	0.512×10^{-3}
x_2	$8.356\,\mu m$	$8.327\,\mu m$	$8.356\,\mu m$
y_2	$0.088\,\mu m$	$-0.029\,\mu m$	$0.088\,\mu m$

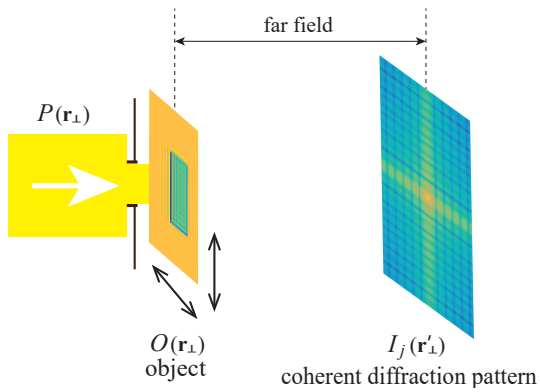

Figure 4.5: The configuration of application 2.

be written in the following form:

$$\begin{aligned} O(\mathbf{r}_\perp)(A_1,\phi_1,a_1,b_1,\mathbf{r}_{\perp,1}) &= 1+(A_1e^{i\phi_1}-1)\Pi_{a_1,b_1}(\mathbf{r}_\perp-\mathbf{r}_{\perp,1}) \\ &= 1+C_1\Pi_{a_1,b_1,\mathbf{r}_{\perp,1}}, \end{aligned} \tag{4.21}$$

where $C_1 = A_1e^{i\phi_1}-1$ is a complex valued coefficient. and $\Pi_{a_1,b_1}(\mathbf{r}_\perp-\mathbf{r}_{\perp,1})$ is the 2D rectangular function defined by parameters:

$$\Pi_{a_1,b_1}(\mathbf{r}_\perp-\mathbf{r}_{\perp,1}) = \Pi_{a_1}(x-x_1)\Pi_{b_1}(y-y_1) = \begin{cases} 0, & |x-x_1|>\frac{a_1}{2} \text{ or } |y-y_1|>\frac{b_1}{2}, \\ 1, & |x-x_1|<\frac{a_1}{2} \text{ and } |y-y_1|<\frac{b_1}{2}. \end{cases} \tag{4.22}$$

We aim to retrieve the parameters:

$$\Theta = \left[A_1,\phi_1,a_1,b_1,\mathbf{r}_{\perp,1}\right]^T, \quad \text{where:} \quad A_1\in(0,1],\ a_1>0,\ b_1>0. \tag{4.23}$$

The diffracted wavefield in the far field for the jth illumination is:

$$\mathscr{F}\left(\Psi_j\right)\left(\mathbf{k}'_\perp\right) = \mathscr{F}\left(P_j\right)\left(\mathbf{k}'_\perp\right) + \mathscr{F}\left(P_j\right)\left(\mathbf{k}'_\perp\right) \otimes \left[C_1a_1b_1\mathrm{sinc}\left(\frac{a_1k_x}{2}\right)\mathrm{sinc}\left(\frac{b_1k_y}{2}\right)e^{i\mathbf{k}'_\perp\cdot\mathbf{r}_{\perp,1}}\right], \tag{4.24}$$

where $\otimes$ denotes convolution. Note in Eq. (4.22) we leave the values of the function at $x = x_1\pm\frac{a_1}{2}$ and $y = y_1\pm\frac{b_1}{2}$ be undefined because these values cannot be retrieved under the projection approximation given by Eq. (1.37). We can see in Eq. (4.24) that the diffracted wavefield is not a function w.r.t. the value of $O(\mathbf{r}_\perp)$ at position $x = x_1\pm\frac{a_1}{2}$ and $y = y_1\pm\frac{b_1}{2}$. The validity of the projection approximation have been discussed in [24, 25] and we assume in the paper that this approximation is valid.

4.3.2. RETRIEVING THE PARAMETER OF THE RECTANGLE

We can see in Eq. (4.24) that, when we have exact knowledge of the probe, the diffraction pattern is a function of the parameters of the rectangle. This fact offers us the chance to retrieve the parameters given in Eq. (4.23) from the measurements $I_j(\mathbf{k}'_\perp)$ for all j. In this section we propose and validate a feasible method to retrieve the parameters from a ptychographic measurement.

The first step of the proposed method is to reconstruct the object function in real space, denoted by: $\hat{O}(\mathbf{r}_\perp)$, from $I_j(\mathbf{k}'_\perp)$ for all j. This can be done by applying the PIE [26, 27] algorithm or other ptychography algorithms [28–31]. The discretization of $\mathbf{r}_\perp$ and $\mathbf{k}'_\perp$ follows Eq. (4.1). Note that $\hat{O}(\mathbf{r}_\perp)$ can be obtained even if the probe function is unknown, which is due to the data redundancy of the ptychographic measurement.

Once the minimum of the likelihood function is found, we can compute the Fourier transform of the reconstructed object, denoted by $\mathscr{F}(\hat{O})(\mathbf{k}_\perp)$. The spacing of grid $\mathbf{r}_\perp$ and $\mathbf{k}_\perp$ is given in Eq. (4.3). The parameter of the rectangle can be retrieved by minimizing a cost function $\mathscr{G}$ defined by:

$$\mathscr{G} = \left\| \mathscr{F}\left(\hat{O}-1\right) - C_1a_1b_1\mathrm{sinc}\left(\frac{a_1k_x}{2}\right)\mathrm{sinc}\left(\frac{b_1k_y}{2}\right)e^{i\mathbf{k}_\perp\cdot\mathbf{r}_{\perp,1}} \right\|^2, \tag{4.25}$$

Table 4.3: The characteristic parameters of the configuration in the simulation

probe	grid size	grid spacing	wavelength	scanning grid	overlap ratio	radius of circular support
	60×60	$30nm$	$30nm$	5×5	75%	$0.45\mu m$

object	grid size	grid spacing	detector	pixel number	pixel size	propagation distance
	90×90	$30nm$		60×60	$50\mu m$	$1.88cm$

where $\|\cdot\|^2$ denotes the l_2 norm. To give an example about the relation between $\mathscr{G}$ and the rectangle parameters, we show in Fig. 4.7 the value of $\mathscr{G}$ as a function of a_1 and x_1. The configuration parameter of Fig. 4.7 will be given later in Section 4.4.2. It is seen that $\mathscr{G}$ is convex in the neighborhood of the actual a_1 and x_1, which offers us the chance to retrieve the parameter by minimizing $\mathscr{G}$. In order to find the minimum of $\mathscr{G}$, it will be beneficial to start the algorithm from a point close to the actual value. This starting point can be determined from $\hat{O}(\mathbf{r})$.

In summary, our proposed method includes the following steps:

(1) Use the MLE algorithm to retrieve the complex valued wavefield $\hat{O}(\mathbf{r}_\perp)$.

(2) Find the lower and upper bound of Θ from $\hat{O}(\mathbf{r}_\perp)$. Θ is the parameter vector defined by Eq. (4.23). These bounds are denoted by: Θ_l and Θ_u.

(3) Solve the following problem:

$$\arg\min_{\Theta} \ \mathscr{G}, \quad \text{subject to } \ \Theta_l \leq \Theta \leq \Theta_u. \tag{4.26}$$

4.3.3. SIMULATION

To validate our proposed method, a preliminary simulation is shown. We consider the setup as shown in Fig. 4.5. Details of the configuration are shown in Table. 4.3. The Fresnel number of this configuration is 0.0014. According to Eq. (4.24), we first generate the complex valued wavefield in Fourier space $\mathscr{F}\left(\Psi_j\right)\left(\mathbf{k}'_\perp\right)$ based on the given probe and object. The Fourier transform of the object function $\mathscr{F}\left(O\right)\left(\mathbf{k}_\perp\right)$ is illustrated in Fig. 4.6(a). The object consists of one rectangle with sizes listed in Table. 4.4. Fig. 4.6(b) shows the normalized amplitude and the phase of the probe. In this simulation we assume the probe is known and the ptychographic measurement is noise-free. In Fig. 4.6(c) we illustrate the Fourier transform of the reconstructed object function $\mathscr{F}(\hat{O})(\mathbf{k}_\perp)$. The inverse Fourier transform of $\mathscr{F}(\hat{O})(\mathbf{k}_\perp)$ is shown in Fig. 4.6(d).

After obtaining $\mathscr{F}(\hat{O})(\mathbf{k})$, we can retrieve the parameters of the rectangle by solving the optimization problem in Eq. (4.26). In Fig. 4.7 we demonstrate the evaluation of the cost function $\mathscr{G}$ with respect to a_1 and x_1, which are the width and position of the rectangular in the x-direction. The orange arrows in both plots points to the actual values of a_1 and x_1. We see in Fig. 4.7 that it is possible to accurately retrieve the values of a_1 and x_1 by minimizing $\mathscr{G}$. To compute the solution of the problem in Eq. (4.26), we again implemented the 'fmincon' solver in MATLAB. Furthermore, Fig. 4.7 shows that the value

of $\mathscr{G}$ is approximately a quadratic function w.r.t. a_1 and a linear function w.r.t. x_1 in the neighborhood of the actual values, which is explained in Section 4.7.2 in Supplement. The actual value of the parameters, the starting point and the retrieved results are presented in Table. 4.4. We can see that the proposed method can successfully retrieve the parameters of the rectangle.

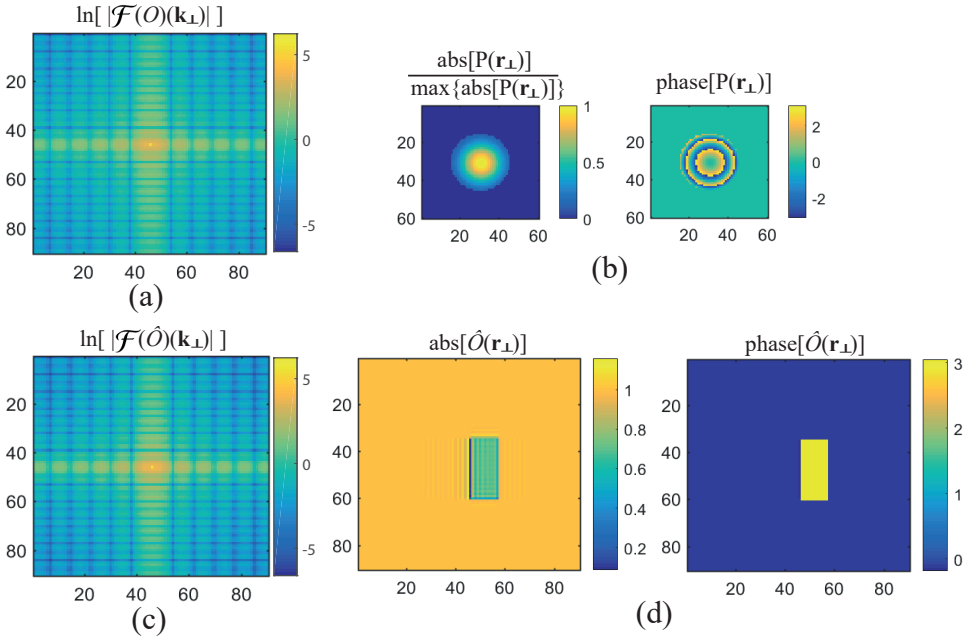

Figure 4.6: (a) The simulated object in Fourier space. The object has one rectangle which is embedded in a constant surrounding. (b) The normalized amplitude and the phase of the probe, which is known in the simulation. (c) The retrieved object function in Fourier space from ptychographic measurement. (d) The inverse Fourier transform of $\mathscr{F}(\hat{O})(\mathbf{k}_\perp)$.

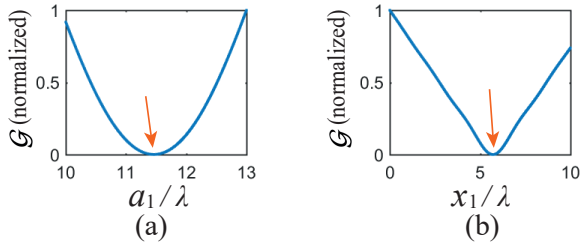

Figure 4.7: The evaluation of $\mathscr{E}$ with respect to a_1 and x_1. The value of $\mathscr{E}$ is normalized to its maximum in both plots. The orange arrow points to the actual value of a_1 and x_1 in this simulation.

Table 4.4: Retrieved parameters of one rectangle

	a_1/λ	b_1/λ	x_1/λ	y_1/λ	A_1	ϕ_1
actual value	11.46	25.99	5.71	1.42	0.70	3.14
initial guess	11.00	28.00	4.00	3.00	0.73	3.17
retrieved value	11.46	25.99	5.71	1.42	0.70	3.14

4.4. THE CRLB ANALYSIS OF APPLICATION 1

4.4.1. THE FISHER INFORMATION MATRIX FOR RETRIEVAL OF THE DIPOLE

Now we calculate the Fisher matrix for the ith dipole. According to Eq. (4.19), the parameters we aim to estimate are:

$$\Theta = [\theta_1, \theta_2, \cdots, \theta_N]^T = \left[\alpha_1, x_1, y_1, \alpha_2, x_2, y_2, \cdots, \alpha_N, x_N, y_N\right]^T. \tag{4.27}$$

We consider that we aim to retrieve the parameters of the ith dipole while assuming that the parameters of all other dipoles are known. To find the Fisher matrix, we need to calculate the derivative of I_j with respect to the parameters of dipole i. The derivatives of I_j are given in Section 4.7.1 the Supplement. The number of elements of I_j are determined by the amount of dipoles. For the case of two dipoles in application 1, we have the 6×6 Fisher matrix with elements:

$$I_F^{\text{dip}} = \begin{bmatrix} I^{\text{dip}}_{F,\alpha_1\alpha_1} & I^{\text{dip}}_{F,\alpha_1\mathbf{r}_{\perp,1}} & I^{\text{dip}}_{F,\alpha_1\alpha_2} & I^{\text{dip}}_{F,\alpha_1\mathbf{r}_{\perp,2}} \\ I^{\text{dip}}_{F,\mathbf{r}_{\perp,1}\alpha_1} & I^{\text{dip}}_{F,\mathbf{r}_{\perp,1}\mathbf{r}_{\perp,1}} & I^{\text{dip}}_{F,\mathbf{r}_{\perp,1}\alpha_2} & I^{\text{dip}}_{F,\mathbf{r}_{\perp,1}\mathbf{r}_{\perp,2}} \\ I^{\text{dip}}_{F,\alpha_2\alpha_1} & I^{\text{dip}}_{F,\alpha_2\mathbf{r}_{\perp,1}} & I^{\text{dip}}_{F,\alpha_2\alpha_2} & I^{\text{dip}}_{F,\alpha_2\mathbf{r}_{\perp,2}} \\ I^{\text{dip}}_{F,\mathbf{r}_{\perp,2}\alpha_1} & I^{\text{dip}}_{F,\mathbf{r}_{\perp,2}\mathbf{r}_{\perp,1}} & I^{\text{dip}}_{F,\mathbf{r}_{\perp,2}\alpha_2} & I^{\text{dip}}_{F,\mathbf{r}_{\perp,2}\mathbf{r}_{\perp,2}} \end{bmatrix}, \tag{4.28}$$

where $I^{\text{dip}}_{F,\mathbf{r}_{\perp,i}\mathbf{r}_{\perp,i}}$, $I^{\text{dip}}_{F,\mathbf{r}_{\perp,i}\alpha_{\perp,i}}$ and $I^{\text{dip}}_{F,\alpha_{\perp,i}\mathbf{r}_{\perp,i}}$ are 2×2, 2×1 and 1×2 sub-matrices, respectively. The diagonal elements of I_F^{dip} are:

$$I^{\text{dip}}_{F,\alpha_i\alpha_i} = \frac{2}{\hbar\omega}\sum_{\mathbf{r}'_\perp,j}\left[\frac{\left|\mathscr{F}^{-1}\left(\Psi_{j,i}\right)\left(\mathbf{r}'_\perp\right)\right|^2}{\alpha_i^2} + \Re\left(\frac{\mathscr{F}^{-1}\left(\Psi_j\right)^*\left(\mathbf{r}'_\perp\right)\left[\mathscr{F}^{-1}\left(\Psi_{j,i}\right)\left(\mathbf{r}'_\perp\right)\right]^2}{\alpha_i^2\mathscr{F}^{-1}\left(\Psi_j\right)\left(\mathbf{r}'_\perp\right)}\right)\right], \tag{4.29}$$

$$I^{\text{dip}}_{F,\mathbf{r}_{\perp,i}\mathbf{r}_{\perp,i}} = \frac{2}{\hbar\omega}\sum_{\mathbf{r}'_\perp,j}\left[\left|\nabla_{\mathbf{r}'_\perp}\mathscr{F}^{-1}\left(\Psi_{j,i}\right)\left(\mathbf{r}'_\perp\right)\right|^2 + \Re\left(\frac{\mathscr{F}^{-1}\left(\Psi_j\right)^*\left(\mathbf{r}'_\perp\right)\left[\nabla_{\mathbf{r}'_\perp}\mathscr{F}^{-1}\left(\Psi_{j,i}\right)\left(\mathbf{r}'_\perp\right)\right]^2}{\mathscr{F}^{-1}\left(\Psi_j\right)\left(\mathbf{r}'_\perp\right)}\right)\right], \tag{4.30}$$

which are given by Eq. (4.49) and Eq. (4.50) in the Supplement.

It is of interest to first study the diagonal terms in I_F. For instance, suppose that we have exact knowledge about the illumination power, the first dipole's position and the second dipole's strength and position, then $(I^{\text{dip}}_{F,\alpha_1\alpha_1})^{-1}$ is the CRLB of α_1 for any unbiased estimator. When only one dipole exists in the sample, the diagonal terms in I_F^{dip} can be

rewritten as:

$$I^{\text{dip}}_{F,\alpha_1\alpha_1} = \frac{4}{\hbar\omega}\sum_{\mathbf{r}'_{\perp},j}\left|\mathscr{F}^{-1}\left[Q(\mathbf{k}_{\perp}+\mathbf{k}_{\perp,j})e^{-i\mathbf{k}_{\perp}\cdot\mathbf{r}_{\perp,1}}\right]\right|^2, \tag{4.31}$$

$$I^{\text{dip}}_{F,\mathbf{r}_{\perp,1}\mathbf{r}_{\perp,1}} = \frac{4}{\hbar\omega}\left|C_1^{\text{dip}}\right|^2\sum_{\mathbf{r}'_{\perp},j}\left[\frac{J_2\left(k\text{NA}\left|\mathbf{r}'_{\perp}-\mathbf{r}_{\perp,1}\right|\right)^2}{\left|\mathbf{r}'_{\perp}-\mathbf{r}_{\perp,1}\right|^2}\right], \tag{4.32}$$

where C_1^{dip} is the complex valued constant:

$$C_1^{\text{dip}} = \frac{\alpha_1 A_{\text{in}} k^4 \text{NA}^2}{8i\pi\epsilon_0 k_z}. \tag{4.33}$$

In Eq. (4.32) we used the following relation [32]:

$$\frac{d}{dx}\left(\frac{J_1(x)}{x}\right) = \frac{-J_2(x)}{x}, \tag{4.34}$$

where J_1 and J_2 are the Bessel function of the first kind of order 1 and 2, respectively.

We can see in Eq. (4.31) that the CRLB of α_i is inversely proportional to the total illumination power A_{in}^2. Therefore, it is needed to enhance the illumination power to determine the value of α_i for smaller particles. However,when the illumination power is enhanced too much, one may reach a saturation point due to the limited dynamic range of the detector. By taking dark field images of the sample, as shown in Fig. 4.3, one can avoid this limit. Furthermore, we observe that $I^{\text{dip}}_{F,\mathbf{r}_{\perp,1}\mathbf{r}_{\perp,1}}$ does not only depend on the values of A and α_1, but also on the NA. Therefore, to decrease the CRLB of $\mathbf{r}_{\perp,1}$, one can increase the illumination power or one can enlarge NA, or enhance both. It is interesting that $I^{\text{dip}}_{F,\mathbf{r}_{\perp,1}\mathbf{r}_{\perp,1}}$ is not a function of $\mathbf{k}_{\perp,j}$, which indicate that adjusting the illumination's incident angle can lead to any change of the CRLB of $\mathbf{r}_{\perp,1}$ for the case of a single particle.

When more than one particle is on the planar surface, we have to calculate the Fisher information by Eq. (4.28). We see from these equations that there is a correlation between the particles. Suppose there are two particles, then the CRLB of one of the particles is a function of the parameters of the other particle, as follows from Eq. (4.29) and Eq. (4.30) where the second terms consist of the complete field Ψ_j instead of only the partial field $\Psi_{j,i}$. A more detailed study of the cross-correlation is presented in the next section.

4.4.2. THE CRLB OF THE DIPOLE

We study the CRLB of the dipole strength and the position of the dipole along the x-axis. We follow the configuration as described in Fig. (4.3) and Table. 4.1. We first investigate the variance and the squared bias of parameters, α_1 and x_1, of the dipole $i = 1$. To find the variance and bias for various noise levels, we define the illumination power by counting the time-averaged number of photons scattered by the dipole $i = 1$, which is given by:

$$\text{PN}^{\text{dip}} = \frac{\left\|\mathscr{F}^{-1}\left(\frac{A_{\text{in}}k^2}{8i\pi\epsilon_0 k_z}\alpha_i e^{-i\mathbf{r}_{\perp,i}\cdot\mathbf{k}_{\perp}}\right)\right\|^2_{i=1}}{\hbar\omega}. \tag{4.35}$$

Table 4.5: The variance and squared bias of α_1 and x_1 of the dipole of $i = 1$ for different photon counts $\mathrm{PN}^{\mathrm{dip}}$, obtained from Monte Carlo result.

$\mathrm{PN}^{\mathrm{dip}}$	10^4	10^6	10^8
$\mathrm{Var}\left[\alpha_{i=1}/(\lambda^3)\right]$	3.14×10^{-12}	2.54×10^{-14}	2.62×10^{-16}
$\mathrm{Bias}\left[\alpha_{i=1}/(\lambda^3)\right]^2$	3.22×10^{-10}	1.03×10^{-13}	1.26×10^{-17}
$\mathrm{Var}\left(x_{i=1}/\lambda\right)$	4.54×10^{-6}	4.28×10^{-8}	4.23×10^{-10}
$\mathrm{Bias}\left(x_{i=1}/\lambda\right)^2$	4.32×10^{-7}	4.03×10^{-11}	1.89×10^{-13}

The variance and bias are obtained from Monte Carlo simulations. We generated 1000 Fourier ptychographic dark field data-sets for $\mathrm{PN}^{\mathrm{dip}} = 10^4, 10^6, 10^8$. The parameters are reconstructed from the data-sets by applying the parameter retrieval algorithm described in Section 4.2.4. The variance and squared bias for $\mathrm{PN}^{\mathrm{dip}} = 10^4, 10^6, 10^8$, are shown in Table. 4.5.

When $\mathrm{PN}^{\mathrm{dip}} = 10^4$, we see that the variance of x_1 obtained from the retrieval method is 10 times larger than the squared bias. This variance-bias-ratio becomes higher when $\mathrm{PN}^{\mathrm{dip}}$ is increased. This observation means that the retrieval method of x_1 is asymptotically unbiased when $\mathrm{PN}^{\mathrm{dip}} > 10^4$. These variances are illustrated in Fig. 4.8, together with the computed CRLB. It is shown that the variance of the retrieval of x_1 is indeed bounded by the CRLB when $\mathrm{PN}^{\mathrm{dip}} > 10^4$. The value of the bound is inversely proportional to the value of $\mathrm{PN}^{\mathrm{dip}}$.

However, Table. 4.5 also shows that the variance of α_1 obtained from the algorithm is much smaller than the squared bias when $\mathrm{PN}^{\mathrm{dip}} < 10^6$, and indeed the retrieval algorithm of α_1 is not unbiased as long as $\mathrm{PN}^{\mathrm{dip}} < 10^8$ for the current setup. Therefore, the variance of the retrieved α_i may not be bounded by the CRLB when $\mathrm{PN}^{\mathrm{dip}} < 10^8$. On the other hand, we can see in Eq. (4.9) that the accuracy of the reconstruction of α_i is not only influenced by the Poisson noise, but also by the fluctuation of the illumination power A_{in}^2. That is, the uncertainty about the exact value of A will lead to uncertainty of the retrieval of α_1. Therefore, it is more difficult to determine α_1 than the position with the current scheme.

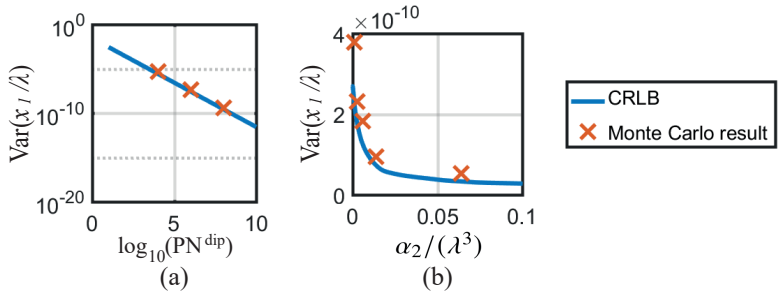

Figure 4.8: (a) The computed CRLB and variance of the position of the first dipole, i.e. x_1, for various $\mathrm{PN}^{\mathrm{dip}}$. (b) The computed CRLB and variance of x_1 for various values of the polarisability of the second dipole, i.e. α_2, for the case of $\mathrm{PN}^{\mathrm{dip}} = 10^8$. The blue line of both plots are the computed CRLB and the red crosses show the variance obtained from the Monte Carlo experiment.

4.4.3. THE CORRELATION BETWEEN TWO DIPOLES

As has been noted in Section 4.5.1, when there are two particles on the surface, varying the parameters of one particle can lead to a change of the CRLB of another particle. To verify this correlation between the particles, we calculated the CRLB of x_1 with various values of α_2. The value of $\mathrm{PN}^{\mathrm{dip}}$ is chosen to be 10^8 because the retrieval algorithm is asymptotically unbiased for this noise level, as has been shown in Section 4.5.2. The computed CRLB is validated by using Monte Carlo simulations, as illustrated in Fig. 4.8(b).

It is seen in Fig. 4.8(b) that one can lower the CRLB of x_1 obtained from the algorithm by enhancing the scattering power of the dipole $i = 2$. This observation can be understood by studying the property of the Poisson distribution. The signal-to-noise ratio (SNR) of Poisson noise is equal to $\sqrt{n(\mathbf{r}'_\perp)}$, where $n(\mathbf{r}'_\perp)$ is the number of photons detected by the pixel at $\mathbf{r}'_\perp$. When the scattering power of particle $i = 1$ is fixed, $n(\mathbf{r}'_\perp)$ is increased by enhancing the scattering power of the other particle, and therefore the signal-to-noise ratio of the system is increased. One may argue that this conclusion is inconsistent with the case where incoherent illumination is used. Let us imagine that we apply incoherent illumination to the setup in Fig. 4.2, then the radiation of each dipole is independent to the other and hence the image recorded by the detector is given by:

$$I_j^{\mathrm{incoh}}(\mathbf{r}'_\perp) = \sum_i \left|\mathscr{F}^{-1}\left[\alpha_i Q(\mathbf{k}_\perp + \mathbf{k}_{\perp,j})\right]\right|^2 (\mathbf{r}'_\perp - \mathbf{r}'_{\perp,i}) = \sum_i I_{j,i}^{\mathrm{incoh}}(\mathbf{r}'_\perp). \tag{4.36}$$

When there are two dipoles, Eq. (4.36) shows that the signal of dipole $i = 1$ is $I_{j,1}^{\mathrm{incoh}}(\mathbf{r}'_\perp)$ whereas the variance of the signal is determined by $\sum_i I_{j,i}^{\mathrm{incoh}}(\mathbf{r}'_\perp)$ at the neighborhood of position $\mathbf{r}_{\perp,1}$. Therefore, for the case of incoherent illumination, the SNR of dipole $i = 1$ should be decreased by enhancing the scattering power of the dipole $i = 2$ because the variance is proportional to $\sum_i I_{j,i}^{\mathrm{incoh}}(\mathbf{r}'_\perp)$ for Poisson noise. However, we emphasize that Eq. (4.36) is not the case of application 1. By comparing Eq. (4.17) to Eq. (4.36), we see that the measurement in application 1 contains the interference pattern of the point spread function of the dipoles. Hence, the conclusion for incoherent illumination is not applicable in application 1 and the SNR should be determined by the computed CRLB and the Monte Carlo simulations. Note that second order scattering is neglected in the current model, i.e. we ignore the scattered wavefield from the first particle which is excited by the second one because the particles are sparsely distributed on the sample.

4.5. THE CRLB ANALYSIS OF APPLICATION 2

4.5.1. FISHER INFORMATION MATRIX FOR SINGLE RECTANGULAR OBJECT

For application 2, the parameter vector we want to retrieve is:

$$\Theta = [\theta_1, \theta_2, \cdots]^T = \left[A_1, \phi_1, a_1, b_1, \mathbf{r}_{\perp,1}\right]^T, \tag{4.37}$$

To find the Fisher information matrix, we start from the expectation of the second order perturbation of $\mathscr{L}_P$:

$$E\left(\delta^2\mathscr{L}_P\right)(\Theta)(\delta\Theta,\delta\tilde{\Theta}) = \frac{2}{\hbar\omega}\sum_{\mathbf{k}'_\perp,j}\Re\left[\mathscr{F}\left[P_j\delta O(\Theta)(\delta\Theta)\right]\mathscr{F}\left[P_j\delta O(\Theta)(\delta\tilde{\Theta})\right]^*\right] + \frac{2}{\hbar\omega}\sum_{\mathbf{k}'_\perp,j}\Re\left[\frac{\mathscr{F}\left(\Psi_j\right)}{\mathscr{F}\left(\Psi_j\right)^*}\mathscr{F}\left[P_j\delta O(\Theta)(\delta\Theta)\right]^*\mathscr{F}\left[P_j\delta O(\Theta)(\delta\tilde{\Theta})\right]^*\right]. \tag{4.38}$$

which is derived from Eq. (3.21) in Chapter 3. The function O is defined in Eq. (4.21). δO is the derivative of O w.r.t. Θ. $\delta\Theta$ and $\delta\tilde{\Theta}$ are small perturbations of the parameters of the rectangle. The explicit expression of δO, $\delta\Theta$ and $\delta\tilde{\Theta}$ are given in Section 4.7.2 of the Supplement.

By using Eq. (4.38), Eq. (4.54) and Eq. (4.54) in the Supplement, we obtain the diagonal elements of the Fisher matrix:

$$I^{\text{rect}}_{F,A_1A_1} = \frac{2}{\hbar\omega}\sum_{\mathbf{r},j}\left|P_j\Pi_{a_1,b_1,\mathbf{r}_1}\right|^2 + \frac{2}{\hbar\omega}\sum_{\mathbf{r},j}\Re\left[\mathscr{F}^{-1}\left(\frac{\mathscr{F}\left(\Psi_j\right)}{\mathscr{F}\left(\Psi_j\right)^*}\right)e^{-2i\phi_1}\left[\left(P_j\Pi_{a_1,b_1,\mathbf{r}_1}\right)^*\right]^2\right]. \tag{4.39}$$

$$I^{\text{rect}}_{F,\phi_1\phi_1} = A_1^2 I_{F,A_1A_1}. \tag{4.40}$$

$$\begin{aligned} I^{\text{rect}}_{F,a_1a_1} = {} & \frac{1}{2\hbar\omega}\sum_{y,j}\left|C_1\Pi_{b_1,y_1}\right|^2\left[\left|P_j\right|^2(x_1+\frac{a_1}{2},y)+\left|P_j\right|^2(x_1-\frac{a_1}{2},y)\right] \\ & + \frac{1}{2\hbar\omega}\sum_{y,j}\Re\left[\left(C_1^*\Pi_{b_1,y_1}\right)^2\mathscr{F}^{-1}\left(\frac{\mathscr{F}\left(\Psi_j\right)}{\mathscr{F}\left(\Psi_j\right)^*}\right)(2x_1+a_1,y)\left(P_j^*\right)^2(x_1+\frac{a_1}{2},y)\right] \\ & + \frac{1}{2\hbar\omega}\sum_{y,j}\Re\left[\left(C_1^*\Pi_{b_1,y_1}\right)^2\mathscr{F}^{-1}\left(\frac{\mathscr{F}\left(\Psi_j\right)}{\mathscr{F}\left(\Psi_j\right)^*}\right)(2x_1-a_1,y)\left(P_j^*\right)^2(x_1-\frac{a_1}{2},y)\right] \\ & + \frac{1}{\hbar\omega}\sum_{y,j}\Re\left[\left(C_1^*\Pi_{b_1,y_1}\right)^2\mathscr{F}^{-1}\left(\frac{\mathscr{F}\left(\Psi_j\right)}{\mathscr{F}\left(\Psi_j\right)^*}\right)(2x_1,y)P_j^*(x_1+\frac{a_1}{2},y)P_j^*(x_1-\frac{a_1}{2},y)\right]. \end{aligned} \tag{4.41}$$

$I^{\text{rect}}_{F,b_1b_1}$ can be obtained by taking the above equation and interchanging x with y and a_1

with b_1.

$$
\begin{aligned}
I^{\text{rect}}_{F,x_1x_1} = & \frac{2}{\hbar\omega}\sum_{y,j}\left|C_1\Pi_{b_1,y_1}\right|^2\left[\left|P_j\right|^2(x_1+\frac{a_1}{2},y)+\left|P_j\right|^2(x_1-\frac{a_1}{2},y)\right] \\
& + \frac{2}{\hbar\omega}\sum_{y,j}\Re\left[\left(C_1^*\Pi_{b_1,y_1}\right)^2\mathscr{F}^{-1}\left(\frac{\mathscr{F}\left(\Psi_j\right)}{\mathscr{F}\left(\Psi_j\right)^*}\right)(2x_1+a_1,y)\left(P_j^*\right)^2(x_1+\frac{a_1}{2},y)\right] \\
& + \frac{2}{\hbar\omega}\sum_{y,j}\Re\left[\left(C_1^*\Pi_{b_1,y_1}\right)^2\mathscr{F}^{-1}\left(\frac{\mathscr{F}\left(\Psi_j\right)}{\mathscr{F}\left(\Psi_j\right)^*}\right)(2x_1-a_1,y)\left(P_j^*\right)^2(x_1-\frac{a_1}{2},y)\right] \\
& - \frac{4}{\hbar\omega}\sum_{y,j}\Re\left[\left(C_1^*\Pi_{b_1,y_1}\right)^2\mathscr{F}^{-1}\left(\frac{\mathscr{F}\left(\Psi_j\right)}{\mathscr{F}\left(\Psi_j\right)^*}\right)(2x_1,y)P_j^*(x_1+\frac{a_1}{2},y)P_j^*(x_1-\frac{a_1}{2},y)\right].
\end{aligned}
\tag{4.42}
$$

$I^{\text{rect}}_{F,y_1y_1}$ can be obtained by taking the above equation and interchanging x with y and a_1 with b_1.

We again focus on the diagonal elements of the Fisher matrix. Referring to the first term on the right-hand side of Eq. (4.39) and Eq. (4.40), we can immediately see that the CRLB of A_1 and ϕ_1 is partially determined by the illumination power. Similarly, in Eq. (4.41) and Eq. (4.42) we see that the CRLB of a_1 and x_1 is partially determined by the illumination power at $x_1 \pm \frac{a_1}{2}$, which is the edge of the rectangle. We can also notice in Eq. (4.40) that the CRLB of ϕ_1 is inversely proportional to A_1^2. This observation means that one can retrieve ϕ_1 more accurately by increasing the transmission of the rectangle, assuming that the estimator is unbiased.

It is interesting that $I^{\text{rect}}_{F,a_1a_1}$ and $I^{\text{rect}}_{F,x_1x_1}$ are functions of Π_{b_1,y_1}. This fact means that enlarging the width of the rectangle in the y-direction will decrease the CRLB of a_1 and x_1, which are parameters along the x-axis. This correlation between b_1 and the CRLB of a_1 and x_1 is demonstrated in the next subsection. The computed CRLB is validated by Monte Carlo simulations.

4.5.2. THE CRLB OF THE WIDTH AND THE POSITION OF THE RECTANGLE

Now we consider the configuration of Section 4.3. As described in Section 4.5.2, we need to provide a measure of the noise level in terms of photon counting. For application 2, we define the illumination power by means of the total photon number counting over the cross section of the probe:

$$
\text{PN}^{\text{rect}} = \sum_{\mathbf{r}_\perp}^{N_x^{\text{det}},N_y^{\text{det}}}\frac{\|P(\mathbf{r}_\perp)\|^2}{\hbar\omega},
\tag{4.43}
$$

where the probe $P(\mathbf{r}_\perp)$ is shown in Fig. 4.6(b).

Here we study the influence of the width of the rectangle in the y-direction on the variance of retrieved width and position along the x-axis. The computed CRLB of a_1 and x_1 are shown in Fig. 4.9, for various values of b_1. The value of PN^{rect} is chosen to be 10^8. To validate the computation of the CRLB, the result of Monte Carlo Monte simulations is shown in Fig. 4.9 also. To obtain the variance, 1000 ptychographic data-sets are created

Table 4.6: The variance and squared bias of a_1 and x_1 of the rectangle, obtained from the Monte Carlo simulation for $\mathrm{PN}^{\mathrm{rect}} = 10^8$.

b_1/λ	1	5	15
$\mathrm{Var}(a_1/\lambda)$	3.576×10^{-7}	1.455×10^{-7}	9.017×10^{-8}
$\mathrm{Bias}(a_1/\lambda)^2$	7.825×10^{-10}	4.254×10^{-10}	8.386×10^{-11}
$\mathrm{Var}(x_1/\lambda)$	9.057×10^{-8}	2.527×10^{-8}	1.824×10^{-8}
$\mathrm{Bias}(x_1/\lambda)^2$	6.423×10^{-12}	6.879×10^{-11}	4.947×10^{-11}

in the Monte Carlo analysis. The data-sets are post-processed by using the parameter retrieval algorithm given in Section 4.3.2. The exact value of the variance and the squared bias of the parameters for the case of $b_1/\lambda = 1, 5, 15$, are listed in Table. 4.6.

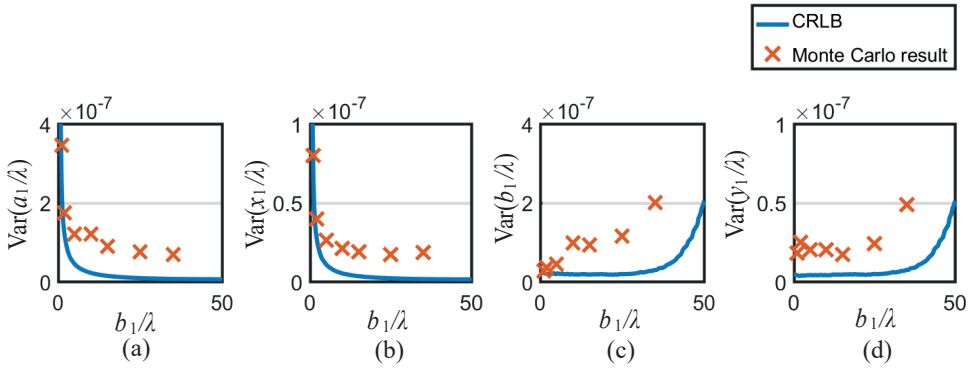

Figure 4.9: The CRLB and variance of a_1, x_1, b_1 and y_1 of the rectangle, for various of b_1. The $\mathrm{PN}^{\mathrm{rect}}$ of this figure is 10^8. The blue line is the computed CRLB and the red crosses show the variance obtained from the Monte Carlo simulations.

We see in Fig. 4.9(a) and Fig. 4.9(b) that when $\mathrm{PN}^{\mathrm{rect}} = 10^8$ the CRLB of a_1/λ and x_1/λ are in the order of 10^{-6}, which indicates that the resolution of the current parameter retrieval scheme is not limited by the grid discretization in real space. The Monte Carlo result confirm this conclusion. Moreover, the squared bias of a_1/λ and x_1/λ is around 10^3 times smaller that the variance, which means the that algorithm is asymptotically unbiased when $\mathrm{PN}^{\mathrm{rect}} = 10^8$, and hence the variance obtained by the algorithm should be bounded by the CRLB. The CRLB of both a_1/λ and x_1/λ decrease when the value of b_1 is increased. This result agrees with Eq. (4.41) and Eq. (4.42). The CRLB of a_1/λ and x_1/λ in Fig. 4.9 decreases rapidly when $b_1/\lambda < 5$. The reason is that the sensitivity of the retrieval of the parameters is determined by the number of photons which encodes the information about the parameters. That is, there are more photons which contain information about a_1 and x_1 when b_1 is larger. On the other hand, we can see that the CRLB of b_1/λ and y_1/λ do not vary much when the value of b_1/λ is sufficiently small. When $b_1/\lambda > 40$, the CRLB of b_1/λ and y_1/λ start to increase as the value of b_1/λ is enlarged. This is because the boundary of the rectangle parallel to the y-axis falls outside of the illuminated area, which is an undesirable situation since b_1/λ and y_1/λ need

also to be retrieved. To be explicit, the size of the illuminated area is determined by the non-zero area of $\sum_j \left|P(\mathbf{r}_\perp - \mathbf{R}_{\perp,j})\right|^2$. In the simulation, the size of the illuminated area in the y direction is roughly 60λ. Meanwhile, the beam profile of the illumination, i.e. $|P(\mathbf{r}_\perp)|^2$, is simulated by the Gaussian function as shown in Fig. 4.6(b). The full-width at half-maximum (FWHM) of the probe is around 15λ. These characteristic parameters of the probe agree with Fig. 4.9(c) and Fig. 4.9(d) that the CRLB of b_1/λ and y_1/λ start to increase as $b_1/\lambda > 40$. Overall, the computed CRLB as shown in Fig. 4.9 indicates that, the optimal chosen range of values of b_1/λ is $(5, 40)$ for the current configuration.

4.6. CONCLUSION

In summary, a parameter retrieval method is demonstrated in this paper. The idea of the method is to incorporate available *a priori* information about the object in the general ptychography framework. Two applications of the method are studied. In application 1 we explore how the parameters of small particles can be retrieved from Fourier ptychographic dark field measurements. The simulation result shows that, when the diameters of the particles are sufficiently small, e.g. $\sim 0.1\lambda$, so that the scattered wavefields can be modeled as radiation of dipoles, the parameters of the particles can be uniquely determined from dark field measurement only. In application 2 the retrieval of the parameters of a rectangular object embedded in constant surrounding was studied.

The influence of Poisson noise on the parameter retrieval method is discussed in the second part of the paper. The CRLB of the parameters are theoretically derived and numerically computed from the Fisher information matrix for both applications. Monte Carlo analysis is used to validate the computed CRLB. The CRLB, variance and bias of the retrieved parameters in application 1 were determined for various photon counts. It was found that the uncertainty of the parameter retrieval is inversely proportional to the photon counts, and potentially is not limited by the sizes of individual cells of the discretized meshgrid in object space. The correlation between at least two particles is evaluated from the calculation of the CRLB. We proved that the CRLB of the position of one particle is influenced by the scattering power of the other particle. This conclusion is confirmed by the Monte Carlo result. The correlation of parameters in application 2 is also inferred from the computed CRLB. The influence of the width of the rectangle in the y-direction on the CRLB of the parameters along the x-axis is investigated by analyzing the CRLB and the Monte Carlo result. For the same number of photons in the illuminating probe, the uncertainty of the parameters along the x-axis can be reduced by enlarging the width in the y-direction.

Following this study, there are many related subjects which deserve further research. For Application 1, we only test the proposed method with PSL beads. In practice, the PSL beads are used as the calibration standard with which we can determine the lower detection limit of the 'RapidNano' particle scanner. Generally speaking, the scanner should be able to detect particles of any material. Therefore, to apply the proposed method to other particles is an interesting subject for the next step. Note that the refraction index of the particle is possibly unknown or/and is not the same for different particle on the substrate. For this case, the model used in the paper is unable to retrieve the volume of the particle. To incorporate the proposed method to this case, a more complex model is

needed and the subject is out of the scope of the paper. Another issue in Application 1 relates to the fact that we have not considered the secondary scattering effect between adjacent dipoles. This is because that in practice the particles are sparsely distributed on the substrate for the most of time. When two dipoles are very close to each other, the present scattering model cannot accurately describe the scattered field, and hence multiple scattering has to be considered. The multiple scattering is one of the major topics which deserve further research.

For Application 2, one of the subjects for the next step is to investigate influence of unknown background transmission. When the background transmission is homogeneous but unknown, it is clear that the background transmission can be retrieved from the reconstructed object that obtained from the MLE ptychographic algorithm. Whereas when there is small unknown perturbation in the background transmission, the effect of the perturbation may also be studied via CRLB analysis or Monte Carlo simulation. This analysis could be conducted when we have more knowledge about how/why can we model the perturbation of background. As far as we know, this subject is still an open question and deserves further research.

4.7. SUPPLEMENT

4.7.1. THE DERIVATIVE OF I_j WITH RESPECT TO THE PARAMETERS OF DIPOLE i IN APPLICATION 1

Now we calculate the Fisher matrix for the ith dipole. According to Eq. (4.19) in this chapter, the parameters we aim to estimate are:

$$\Theta = [\theta_1, \theta_2, \cdots, \theta_N]^T = \left[\alpha_1, x_1, y_1, \alpha_2, x_2, y_2, \cdots, \alpha_N, x_N, y_N\right]^T. \tag{4.44}$$

The perturbation of I_j with respect to the parameters of dipole i are given by:

$$\delta I_j(\delta\theta_i) = \begin{bmatrix} 2\alpha_i^{-1}\Re\left[\mathscr{F}^{-1}\left(\Psi_j\right)^* \mathscr{F}^{-1}\left(\Psi_{j,i}\right)\right]\delta\alpha_i \\ -2\Re\left[\mathscr{F}^{-1}\left(\Psi_j\right)^* \nabla_{\mathbf{r}'_\perp} \mathscr{F}^{-1}\left(\Psi_{j,i}\right)\right]\delta\mathbf{r}_{\perp,i} \end{bmatrix}, \tag{4.45}$$

where $*$ denotes complex conjugation. The ith partial field $\Psi_{j,i}$ is given by:

$$\Psi_{j,i}(\mathbf{k}_\perp) = Q(\mathbf{k}_\perp + \mathbf{k}_{\perp,j})\alpha_i e^{-\mathrm{i}\mathbf{r}_{\perp,i}\cdot\mathbf{k}_\perp}. \tag{4.46}$$

which is the contribution of the ith dipole to the total field for the jth illumination, according to Eq. (4.14) in this chapter.

In Eq. (4.45) we used:

$$\mathscr{F}^{-1}\left[-\mathrm{i}\mathbf{k}_\perp \cdot \Psi(\mathbf{r}'_\perp)\right] = -\nabla_{\mathbf{r}'_\perp} \mathscr{F}^{-1}(\Psi)(\mathbf{r}'_\perp). \tag{4.47}$$

The elements of the Fisher matrix can be computed by substituting Eq. (4.45) into Eq. (3.21). The number of elements of I_j are determined by the amount of dipoles. For the

case of two dipoles in application 1, we have the 6×6 Fisher matrix with elements:

$$I_F^{\text{dip}} = \begin{bmatrix} I^{\text{dip}}_{F,\alpha_1\alpha_1} & I^{\text{dip}}_{F,\alpha_1\mathbf{r}_{\perp,1}} & I^{\text{dip}}_{F,\alpha_1\alpha_2} & I^{\text{dip}}_{F,\alpha_1\mathbf{r}_{\perp,2}} \\ I^{\text{dip}}_{F,\mathbf{r}_{\perp,1}\alpha_1} & I^{\text{dip}}_{F,\mathbf{r}_{\perp,1}\mathbf{r}_{\perp,1}} & I^{\text{dip}}_{F,\mathbf{r}_{\perp,1}\alpha_2} & I^{\text{dip}}_{F,\mathbf{r}_{\perp,1}\mathbf{r}_{\perp,2}} \\ I^{\text{dip}}_{F,\alpha_2\alpha_1} & I^{\text{dip}}_{F,\alpha_2\mathbf{r}_{\perp,1}} & I^{\text{dip}}_{F,\alpha_2\alpha_2} & I^{\text{dip}}_{F,\alpha_2\mathbf{r}_{\perp,2}} \\ I^{\text{dip}}_{F,\mathbf{r}_{\perp,2}\alpha_1} & I^{\text{dip}}_{F,\mathbf{r}_{\perp,2}\mathbf{r}_{\perp,1}} & I^{\text{dip}}_{F,\mathbf{r}_{\perp,2}\alpha_2} & I^{\text{dip}}_{F,\mathbf{r}_{\perp,2}\mathbf{r}_{\perp,2}} \end{bmatrix}, \tag{4.48}$$

where $I^{\text{dip}}_{F,\mathbf{r}_{\perp,i}\mathbf{r}_{\perp,i}}$, $I^{\text{dip}}_{F,\mathbf{r}_{\perp,i}\alpha_{\perp,i}}$ and $I^{\text{dip}}_{F,\alpha_{\perp,i}\mathbf{r}_{\perp,i}}$ are 2×2, 2×1 and 1×2 sub-matrices, respectively. The diagonal elements of I_F^{dip} are:

$$I^{\text{dip}}_{F,\alpha_i\alpha_i} = \frac{2}{\hbar\omega}\sum_{\mathbf{r}'_\perp,j}\left[\frac{\left|\mathscr{F}^{-1}\left(\Psi_{j,i}\right)(\mathbf{r}'_\perp)\right|^2}{\alpha_i^2} + \Re\left(\frac{\mathscr{F}^{-1}\left(\Psi_j\right)^*(\mathbf{r}'_\perp)\left[\mathscr{F}^{-1}\left(\Psi_{j,i}\right)(\mathbf{r}'_\perp)\right]^2}{\alpha_i^2\mathscr{F}^{-1}\left(\Psi_j\right)(\mathbf{r}'_\perp)}\right)\right], \tag{4.49}$$

$$I^{\text{dip}}_{F,\mathbf{r}_{\perp,i}\mathbf{r}_{\perp,i}} = \frac{2}{\hbar\omega}\sum_{\mathbf{r}'_\perp,j}\left[\left|\nabla_{\mathbf{r}'_\perp}\mathscr{F}^{-1}\left(\Psi_{j,i}\right)(\mathbf{r}'_\perp)\right|^2 + \Re\left(\frac{\mathscr{F}^{-1}\left(\Psi_j\right)^*(\mathbf{r}'_\perp)\left[\nabla_{\mathbf{r}'_\perp}\mathscr{F}^{-1}\left(\Psi_{j,i}\right)(\mathbf{r}'_\perp)\right]^2}{\mathscr{F}^{-1}\left(\Psi_j\right)(\mathbf{r}'_\perp)}\right)\right], \tag{4.50}$$

where we used the following relation:

$$\Re(z_1)\Re(z_2) = \frac{1}{2}\left[\Re(z_1z_2)+\Re(z_1z_2^*)\right], \tag{4.51}$$

for any complex number z_1 and z_2.

4.7.2. THE DERIVATIVE OF O WITH RESPECT TO THE PARAMETERS OF THE RECTANGLE IN APPLICATION 2

For Application 2, the parameter vector we want to retrieve is:

$$\Theta = [\theta_1,\theta_2,\cdots]^T = \left[A_1,\phi_1,a_1,b_1,\mathbf{r}_{\perp,1}\right]^T, \tag{4.52}$$

To find the Fisher information matrix, we start from the expectation of the second order perturbation of $\mathscr{L}_P$ as shown in Eq. (3.21). It is seen that we needs to compute the derivative of O w.r.t. Θ, which is denoted by $\delta O(\Theta)(\delta\Theta)$ and $\delta O(\Theta)(\delta\tilde{\Theta})$. $\delta\Theta$ and $\delta\tilde{\Theta}$ are small perturbations of the parameters of the rectangular object:

$$\delta\Theta = [\delta A_1,\delta\phi_1,\delta a_1,\delta b_1,\delta x_1,\delta y_1]^T, \quad \delta\tilde{\Theta} = [\delta\tilde{A}_1,\delta\tilde{\phi}_1,\delta\tilde{a}_1,\delta\tilde{b}_1,\delta\tilde{x}_1,\delta\tilde{y}_1]^T. \tag{4.53}$$

δO is given by:

$$\delta O(\Theta)(\delta\Theta) = \begin{bmatrix} e^{\mathrm{i}\phi_1}\Pi_{a_1,b_1,\mathbf{r}_1}\delta A_1 \\ \mathrm{i}A_1e^{\mathrm{i}\phi_1}\Pi_{a_1,b_1,\mathbf{r}_1}\delta\phi_1 \\ C_1\Pi_{b_1}(y-y_1)\frac{1}{2}\left[\delta_D(x-x_1-\frac{a_1}{2})+\delta_D(x-x_1+\frac{a_1}{2})\right]\delta a_1 \\ C_1\Pi_{a_1}(x-x_1)\frac{1}{2}\left[\delta_D(y-y_1-\frac{b_1}{2})+\delta_D(y-y_1+\frac{b_1}{2})\right]\delta b_1 \\ C_1\Pi_{b_1}(y-y_1)\left[\delta_D(x-x_1-\frac{a_1}{2})-\delta_D(x-x_1+\frac{a_1}{2})\right]\delta x_1 \\ C_1\Pi_{a_1}(x-x_1)\left[\delta_D(y-y_1-\frac{b_1}{2})-\delta_D(y-y_1+\frac{b_1}{2})\right]\delta y_1 \end{bmatrix}, \tag{4.54}$$

where δ_D is Dirac delta function:

$$\delta_D(t) = \begin{cases} \infty, & t = 0, \\ 0, & t \neq 0, \end{cases} \qquad \int_{-\infty}^{\infty} f(x)\delta_D(t-t')dt = f(t'). \tag{4.55}$$

By using Eq. (4.38), Eq. (4.54) and Eq. (4.55), we obtain the elements of the Fisher matrix. The diagonal elements of the Fisher matrix are shown in Section 4.6.1.

4.7.3. DISCUSSION ABOUT FIG. 4.7

It is seen in Fig. 4.7 that the value of the cost function $\mathscr{G}$ is approximately a quadratic function w.r.t. a_1 and a linear function w.r.t. x_1 in the neighborhood of the actual values. This trend is explained in this section. Suppose now the measurements are noise-free. We start with Eq. (4.26) in this chapter and rewrite $\mathscr{G}$ by:

$$\mathscr{G} = \sum_{\mathbf{k}_\perp} \left| \mathscr{F}\left(\hat{O}-1\right)(\mathbf{k}_\perp) - h_1(k_y) a_1 \operatorname{sinc}\left(\frac{a_1 k_x}{2}\right) e^{\mathrm{i}k_x x_1} \right|^2, \tag{4.56a}$$

$$\mathscr{F}\left(\hat{O}-1\right)(\mathbf{k}_\perp) = h_1^{(\mathrm{o})}(k_y) a_1^{(\mathrm{o})} \operatorname{sinc}\left(\frac{a_1^{(\mathrm{o})} k_x}{2}\right) e^{\mathrm{i}k_x x_1^{(\mathrm{o})}}, \tag{4.56b}$$

where $a_1^{(\mathrm{o})}$ and $x_1^{(\mathrm{o})}$ are the actual values of a_1 and x_1, respectively. $h_1(k_y)$ is the auxiliary function give by:

$$h_1(C_1, b_1, k_y) = C_1 b_1 \operatorname{sinc}\left(\frac{b_1 k_y}{2}\right) e^{\mathrm{i}k_y y_1}, \tag{4.57}$$

and $h_1^{(\mathrm{o})}$ is the actual value of h_1. Note that h_1 and $h_1^{(\mathrm{o})}$ are not of interest for now because we are currently paying attention to a_1 and x_1. Suppose we assume the value of $\left|a_1 - a_1^{(\mathrm{o})}\right|$ and $\left|x_1 - x_1^{(\mathrm{o})}\right|$ are sufficiently small, we can expand Eq. (4.56a), yields:

$$\mathscr{G} \approx \sum_{\mathbf{k}_\perp} |B|^2 + \sum_{\mathbf{k}_\perp} |D|^2 - \sum_{\mathbf{k}_\perp} 2\Re\left[B^* \cdot D \cdot \mathrm{i}k_x \left(x_1 - x_1^{(\mathrm{o})}\right)\right], \tag{4.58}$$

where B and D are given by:

$$B = h_1^{(\mathrm{o})} a_1^{(\mathrm{o})} \operatorname{sinc}\left(\frac{a_1^{(\mathrm{o})} k_x}{2}\right), \tag{4.59}$$

$$D = \frac{2h_1}{k_x}\left[\sin\left(\frac{a_1^{(\mathrm{o})} k_x}{2}\right) + \frac{k_x}{2}\cos\left(\frac{a_1^{(\mathrm{o})} k_x}{2}\right)\left(a_1 - a_1^{(\mathrm{o})}\right)\right]. \tag{4.60}$$

It can be seen in Eq. (4.58) and Eq. (4.60) that $\mathscr{G}$ is approximately a quadratic function w.r.t. a_1 and a linear function w.r.t. x_1 when the value of $\left|a_1 - a_1^{(\mathrm{o})}\right|$ and $\left|x_1 - x_1^{(\mathrm{o})}\right|$ are sufficiently small.

4.7.4. DISCUSSION ABOUT THE DIAGONAL AND OFF-DIAGONAL TERMS OF THE FISHER INFORMATION MATRIX IN APPLICATION 2

In this section we compare the value of the diagonal and off-diagonal terms of the Fisher information matrix. We start by the expectation of the second order perturbation of $\mathscr{L}_P$ as given by Eq. (4.38):

$$E\left(\delta^2\mathscr{L}_P\right)(\Theta)(\delta\Theta,\delta\tilde{\Theta}) = \frac{2}{\hbar\omega}\sum_{\mathbf{k}'_\perp,j}\Re\left[\mathscr{F}\left[P_j\delta O(\Theta)(\delta\Theta)\right]\mathscr{F}\left[P_j\delta O(\Theta)(\delta\tilde{\Theta})\right]^*\right] + \frac{2}{\hbar\omega}\sum_{\mathbf{k}'_\perp,j}\Re\left[\frac{\mathscr{F}\left(\Psi_j\right)}{\mathscr{F}\left(\Psi_j\right)^*}\mathscr{F}\left[P_j\delta O(\Theta)(\delta\Theta)\right]^*\mathscr{F}\left[P_j\delta O(\Theta)(\delta\tilde{\Theta})\right]^*\right], \tag{4.61}$$

Suppose the perturbation δO has the following form:

$$\delta O(\Theta)(\delta\Theta) = f(\mathbf{r}_\perp)\delta_D(x-x_l), \quad \delta O(\Theta)(\delta\tilde{\Theta}) = f(\mathbf{r}_\perp)\delta_D(x-x_m), \tag{4.62}$$

where $l = 1,2,\cdots$, and $m = 1,2,\cdots$. δ_D is Dirac delta function. We can write:

$$\mathscr{F}\left[P_j\delta O(\Theta)(\delta\Theta)\right](\mathbf{k}'_\perp) = P_j(x_l,k'_y)f(x_l,k'_y)e^{-\mathrm{i}k'_x x_l}, \tag{4.63}$$

$$\mathscr{F}\left[P_j\delta O(\Theta)(\delta\tilde{\Theta})\right](\mathbf{k}'_\perp) = P_j(x_m,k'_y)f(x_m,k'_y)e^{-\mathrm{i}k'_x x_l}. \tag{4.64}$$

For simplicity, we define real valued auxiliary functions $u, v^{(1)}, v^{(2)}, w$ by:

$$u_j(x_l,x_m,k'_y)e^{\mathrm{i}v_j^{(1)}(x_l,x_m,k'_y)} = P_j(x_l,k'_y)f(x_l,k'_y)\cdot\left[P_j(x_m,k'_y)f(x_m,k'_y)\right]^*, \tag{4.65}$$

$$u_j(x_l,x_m,k'_y)e^{\mathrm{i}v_j^{(2)}(x_l,x_m,k'_y)} = \left[P_j(x_l,k'_y)f(x_l,k'_y)\cdot P_j(x_m,k'_y)f(x_m,k'_y)\right]^*, \tag{4.66}$$

$$e^{\mathrm{i}w_j(k'_x,k'_y)} = \mathscr{F}\left(\Psi_j\right)\left[\mathscr{F}\left(\Psi_j\right)^*\right]^{-1}. \tag{4.67}$$

Then Eq. (4.61) can be re-written as:

$$E\left(\delta^2\mathscr{L}_P\right) = \frac{2}{\hbar\omega}\sum_{k'_y,j}u_j^2(x_l,x_m,k'_y)\left[g_j^{(1)}(x_l,x_m,k'_y)+g_j^{(2)}(x_l,x_m,k'_y)\right], \tag{4.68}$$

where $g_j^{(1)}$ and $g_j^{(2)}$ are auxiliary functions given by:

$$g_j^{(1)}(x_l,x_m,k'_y) = \sum_{k'_x}\cos\left[(x_l-x_m)k'_x + v_j^{(1)}(x_l,x_m,k'_y)\right], \tag{4.69}$$

$$g_j^{(2)}(x_l,x_m,k'_y) = \sum_{k'_x}\cos\left[-(x_l+x_m)k'_x + w_j(k'_x,k'_y) + v_j^{(2)}(x_l,x_m,k'_y)\right]. \tag{4.70}$$

Note that $\mathbf{r}_\perp$ and $\mathbf{k}'_\perp$ have the relation as shown in Eq.(6) in this chapter.

We note that, when $l = m$, $g_j^{(1)}$ and $g_j^{(2)}$ are the diagonal elements of the Fisher matrix. When $l \neq m$, $g_j^{(1)}$ and $g_j^{(2)}$ corresponds to the off-diagonal elements of the Fisher matrix.

First we focus on $g_j^{(1)}$ which relates to the first term on the right hand side of Eq. (4.61). $g_j^{(1)}(x_l, x_m, k'_y)$ can be re-written as:

$$g_j^{(1)}(x_l, x_m, k'_y) = \begin{cases} N_x^{\text{det}} \cos[v_j^{(1)}(x_l, x_m, k'_y)], & l = m, \\ \dfrac{\sin[\pi(\Delta x)^{-1}(x_l - x_m)]}{\sin[\pi(N^{\text{det}}\Delta x)^{-1}(x_l - x_m)]} \cos\left[v_j^{(1)}(x_l, x_m, k'_y) + \frac{\pi(N^{\text{det}}-1)}{N^{\text{det}}\Delta x}(x_l - x_m) \right], & l \neq m. \end{cases} \tag{4.71}$$

To compare the value of $g_j^{(1)}$ for $l = m$ and $l \neq m$, we compute the ratio $g_{j,l\neq m}^{(1)} / g_{j,l=m}^{(1)}$ for various value of $v_j^{(1)}$. The results are shown in Fig. 4.10.

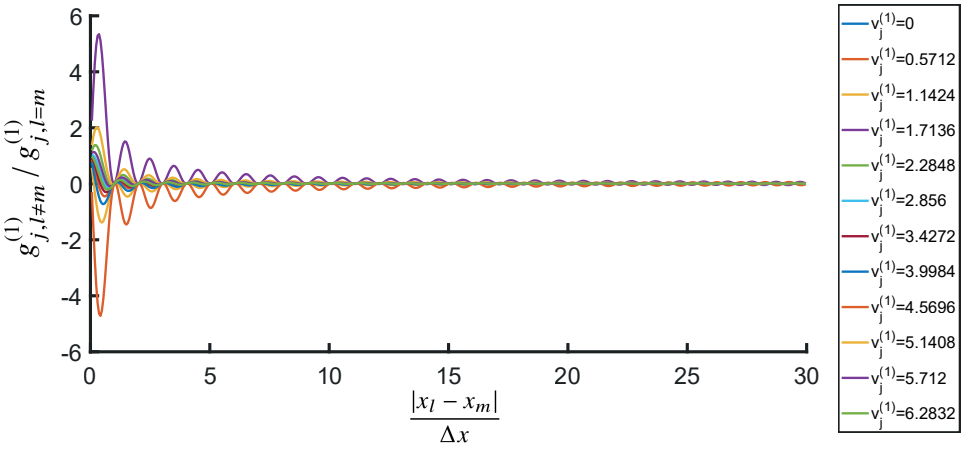

Figure 4.10: The ratio $g_{j,l\neq m}^{(1)} / g_{j,l=m}^{(1)}$ w.r.t. $|x_l - x_m|$ for various value of $v_j^{(1)}$. Here Δx is the size of individual cells of the discretized meshgrid $\mathbf{r}_\perp$ along the x-axis.

When $|x_l - x_m|(\Delta x)^{-1}$ is an integer, the perturbation in Eq. (4.62) can be used to calculate the descent gradient in conventional ptychography. This is because the variables in conventional ptychography are the values at the center of every individual grid cells of $\mathbf{r}_\perp$. We see in Fig. 4.10 that the ratio $g_{j,l\neq m}^{(1)} / g_{j,l=m}^{(1)}$ is extremely small when $|x_l - x_m|(\Delta x)^{-1}$ is integer, meaning that the off-diagonal elements of the Fisher matrix is extremely small compared to the diagonal elements. Therefore, there is no correlation between the variables in conventional ptychography.

When $|x_l - x_m|(\Delta x)^{-1}$ is a non-negative real number, the perturbation in Eq. (4.62) can be used to calculate the descent gradient in the proposed parameter retrieval scheme. We see in Fig. 4.10 that absolute value of the ratio $g_{j,l\neq m}^{(1)} / g_{j,l=m}^{(1)}$ decreases drastically when $|x_l - x_m|(\Delta x)^{-1}$ is increasing, which means that the off-diagonal elements of the Fisher matrix is extremely small comparing to the diagonal elements for large $|x_l - x_m|(\Delta x)^{-1}$. In our simulation for application 2, in which the characteristic parameters are shown in

Table. 3 in this chapter, the off-diagonal elements are negligible compared to the diagonal elements when $|x_l - x_m|(\Delta x)^{-1} > 10$. On the other hand, Fig. 4.10 indicates that $g^{(1)}_{j,l\neq m}$ cannot be neglected when $|x_l - x_m|(\Delta x)^{-1}$ is small. In particular, $g^{(1)}_{j,l\neq m}$ is even larger than $g^{(1)}_{j,l=m}$ when $|x_l - x_m|(\Delta x)^{-1} < 1$. Hence the off-diagonal elements of the Fisher matrix become dominant when x_l and x_m are in the same grid cell.

The value of $g^{(2)}_j$ is more difficult to be analyzed because the auxiliary function $w_j(k'_x, k'_y)$ is a function of k'_x. Since $w_j(k'_x, k'_y)$ is two times the phase of the diffracted wavefield in the far field, it is more difficult to find an analytic expression for $w_j(k'_x, k'_y)$.

REFERENCES

[1] X. Wei, H. P. Urbach, P. van der Walle, and W. M. Coene, *Parameter retrieval of small particles in dark-field fourier ptychography and a rectangle in real-space ptychography,* Ultramicroscopy **229**, 113335 (2021).

[2] A. M. Maiden, M. J. Humphry, F. Zhang, and J. M. Rodenburg, *Superresolution imaging via ptychography,* Journal of the Optical Society of America A **28**, 604 (2011).

[3] A. Szameit, Y. Shechtman, E. Osherovich, E. Bullkich, P. Sidorenko, H. Dana, S. Steiner, E. B. Kley, S. Gazit, T. Cohen-Hyams, S. Shoham, M. Zibulevsky, I. Yavneh, Y. C. Eldar, O. Cohen, and M. Segev, *Sparsity-based single-shot subwavelength coherent diffractive imaging,* Nature Materials **11**, 455 (2012).

[4] P. Sidorenko, O. Kfir, Y. Shechtman, A. Fleischer, Y. C. Eldar, M. Segev, and O. Cohen, *Sparsity-based super-resolved coherent diffraction imaging of one-dimensional objects,* Nature Communications **6** (2015), 10.1038/ncomms9209.

[5] D. Slepian and H. O. Pollak, *Prolate spheroidal wave functions, fourier analysis and uncertainty - i,* Bell System Technical Journal **40**, 43 (1961).

[6] A. Papoulis, *A new algorithm in spectral analysis and band-limited extrapolation,* IEEE Transactions on Circuits and Systems **22**, 735 (1975).

[7] P. Delsarte, A. J. E. M. Janssen, and L. B. Vries, *Discrete prolate spheroidal wave functions and interpolation,* SIAM Journal on Applied Mathematics **45**, 641 (1985).

[8] P. van der Walle, S. Hannemann, D. van Eijk, W. Mulckhuyse, and J. C. J. van der Donck, *Implementation of background scattering variance reduction on the rapid nano particle scanner,* in *Metrology, Inspection, and Process Control for Microlithography XXVIII*, edited by J. P. Cain and M. I. Sanchez (SPIE, 2014).

[9] P. van der Walle, E. Kramer, J. C. J. van der Donck, W. Mulckhuyse, L. Nijsten, F. A. B. Arango, A. de Jong, E. van Zeijl, H. E. T. Spruit, J. H. van den Berg, G. Nanda, A. K. van Langen-Suurling, P. F. A. Alkemade, S. F. Pereira, and D. J. Maas, *Deep subwavelength metrology for advanced defect classification,* in *Optical Measurement Systems for Industrial Inspection X*, edited by P. Lehmann, W. Osten, and A. A. Gonçalves (SPIE, 2017).

[10] P. J. S. Ferreira, *The stability of a procedure for the recovery of lost samples in band-limited signals,* Signal Processing **40**, 195 (1994).

[11] A. J. den Boef, *Optical wafer metrology sensors for process-robust CD and overlay control in semiconductor device manufacturing,* Surface Topography: Metrology and Properties **4**, 023001 (2016).

[12] P. Ansuinelli, W. M. J. Coene, and H. P. Urbach, *Automatic feature selection in EUV scatterometry,* Applied Optics **58**, 5916 (2019).

[13] D. J. Griffiths, *Introduction to Electrodynamics (3rd Edition)* (Prentice Hall, 1999).

[14] L. Novotny and B. Hecht, *Principles of Nano-Optics* (Cambridge University Press, 2012).

[15] J. Goodman, *Introduction to Fourier Optics*, McGraw-Hill physical and quantum electronics series (W. H. Freeman, 2005).

[16] P. van der Walle, P. Kumar, D. Ityaksov, R. Versluis, D. J. Maas, O. Kievit, J. Janssen, and J. C. J. van der Donck, *Increased particle inspection sensitivity by reduction of background scatter variance,* in *Metrology, Inspection, and Process Control for Microlithography XXVII*, edited by A. Starikov and J. P. Cain (SPIE, 2013).

[17] P. Godard, M. Allain, V. Chamard, and J. Rodenburg, *Noise models for low counting rate coherent diffraction imaging,* Optics Express **20**, 25914 (2012).

[18] P. Thibault and M. Guizar-Sicairos, *Maximum-likelihood refinement for coherent diffractive imaging,* New Journal of Physics **14**, 063004 (2012).

[19] W. Murray, M. H. Wright, and P. E. Gill, *Practical Optimization* (Emerald Publishing Limited, 1982).

[20] R. Fletcher, *Practical Methods of Optimization, 2nd Edition* (Wiley, 1988).

[21] X. Wei, H. P. Urbach, and W. M. J. Coene, *Cramér-rao lower bound and maximum-likelihood estimation in ptychography with poisson noise,* Physical Review A **102** (2020), 10.1103/physreva.102.043516.

[22] O. Bunk, M. Dierolf, S. Kynde, I. Johnson, O. Marti, and F. Pfeiffer, *Influence of the overlap parameter on the convergence of the ptychographical iterative engine,* Ultramicroscopy **108**, 481 (2008).

[23] X. Wei and P. Urbach, *Ptychography with multiple wavelength illumination,* Optics Express **27**, 36767 (2019).

[24] J. M. Rodenburg and R. H. T. Bates, *The theory of super-resolution electron microscopy via wigner-distribution deconvolution,* Philosophical Transactions of the Royal Society of London. Series A: Physical and Engineering Sciences **339**, 521 (1992).

[25] P. Thibault, M. Dierolf, A. Menzel, O. Bunk, C. David, and F. Pfeiffer, *High-resolution scanning x-ray diffraction microscopy,* Science **321**, 379 (2008).

[26] H. M. L. Faulkner and J. M. Rodenburg, *Movable aperture lensless transmission microscopy: A novel phase retrieval algorithm,* Physical Review Letters **93**, 023903 (2004).

[27] J. M. Rodenburg and H. M. L. Faulkner, *A phase retrieval algorithm for shifting illumination,* Applied Physics Letters **85**, 4795 (2004).

[28] P. Thibault, M. Dierolf, O. Bunk, A. Menzel, and F. Pfeiffer, *Probe retrieval in ptychographic coherent diffractive imaging,* Ultramicroscopy **109**, 338 (2009).

[29] S. Marchesini, A. Schirotzek, C. Yang, H. tieng Wu, and F. Maia, *Augmented projections for ptychographic imaging,* Inverse Problems **29**, 115009 (2013).

[30] J. Zhong, L. Tian, P. Varma, and L. Waller, *Nonlinear optimization algorithm for partially coherent phase retrieval and source recovery,* IEEE Transactions on Computational Imaging **2**, 310 (2016).

[31] M. Odstrčil, A. Menzel, and M. Guizar-Sicairos, *Iterative least-squares solver for generalized maximum-likelihood ptychography,* Optics Express **26**, 3108 (2018).

[32] H. J. W. George B. Arfken, *Mathematical Methods for Physicists* (Elsevier LTD, Oxford, 2012).

5

Conclusion and Outlook

5.1. CONCLUSION

In this thesis we have discussed different subjects in ptychography. In short, this thesis consists of three contributions:

(1) In Chapter 2 we have proposed a polychromatic ptychographic algorithm. With varying parameter settings (i.e. noise and the number of spectral components in the probe), different behaviors of the proposed method were observed and discussed in this chapter. The comparison between the proposed method and the PIM approach has been discussed also.

(2) In Chapter 3 we have studied the influence of Poisson noise on ptychography by analyzing the CRLB. The CRLB was derived and numerically computed for both top-hat plane wave and structured illumination. The computed results were validated with Monte Carlo analysis. Furthermore, the statistical properties of the maximum likelihood estimation and the cost function minimization algorithm were studied in this chapter.

(3) In Chapter 4 we have demonstrated a parameter retrieval method in ptychography by implementing the method for two applications. In application 1 we explored how to retrieve the parameters of small particles from Fourier ptychographic dark field measurements. In application 2 we studied the retrieval of the parameters of a rectangular shaped object embedded in a homogeneous background. The influence of Poisson noise on the parameter retrieval method was discussed by analyzing the CRLB.

There are some research subjects which have not been presented in this thesis and which deserve further attention. These subjects are listed in the next section.

5.2. OUTLOOK

5.2.1. MINIMIZATION OF THE CRLB IN PTYCHOGRAPHY

In Chapter 4 we have discussed the parameter retrieval method in ptychography, and it was shown that the CRLB of the retrieved parameters depend on the probe. Therefore, when the illuminating photon count is constant, it should be possible to minimize the CRLB of parameter that is to be retrieved by engineering the probe. In this section we attempt to find the minimum of the CRLB by shaping the wavefront of the illumination.

In this section we try to continue the work of application 2 in Chapter 4, and consider again the setup as shown in Fig. 4.5. The probe function $P(\mathbf{r}_\perp)$ is in the object plane. We have already assumed that the probe has a finite support with a circular boundary. Inside the circular boundary, the amplitude of the probe is assumed to be uniform. Hence the probe can be written as:

$$P(\mathbf{r}_\perp) = \begin{cases} \exp\left[\mathrm{i}\phi(\mathbf{r}_\perp)\right], & |\mathbf{r}_\perp| \leq r_0, \\ 0, & |\mathbf{r}_\perp| > r_0, \end{cases} \tag{5.1}$$

and we assume that the wavefront of the probe can be decomposed into Zernike poly-

nomials:

$$\phi(\mathbf{r}_\perp) = \sum_{q=1}^{N_Z} \rho_q Z_q(\frac{\mathbf{r}_\perp}{r_0}), \tag{5.2}$$

where Z_q is the Zernike polynomials of qth order and ρ_q is its coefficient. Note that only the first N_Z Zernike polynomials are considered, hence N_Z is also the number of degrees of freedom of the optimization problem.

In Chapter 4, the Fisher information matrix was calculated analytically. The CRLB of the parameters of the rectangle can be computed numerically by inversion of the Fisher matrix. The computed CRLBs are denoted by:

$$\text{CRLB}(\theta_i) = \left[\text{CRLB}(a_1), \text{CRLB}(b_1), \text{CRLB}(x_1), \text{CRLB}(y_1)\right]^T. \tag{5.3}$$

First we try to find the minimum of the CRLB of one of the parameters, e.g. $\text{CRLB}(a_1)$. To minimize the CRLB, one can apply optimization techniques, e.g. gradient descent method, to $\text{CRLB}(\theta_i)$ w.r.t. the Zernike coefficients ρ_q for all q. Therefore the problem we want to address is:

$$\arg\min_{\rho_q} \ \text{CRLB}(\theta_i), \quad \text{for } \ q = 1, \cdots, N_Z. \tag{5.4}$$

The problem given in Eq. (5.4) is solved by using the 'fminunc' solver in MATLAB. It is likely that the landscape of $\text{CRLB}(\theta_i)$ w.r.t. the Zernike coefficients ρ_q is not convex, i.e. there could be many local minimas. A semi-global minima could be found by starting the algorithm with many different initial choices. For now we let the probe function be such that $\rho_q = 0$ for all q. Hence the local minima we find may be expected to be a probe with a smooth wavefront.

Now we try to minimize $\text{CRLB}(a_1)$. We define the illumination power by means of the total photon number counting in the cross section of the probe:

$$\text{PN}^{\text{rect}} = \sum_{\mathbf{r}_\perp}^{N_x^{\text{det}}, N_y^{\text{det}}} \frac{|P(\mathbf{r}_\perp)|^2}{\hbar\omega}, \tag{5.5}$$

In the following we choose $\text{PN}^{\text{rect}} = 10^6$. The obtained $N_Z = 20$ are shown in Table. 5.1 and Table. 5.2, respectively. The corresponding amplitude and phase of the probe are shown in Fig. 5.1 and Fig. 5.2. For $N_Z = 5$ the computed minimum value of $\text{CRLB}(a_1)$ is 3.29×10^{-7}, while for $N_Z = 20$ it is 3.11×10^{-7}. Therefore, we conclude that a larger value of N_Z will lead to a lower CRLB. We remark that these results correspond to the current simulation settings, i.e. the actual object, the initial probe and the characteristic parameters as shown in Table. 4.4. Adjusting any of these settings can lead to a different result.

We can see in the simulation that the proposed method can indeed leads to a minimization of the CRLB. Since the CRLB is the lower bound on the variance of any unbiased estimator, the minimization of the CRLB in principle leads to a more noise insensitive system. To minimize the CRLB, we need to select a couple of parameters as the variables. In practice, this selection could be constrained by the system. For example, suppose we

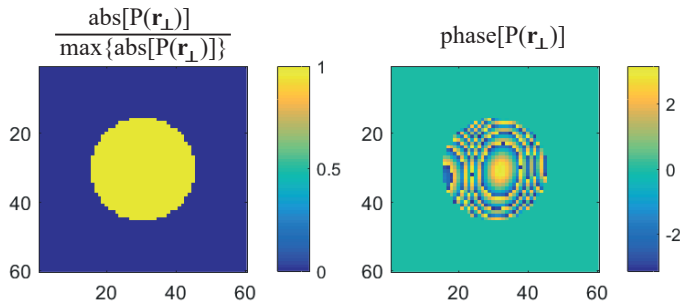

Figure 5.1: The optimized probe which consists 5 Zernike polynomials in its phasor, i.e. $N_Z = 5$.

Table 5.1: The optimized Zernike coefficients when $N_Z = 5$.

Zernike order index q	1	2	3	4	5
initial value ρ_q	0	0	0	0	0
optimal value ρ_q	9.7418	1.8836	-15.1287	-9.1700	-3.0251

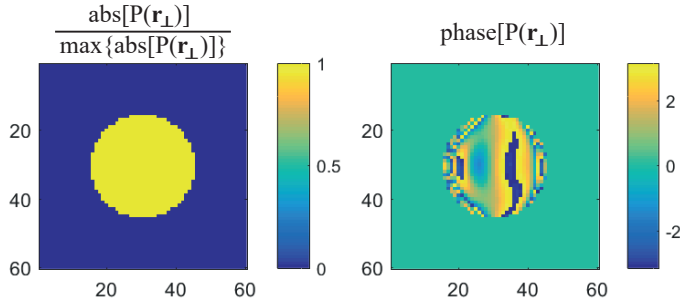

Figure 5.2: The optimized probe which consists 20 Zernike polynomials in its phasor, i.e. $N_Z = 20$.

Table 5.2: The optimized Zernike coefficients when $N_Z = 20$.

Zernike order index q	1	2	3	4	5
initial value ρ_q	0	0	0	0	0
optimal value ρ_q	2.5966	0.2292	-3.8777	-4.5659	0.0016
Zernike order index q	6	7	8	9	10
initial value ρ_q	0	0	0	0	0
optimal value ρ_q	1.0909	0.0199	-4.3500	-2.4350	0.3744
Zernike order index q	11	12	13	14	15
initial value ρ_q	0	0	0	0	0
optimal value ρ_q	-5.0278	0.2344	3.8402	-0.0355	-2.0779
Zernike order index q	16	17	18	19	20
initial value ρ_q	0	0	0	0	0
optimal value ρ_q	-0.4372	0.0562	0.6778	-0.0866	-2.7368

wish to implement application 2 in Chapter 4 with X-ray sources. It is not easy to manipulate the amplitude and the wavefront of the probe in the object plane and the probe is usually de-focused. Therefore, one may try to minimize the CRLB by manipulating the probe at far away before the object. On the other hand, we emphasize that the CRLB is a function of the actual object. Therefore, it is not easy to find a system where the CRLB is minimized for all kinds of objects.

5.2.2. PTYCHOGRAPHY WITH SPATIALLY PARTIAL COHERENT ILLUMINATION

As said in the first part of Section 1.3.4, it is necessary to develop a ptychographic algorithm for partial coherent illumination because many X-ray light sources are either spatially partially coherent (e.g. synchrotron radiation [1, 2]) or temporally partial coherent (e.g. tabletop high-harmonic generation laser [3, 4]). To increase the spatial coherence of the light beam in practice, a pinhole is usually placed in the illumination path between the light source and the object. This approach is undesirable because it leads to a decrease of the throughput and hence decreases the SNR. For quasi-monochromatic and spatially partial coherent wavefield, it has been shown that one can use the mode decomposition method [5–7], the de-convolution methods [8–12], etc. Here we demonstrate a spatially partial coherent ptychographic method which is based on the gradient descent scheme. Simulation result shows that, by using the proposed method, both the object and the mutual coherence function of the illumination can be retrieved simultaneously.

Let us consider a system as shown in Fig. 5.3. A quasi-monochromatic and spatially partial coherent light beam illuminates an object with a complex transmission function $O(\mathbf{r}_\perp)$. We assume that the illumination has a finite support with a circular boundary and that it has a uniform distributed intensity over the object plane. The mutual coherence function of the illumination beam is denoted by J. J is a 4D array in principle. Here for the sake of simplicity we assume that J is transverse invariant: $J = J(\Delta\mathbf{r}_\perp)$, where $\Delta\mathbf{r}_\perp$ denotes distance between two position vectors in the object plane. Note that J is in this way reduced to a 2D array.

The goal is to retrieve $O(\mathbf{r}_\perp)$ and $J(\Delta\mathbf{r}_\perp)$ from ptychographic measurements $I_j(\mathbf{k}'_\perp)$, which for probe position j is given by [13]:

$$\begin{aligned} I_j(\mathbf{k}'_\perp) &= \iint \left[\left(\mathbf{1}_{\circ,j}\cdot O\right) \star \left(\mathbf{1}_{\circ,j}\cdot O\right)^*\right](\Delta\mathbf{r}_\perp)\cdot J(\Delta\mathbf{r}_\perp) e^{-\mathrm{i}\frac{2\pi}{\lambda z'}\Delta\mathbf{r}_\perp\cdot\mathbf{r}'_\perp} d\Delta\mathbf{r}_\perp \\ &= \left|\mathscr{F}\left(\mathbf{1}_{\circ,j}\cdot O\right)\right|^2(\mathbf{k}'_\perp) \otimes \mathscr{F}(J)(\mathbf{k}'_\perp), \end{aligned} \tag{5.6}$$

where $\mathbf{k}'_\perp = 2\pi\mathbf{r}'_\perp(\lambda z')^{-1}$ according to Eq. (1.65), $*$ denotes complex conjugate, and $\star$ and $\otimes$ denote correlation and convolution, respectively. $\mathbf{1}_{\circ,j}$ is the binary window function determined by the circular support of the probe, which is defined by:

$$\mathbf{1}_{\circ,j}(\mathbf{r}_\perp) = \begin{cases} 1, & \left|\mathbf{r}_\perp - \mathbf{R}_{\perp,j}\right| \le r_0, \\ 0, & \left|\mathbf{r}_\perp - \mathbf{R}_{\perp,j}\right| > r_0. \end{cases} \tag{5.7}$$

Note that, according to the van Cittert–Zernike theorem [13, 14], the mutual coherent function $J(\Delta\mathbf{r}_\perp)$ is equal to the Fourier transform of the intensity of the extended spatially incoherent source if the distance from the source to the object is much greater than the

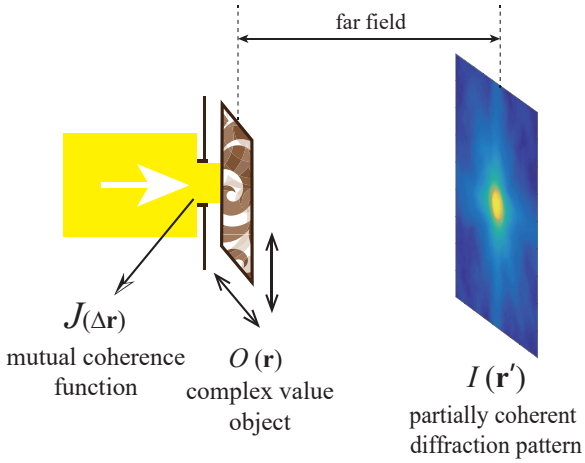

Figure 5.3: Schematic illustration of spatially partial coherent ptychography.

size of the object. Therefore, $\mathscr{F}(J)$ is always a function with non-negative real value, and hence I_j as given in Eq. (5.6) is always an array with non-negative values, as should be.

To retrieve $O(\mathbf{r}_\perp)$ and $J(\Delta\mathbf{r}_\perp)$, we minimize the cost function defined by:

$$\mathscr{E} = \sum_j \sum_{\mathbf{k}'_\perp} \left[\sqrt{I_j^{\mathrm{m}}(\mathbf{k}'_\perp)} - \sqrt{I_j(\mathbf{k}'_\perp)} \right]^2, \tag{5.8}$$

where $I_j^{\mathrm{m}}(\mathbf{r}'_\perp)$ is the measured intensity when the probe is at position $\mathbf{R}_{\perp,j}$ and $I_j(\mathbf{r}'_\perp)$ is the estimated diffraction intensity. The minimization is done by applying the gradient descent method. Using a similar calculation as in Section 1.3.1, we can derive the update formula for $O(\mathbf{r}_\perp)$:

$$O_{n+1}(\mathbf{r}_\perp) = O_n(\mathbf{r}_\perp) - \beta_O \sum_j \mathscr{F}^{-1} \left[\left(\frac{\sqrt{I_j^{\mathrm{m}}(\mathbf{k}'_\perp)}}{\sqrt{I_{j,n}(\mathbf{k}'_\perp)}} - 1 \right) \otimes \mathscr{F}(J_n)(-\mathbf{k}'_\perp) \right] (\mathbf{r}_\perp) \otimes \left(\mathbf{1}_j \cdot O_n \right)(\mathbf{r}_\perp), \tag{5.9}$$

where n is the index of the iteration and β_O denotes the step size coefficient which is chosen to be constant. As for the retrieval of the mutual coherence function, we choose to apply the gradient descent method w.r.t. the Fourier transform of J, and we obtain:

$$\mathscr{F}(J_{n+1})(\mathbf{k}'_\perp) = \mathscr{F}(J_n)(\mathbf{k}'_\perp) - \beta_J \sum_j \left[\left(\frac{\sqrt{I_j^{\mathrm{m}}(\mathbf{k}'_\perp)}}{\sqrt{I_{j,n}(\mathbf{k}'_\perp)}} - 1 \right) \otimes \mathscr{F}^{-1} \left[\left(\mathbf{1}_j \cdot O \right) \star \left(\mathbf{1}_j \cdot O \right)^* \right] (\mathbf{k}'_\perp) \right], \tag{5.10}$$

where β_J is a step size coefficient as well.

It is interesting that the proposed partial coherent ptychographic method has update formulas which are very similar to the method given in [11]. On the one hand,

both methods deal with the spatially partial coherence effect in ptychography by simultaneously retrieving the object's transmission function and the intensity of the extended incoherent source in the detector plane, i.e. $\mathscr{F}(J)$. On the other hand, in both methods the gradient descent approach to formulate their iterative retrieval algorithms is used. However, the two methods are not identical because the cost function that is minimized is different for the two methods. For the fully coherent case, it has been shown that the cost function given in Eq. (5.8) is more preferred when the measurement is noisy [15]. However, to the best of our knowledge, it is still an open question which cost function is more favorable. Therefore, it maybe worth to compare the performance of the two methods in the more general case of partial coherent illumination and it is desirable to further study this topic.

5.2.3. EXTRACTING 3D INFORMATION IN PTYCHOGRAPHY WITH POLYCHROMATIC ILLUMINATION

In Chapter 2 we have developed a polychromatic ptychography algorithm which is based on the projection approximation given in Eq. (1.37) and Eq. (2.1). However, if we discard the projection approximation and instead use the first Born approximation, we show in the following derivation that the polychromatic diffraction pattern in fact encodes a certain amount of 3D information about the object.

Suppose that the incident wavefield have many wavelenths and is fully coherent for each wavelength. Let $U_{\text{in}}(\mathbf{r},\lambda_k)$ be the incident scalar wavefield of kth wavelength and assume that all incident wavefields are plane waves:

$$U_{\text{in}}(\mathbf{r},\lambda_k) = A(\lambda_k)e^{\mathrm{i}\mathbf{k}_{\text{in},k}\cdot\mathbf{r}}, \tag{5.11}$$

where $\mathbf{k}_{\text{in},k}$ is the wave number of the incident wavefield of kth wavelength and $\left|\mathbf{k}_{\text{in},k}\right| = 2\pi(\lambda_k)^{-1}$ where λ_k is the kth wavelength in free space. $A(\lambda_k)$ denotes the temporal spectrum of the incident wavefield. According to Eq. (1.31) and Eq. (1.32), the scattered wavefield of the kth wavelength at position $\mathbf{r}'$ is given by:

$$\begin{aligned} U_{\text{scat}}(\mathbf{r}',\lambda_k) &\approx \frac{k_k^2}{4\pi}\frac{\exp\left(\mathrm{i}\frac{2\pi}{\lambda_k}\left|\mathbf{r}'\right|\right)}{\left|\mathbf{r}'\right|}\cdot A(\lambda_k)\mathscr{F}\left[\left(n_{\text{r}}^2(\mathbf{r})-1\right)\right]\left(k_k\frac{\mathbf{r}'}{\left|\mathbf{r}'\right|}+\mathbf{k}_{\text{in},k}\right) \\ &= \frac{k_k^2}{4\pi}\frac{\exp\left(\mathrm{i}\frac{2\pi}{\lambda_k}\left|\mathbf{r}'\right|\right)}{\left|\mathbf{r}'\right|}\cdot A(\lambda_k)\mathscr{F}\left[V_{\text{r}}(\mathbf{r})\right]\left(k_k\frac{\mathbf{r}'}{\left|\mathbf{r}'\right|}+\mathbf{k}_{\text{in},k}\right), \end{aligned} \tag{5.12}$$

where $\mathscr{F}$ is the 3D Fourier transform and $V_{\text{r}}(\mathbf{r}) = n_{\text{r}}^2(\mathbf{r})-1$ denotes the contrast of refractive index of the object to the free space. We assume that material dispersion can be neglected. $k_k = 2\pi(\lambda_k)^{-1}$ is the wavenumber of the kth wavelength in free space. The measurements consist of the sum of the intensities of the scattered wavefields of the different wavelengths in a plane z':

$$I(\mathbf{r}'_\perp,z') = \mathbf{1}_D(\mathbf{r}'_\perp)\cdot\sum_k\left|U_{\text{scat}}(\mathbf{r}'_\perp,z',\lambda_k)\right|^2, \tag{5.13}$$

where $\mathbf{1}_D(\mathbf{r}'_\perp)$ is the binary window function representing the region of the detector as given in Eq. (2.5), z' is the distance between the detector and the object and $\mathbf{r}'_\perp$ is the 2D coordinate in the detector plane.

Eq. (5.13) shows that, the scattered wavefield of different wavelengths contain different information about the object. This is schematically shown in Fig. 5.4. As example, we illustrate the scattering of three wavelengths in Fig. 5.4(b) and Fig. 5.4(c). Fig. 5.4(b) is plotted in real space and Fig. 5.4(c) in reciprocal space. The relation of the wavenumber of three wavelength components in the wavefield, i.e. k_1, k_2 and k_3, is also shown in Fig. 5.4(b) and Fig. 5.4(c). The wavefield of each wavelength can be mapped onto the corresponding Ewald sphere. The radius of each Ewald sphere equals to the wavenumber. Fig. 5.4(c) indicates the opportunity of extracting 3D information of the object from the polychromatic diffraction pattern, which is an interesting subject for future research. The validity of the idea relates to the validity of the first Born approximation of course, and also depends on how much of reciprocal space can be covered by the Ewald spheres.

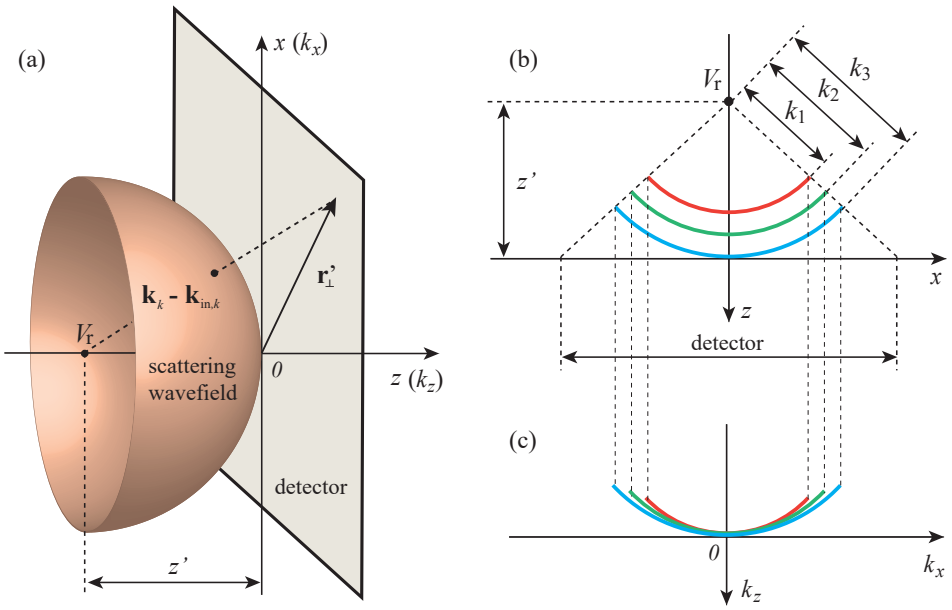

Figure 5.4: Schematic illustration of the scattering model to the far field, with plane wave illumination along the z axis. The y axis is ignored in this plot. (a) The set of plane wave vectors that occur in the scattered (reflected) far field when the sample is illuminated by a plane wave with wave vector $\mathbf{k}_{\text{in},k}$ along the z-axis. (b) A schematic example on polychromatic scattering from the scatterer V_r to the far field detector. The distance of the scatterer and the detector is z'. The wavefield contains 3 wavelength components, i.e. k_1, k_2 and k_3. The relation of the wavenumber of these components is also shown in this subplot. (c) Cross-section in the $k_x$and k_z plane of the set of plane wave vectors that occur in the reflected far field when the sample is illuminated by perpendicular incident plane wave for three different wavelengths. that occur in the reflected far field.

REFERENCES

[1] L. W. Whitehead, G. J. Williams, H. M. Quiney, D. J. Vine, R. A. Dilanian, S. Flewett, K. A. Nugent, A. G. Peele, E. Balaur, and I. McNulty, *Diffractive imaging using partially coherent x rays,* Phys. Rev. Lett. **103**, 243902 (2009).

[2] J. Clark, X. Huang, R. Harder, and I. Robinson, *High-resolution three-dimensional partially coherent diffraction imaging,* Nature Communications **3** (2012), 10.1038/ncomms1994.

[3] B. Chen, R. A. Dilanian, S. Teichmann, B. Abbey, A. G. Peele, G. J. Williams, P. Hannaford, L. Van Dao, H. M. Quiney, and K. A. Nugent, *Multiple wavelength diffractive imaging,* Phys. Rev. A **79**, 023809 (2009).

[4] S. Witte, V. T. Tenner, D. W. Noom, and K. S. Eikema, *Lensless diffractive imaging with ultra-broadband table-top sources: from infrared to extreme-ultraviolet wavelengths,* Light: Science & Applications **3**, e163 (2014).

[5] E. Wolf, *New theory of partial coherence in the space–frequency domain part i: spectra and cross spectra of steady-state sources,* Journal of the Optical Society of America **72**, 343 (1982).

[6] A. Starikov and E. Wolf, *Coherent-mode representation of gaussian schell-model sources and of their radiation fields,* Journal of the Optical Society of America **72**, 923 (1982).

[7] S. Flewett, H. M. Quiney, C. Q. Tran, and K. A. Nugent, *Extracting coherent modes from partially coherent wavefields,* Optics Letters **34**, 2198 (2009).

[8] D. H. Parks, X. Shi, and S. D. Kevan, *Partially coherent x-ray diffractive imaging of complex objects,* Physical Review A **89** (2014), 10.1103/physreva.89.063824.

[9] B. Enders, M. Dierolf, P. Cloetens, M. Stockmar, F. Pfeiffer, and P. Thibault, *Ptychography with broad-bandwidth radiation,* Applied Physics Letters **104**, 171104 (2014).

[10] N. Burdet, X. Shi, D. Parks, J. N. Clark, X. Huang, S. D. Kevan, and I. K. Robinson, *Evaluation of partial coherence correction in x-ray ptychography,* Optics Express **23**, 5452 (2015).

[11] J. Zhong, L. Tian, P. Varma, and L. Waller, *Nonlinear optimization algorithm for partially coherent phase retrieval and source recovery,* IEEE Transactions on Computational Imaging **2**, 310 (2016).

[12] W. Yu, S. Wang, S. Veetil, S. Gao, C. Liu, and J. Zhu, *High-quality image reconstruction method for ptychography with partially coherent illumination,* Physical Review B **93** (2016), 10.1103/physrevb.93.241105.

[13] J. Goodman, *Statistical optics* (Wiley, New York, 1985).

[14] M. Born, *Principles of Optics* (Elsevier Science, City, 1980).

[15] M. Guizar-Sicairos and J. R. Fienup, *Phase retrieval with transverse translation diversity: a nonlinear optimization approach,* Optics Express **16**, 7264 (2008).

A

ABBREVIATIONS

BVR	- the bias-variance ratio.87
CDI	- Coherent Diffraction Imaging. ix
CZT	- chirp Z-transform. 9
CRLB	- the Cramér Rao Lower Bound.70
DoF	- depth of focus. 8
DFT	- discrete Fourier transform. 9
DM	- the difference-map algorithm. 15
ER	- the Error-Reduction algorithm. 14
EUV	- extreme ultraviolet.ix
FFT	- discrete fast Fourier transform. 10
FoV	- field-of-view. 17
FTH	- the Fourier transform holography method .23
HIO	- the Hybrid-Input-Output algorithm. 15
MLE	- the maximum likelihood estimator.73
NEF	- the normalized error in Fourier space.48
NER	- the normalized error in real space.48
NA	- numerical aperture.101
PIE	- the Ptychographic Iterative Engine algorithm. 16
PIM	- the ptychographic information multiplexing method.44
PN	- the total photon number counting over the cross section of the probe.76
PN^m	- the total photon number counting over the measured diffraction intensity.52
PSL	- polystyrene latex.101
SNR	- signal-to-noise ratio.30
SNR_P	- the signal-to-noise ratio of Poisson noise.89
TIE	- the transport of intensity equation method .22
Var	- the variance of an estimator.73
w.r.t.	- "with respect to". 5
WDD	- the Wigner Distribution De-convolution method. 16

B

DENOTATIONS

$\mathbf{B}$ - magnetic field. 3
c - the speed of light in vacuum. 4
$\mathbf{D}$ - displacement field. 3
diag - the diagonal elements of a matrix.73
$\mathbf{E}$ - electrical field. 3
E - expectation.73
E_F - the normalized error in Fourier space.48
E_R - the normalized error in real space.48
E_{scat} - scalar scattered amplitude.102
$\mathscr{E}$ - cost function.24
$\mathscr{E}_j$ - the cost function for jth illumination in ptychography.19
$\hat{\mathbf{e}}_p$ - polarization direction.101
$\mathscr{F}$ - 3D Fourier transform. 7
$\mathscr{F}_\perp$ - 2D Fourier transform. 5
$\mathscr{F}_\perp^{-1}$ - 2D inverse Fourier transform. 5
G - scalar Green's function. 6
$\mathbf{H}$ - magnetizing field. 3
h - the Planck constant.52
$\hbar$ - the Planck constant.71
I - intensity measurement. 2
I^{m} - the measured intensity.24
I_F - the Fisher information matrix.73
j - the index of relative position between the probe and the object in ptychography.18
J - mutual coherent function.28
J_1 - Bessel function of the first kind of order 1.113
J_2 - Bessel function of the first kind of order 2.113
$\mathbf{k}$ - 3D Cartesian coordinates in reciprocal space. 5
$\mathbf{k}_\perp$ - 2D Cartesian coordinates of spatial frequency. 5
k - wave number. 4

B

$\mathbf{k}'_\perp$ - 2D coordinates of spatial frequency derived from $\mathbf{r}'_\perp$ in the detector plane. 18
L - Lagrange function.25
$\mathbf{L}_\perp$ - the finite extent of the object. 12
$\mathscr{L}_P$ - the negative log-likelihood functional of Poisson noise model.71
n_r - refractive index. 4
n_j - the number of detected photons for each detector pixel and for jth illumination.71
N_j - the expectation value of n_j.71
$\mathbf{n}_{\mathbf{r},\perp}$ - index of 2D rectangular meshgrid in real space. 9
$\mathbf{n}_{\mathbf{k},\perp}$ - index of 2D rectangular meshgrid in reciprocal space. 9
N_x^det - the number of pixels of the detector in the x-axis.19
N_y^det - the number of pixels of the detector in the y-axis.19
$\mathscr{N}$ - the normal distribution.73
O - object. 2
P - probe. 2
$\mathbf{p}$ - dipole moment.101
$\mathscr{P}_P$ - the probability distribution of Poisson noise model.71
$\mathbf{r}$ - 3D Cartesian coordinates in real space. 3
$\mathbf{r}_\perp$ - 2D Cartesian coordinates in the object plane. 3
$\mathbf{r}'_\perp$ - 2D Cartesian coordinates in the detector plane. 18
$\mathbf{R}_{\perp,j}$ - the jth relative position between the probe and the object in ptychography.18
S - finite size boundary support. 10
U - solution of the scalar Helmholtz equation. 4
W - Wigner distribution function.21
β - feedback parameter of iterative phase retrieval algorithms. 15
γ - regularization parameter.46
$\gamma_{1,2}$ - the complex degree of coherence. 12
δ_D - Dirac's delta function. 6
$\Delta\mathbf{k}_\perp$ - the size of single cell of the 2D meshgrid in reciprocal space. 9
$\Delta\mathbf{r}_\perp$ - the size of single cell of the 2D meshgrid in real space. 9
ϵ - permittivity. 4
Θ - vector of parameters.72
$\hat{\Theta}$ - the estimator ofΘ.73
λ - wavelength. 4
λ_L - Lagrange multiplier.25
Λ - temporal spectrum of the illumination.44
μ - permeability. 4
π_O - the projection in real space. 13
π_F - the projection in Fourier space. 13
σ_S - over-sampling factor. 11
Ψ - exit wave immediately behind the object. 8
ω - temporal frequency. 2
$\Re$ - the real part of a complex number.25
$\Im$ - the imaginary part of a complex number.26
$\mathbf{1}_D$ - the binary window function representing the region of the detector.46
$\mathbf{1}_\Omega$ - binary window function in reciprocal space.104

$\star$ - auto-correlation.23
$*$ - complex conjugation.23
$\otimes$ - convolution.109

CURRICULUM VITÆ

Xukang WEI

22-03-1994 Born in Tianjin, China.

EDUCATION

2012–2016 Undergraduate in Appied Physics
Nankai University

2014–2014 Exange student in Appied Physics
National Taiwan Normal University

2017–2021 PhD. Physics
Delft University of Technology
Thesis: New methods and applications of ptychography
Promotor: Prof. dr. H. P. Urbach

List of Publications

5. **X. Wei**, H.P. Urbach, P. Van der Walle, W.M.J. Coene *Parameter retrieval of small particles in dark-field Fourier ptychography and a rectangle in real-space ptychography*, Ultramicroscopy **229**, 113335 (2021).

4. **X. Wei**, H.P. Urbach, W.M.J. Coene *Cramér Rao lower bound and maximum likelihood estimation in ptychography with Poisson noise*, Physical Review A **102**, 043516 (2020).

3. **X. Wei**, H.P. Urbach, *Ptychography with multiple wavelength illumination*, Optics Express **27**, 25 (2019).

2. S. Roy, S.F. Pereira, H.P. Urbach, **X. Wei**, O. El Gawhary, *Exploiting evanescent-wave amplification for subwavelength low-contrast particle detection*, Physical Review A **96**, 013814 (2017).

1. H. Guo, M. Feng, F. Song, H. Li, A. Ren, **X. Wei**, Y. Li, X. Xu, J. Tian, *Q-Switched Erbium-Doped Fiber Laser Based on Silver Nanoparticles as a Saturable Absorber*, IEEE Photonics Technology Letters **28**, 2 (2015).